Grain Size and Magnitude of Post-Earthquake Debris Flows

Erin Harvey

School of Earth and Environmental Sciences

Cardiff University

Thesis submitted for the degree of

Doctor of Philosophy

October 2022

Summary

Post-earthquake debris flows pose significant hazards to recovering local communities and transport large volumes of co-seismic sediment from hillslopes into higher order channels. In the decade after the 2008 Wenchuan earthquake, several extremely large debris flows have occurred. These debris flows, hereafter referred to as catastrophic debris flows, bulked to volumes (>10^5 m^3) much larger than their initiation volumes by rapidly entraining sediment. Controls on the runout and magnitude of these catastrophic debris flows are poorly constrained due to the lack of in-field measurements and the infrequent and unpredictable nature of large debris flows.

In this thesis I used field investigations of debris flow grain-size distributions (GSDs) and modelling to infer controls on the runout length of catastrophic debris flows. I first compared five different methods to identify the most accurate approach to measure mass movement deposit GSDs. Based on these results, I then used three methods (sieving, manual photo counts and automated tool, pyDGS) to collect high-resolution GSDs for two post-earthquake debris flows in Wenchuan. Both debris flows were triggered from co-seismic sediment in the same storm event but had vastly different runout lengths. The debris flows deposited similar GSDs in terms of width and maximum size, suggesting that grain size was not the primary control on runout length in these locations. Using a multi-temporal inventory, I then analysed controls on debris flow magnitude regionally. I found that catastrophic debris flows were more frequent than estimated when assuming a single magnitude-frequency distribution for all debris flows. Finally, I used the runout model Massflow to demonstrate that bed saturation, basal friction angle and triggering volume all controlled the runout of catastrophic debris flows. Magnitude-frequency distributions based on simulated debris flows, where parameters were described using field and remotely sensed data, also underestimated the frequency of catastrophic debris flows. This thesis used local and landscape-scale datasets to infer that catastrophic debris flows should be considered as a separate process. By currently considering all post-earthquake debris flows on a single continuum we may be underestimating the risk posed by debris flows to infrastructure and life.

Contents Page

List of Figures

List of Tables

List of Equations

Acknowledgements

First and foremost, I would like to thank my main supervisor, TC Hales. TC, I am constantly inspired by your vast scientific understanding, your work-life balance and enthusiasm in the field. Thank you for being so generous with your time, encouraging me to think critically (and concisely) about my research questions, teaching me how to dig a "Twitter-worthy" pit, ensuring I took a break (even if the break involved running) and the many cups of tea from Brodies and beers in Switzerland. This PhD would not have been possible without your support. I also want to thank my second supervisors, Daniel Hobley and Michael Singer. Thank you, Dan, for the enthusiasm, numerous paper recommendations and coding support in the early stages of my PhD as well as taking me under your wing at EGU 2018! Discussions with Michael and Mark Cuthbert, as my review panel convenor, were also invaluable, and their alternative perspectives helped shape my research questions and direction. Thanks must also go to Alex Horton for helping me with Massflow, I know it was a pretty painful process! My PhD was funded by the NERC GW4+ DTP. I am grateful for their support and the opportunities to meet other PhD students.

I spent the last four years surrounded by many great colleagues and friends. Firstly, I must thank all the Cardiff geomorphologists who have helped me along the way; Ollie, Lucy (honorary geomorphologist), Jian, Ming, Danielle, Josh, Claire & Shasta. Ollie, I can't thank you enough for welcoming me into the lab and continuing to support me throughout the last four years (and for the great food recommendations in Cardiff & Chengdu). Thank you Lucy and Danielle for all the distractions (especially the 1.22 allotment and virtual coffees) as well as supporting my successes. Shasta, thank you for the lunches, fun days out and always giving me an honest perspective on academic life. I also can't forget the Switzerland crew – Henrik, Liz, Amy & Sammie. These fieldtrips were a highlight of my PhD, and I always came back motivated and ready to tackle the next PhD related challenge. Thank you also to Jen Pinnion, John Evans and Xiaohong Tang who helped support my lab and fieldwork. The British Society for Geomorphology Postgraduate Forum has also been a great support throughout my PhD, I'm so glad I got the chance to meet so many other geomorphologists (albeit virtually).

I was also lucky enough to travel to Chengdu, Vienna and New Orleans during my PhD. In 2019, I spent two months conducting fieldwork in Chengdu. This would not have been possible without support from Xuanmei Fan, Jessica, Bing Xia, Yang Fan, Pasquale, Sato and all the local people I met in Yingxiu and the neighbouring towns. Thank you for making me feel so welcome and sharing your love of Sichuan food with me, even if my taste buds found everything a *little* spicy. Special shout out to Jessica who helped me organise fieldwork, took me sightseeing and for pizza when I needed home comforts!

Completing a PhD during a pandemic and writing up when everyone else is out having fun has been quite a challenge. I'm really fortunate to have been surrounded by so many supportive PhD students over the past four years. Special thanks go to Ana, Ben, Manny, Erin, Ellie, Sara, and Amy, who have checked in on me, listened to me rant and taught me lots of science. Ana, thank you for sharing *all* the ups and downs, motivating me to go to the gym or the beach and drinking much-needed caffeinated beverages outside main building with me. I wouldn't have got through this last year without you! Ellie, thank you for always being up for a chat/day out/camping trip, selflessly taking over organising the many social events I put upon myself and celebrating each milestone with tea. Sara, thank you for the memes/cat pics, the horoscope motivation and enduring the NOLA hotel drama with me.

I must also acknowledge the many non-Earth Scientists in my life! Sarah, Katherine (& Ellie) I would not have been able to finish this PhD without the endless cups of tea, prosecco-fuelled motivation, coastal walks and strong encouragement to switch off every evening with our shared love of trash TV (shout out to MAFS). Thank you to all my 'home' and 'Durham' friends for your support; for visiting me in Cardiff, providing me with much-needed distractions, and letting me hide to write up. James, thank you for letting me take us to see landslides on holiday, reading my inefficient code and encouraging me to be confident and ambitious.

Finally thank you to my amazing family, especially my mum, dad (my original fieldwork assistant), Megs, and my nans. I would not be where I am today without all of your support. Thank you for listening to me talk about debris flows, taking me on holidays that sparked my love to travel, and looking after me so I could write up my thesis. I cannot thank you enough.

Chapter 1

Introduction

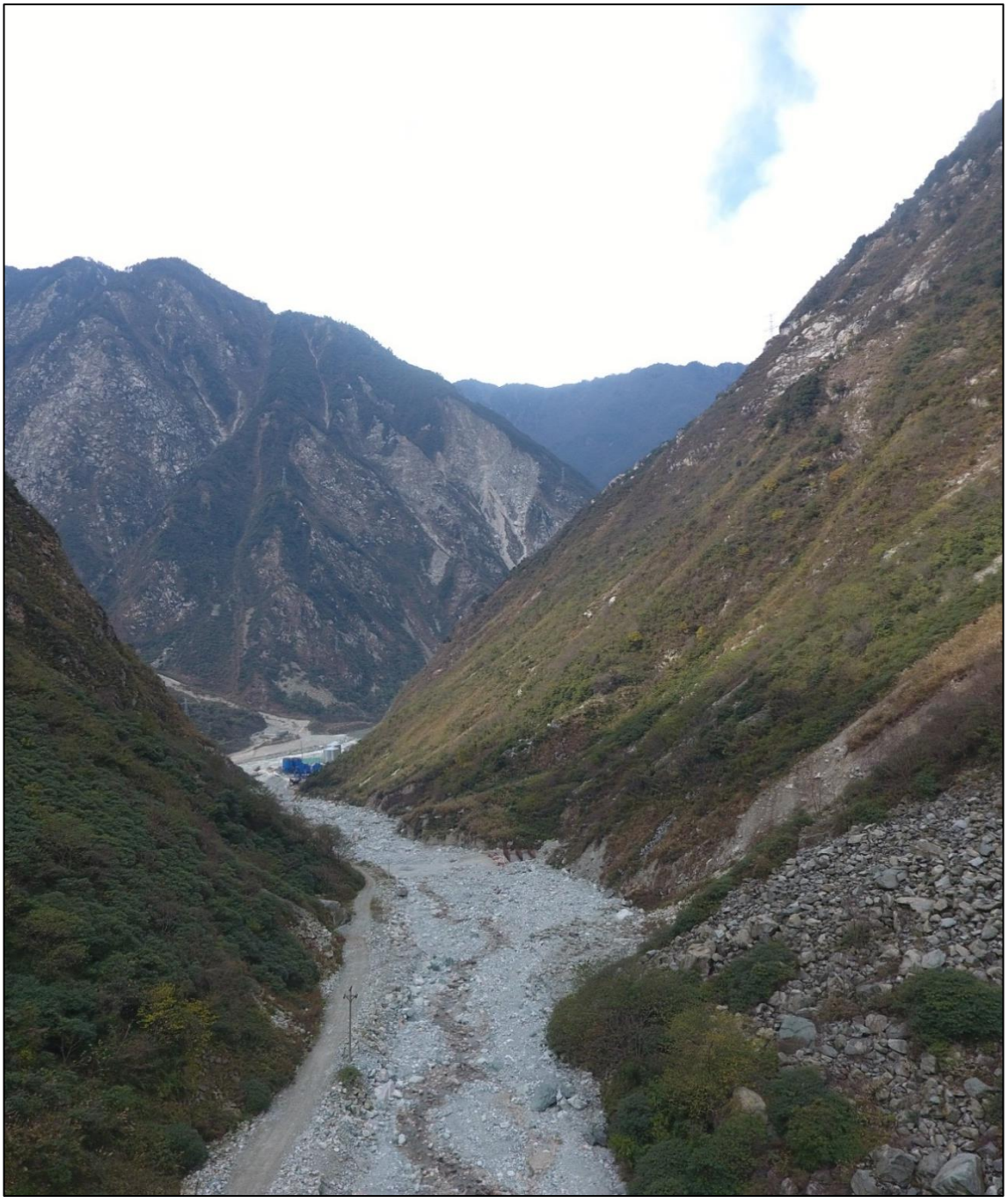

Catastrophic debris flows entrain vast amounts of sediment and can bulk to over an order of magnitude larger than their initiation volume (Iverson, 1997; Scott et al., 2005). These debris flows pose a major hazard to communities directly, by travelling at speeds ~20 m s^{-1} and transporting large boulders ~10 m (Rana et al., 2021; Scott et al., 2005; Takahashi, 2007), and indirectly through the development of landslide dams (Fan et al., 2012). Subsequently, large, catastrophic debris flows are responsible for most debris flow fatalities. In a global inventory of 213 debris flows which occurred over a 61 year period, the two largest debris flows accounted for 53% of the total fatalities (Dowling and Santi, 2014). The low frequency of these high magnitude events leads to catastrophic debris flows typically being excluded from magnitude-frequency analyses (Marchi and D'Agostino, 2004; Stoffel, 2010). Controls on the size of catastrophic debris flows, and why they reach such large volumes, are therefore poorly understood. An understanding of what controls the size of catastrophic debris flows will aid debris flow prediction models that consider magnitude-frequency distributions as well as help to identify areas most at risk from large debris flows.

The 2008 Wenchuan earthquake presents a unique opportunity to study multiple catastrophic debris flows across similar geological and climatic conditions. In 2019 alone, 13 catastrophic debris flows inundated catchments along the Min Jiang River (Yang et al., 2021). These debris flows led to 22 fatalities and caused significant damage to infrastructure. To understand catastrophic debris flows from a hazards perspective, it is crucial to elucidate controls on the runout of large debris flows. Numerical models and flume experiments have demonstrated that debris flow runout length can be attributed to their composition and grain size (de Haas et al., 2015; Hsu et al., 2008), the water content of the flow (de Haas et al., 2015; Hürlimann et al., 2015) and topography (Benda and Cundy, 1990; Cannon and Savage, 1988; Prochaska et al., 2008b). However, controls on the runout of catastrophic debris flow remain poorly constrained due to limited field observations. In this thesis, I intend to utilise a rare field dataset of post-earthquake debris flows from Wenchuan to assess controls on the runout of catastrophic debris flows. I define catastrophic debris flows as debris flows which entrain sufficient

sediment to traverse catchments several kilometres in length before depositing in higher order channels.

Debris flows are masses of sediment and water which surge down hillslopes under the influence of gravity (Cruden and Varnes, 1996; Iverson et al., 1997; Jakob and Hungr, 2005). Debris flows can transport a wide range of grain sizes from clay and silt to boulders >10 m (Iverson, 1997). The wide range of grain sizes transported by debris flows can control the runout length of the flow. For example, the presence of clay and silt in the interstitial fluid phase of the debris flow can decrease the rate at which excess pore pressures dissipate (Pierson, 1981). Too high proportions of silt and clay in the interstitial fluid (>22%) can increase the viscous forces within the flow and decrease runout length (de Haas et al., 2015). Similarly, if the proportion of solid constituents is too high (>60%), the frictional forces at the base of the flow increase and reduce runout length. Pore pressures will also dissipate more readily in a predominantly sand and gravel based mixture (de Haas et al., 2015). The complex interactions between solid and fluid phases in debris flows can additionally lead to high flow velocities and strong impact forces (Iverson, 1997; Iverson et al., 1997). For example, coarse grains transported by the flow, typically in the snout, can lead to high impact forces along the channel and between grain contacts (Hsu et al., 2008, 2014). These high impact forces not only enable scour of the channel bed by the debris flow (de Haas et al., 2022; Roelofs et al., 2022) but also lead to more infrastructural damage (Jakob et al., 2012; Zhang et al., 2021b). Flow velocity can relate to the presence of large grains transported by a debris flow as well as flow depth, slope and discharge (Rickenmann, 1999). The high flow velocities, strong impact forces and long runouts associated with the wide grain-size distributions (GSDs) reiterate that debris flows are one of the most hazardous types of landslide (Iverson, 1997; Iverson et al., 1997).

The combination of long runouts and high flow velocities allow debris flows to transport masses of heterogenous sediment from hillslopes and into channels (Chen et al., 2006; Fan et al., 2019a; Francis et al., 2022). Large debris flows can have particularly lasting impacts on long-term sediment yields (Anderson et al., 2015; Bennett et al., 2014). For example, debris flows which occurred during a 1 in 300 year storm exported hundreds to thousands of years of

weathering products in a single event in Colorado, US (Anderson et al., 2015). Debris flows can also be critical in post-earthquake sediment cascades, transporting sediment from landslide deposits and into channels following earthquakes (Dadson et al., 2004; Fan et al., 2019a; Francis et al., 2022). Estimates of the amount of sediment transported by post-earthquake debris flows can provide insight into how landscapes respond to an earthquake (Fan et al., 2019a; Francis et al., 2020; Marc et al., 2016a), and contribute to efforts predicting debris flow hazards and secondary hazards, such as in the form of landslide dams (Chang et al., 2017; Fan et al., 2012).

1.1 Post-earthquake sediment cascades and debris flows

Post-earthquake sediment cascades evacuate co-seismic sediment from catchments in the years to centuries following an earthquake (Dadson et al., 2004; Francis et al., 2022; Hovius et al., 2011; Wang et al., 2015). For example in the 2008 Wenchuan earthquake at least 60 000 landslides generated close to 3 km^3 of material in a geological instant (Huang and Fan, 2013; Li et al., 2014). Many of these co-seismic landslides eroded bedrock material and have bimodal GSDs of fine and coarse sediment (Fan et al., 2019a; Wang et al., 2015). The coarser fractions of deposits cannot be remobilised through fluvial processes alone, and require in-situ weathering or larger, higher velocity flows to be transported. Debris flows are one of the primary processes that transport coarse grains from hillslopes and into channels (Fan et al., 2019a). In the 10 years after the 2008 Wenchuan earthquake around 15% of the total sediment generated by co-seismic landsliding has been removed from hillslopes through fluvial and debris flow processes. Debris flows mobilised 67% of this material, making them an extremely important erosional mechanism during this period (Francis et al., 2022). The timescale over which earthquake-generated sediment is evacuated from the landscape is not well constrained due to the lack of accurate field data for the coarse fraction of deposits (Pearce and Watson, 1986), a limited understanding of the processes which transport sediment downstream (Francis et al., 2022) and how these processes relate to hillslope-channel connectivity (Croissant et al., 2019; Francis et al., 2020; Li et al., 2016). Current estimates suggest coarse co-seismic debris remains on hillslopes for hundreds to thousands of years (Francis et al., 2020; Pearce and Watson, 1986; Yanites et

al., 2010). Debris flows are extremely important to the post-earthquake landscape response, yet we lack strong frameworks for understanding their role in the amount of erosion, sediment transport and connectivity between different parts of the landscape (Dai et al., 2021; Fan et al., 2019a).

Catastrophic debris flows are the most efficient process transporting hillslope sediment into the main channel in Wenchuan in the ten years after the earthquake (Fan et al., 2019a; Francis et al., 2022; Li et al., 2016; Wang et al., 2015). These large flows are crucial in exporting sediment from catchments by connecting low order tributaries directly to the Min Jiang River (Francis et al., 2022). Several catastrophic debris flows occurred in 2008, 2010, 2013 and 2019 (Ge et al., 2015; Tang et al., 2011a, 2012a; Yang et al., 2021). Despite their importance from a hazard and sediment transport perspective, the mechanisms governing the development of catastrophic, entraining debris flows have only been explored using single field studies (e.g. Vallance and Scott 1997; Breien et al. 2008), numerical models (e.g. Ouyang et al. 2015; Horton et al. 2019) and flume experiments (e.g. Iverson et al. 2010; Iverson et al. 2011) due to their infrequent nature. An understanding of what governs these large debris flows will provide vital insight into controls on the post-earthquake sediment cascade.

1.2 Post-earthquake debris flow grain-size distributions

The GSDs of debris flows can control their runout length, velocity, and impact forces along the bed, as outlined above. Yet the role of debris flow grain size in the post-earthquake sediment cascade is essentially unknown. GSD measurements from field debris flows are limited by the wide range of grain sizes mobilised (from clay to boulders), the heterogenous nature of deposits vertically and laterally, the large size of deposits and inaccessible field sites (Dufresne and Dunning, 2017; Fan et al., 2019a; Iverson, 1997; Vallance and Savage, 2000). To overcome these challenges, studies have used multiple methods to obtain the entire range of grain sizes across different sections of the deposit (Ibbeken et al., 1998; Kim and Lowe, 2004; Major and Voight, 1986; Nishiguchi et al., 2012; Zhang et al., 2015). The comparability of these different approaches is poorly understood, which has limited our ability to compare the effect of GSDs on debris flow dynamics. It is crucial that approaches to measure the GSD of debris flows are developed to better

understand both the runout of post-earthquake debris flows and the size of material transported to fluvial channels (Fan et al., 2019a).

The size of the sediment transported by debris flows can control the onward fate and fluvial export of sediment (Wang et al., 2015; Zhang et al., 2019). In non-seismic settings, pulses from landslides and debris flows have been found to measurably coarsen the grain size of river bed sediments (e.g. Attal and Lavé 2006; Attal et al. 2015; Dingle et al. 2017; Roda-Boluda et al. 2018). However, the effect of landslide and debris flow grain size on the post-earthquake sediment cascade has only been considered qualitatively (Pearce and Watson, 1986). Most studies of post-earthquake fluvial export also focus on only suspended sediment concentrations, which are easier to measure (Dadson et al., 2004; Wang et al., 2015). Yet the processes controlling the export of fine sediment (e.g. <0.25 mm) are different to those controlling the export of coarse material, which can only be delivered to main fluvial channels via debris flows, floods, and landslides (Li et al., 2016; Zhang et al., 2019). Therefore, to fully quantify the rate of sediment export, for all seismically sourced sediment, the transport pathways for coarser debris must be better understood.

The role of debris flow grain size in controlling debris flow magnitude, and subsequently their hillslope-channel connectivity, has also not been explored in a seismic setting despite evidence from flume experiments that debris flow grain size can control runout length and entrainment rates (e.g. Hsu et al. 2008; Iverson et al. 2010; Iverson et al. 2011; de Haas et al. 2015; Haas and Woerkom 2016). The presence of large grains relates to entrainment in debris flows by increasing impact forces and enabling bed erosion (de Haas et al., 2022; Roelofs et al., 2022). Entrainment can also relate to the positive pore pressures which govern debris flow mobility. Flume experiments by Iverson et al. (2011) found that debris flows which travelled over wet, saturated beds entrained sediment more rapidly. Rapid entrainment was driven by a positive momentum feedback, where higher positive pore pressures produced by entraining wet sediment increased momentum and reduced friction at the base of the flow, enabling further sediment entrainment. The presence of fine sediment in a wide GSD, which includes coarse grains, can decrease the rate at which these excess pore pressures dissipate (de Haas et al., 2015; Pierson,

1981). Therefore, to understand controls on hillslope-channel connectivity and post-earthquake hazards, it is important to determine the mechanism which controls the development of a debris flow into a catastrophic debris flow.

1.3 Research aims, questions and objectives

The overarching aim of this thesis is to understand how grain-size distributions of channel and hillslope sediment control the runout of catastrophic post-earthquake debris flows in Wenchuan. I will provide insight into what governs the mobility of post-earthquake debris flows to identify potential processes controlling the development of catastrophic debris flows. The basis for this work has included methodological development (RQ1, Chapter 4), detailed field analysis of individual debris flows (RQ2, Chapter 5) and topographic analysis and modelling (RQ3, Chapter 6).

Research Question 1: How can we accurately measure the grain-size distributions of mass movement deposits?

To answer this question, I measured the GSD of three different mass movement deposits (including two debris flows) using five methods (sieving, Wolman pebble counts, survey tape counts, manual photo counts and an automated approach, pyDGS). I compared the resulting GSDs using the normalised root mean square error values and statistically through two-sample goodness-of-fit chi squared tests. I then considered how the GSDs generated for the same mass movement deposits using different methods would impact the accuracy of the geomorphic interpretations made.

Research Question 2: How do the grain-size distributions of post-earthquake debris flows with different runout lengths vary across all three spatial dimensions?

For this research question, I used the methods discussed in Chapter 4 to develop high-resolution GSDs for two post-earthquake debris flow deposits with different runout lengths. The Luoquan debris flow was a catastrophic debris flow with a runout ~8 km in length. The Liusha debris flow was shorter with a runout length of ~1.5 km. For both debris flows, I measured the GSDs across three dimensions (vertical, lateral and longitudinal). I then compared the GSDs deposited by the two debris flows in terms of composition and the

spatial patterns of deposition. From the deposited GSDs, I inferred potential transport and deposition mechanisms occurring within the two debris flows.

Research Question 3: What controls the development of large, catastrophic debris flows?

To answer this question, I analysed the magnitude-frequency distribution of all post-earthquake debris flows in Wenchuan. From this distribution, I assessed whether the occurrence of catastrophic debris flows was driven by a change in process. I then used the 2D model Massflow to conduct a sensitivity analysis to determine which parameters were required to simulate catastrophic debris flows within the Luoquan catchment, using the 2019 event for reference. Finally, I developed a magnitude-frequency distribution from the simulated debris flows in Luoquan using a Monte Carlo analysis based on statistical distributions constrained by field data. From this, I inferred how the post-earthquake conditions in Wenchuan led to an unprecedented frequency of catastrophic debris flows.

1.4 Thesis structure

Below I will outline the structure of this thesis and how the three main research questions above will be used to achieve the overarching aim. The three research questions will be formatted as research papers with the respective methods found in each section. I will outline how these research chapters interlink below.

In Chapter 2, I review the literature on debris flow entrainment and transport. In particular, I focus on the role of grain size and the development of large debris flow runouts. I then discuss potential controls on the magnitude and frequency of post-earthquake debris flows in the years following an earthquake, with the Wenchuan earthquake central to the discussion.

In Chapter 3, I provide a brief background to the 2008 Wenchuan earthquake. I also explain the inventory of post-earthquake mass movements, which is used in Chapter 6. Finally, I introduce the two post-earthquake debris flows that provide the foundation for the field work and modelling analysis within this PhD.

In Chapter 4, I compare five techniques (sieving, Wolman pebble count, survey tape count, automated pyDGS and manual photo counts) used to

measure mass movement deposit GSDs for three different mass movement deposits (two in Wenchuan, one in South Wales). Based on these comparisons, I determine which techniques most accurately quantify mass movement GSDs and how the choice of method can affect the conclusions made.

In Chapter 5, I use the findings from Chapter 4, to measure high-resolution GSDs for two post-earthquake debris flows across three spatial dimensions. I analyse these GSDs to better understand the processes governing transport and deposition within two debris flows with similar initiation mechanisms and conditions but very different runout lengths.

In Chapter 6, I explore whether the magnitude-frequency distribution of large debris flows in Wenchuan implies that they should be described as a separate process using an inventory of over 2000 post-earthquake debris flows. I then apply the model, Massflow, to determine what controls the development of catastrophic debris flows. From these 132 simulations, I develop a magnitude-frequency distribution of modelled debris flows to elucidate why catastrophic debris flows are so frequent following the 2008 Wenchuan earthquake.

In Chapter 7, I summarise the main findings of this thesis framed around the research questions set out in this introduction. I then discuss potential directions for future work in the field of post-earthquake debris flow dynamics.

Chapter 2

Literature Review

2.1 Introduction

Catastrophic debris flows are slurries of water and sediment that surge down hillslopes and through channels, entraining more sediment to reach extremely large volumes (e.g. 10^6 m^3) (Cruden and Varnes, 1996; Iverson, 1997; Major and Pierson, 1992). Catastrophic debris flows have been triggered by heavy precipitation in Wenchuan, China (Ge et al., 2015; Tang et al., 2012a; Yang et al., 2021), Montecito, California, U.S.A. (Oakley et al., 2018) and Vargas, Venezuela (Reinaldo and López, 2005), in volcanic settings in Nicaragua (Scott et al., 2005) and in the mountain cryosphere (e.g. Evans et al. 2009; Evans et al. 2021; Shugar et al. 2021). In the mountain cryosphere, the events are often referred to as catastrophic mass flows (Evans et al., 2021; Shugar et al., 2021).

The term catastrophic debris flows is typically used to describe debris flows with significant societal consequences, such as fatalities and infrastructural damage (Jakob, 2005; Vilímek et al., 2006; Zhang et al., 2022) as well as extremely large debris flows which travel long distances through processes such as entrainment with the channel bed (Rana et al., 2021; Scott et al., 2005; Tang et al., 2012a; Yang et al., 2021). These two descriptors of catastrophic debris flows are often synonymous, with the number of fatalities caused by debris flows events disproportionately higher for large debris flows (Dowling and Santi, 2014). However, the number of fatalities caused by a debris flow event can also be related to the economic-status of a country, the debris flow trigger and the proximity of the debris flow event to a populated area (Dowling and Santi, 2014). For example, 13 catastrophic debris flows were triggered in Wenchuan in August 2019 through intense precipitation. These catastrophic debris flows filled channels up to 16 km in length. Whilst the debris flows bulked to large volumes, few directly impacted towns and therefore the flows only led to 22 fatalities in total (Yang et al., 2021). In contrast the 1999 Vargas event triggered 24 catastrophic debris flows which travelled up to 20 km in length and led to at least 15 000 fatalities (Dowling and Santi, 2014; Reinaldo and López, 2005). This event accounted for ~20% of all debris flow fatalities recorded between 1960 and 2011 (no. of debris flows in study = 213). The high number of fatalities following this event was attributed to the debris flows inundating the city of Vargas which had been

built on a debris flow fan (Dowling and Santi, 2014). In this thesis, I define catastrophic debris flows as debris flows which entrain sufficient sediment to traverse catchments several kilometres in length before depositing in higher order channels (such as the Min Jiang River). These debris flows have the potential to cause significant destruction, but this is not a requirement (Jakob, 2005) as the main focus of my research is to understand the processes governing their generation.

Debris flows differ to other landslides due to their high water and sediment concentrations that allow them to flow at speed over long distances. The velocity of a debris flow can range from 0.5 to 20 m s^{-1} and they typically travel between 0.2 and 10 km in distance (Takahashi, 2007). Flows can reach volumes greater than 10^9 m^3 and transport grain sizes from clay to boulders >10 m (Iverson, 1997). The size of the grains transported by a debris flow can influence the processes by which a debris flow initiates, entrains, transports and deposits material (Gabet and Mudd, 2006; de Haas and Woerkom, 2016; Iverson et al., 1997; Johnson et al., 2012; Major, 1997). By controlling these processes debris flow grain size in part governs the runout length and volume of debris flows (de Haas et al., 2015; Kaitna et al., 2016). In this chapter, I will review the role of grain size in controlling debris flow erosion and transport mechanisms as well as the constraints on catastrophic debris flow magnitude and runout length. I will also highlight the importance of understanding controls on debris flow size from a sediment transport perspective.

Our current understanding of debris flow grain size is limited to large-scale and small-scale flume experiments (see Iverson et al. 2010; Kaitna et al. 2014; de Haas et al. 2015), multi-phase numerical models (see Gray 2018; Pudasaini and Mergili 2019), and individual debris flow events (see Vallance and Scott 1997; Kim and Lowe 2004; Zhang et al. 2011). Large-scale flume experiments are useful for obtaining accurate constraints on the material properties of a flow (e.g., grain size and water content) and how they affect debris flow properties (e.g., runout length and velocity) as well as quantifying initial and boundary conditions (e.g., roughness of a channel bed) (Iverson, 1997; Iverson et al., 1997, 2010). However, executing experiments in large flumes can be costly and time-consuming, and therefore small-scale flumes

are typically more popular (D'Agostino et al., 2010; de Haas et al., 2015; Major and Iverson, 1999). Small-scale flumes can be used to conduct a higher number of experiments, and therefore explore general relationships between debris flow composition and erosion and deposition mechanisms (de Haas et al., 2015; Roelofs et al., 2022). Though, small-scale flume experiments must account for disproportionately large effects of yield strength, grain inertia and viscous flow resistance (de Haas et al., 2015). More recently, numerical models using bidisperse (two grain sizes) and multi-phase (typically three grain sizes) flows have been used to further understand what mechanisms control processes such as segregation in debris flows (Barker et al., 2021; Golick and Daniels, 2009; Gray, 2018; Gray and Ancey, 2011; Hill and Tan, 2014). These numerical models of grain size are currently limited by the computational power required to model the complex GSDs found in debris flows (Pudasaini and Mergili, 2019; Sanvitale and Bowman, 2017). These GSDs can range in size over eight orders of magnitude from clay to boulders and are often angular so misrepresented when using spherical grains (Iverson et al., 1997; Vallance and Scott, 1997).

Field-based studies of debris flows are rare due to their infrequent and unpredictable nature as well as the inaccessible mountainous locations in which they predominantly occur. As such, GSDs are generally only collected from individual events (Kim and Lowe, 2004; Pierson, 1981; Takahashi, 1981; Vallance and Scott, 1997). Accurately measuring debris flow GSDs can be challenging due to the heterogeneity of deposits and the wide range of grain sizes. These challenges are explored further in Section 2.7.

2.2 Definition of a debris flow

The high sediment content of debris flows (>40 – 60%) and wide grain-size distributions (GSDs) are often used to characterise different types of debris flows (Blair and McPherson, 1998; Iverson, 1997; Johnson et al., 2012; Pierson, 1981; Whipple and Dunne, 1992). Debris flows can be classified in several ways, such as by appearance and composition, by the mechanisms occurring within the flow, by the size of the flow and the initiation mechanism (Iverson, 1997; Iverson et al., 1997; Takahashi, 2007). Classifying debris flows is important to avoid misinterpretation and aid hazard predictions. Early studies classified debris flows based on the sediment

concentration of the flow, for example O'Brien and Julien (1985) divided flows into water floods, mud floods, mudflows and landslides. Takahashi (2007) characterised debris flows into three categories: stony debris flows, turbulent muddy debris flows and viscous debris flows. This assessment was made primarily based on the appearance of the flowing material and the deposit.

Debris flow classifications have also been developed using debris flow size. Jakob (2005) proposed a debris flow classification using total volume, peak discharge, and inundated area. Debris flows were characterised by volume in 10 different classes, each class covers one order of magnitude, for example Class 2 includes debris flows with volumes between 10^2 m^3 and 10^3 m^3. The aim of this classification was to provide a basis for understanding hazard and risk associated with different debris flows (Jakob et al., 2012). Debris flows >10^7 m^3 were thought to only occur during volcanic events (Pierson, 1995; Scott et al., 2005). In supply-limited catchments, only a few different size classes of debris flows are expected, due to the rate of sediment recharge in gullies (Jakob, 2005; Jakob et al., 2005). The size of debris flows produced can also relate to their triggering mechanism, with Class 5 debris flows thought to be debris avalanche-generated and Class 6 debris flows rock avalanche-generated. This reiterates the importance of understanding debris flow composition and triggering mechanism as controls on debris flow magnitude.

Debris flows have also been classified based on their rheological behaviour (Pierson and Costa, 1987; Savage, 1984). Pierson and Costa (1987) defined debris flow type using three rheological boundaries, which related to the sediment concentration and yield strength of the material, where yield strength is the point at which the shear stress applied has been exceeded and the material begins to deform, or flow. The three categories were hyper-concentrated flows, slurry flows and granular flows. The flows were identified based on the dominant forces acting within the flow: inertial, viscous or frictional (Pierson and Costa, 1987). Iverson (1997) developed seven dimensionless parameters to characterise the importance of these forces within different debris flows. The three dimensionless parameters known to

vary the most from flow to flow were the Savage Number, N_{Sav}, the Bagnold Number, N_{Bag}, and Darcy's Number, N_{Dar}.

N_{Sav} is the ratio of collisional (inertial shear stress) to frictional forces within the flow and is represented as

$$N_{Sav} = \frac{\rho_s \delta^2 \gamma^2}{(\rho_s - \rho_f) g H tan\emptyset}, \qquad \textit{Equation 2.1}$$

Where ρ_s and ρ_f are the solid and fluid densities, δ is the mean grain size of the flow, g is the gravitational acceleration, $\emptyset$ is the internal angle of friction and γ is the flow shear rate which equates to $\gamma = \frac{\mu}{H}$, where H is the flow depth and μ is the interstitial fluid viscosity. In flume experiments, (Iverson, 1997) suggests N_{Sav} equates to 0.2, whereas in field experiments $N_{Sav} < 0.2$. N_{Sav} is thought to be much lower for larger debris flows, implying that collisions transmit negligible stress in these flows and that friction dominates (Iverson, 1997).

N_{Bag} is the ratio of particle inertial stresses to interstitial fluid viscous stresses, where

$$N_{Bag} = \frac{v_s \rho_s \delta^2 \gamma}{v_f \mu}, \qquad \textit{Equation 2.2}$$

v_s and v_f are the solid and fluid volume fractions. A high value of N_{Bag} (>200) suggests the flow is dominated by collisional stresses, such as a rock avalanche. A lower value of N_{Bag} suggests viscous stresses dominate, such as in a mudflow. Iverson (1997) states that N_{Bag} can vary from 0.2 to 400, with a value of 400 in the USGS flume suggesting collisional stresses dominate.

N_{Dar} describes the tendency for pore fluid pressure to buffer grain interactions, with

$$N_{Dar} = \frac{\mu}{v_s \rho_s \gamma K}, \qquad \textit{Equation 2.3}$$

Where K is the hydraulic permeability of the flow. Large values of N_{Dar} in large debris flows suggests viscous drag is important. N_{Dar} equated to approximately 600 for the USGS flume debris flows but can be much larger in field debris flows (Iverson, 1997). These three parameters can be used to define a debris

flow when compared to other types of mass movements as well as characterise different types of debris flows, as shown in Figure 2.1.

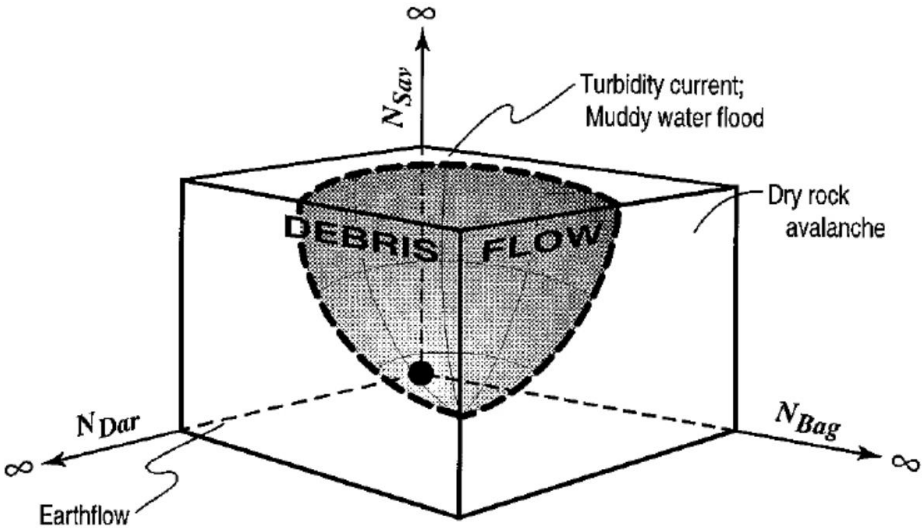

Figure 2.1

The relationship between three dimensionless parameters (N_{Dar}, N_{Sav} and N_{Bag}) and how they relate to different types of debris flows. Figure taken from Iverson (1997).

Takahashi (2007) built on the definition of debris flows in Iverson (1997) using the three dimensionless parameters in Figure 2.1 by including the solid volume fraction to differentiate mechanistically between stony debris flows, turbulent muddy debris flows and viscous debris flows. According to Takahashi (2007) debris flows with a coarse solid volume concentration between 0.2 and 0.5 fit this classification. Above a threshold of 0.5 coarse solid volume fraction, quasi-static motion develops within the debris flow. Quasi-static motion occurs when the inertial stresses in the debris flow are negligible, which is typical during initiation and deposition of the flow (Iverson, 1997). Typical debris flow solid volume fractions range between 0.4 and 0.6 (Iverson, 1997).

Dimensionless numbers are a useful method of quantifying the stresses driving debris flow mobility, particularly when comparing flume-based observations to field studies (Iverson and Vallance, 2001; Kaitna et al., 2014, 2016; Roelofs et al., 2022). However, based on the complex interactions between solid and fluid components in different parts of a debris flow, for example a coarse friction snout in comparison to a wet, fluid body, it is likely that the N_{Sav}, N_{Bag} and N_{Dar} will vary across the flow (Iverson, 1997, 2003; McArdell et al., 2007;

Parsons et al., 2001). I will discuss the formation of debris flow snouts and the importance of the fluid tail in Section 2.3.

The dimensionless parameters can also provide insight into how flow composition can affect debris flow internal dynamics, runout length and volume (de Haas et al., 2015; Kaitna et al., 2016; Roelofs et al., 2022). Debris flow grain size can have considerable implications for the N_{Sav} and N_{Bag} due to its importance in governing collisional forces within the flow (Equations 2.1 and 2.2). Flume experiments have been used to explore the relationship between grain size, dimensionless parameters and debris flow processes, such as erosion and deposition (de Haas et al., 2015; Iverson et al., 2010; Roelofs et al., 2022). Most recently, small-scale flume experiments showed that both N_{Sav} and N_{Bag} correlated with erosion, with impact forces in the flows increasing due to an increase in the median grain size (Roelofs et al., 2022). They found that gravel content (and N_{Sav}) positively correlated with erosion quantity. The N_{Sav} and N_{Bag} dimensionless parameters therefore highlight the importance of grain size in controlling debris flow runout length and erosion.

2.3 Debris flow processes

2.3.1 Debris flow initiation

Debris flows can also be categorised by their triggering mechanisms (Takahashi, 2007). Debris flows can be triggered by rainfall, snow and ice melt (e.g. Pierson et al. 1990), landslides (e.g. Gabet and Mudd 2006; Huang and Li 2014), earthquakes (e.g. Chen and Petley 2005; Dahlquist and West 2019; Fan et al. 2019a), volcanic eruptions (e.g. Major et al. 2007; Davies et al. 2010) and lake outburst floods (e.g. Breien et al. 2008; Sattar et al. 2022). All of these triggers can supply a large volume of water or sediment, which is required for a debris flow to initiate.

Debris flows can initiate from landslides and landslide deposits (Brayshaw and Hassan, 2009; Gabet and Mudd, 2006; Iverson et al., 1997), in-channel deposits (Berti et al., 1999; Cannon et al., 2001b; Takahashi, 2007; Yang et al., 2021) or through the erosion of bedrock (Johnson and Rodine, 1984). For a debris flow to occur three requirements must be met, (1) the failure of a rigid mass of water-laden sediment; (2) enough water to saturate the mass, and (3) the conversion of gravitational potential energy to internal kinetic energy so

that the mass travels as a flow. A detailed account of the mobilisation of landslide deposits into debris flows can be found in Iverson et al. (1997). Iverson et al. (1997) stated that for a debris flow to occur, the rigid mass must first fail. They described this failure using the Coulomb failure law, which remains included in many subaerial debris flows models due to its simplicity (Iverson, 1997; Iverson et al., 1997; Iverson and Denlinger, 2001; Ouyang et al., 2015a; Pudasaini and Mergili, 2019). The Coulomb failure rule can be described as the criterion for slope failure along a discrete surface, with failure occurring when the stresses obey Equation 2.4,

$$\tau = (\sigma - p)tan\emptyset + c \qquad \textbf{\textit{Equation 2.4}}$$

where τ is the mean shear stress acting on the surface, σ is the grain contact stress, p is the pore fluid pressure, ø is the angle of internal friction in the soil and c is cohesion, from root strength or clay. The law states that the strength of the resisting forces is governed by the bulk friction angle, the normal stress component and cohesion. In Iverson et al. (1997), they use the effective normal stress, where pore fluid pressures can reduce the normal stress acting on the mass. Generally, debris flows initiate once the mass is saturated. Saturation occurs due to infiltration from intense rainfall or snowmelt, which can lead to sudden changes in pore water pressures (Major et al., 2007; Pierson et al., 1990; Shugar et al., 2021). The GSD of the initiating and flowing mass can also control the rate at which excess pore pressures in the deposit dissipate (Pierson, 1981). For example, a higher proportion of fines in a wide GSD can trap fluid and elevate pore pressures (Major, 1997; Pierson, 1981). In contrast, coarse grains with large pore spaces allow excess pore pressures to dissipate rapidly. The bulk friction angle of a failing deposit may also change because of compaction and the packing geometry of grains, however this effect is likely to be less important than the role of pore fluid pressures (Iverson, 1997).

Pore fluid pressures can also change as the mass shears. This is referred to as Critical State Theory. Critical State Theory states that the grains in the shearing zone rearrange in order to approach a critical void ratio (Gabet and Mudd, 2006; Iverson et al., 1997). Loose soils will contract, and dense soils will dilate to overcome the resistance from interlocking grains and reach the

critical state. The contraction of loose soils in this process is particularly important for debris flow mobilisation, due to the fact when loose soils contract, pore water pressures can increase if the rate at which pore space is reduced exceeds the rate at which the induced fluid pressure dissipates (Iverson et al., 1997; Reid et al., 1997; Wang and Sassa, 2003). Gabet and Mudd (2006) demonstrated using case examples and a numerical model that dilating soils could also fail and trigger a debris flow through the following feedback relationship. Firstly, the Coulomb slope failure equation is obeyed and the slump slides partway downslope. The soils then dilate, which inhibits further movement and decreases soil pore pressure. The looser soil then absorbs water, either through rainfall or ponding on the surface, allowing the slump to resaturate. This increases pore fluid pressures and induces a second failure. The loose soils then contract during failure, which enables liquefaction and the occurrence of a debris flow (Gabet and Mudd, 2006; Iverson, 2005).

The final process thought to initiate a debris flow from a landslide is via increases in granular temperature (Iverson et al., 1997), which is only briefly outlined here. Granular temperature describes the degree of agitation between solid grains (Iverson et al., 1997). High granular temperatures result in a reduced concentration of solids and more fluidity, in the form of a debris flow. In debris flows, the downslope movement of the mass supplies the bulk translational energy. The translational energy is then converted into grain fluctuational energy by the shearing of grains along the irregular surface in order to maintain the flow momentum (Iverson et al., 1997).

2.3.2 Transport and deposition by debris flows

The complex interactions between solid and fluid constituents in the flow allow debris flows to travel long distances. These interactions govern the development of distinct features in debris flows, such as the coarse snout and levees which entrain sediment and channelise the flow as well as the finer, fluid tail which pushes the coarse front forward (Figure 2.2; Johnson et al., 2012; Major and Iverson, 1999; McArdell et al., 2007; Vallance and Scott, 1997). Friction along the coarse front of the debris flow is thought to explain how many debris flows deposit sediment, with positive pore pressures absent in this section of the flow (Major, 1997; Major and Iverson, 1999; Schürch et

al., 2011). Debris flows can deposit sediment through the mass freezing of a deposit, the lateral shunting of deposited sediment and by incremental deposition (Iverson, 1997; Iverson et al., 2010; Major, 1997). In the paragraphs below I explore how grain size relates to patterns of deposition found in debris flows and how the deposition of grains can provide insight into transport mechanisms.

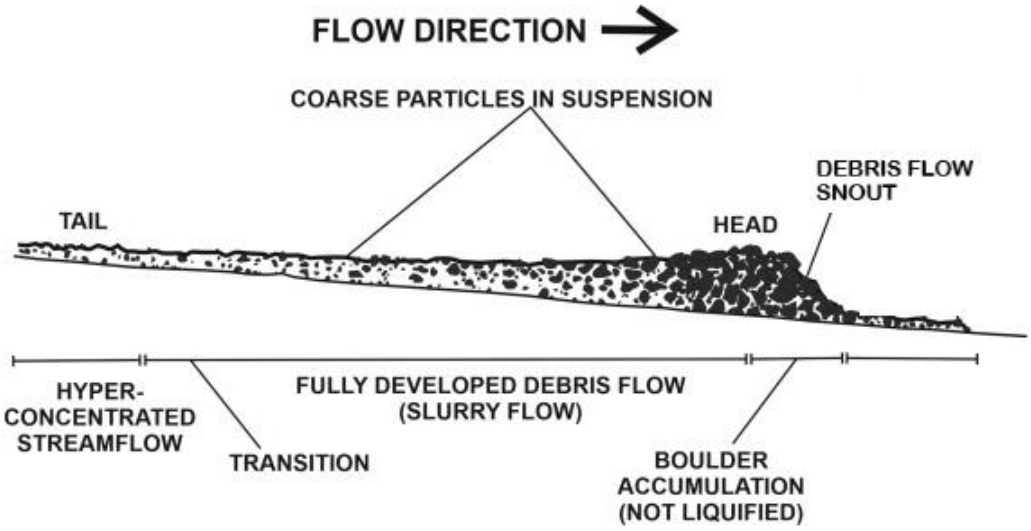

Figure 2.2

A cartoon showing the structure of a debris flow including the coarse snout and liquified, finer tail. This figure was adapted from Pierson (2006).

The proportion of different grain sizes, such as clays, silt and gravel, have previously been shown to control the runout length of debris flows (de Haas et al., 2015; Kaitna et al., 2016; Pierson, 1981). For example, the content of silt and clay in the interstitial fluid of the flow can reduce the rate at which excess pore pressures dissipate (Blair, 1999; Cannon et al., 2001a; Pierson, 1981). As such, debris flows with a wide GSD and high proportion of clay and silt, may have longer runout distances due to the slower rate at which excess pore pressures dissipate (Iverson et al., 2010). The proportion of clay in a debris flow can also result in very viscous flows, as shown in small-scale flume experiments in de Haas et al. (2015). In their experiments once the clay content reached 22% by volume the flow became extremely viscous and the runout length sharply decreased. Debris flows with a clay fraction of 38% were unable to reach the end of the flume channel. The gravel fraction was also an important control on debris flow runout in these experiments, with increasing

coarse grains also initially increasing runout length. The long runout with increasing gravel content was attributed to the fact that the debris flow produced levees which channelised the flow. Beyond a gravel fraction of 60%, they found a decrease in runout length. They attribute this to the higher frictional resistance exerted by the coarse grained snout and the fact that high pore pressures may not be sustained due to the higher diffusivity in a coarsely-grained mixture (de Haas et al., 2015; Kaitna et al., 2016). At low gravel contents, flow velocities were lower due to the fact few collisions were occurring within viscous flows. These small-scale experiments demonstrate how obtaining GSDs for debris flows in the field may help to predict debris flow runout length.

The heterogenous deposition of different sized grains can provide insight into the different processes controlling debris flow mobility and deposition (Hungr et al., 1984; Johnson and Rodine, 1984; Kim and Lowe, 2004; Major and Pierson, 1992; Pierson, 1981; Takahashi, 1981; Vallance and Scott, 1997). Field analyses that consider grain size with depth have found evidence of inverse grading, where larger grains are found on the surface of deposits and grain size decreases with depth (Genevois et al., 2000; Sosio et al., 2007; Zhang et al., 2011). The processes segregating different grains within the flow, which can lead to inverse grading, levees and coarse fronts, are most commonly thought to be driven by kinetic sieving and squeeze expulsion. Kinetic sieving refers to the percolation of smaller grains through gaps between the larger grains (Golick and Daniels, 2009; Johnson et al., 2012; Naylor, 1980; Vallance and Savage, 2000). Squeeze expulsion describes how larger grains are propelled to the surface layers (Gray, 2018; Savage and Lun, 1988; Vallance and Savage, 2000). An exact explanation for how segregation within debris flows occurs remains at the forefront of many modelling studies (Johnson et al. 2012; Hill and Tan 2014; Sanvitale and Bowman 2017; Gray 2018). Interestingly, debris flow deposits in the field commonly have a massive texture, with little or no evidence of segregation (Phillips and Davies, 1991; Vallance and Scott, 1997; Whipple, 1992). The absence of inverse grading may relate to progressive incremental deposition by multiple flows (Major, 1997). Incremental deposition from surges during the Osceola mudflow encouraged the development of normally graded deposits as the tail

of the flow was typically composed of finer sediments (Figure 2.3, Vallance and Scott 1997). The composition and strength of the interstitial fluid, for example higher clay contents and more cohesive fluid, can also hinder settling and segregation within the flow (de Haas et al., 2015; Vallance and Scott, 1997). The spatial pattern of deposited grain sizes can therefore provide an indication of mechanisms driving transport and deposition in debris flows.

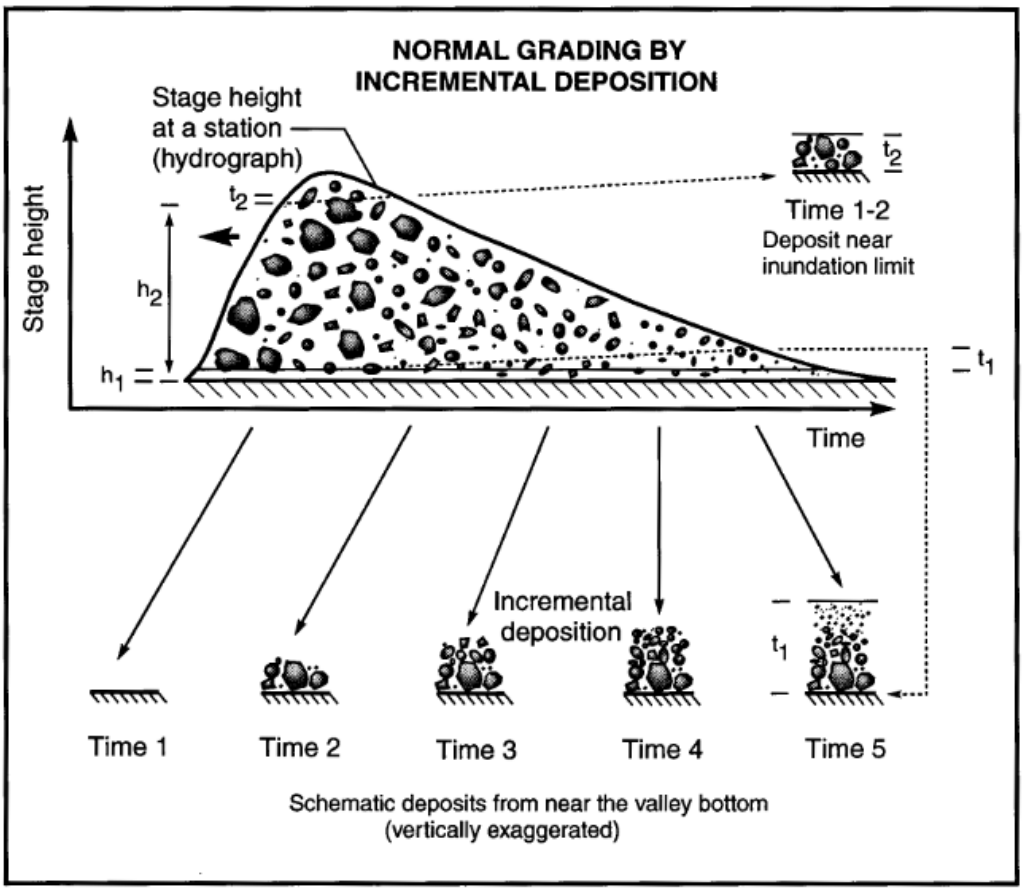

Figure 2.3

Simplified diagram for how debris flows may deposit grains by incremental deposition. This method of deposition can lead to normally graded deposits. Figure taken from Vallance and Scott (1997).

Segregation by grain size in debris flows is one of the main explanations put forward to explain the coarse snout observed in experiment and natural debris flows (Iverson, 1997; Iverson et al., 2010; Major and Iverson, 1999; McArdell et al., 2007; Schürch et al., 2011). Coarser, surface grains are preferentially transported to the front of the flow due to the depth-dependent velocity gradient, with the lower shear rates at the surface resulting in higher flow velocities (Iverson, 1997; Johnson et al., 2012; Kaitna et al., 2014; Savage and Hutter, 1989). Coarse debris flow fronts have been associated with high

collisional and shear stresses within the flow (Berger et al., 2011a; McArdell et al., 2007). The high stresses at the front of the debris flow are one of many factors thought to control the ability of the flow to entrain more material (Berger et al., 2011a; McCoy et al., 2013; Schürch et al., 2011). Larger grain sizes can also increase erosion by the debris flow (as explored in Section 2.3.3 and 2.5; Hsu et al. 2014; Roelofs et al. 2022). Seismic signals of debris flows complement these observations, with the strongest seismic signals, and subsequently basal force fluctuations, found to correspond with the concentration of and interactions between coarse particles (Allstadt et al., 2020; Kean et al., 2015; Lai et al., 2018; Zhang et al., 2021a). The amplitude and frequency of these signals have also been used to predict the size of boulders transported by debris flows downstream (Lai et al., 2018; Zhang et al., 2021a).

Topography can also affect debris flow momentum and therefore control runout length and deposition in debris flows (Benda and Cundy, 1990; Berti et al., 1999; Fannin and Wise, 2001). Slope and channel confinement were important controls on deposition in an empirical-statistical model for debris flows in British Columbia by Fannin and Wise (2001). In unconfined sections of the channel, increases in flow width and decreases in slope, decrease the momentum of the flow and encourage deposition. Though, as is the concern with many empirical models, these models require large datasets for a single region and are not necessarily applicable to other locations (Benda and Cundy, 1990; Fannin and Wise, 2001). The study also found that over a certain range of slopes, such as between 19° and 24° for an unconfined slope, the debris flow may deposit or may entrain material (Fannin and Wise, 2001). Therefore, other controls, such as debris flow rheology and composition, should also be considered. Channel-junction angle can also control the runout length of debris flows, as seen in British Columbia (Guthrie et al., 2010) and in the Oregon Coast Range (Benda and Cundy, 1990). However, a study by May and Gresswell (2004) found that the spatial pattern of deposition may vary temporally based on other parameters, such as water and sediment concentrations (Whipple, 1992) and the presence of woody debris. This suggests that controls on debris flow runout and deposition should not be considered only deterministically.

2.3.3 Entrainment by debris flows

The volume of a debris flow can change during transit due to processes of bulking (when the debris flow entrains material to grow in size) and debulking (where the debris flow decreases in volume) (Iverson, 1997). Debulking can occur when a debris flow becomes progressively more diluted and therefore cannot transport the coarsest grains (Iverson, 1997; Makris et al., 2020). The process of debulking is poorly understood, however as this is not the focus of this research, I will focus on entrainment in this literature review. Debris flow entrainment occurs through the exchange of water and sediment along the base of the flow, where drag forces can remove sediment from the channel bed, and the banks of the channel, through processes such as undercutting (Hungr et al., 2005a; Iverson, 1997; Pierson et al., 1990). The process of bulking in debris flows is nonlinear, with some debris flows increasing in volume by up to 50 times their initial volume, while others barely change in size (de Haas et al., 2022; Hungr et al., 2005b; Santi et al., 2008). The process of bulking and why some debris flows reach such large volumes is poorly understood. The lack of knowledge about debris flow entrainment stems from the unpredictable nature of debris flows, the inaccessible field locations and the complexities associated with surveying the channel bed (Iverson and Ouyang, 2015; Kean et al., 2015). Much research on debris flow entrainment has therefore been conducted using flume experiments (de Haas and Woerkom, 2016; Iverson et al., 2011; Reid et al., 2011; Roelofs et al., 2022), in well-monitored individual catchments (de Haas et al., 2020, 2022; Schürch et al., 2011) and using numerical modelling (Frank et al., 2015; Horton et al., 2019; Iverson and Ouyang, 2015).

The process of debris flow entrainment is complex and current advances in the field have revolved around using experimental observations to improve our understanding of the physics behind the process (Breien et al., 2008; Iverson et al., 2011). Iverson et al. (2011) used large-scale flume experiments to assess how debris flows entrain bed material. From a momentum conservation perspective, when a debris flow entrains material from a static bed, it is expected that the flow would decrease in velocity and momentum due to the increased sediment content of the flow. However, Iverson et al. (2011) found that the ability of a debris flow to entrain sediment was largely

related to the how saturated the bed material was (Figure 2.4). For example, when the debris flow entrained material from a wet bed, positive pore pressures in the flow were enhanced, which reduced basal friction at the base of the flow and increased flow momentum (Figure 2.5). The positive pore pressures also facilitate further scour of the channel bed, causing the flow velocity, mass, and momentum to all increase. They termed this process, the positive momentum feedback effect (Iverson et al., 2011).

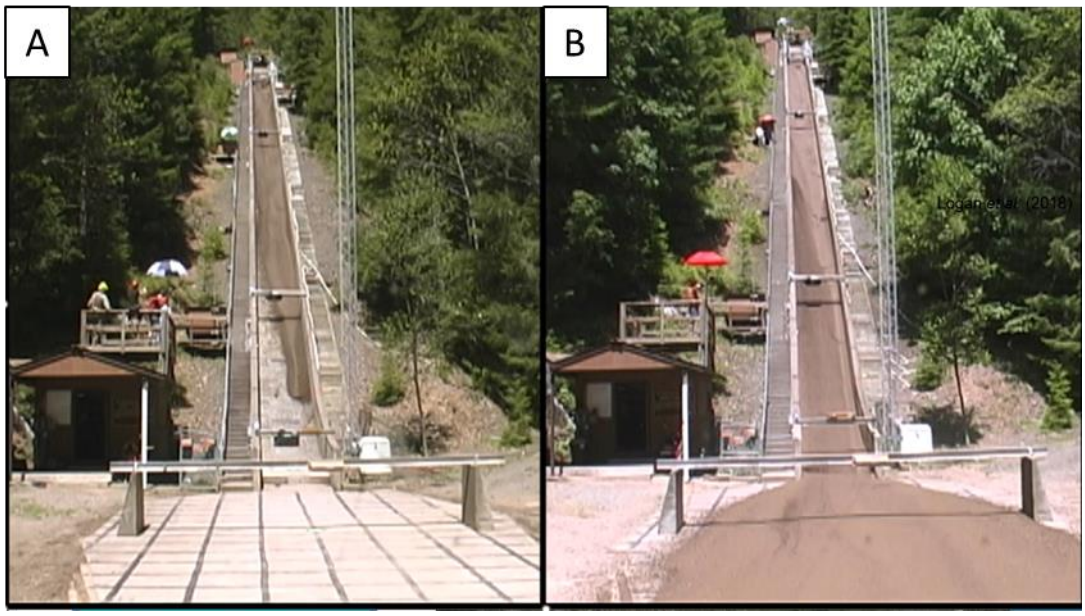

Figure 2.4
A photo taken of two large scale debris flow flume experiments taken from the videos by Logan et al. (2018). Both photos were taken at the same point in the experiment. A) shows a debris flow travelling over a dry erodible bed and B) shows a debris flow travelling over a wet erodible bed.

Evidence in support of the positive momentum feedback effect has been found through field datasets (de Haas et al., 2022; McCoy et al., 2012), experiments (de Haas and Woerkom, 2016; Kaitna et al., 2016; Reid et al., 2011), and numerical models (Horton et al., 2019). McCoy et al. (2012) used a sensor network to measure flow and bed properties for debris flows in the Chalk Cliffs catchment, US. They found that whilst the same thickness of sediment was entrained by each flow, that entrainment rates were quicker for debris flows travelling over saturated bed sediment. When travelling over wet sediment beds, the sensors detected high frequency pore pressure fluctuations. Their findings suggest that debris flows travelling over wet beds will be larger in volume than debris flows travelling over dry beds, as also shown by the positive momentum feedback effect (Iverson et al., 2011). A

recent modelling study of a catchment in Wenchuan, China, also found that once a threshold bed saturation had been reached, debris flow volume rapidly increased (Horton et al., 2019).

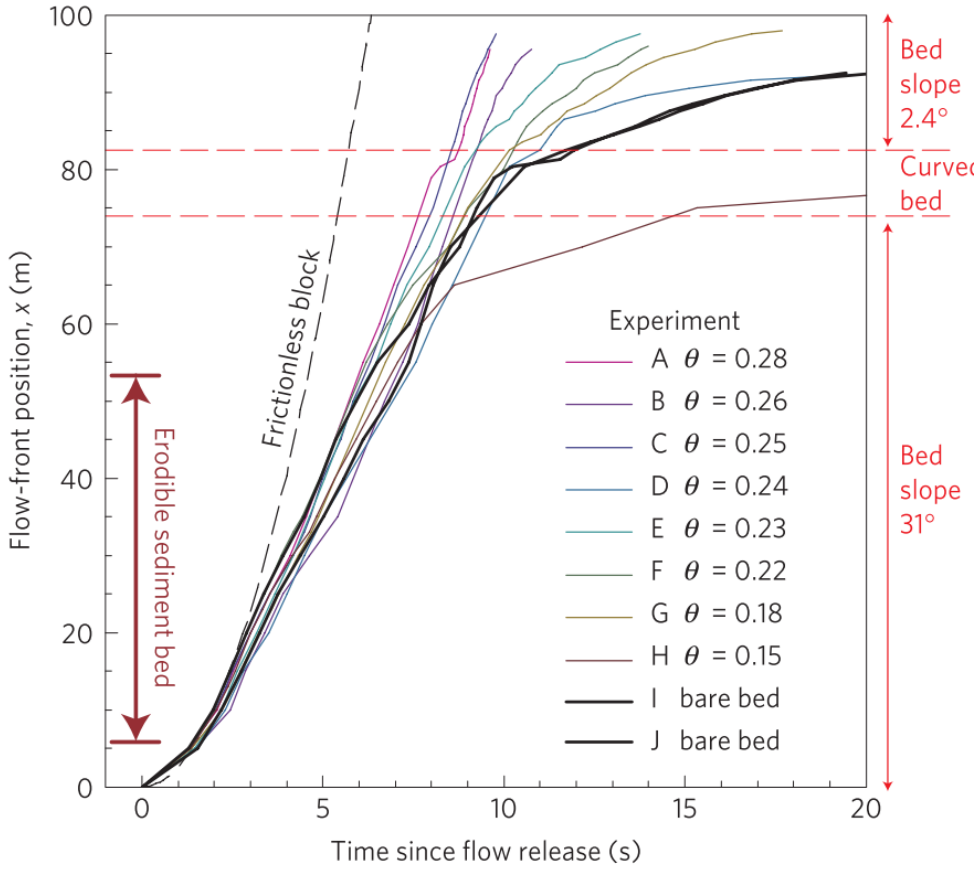

Figure 2.5

Relationship between channel bed saturation (Θ) and debris flow runout length for large-scale flume experiments. The debris flows travelling over the beds with the highest saturation travelled further, more quickly. Figure taken from Iverson et al. (2011).

Additional controls on the ability of a debris flow to erode material include topography, such as slope (Berti et al., 1999; Guthrie et al., 2010) and drainage area (Benda, 1990), impact forces within the flow (de Haas et al., 2022; Hsu et al., 2008; Stock and Dietrich, 2006), sediment supply (Edwards et al., 2021; Horton et al., 2019) and debris flow volume (Breien et al., 2008). Though I note that debris flow erosion is not interchangeable with entrainment. Here, erosion refers to the process of mobilising sediment, whereas entrainment refers to the debris flow's ability to transport the eroded sediment downstream, which typically involves an increase in volume. The role of coarse grains in eroding material from bedrock and in-channel

deposits is discussed in more detail in Section 2.5. The impact force and frequencies exerted by grain collisions on the bed and how they may facilitate grain bulking were demonstrated at Illgraben in de Haas et al. (2022). The importance of gravel content, as opposed to simply solid volume fraction, was demonstrated in small scale flume experiments in Roelofs et al. (2022), where increasing gravel content led to increased erosion along the erodible bed. The experiments also found that larger debris flows in terms of volumes also eroded more material from the bed (Roelofs et al., 2022). The same relationship was observed for a debris flow in western Norway. This debris flow increased in volume from 25 000 m^3 to 240 000 m^3, through a self-sustaining mechanism, whereby, as the debris flow increased in volume, there was greater potential for erosion (Breien et al., 2008).

The role of erodible channel bed material in controlling the length of debris flows has been shown in small-scale experiments of dry granular flows. For example, Edwards et al. (2021) found that, where sufficient sediment was available, granular flows could continue to entrain sediment at steady states to reach much larger volumes. They used different coloured particles to represent the flow and bed sediment. In most scenarios they demonstrated that the end of the flow was comprised predominantly of bed sediment. The exchange highlights the importance of further understanding how debris flow channel sediment can facilitate the development of extremely large hazardous flows.

2.4 Modelling debris flows

Debris flow mobility can be described using three modelling styles: continuum constituent models, discrete particle models, and empirical models (Takahashi, 2007). Continuum constituent models use mass and momentum conservation equations to describe the debris flow mixture (Iverson, 1997; Iverson and Denlinger, 2001; Pudasaini and Mergili, 2019; Takahashi, 2007). These models can provide insight into the macrobehaviour of motion for debris flows and be used to predict properties such as flow velocity, depth, and pore fluid pressure. To describe the flow using a continuum model, assumptions must be made about the rheology of the fluid and solid components. Discrete particle models alternatively are more mathematically complex and therefore have high processing times but can account for

discrete characteristics of grain motion (Takahashi, 2007). Recently discrete particle models have been used to better understand controls on the movement of different sized grains within a flow during segregation (Gray and Ancey, 2015; Hill and Tan, 2014). Debris flow behaviour, such as velocity and runout length, can also be determined empirically using parameters such as debris flow volume and slope (Fannin and Wise, 2001; Frank et al., 2015; Rickenmann, 1999). In the following sections, I will expand on the use of continuum constituent models to model debris flow behaviour. Continuum constituent models consider the importance of debris flow rheology through a less computationally complex approach in comparison to discrete particle models. In Chapter 6, I will use a debris flow runout model, Massflow, which is based on the mass and momentum conservation equations.

The mass and momentum conservation equations are the foundation for many models of debris flow mobility (Iverson, 1997; Iverson and Denlinger, 2001; Pudasaini et al., 2005; Pudasaini and Hutter, 2003). The models describe debris flows as single or two-phase mixtures. Single phase mixtures only consider the mass and momentum equation for the fluid phase of the mixture and dominate early models of debris flow behaviour (Coussot et al., 1998; Iverson, 1997; Takahashi, 2007). In single phase models, debris flows are described using rheological formulas, with the mixture of solid and fluid grains often described to behave as a non-Newtonian fluid (Takahashi, 2007). These simple mechanical models suggest that the mobilisation of a mixture is dependent on its yield strength, which can be described as a constant or as a function of the solid concentration of the flow (Von Boetticher et al., 2016). For example Johnson (1970; 1984) described debris flows using a Bingham model or viscoplastic rheology, meaning that the mixture remained rigid until the yield strength of the mixture was exceeded, at which point the mixture would then flow like a viscous fluid. In addition to the Bingham model, debris flows have been described using the Herschel-Bulkley model (Coussot et al., 1998; Schippa, 2020) and a dilatant plastic rheology (Phillips and Davies, 1991). These rheological models were validated using small-scale experiments with an abundance of fine grains (Coussot et al., 1998; Johnson, 1970; O'Brien and Julien, 1985, 1988; Phillips and Davies, 1991). In fact, it was observed that by increasing the fine content of the material, the yield strength of the

mixture increased (Major and Pierson, 1992; Parsons et al., 2001). Alternatively Takahashi (1981) focused on grain collisions as the main component of debris flow mobility using Bagnold's dilatant fluid model, which accounts for dispersive pressures generated through grain collisions (Chen, 1988; Takahashi, 1981). However, large-scale flume experiments by Iverson (1997) and Major and Iverson (1999) demonstrated that interactions between both grain collisions and pore fluid pressures determined debris flow mobility. These interactions cannot be captured using a single-phase rheological model.

Two-phase, or even multi-phase, models can account for the changes in solid and fluid properties within the flow independently (Iverson, 1997; Pudasaini and Mergili, 2019). These are referred to as mixture theory models (Iverson, 2003). The fluid (water + suspended sediment) and solid phases are represented by separate mass and momentum conservation equations, which are coupled. Iverson and Denlinger (2001) used these equations to develop a depth-averaged, two-dimensional grain-fluid mixture model (Iverson, 1997; Iverson et al., 1997; Savage and Hutter, 1989). The solid granular phase in the model was governed by Coulomb friction law and the fluid phase behaved as a Newtonian viscous fluid (Iverson, 2003). The coupling between the two phases obeyed Terzaghi's effective-stress principal and Darcy's law for drag. The model required a pore fluid pressure component for the fluid phase of the model, without which the mixture was simply a Coulomb solid (Iverson, 2003; Iverson and Denlinger, 2001). The main benefits of a mixture theory-based model are the fact that they can model behaviour from initiation to deposition and also account for variation in the fluid (pore fluid pressures) and solid (granular temperature) constituents. Most recently, Pudasaini and Mergili (2019) developed a three-phase model, which has a fluid phase (water + clay and silt), a fine-solid phase (sand particles) and a solid phase (gravels, cobbles and boulders). The three phases are modelled as a viscoplastic fluid, a Coulomb viscoplastic material (or Herschel-Bulkley or Bingham plastic) and a Coulomb material, respectively. The fact that progress within the field of debris flow mobility models has focused on understanding the roles of the individual constituents in the flow, highlights the importance of these constituents in understanding debris flow dynamics.

2.5 Debris flows as geomorphic agents

Debris flows, and the size of debris flows, are an important control on landscape evolution in steep hillslopes due to their ability to erode, transport and deposit large volumes of sediment (Benda and Dunne, 1997b; Stock and Dietrich, 2003, 2006). In steep, low order catchments, debris flows are one of the main processes eroding sediment from hollows and channels as well as incising into bedrock. Incision by debris flows can lead to distinct topographic features in comparison to fluvial incision, which can be identified from channel slope drainage area plots (Stock and Dietrich, 2003). An early incision law developed by Stock and Dietrich (2006) demonstrated that inertial normal stresses at the base of the channel may govern the rate of channel incision using catchments in the western US. Inertial stresses at the base were related to the impact frequency and impact forces exerted by grains. Stock and Dietrich (2006) crudely used the D_{50} value from the debris flow GSDs for gravels and coarser sediments when determining inertial normal stresses in an early example of how grain size influences debris flow erosion. They emphasised the need to better constrain the model inputs using detailed accounts of debris flow properties. Since then, the relationship between grain size and impact force and bedrock incision has also been found in experimental (Hsu et al., 2008, 2014) and field studies (Kean et al., 2015; McArdell et al., 2007; Zhang et al., 2021a). Additional controls such as how much sediment is in the channel, which can buffer interactions between grains and bedrock (Kean et al., 2015), as well as the water content and flow mechanisms (Hsu et al., 2008) should also be considered alongside grain impacts. The complexities and challenges associated with understanding what controls debris flow erosion and deposition on a spatial and temporal scale has made it hard to consider the wider impact of debris flow incision on landscape evolution (McGuire et al., 2022; Perron, 2017; Tucker and Hancock, 2010). Recently, Mcguire et al. (2022) developed a landscape evolution model which considered the role of debris flows. They compared debris flow incision laws with field observations to determine that debris flow incision scaled with slope and flow depth. Both parameters have been found to scale with impact frequency and force (McCoy, 2012; McGuire et al., 2022). The incision law however does not account for entrainment and a change in volume along the

flow, which can also affect the ability of debris flows to entrain sediment (Section 2.3.3; Iverson et al. 2011; Mcguire et al. 2022) and the changes in debris flow initiation location which may affect debris flow magnitude and frequency (Horton et al., 2019; McGuire et al., 2022; Stock and Dietrich, 2006). Therefore, improvements are needed in our ability to relate debris flow magnitude and frequency with entrainment mechanisms to truly understand how debris flows can impact landscapes.

Episodic, high magnitude debris flow events can have lasting impacts on sediment yields and the onward fate of material (Anderson et al., 2015; Benda and Dunne, 1997a, 1997b; Eaton et al., 2003; Kober et al., 2012; Pearce and Watson, 1986). For example, debris flows triggered by a 1 in ~300 years storm in the Front Range of Colorado, USA, mobilised the equivalent of hundreds to thousands of years of weathering products (Anderson et al., 2015). Long-term sediment yields that do not account for these high magnitude, low frequency events may therefore underestimate potential sediment yields in catchments (Kirchner et al., 2001). These episodic influxes of sediment by catastrophic debris flows can also influence sediment dynamics, leading to secondary hazards such as landslide dams (Casagli et al., 2003; Cui et al., 2009) and altering ecosystems (Foster et al., 2020). The coarse sediment delivered to higher order channels by debris flows can also control the rate of fluvial sediment export, as has been demonstrated for landslide deposits (Attal et al., 2015; Attal and Lavé, 2006; Dingle et al., 2017; Roda-Boluda et al., 2018; Sklar et al., 2017). Episodic pulses of coarse grains by mass movement deposits can affect rates of fluvial bedrock incision (Cowie et al., 2008; Sklar and Dietrich, 2004) and offset the fining in grain size observed due to other fluvial processes such as abrasion (Attal and Lavé, 2006; Sklar et al., 2006). The size of the grains delivered to channels and what controls this is still not well understood for debris flows, and other landslide deposits due to the fact that there are few detailed accounts of mass movement deposit GSDs (Attal et al., 2015; Attal and Lavé, 2006; Casagli et al., 2003). Despite the abundance of sediment delivered to channels following an earthquake (See Section 2.6), little research has attempted to directly link the GSDs of landslide and debris flow deposits to their onward

fate in a seismic setting (Howarth et al., 2012; Xie et al., 2022; Zhang et al., 2019).

Debris flow magnitude-frequency relationships can provide insight into how debris flows have shaped landscapes as well as be used to predict future hazards (Bennett et al., 2014; Innes, 1985; Riley et al., 2013; Stoffel, 2010). Previous magnitude-frequency distributions for debris flows have been described by non-normal distributions with a heavy tail, such as double Pareto and powerlaw distributions (Bennett et al., 2014; de Haas et al., 2018; Riley et al., 2013). Heavy-tailed distributions have been used to describe landslide magnitudes for decades to account for the high proportion of small and intermediate mass movements relative to the infrequent, catastrophic mass movements (Guzzetti et al., 2002; Hovius et al., 1997; Malamud et al., 2004). Though, many magnitude-frequency distributions for debris flows are limited by the time frame of observations and therefore do not include extremely large events (Marchi and D'Agostino, 2004). For a study covering 150 years in the Swiss Alps, only three events >50 000 m^3 occurred (Stoffel, 2010). The inventory was therefore dominated by smaller flows, which are thought to be less erosive (Bardou and Jaboyedoff, 2008; Stoffel, 2010). For larger datasets, we can compare magnitude-frequency distributions to develop further insight into the process governing the size of flows. For example, a global study of ~900 fire and non-fire debris flows, found that post-fire debris flows had a steeper distribution, suggesting that wildfires led to more frequent small debris flows (Riley et al., 2013). It is currently challenging to determine whether the factors governing the magnitude and frequency of catastrophic debris flows are consistent with those for smaller flows due to the lack of data available. The large increase in landslide and debris flow frequency following an earthquake presents rare opportunities to develop high resolution modern-day magnitude-frequency distributions, and thus explore controls on the size and frequency of mass movements (Fan et al., 2018a; Jones et al., 2021; Marc et al., 2016b; Valagussa et al., 2019).

2.6 Debris flows and the post-earthquake sediment cascade

Earthquakes can trigger widespread landsliding (Densmore and Hovius, 2000; Hovius et al., 2000; Keefer, 1984). Co-seismic landslides that occur during an earthquake are primarily triggered when the sudden release of energy in the

form of elastic strain waves leads to ground shaking and short-term episodic changes in the hillslope normal and shear stresses (Meunier et al., 2008). The widespread shaking associated with earthquakes also fractures rocks and reduces cohesion within soils and rocks (Hovius and Meunier, 2012; Meunier et al., 2008). This decreases substrate strength and can also trigger a landslide. Keefer (1984) was one of the first to demonstrate the relationship between landslide occurrence and earthquake magnitude, finding that landslides commonly occur in response to any earthquake M_W >4.0. More recent studies (e.g. Havenith et al., 2016; Hovius and Meunier, 2012; Meunier et al., 2008, 2007) have sought to demonstrate the importance of other factors in controlling the occurrence of landslides, in addition to earthquake magnitude, such as peak ground acceleration, earthquake depth and earthquake focal mechanisms. Climate, topography and lithology are also thought to play an important role in determining the spatial distribution of co-seismic landslides (Havenith et al., 2016; Meunier et al., 2008).

Co-seismic landslides are renowned for mobilising large volumes of sediment on hillslopes in minutes (Dadson et al., 2004; Densmore and Hovius, 2000; Hovius et al., 2000, 2011; Keefer, 1984). The abundance of sediment generated by landslides following an earthquake can lead to secondary hazards from unstable deposits, such as debris flows (Dadson et al., 2004; Francis et al., 2022; Zhang et al., 2014b), and the deposition of sediment in channels, such as lake outburst floods and landslide dams (Cui et al., 2009; Fan et al., 2012) as well as limit rates of surface uplift generated during the earthquake (Li et al., 2014; Marc et al., 2016a; Parker et al., 2011). Yet, the amount of sediment mobilised, and the onward fate of this material is poorly constrained. Poor constraints stem from the lack of understanding of the processes which remobilised co-seismic sediment and the rates at which the sediment is remobilised (Figure 2.6; Fan et al. 2019a; Francis et al. 2022). Fine sediment in fluvial channels has been shown to return to pre-earthquake levels in a matter of years to decades (Hovius et al., 2011; Huang and Montgomery, 2012; Wang et al., 2015). However, coarser fractions of co-seismic sediment are expected to take between hundreds to thousands of years to fully export (Francis et al., 2020; Pearce and Watson, 1986; Yanites et al., 2010). Thus, to determine how, and the rate at which, sediment is

evacuated from a catchment following an earthquake, we need to understand the processes transporting coarse sediment.

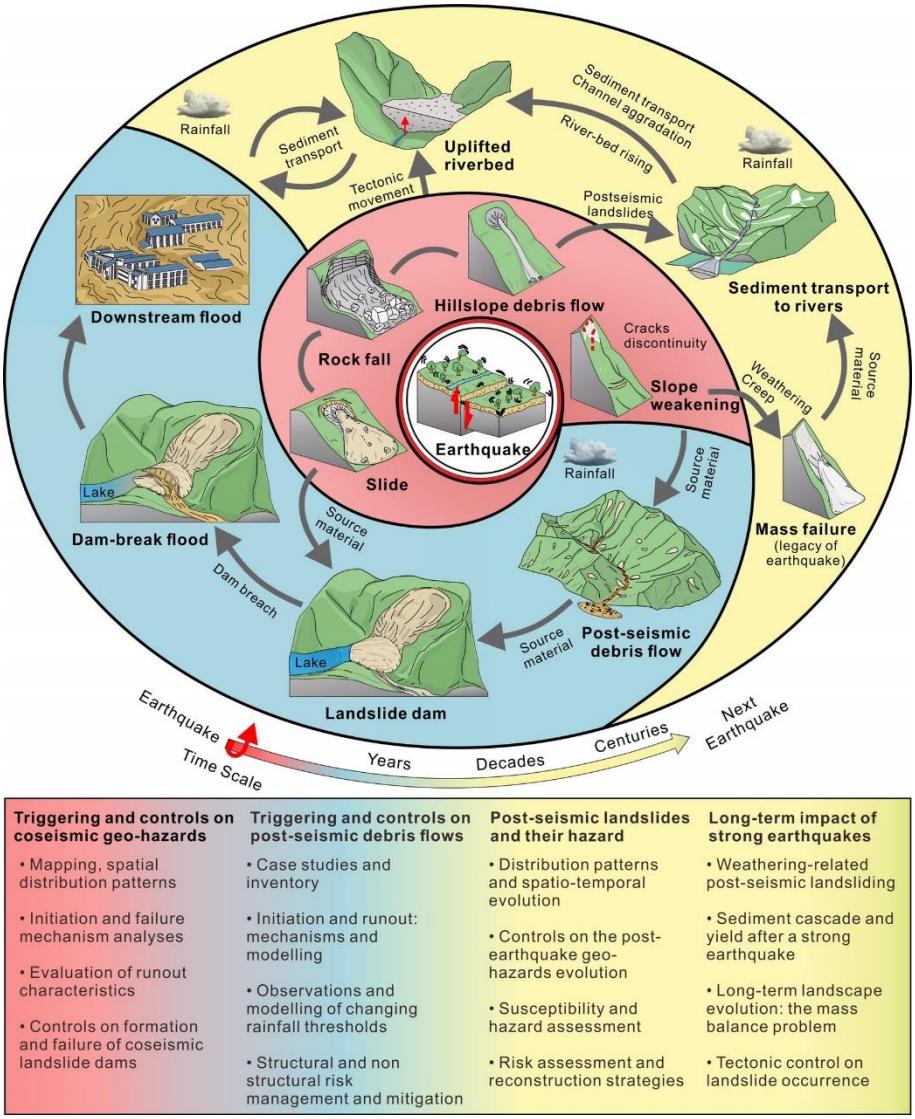

Triggering and controls on coseismic geo-hazards	Triggering and controls on post-seismic debris flows	Post-seismic landslides and their hazard	Long-term impact of strong earthquakes
• Mapping, spatial distribution patterns	• Case studies and inventory	• Distribution patterns and spatio-temporal evolution	• Weathering-related post-seismic landsliding
• Initiation and failure mechanism analyses	• Initiation and runout: mechanisms and modelling	• Controls on the post-earthquake geo-hazards evolution	• Sediment cascade and yield after a strong earthquake
• Evaluation of runout characteristics	• Observations and modelling of changing rainfall thresholds	• Susceptibility and hazard assessment	• Long-term landscape evolution: the mass balance problem
• Controls on formation and failure of coseismic landslide dams	• Structural and non structural risk management and mitigation	• Risk assessment and reconstruction strategies	• Tectonic control on landslide occurrence

Figure 2.6

The hazards associated with the post-earthquake sediment cascade through time. Figure taken from Fan et al. (2019a).

Hillslope-channel connectivity provides insight into which processes deliver sediment to channels as part of the post-earthquake sediment cascade and how much co-seismic sediment enters the fluvial network (Fan et al., 2019a). Most studies of recent earthquakes found between 5% and 20% of co-seismic landslides were connected to fluvial channels (Dadson et al., 2004; Fan et al., 2019a; Li et al., 2016; Roback et al., 2018; Xie et al., 2022). However, several challenges limit the accuracy of these estimates, such as changes to the location of channel-heads and the course of rivers by co-seismic landslides as

well as resolution errors (~10 % in Li et al. 2016). In addition, landslide-channel connectivity does not reveal how much, and the rate at which, sediment is deposited into channels (Fan et al., 2019a; Roback et al., 2018). Therefore, the metric can only estimate the maximum amount of sediment which may have been delivered to channels. Estimates of hillslope-channel connectivity are also sensitive to the metric used to describe landslide size. For example, larger landslides were more likely to connect to fluvial channels in Wenchuan and therefore the volume of co-seismic landslides connected to channels was larger than when considering the number of landslides (Li et al., 2016). There were no clear relationships between mapped hillslope-channel connectivity and post-earthquake sediment fluxes for co-seismic landslide number, area and volume (Li et al., 2016). The bimodal GSD of landslide deposits may explain the lack of relationship between connectivity and suspended sediment flux. Fine grains within the deposits can be transported downstream fluvially by overland flow and therefore do not rely on landslides or debris flows to be transported. The winnowing of fine grains downstream may explain the poor correlation between the fine sediment flux and hillslope-channel connectivity in Wenchuan (Li et al., 2016; Wang et al., 2015). Fluidised, high velocity flows, such as debris flows, may be more crucial for transporting the coarsest sediment downstream and into channels. How much sediment is delivered to channels and the size of the grains transported are important in governing the rate at which sediment will be exported (Attal and Lavé, 2006; Roda-Boluda et al., 2018). However, accurate constraints on the proportion of coarse sediment in deposits remain a challenge (Section 2.7).

Post-earthquake debris flows are the main process transporting the coarse sediment remaining on hillslopes into fluvial channels (Dadson et al., 2004; Dahlquist and West, 2019; Domènech et al., 2019; Francis et al., 2022). The frequency of debris flows rapidly increases following an earthquake due to the masses of poorly sorted material deposited on hillslopes (Lin et al., 2004; Zhang and Zhang, 2017a). For example, in Wenchuan the number of debris flows increased by at least three-fold when comparing the number of debris flows between 2003 and 2007 (758) with the number following the earthquake in 2008 until 2012 (2333) (Huang and Fan, 2013; Tang et al., 2011b). An

elevated number of debris flows at unprecedented scales are still occurring over a decade after the earthquake (Yang et al., 2021). Post-earthquake debris flows initiate due to different mechanisms, including from co-seismic landslide deposits which saturate and liquefy (Dahlquist and West, 2019; Iverson et al., 1997; Lin et al., 2004; Takahashi, 1981) as well as by Hortonian overland flow, which can remobilise channel deposits (Dahlquist and West, 2019; Yang et al., 2021; Zhang et al., 2013). The significance of post-earthquake debris flows in sediment transfers following the 2008 Wenchuan earthquake is shown in Francis et al. (2022). By 2018, the sediment budget shows that of the co-seismic sediment which had been mobilised (only 13%), 67% of the sediment was mobilised by debris flows. Of the sediment mobilised by debris flows, a large proportion of this sediment was transported by catchment-clearing debris flows. These debris flows are extremely large and transit catchments to deposit masses of sediment in higher order channels, such as the Min Jiang River (Figure 2.7). Therefore, they fit with my definition of catastrophic debris flows. In the ten years following the Wenchuan earthquake, catastrophic debris flows accounted for 61% of the sediment deposited in the Min Jiang river (Francis et al., 2022). To my knowledge, the conditions and processes which led to the development of catastrophic debris flows in Wenchuan have not been assessed. Despite the dominance of post-earthquake debris flows in the post-earthquake sediment cascade, controls on the frequency and magnitude of the debris flows remain poorly understood. I provide an overview of potential controls on debris flow frequency and magnitude in Wenchuan in Chapter 3.

The frequency of post-earthquake debris flows has been found to change temporally across recent earthquakes in Chi-Chi, Wenchuan and Gorkha (Dahlquist and West, 2019; Lin et al., 2004; Tang et al., 2011b; Zhang and Zhang, 2017a). The immediate increase in post-earthquake debris flow frequency is reflected in the lower intensity-duration thresholds used to describe the initiation conditions for debris flows (Caine, 1980; Cannon and Ellen, 1985; Dai et al., 1999; Marchi et al., 2002). Thresholds were found to decrease rapidly following an earthquake as a result of the abundance of loose regolith, which fails more easily (Lin et al., 2008; Zhang and Zhang, 2017b). Following the Chi-Chi earthquake, the rainfall required to initiate a

debris flow decreased to as low as one third of pre-earthquake levels (Lin et al., 2004). Similarly, in Wenchuan triggering thresholds were ~75% of pre-earthquake levels (Tang et al., 2009). In the years that follow an earthquake, debris flow initiation thresholds have been found to recover and the frequency of debris flows decrease (Figure 2.8) (Guo et al., 2016a; Marino et al., 2022; Zhang and Zhang, 2017a). The intensity of monsoons in Wenchuan has not changed in the years since the earthquake, suggesting that the change in debris flow frequency observed may relate to changes in the properties of hillslope sediment (Francis et al., 2022).

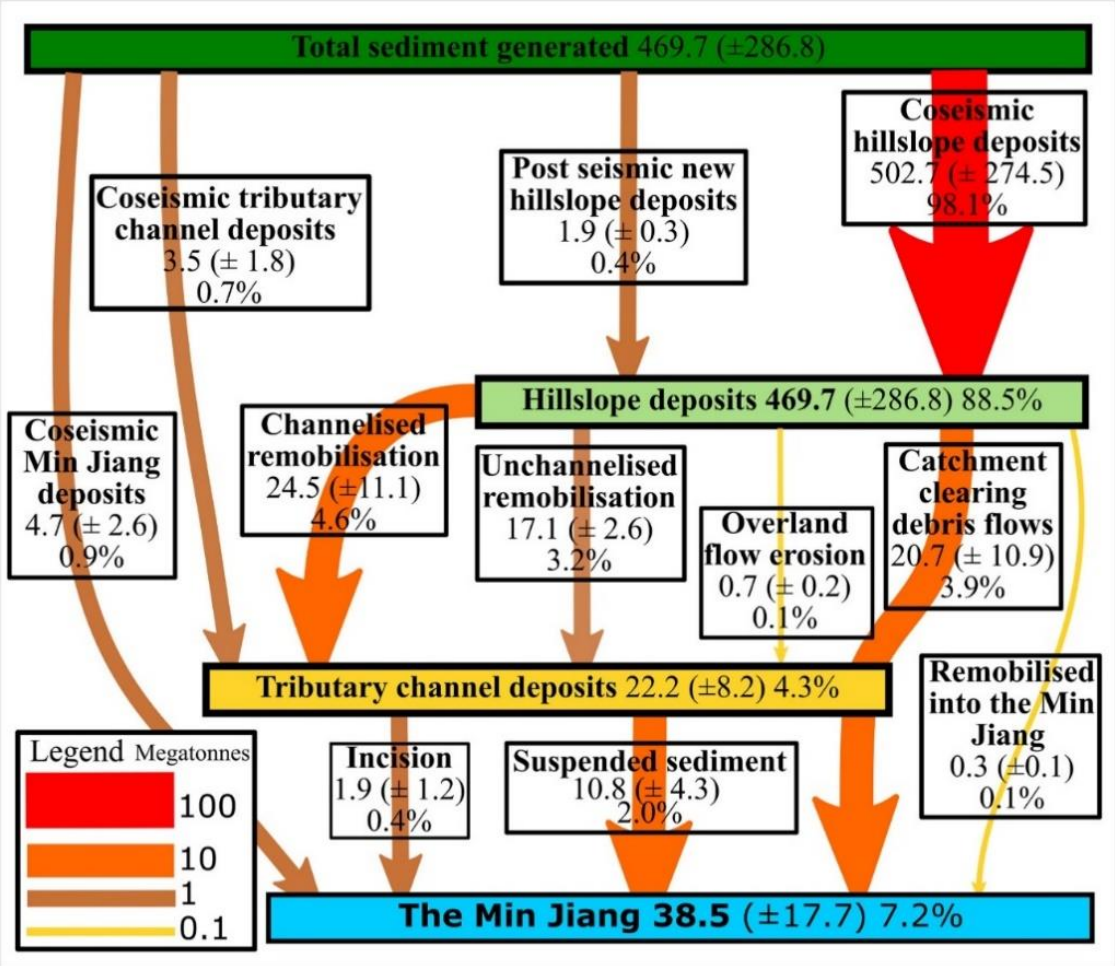

Figure 2.7

A sediment budget for the 2008 Wenchuan earthquake between 2008 and 2018. The arrows are scaled based on the amount of sediment transported. Stores of sediment are represented by coloured boxes. Figure taken from Francis et al. (2022).

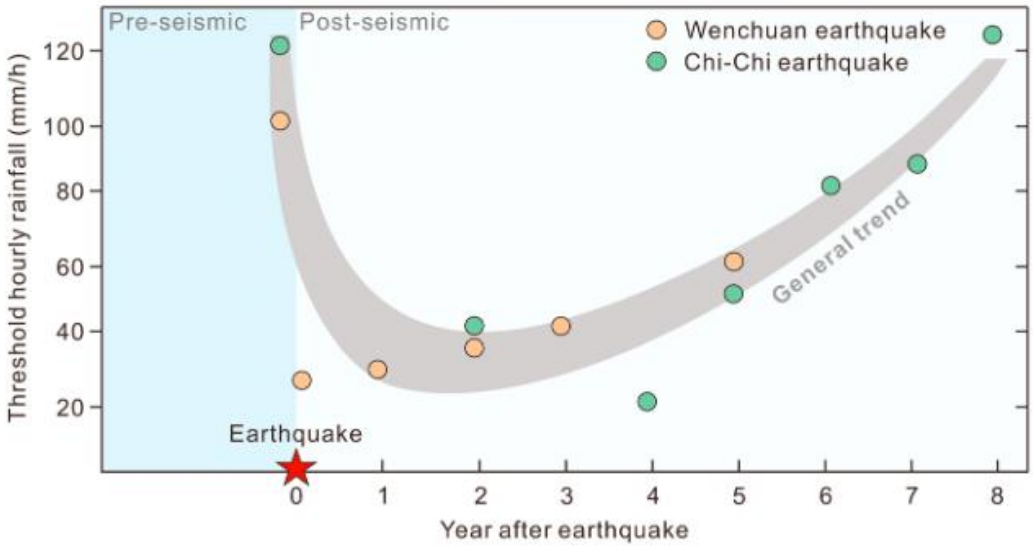

Figure 2.8

The amount of rainfall required to initiate a debris flow plotted against years following an earthquake. The rainfall required to trigger a debris flow increases with time in the years after an earthquake. Data plotted is from the 1999 Chi-Chi and 2008 Wenchuan earthquakes. Figure taken from Fan et al. (2019a).

2.7 Measuring debris flow GSDs

Debris flows transport grains over eight orders of magnitude in size, from clays to boulders (>10 m) (Iverson, 1997). As such, studies of debris flow GSDs often only analyse a fraction of the true GSD (Figure 2.9; de Scally and Owens 2005; Kean et al. 2011; Chen et al. 2014). To obtain GSDs which fit across the full range of sizes, a variety of different methods are required, such as sieving (e.g. Major and Voight 1986; Nishiguchi et al. 2012; Zhang et al. 2015), Wolman pebble counts (e.g. Whipple and Dunne 1992; Kim and Lowe 2004; de Scally and Owens 2005) and photo-based analyses (e.g. Ibbeken et al. 1998; Tecca et al. 2003). The array of methods used to measure debris flow GSDs and the various protocols used, for example sometimes the sieved fraction is <10 mm or <75 mm (Nishiguchi et al., 2012; Tiranti et al., 2008; Whipple and Dunne, 1992), make it challenging to produce comparable GSDs. The weight of material sieved also varies across studies, with most sieving <30 kg (Boniello et al., 2010; Major and Voight, 1986; Sosio et al., 2007; Whipple and Dunne, 1992). These small samples sizes are likely to be far below the weight limit set out in Church et al. (1987) where the largest grain must not exceed 5% of the total weight. In some studies, the methods used to estimate deposit GSDs are not provided at all (Yong et al., 2013). Where studies have used

different approaches, the GSDs may not be comparable (Bunte and Abt, 2001b). To overcome challenges associated with only measuring part of the distribution, studies may provide an estimate of the proportion of the distribution missing (Roda-Boluda et al., 2018). Though, this is rare and therefore where studies do not acknowledge how much of the distribution is missing, the conclusions made may provide inaccurate insight into the mechanisms controlling debris. Subsequently clear, detailed methods are crucial to produce comparable debris flow GSDs.

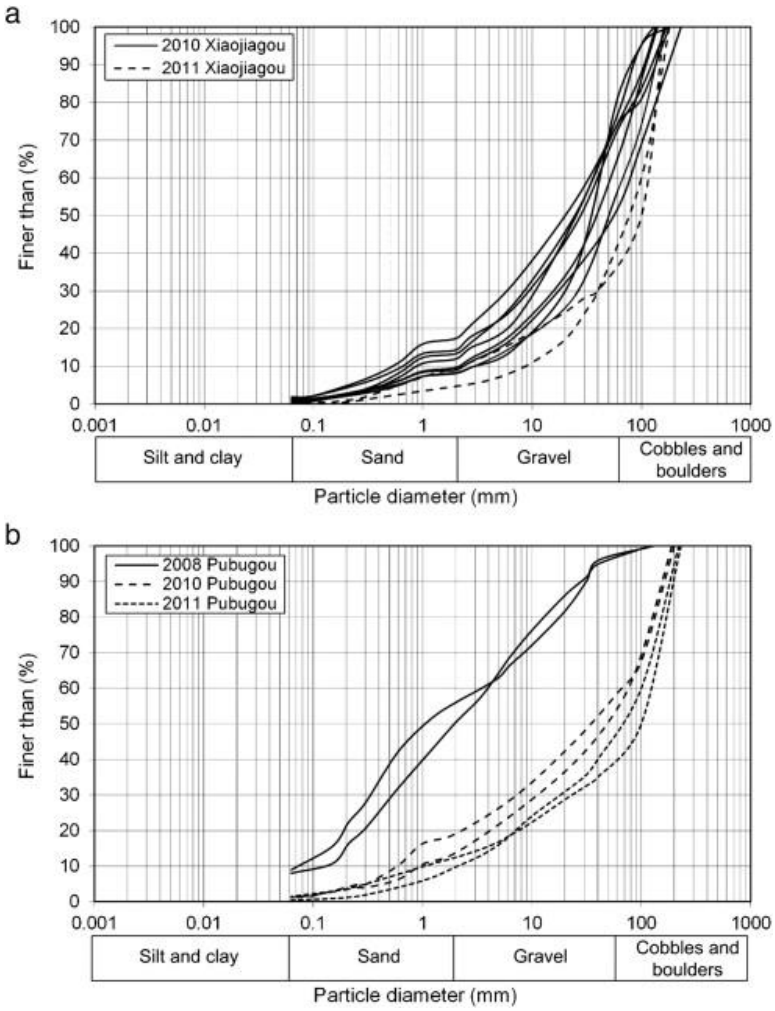

Figure 2.9

Grain-size distributions collected for two debris flow deposits which were triggered following the 2008 Wenchuan earthquake. The deposits appear to coarsen through time. The GSD suggests a maximum grain size of ~200 mm. Figure taken from Chen et al. (2014).

The complexities associated with measuring debris flow GSDs are exacerbated by the infrequent, unpredictable nature of debris flows as well as the processes which can alter GSDs during transit. The unpredictable and

inaccessible nature of debris flows mean that studies of GSDs temporally in debris flows are limited to flume experiments (de Haas et al., 2015; Iverson et al., 2010; Kaitna et al., 2016) and numerical models (Johnson et al., 2012; Kokelaar et al., 2014; Sanvitale and Bowman, 2017). In some rare instances, studies have obtained grab samples from flowing debris flows (Pierson, 1981). However, these samples can obscure the behaviour of the flow and are unlikely to include the largest grains (Iverson, 1997). Therefore, most field GSDs are sampled from debris flow deposits (e.g. Whipple and Dunne 1992; Vallance and Scott 1997; Kim and Lowe 2004). However, debris flow deposit GSDs also introduce challenges. For example, as outlined above, debris flows are heterogenous in planform-view and with depth due to processes that segregate by grain size (Johnson et al., 2012; Tiranti et al., 2008). As such, different methods may be required to sample both the surface and subsurface of deposits. Most approaches which sample debris flow deposit GSDs with depth rely on vertical exposures (Major and Voight, 1986; Whipple and Dunne, 1992; Zhang et al., 2015) or pits dug into the deposit (Chen et al., 2001; Hubert and Filipov, 1989). Both of which can only be sampled over a small proportion of the entire deposit. The presence of a coarse snout and coarse levees in some debris flow deposits can also present challenges with respect to finding a method that can accurately constrain all grain sizes but also be readily applied to the entire deposit. For example, sieving is required to obtain the fraction of clay, silt and sand, but is extremely time consuming and therefore must be complemented with other techniques to cover wide areas (Attal and Lavé, 2006; Dunning, 2006; Zhang et al., 2015). Despite the challenges faced when measuring mass movement deposit GSDs, to my best knowledge, no studies have explicitly compared traditional methods to measure GSDs in the context of mass movement deposits.

2.8 Conclusions and research gaps to be addressed

Catastrophic debris flows shape landscapes, deliver large volumes of sediment to channels, and pose major hazards to local communities. To fully understand the role debris flows play in each of these scenarios, it is crucial to determine what controls mechanisms of initiation, transport and deposition. In this literature review, I demonstrated the importance of debris flow grain size in accelerating erosion, through impact forces in the coarse

snout (Hsu et al., 2008; Stock and Dietrich, 2006), and facilitating deposition via the dissipation of excess pore pressures (de Haas et al., 2015; Iverson et al., 2010; Major and Iverson, 1999). Not only does debris flow grain size control debris flow dynamics, but the deposit GSDs can also influence the fluvial export of material (Attal and Lavé, 2006; Benda and Dunne, 1997b; Pearce and Watson, 1986). Catastrophic debris flows are the main conduit by which coarse sediment is transported following earthquakes (Dai et al., 2021; Francis et al., 2022). However, the amount of sediment they transport and controls on their magnitude and frequency are not well constrained (Fan et al., 2019a). Despite clear interest in how debris flows perturb systems, and the role of catastrophic debris flows in sediment cascades, our understanding of these debris flows in the post-earthquake sediment cascade is limited.

The 2008 Wenchuan earthquake offers a unique opportunity to explore how debris flows contribute to post-earthquake sediment cascades. In particular, the abundance of debris flows triggered following the earthquake (>2000) provide strong foundations from which I will (1) better constrain the GSD of debris flow deposits; (2) use these GSDs to identify mechanisms controlling the runout length of debris flows; (3) infer controls on the magnitude-frequency distribution of debris flows in Wenchuan, and (4) determine what controls the development of catastrophic debris flows in Wenchuan. By analysing this large dataset of post-earthquake debris flows in a single geological location, we can improve current understanding of debris flow mechanisms, such as controls on size and entrainment, which are currently poorly understood, particularly in a field context. To achieve the aims listed above, I will first compare previous methods used to measure debris flow GSDs and infer how using different methods to measure grain size will affect my geomorphic interpretation of GSDs.

Chapter 3

Study Area

Co-seismic landslides triggered by the 2008 Wenchuan earthquake mobilised almost 3 km^3 of sediment (Li et al., 2014). The abundance of sediment deposited on steep hillslopes in combination with annual monsoons has resulted in a high frequency of post-earthquake debris flows (Tang et al., 2011a). Detailed inventories of these post-earthquake debris flows, including several catastrophic events, mean that the 2008 Wenchuan earthquake is an excellent setting to explore controls on the runout of catastrophic debris flows. In this section I provide a brief background of the 2008 Wenchuan earthquake and introduce the two post-earthquake debris flows analysed in this thesis.

3.1 The Longmen Shan Mountain Range

The Longmen Shan is a mountain range dividing the western edge of the Sichuan Basin and the eastern rim of the Tibetan Plateau (Liu-Zeng et al., 2009). The mountain range is renowned for its steep relief and deeply incised valleys, with increases in elevation in excess of 5000 m over 50 km in length (Figure 3.1, Densmore et al. 2007). Uplift rates for the mountain range can reach 6 mm yr^{-1} (Kirby et al., 2003). The geology of the region is complex due to its multiphase tectonic history and extensive faulting (Godard et al., 2009). The catchments in this study, as shown in Figure 3.2, are underlain by predominantly Mesoproterozoic granite and granodiorite basement rock, typically known as the Pengguan Massif. The Pengguan Massif denotes the highest part of the Longmen Shan mountain range (Chen and Wilson, 1996; Cook et al., 2013; Godard et al., 2010). Sedimentary rocks from the Palaeozoic (greywacke and shale) and Triassic (mudstone, sandstone and conglomerates) surround the Pengguan Massif (Godard et al., 2009, 2010; Ma, 2002).

Climate in the Longmen Shan is controlled by the East Asian and Indian monsoons, which are characterised by warm, wet summers (Liu-Zeng et al., 2011; Wang et al., 2015). The Longmen Shan has an average annual precipitation of ~1200 mm, with 70% to 80% of all rainfall occurring between May and September (Liu-Zeng et al., 2011). The high precipitation rates in summer months, comprised of predominantly rainfall, correspond to high suspended sediment concentrations between June and August. In fact, 97% of all suspended sediment is transported by monsoonal rainfall between May and

October (Wang et al., 2015). This figure is true for both pre- and post-earthquake scenarios. The high precipitation intensity during summer has considerable effects on the post-earthquake sediment cascade, with catastrophic debris flows typically triggered by heavy rainfall events in July and August (Ge et al., 2015; Tang et al., 2012a; Yang et al., 2021). Warm, wet summers in the Longmen Shan also encourage high rates of biodiversity in the region (Di et al., 2010). As such, inactive co-seismic landslide deposits are predicted to revegetate in as little as 18 years after the 2008 Wenchuan earthquake (Yunus et al., 2020).

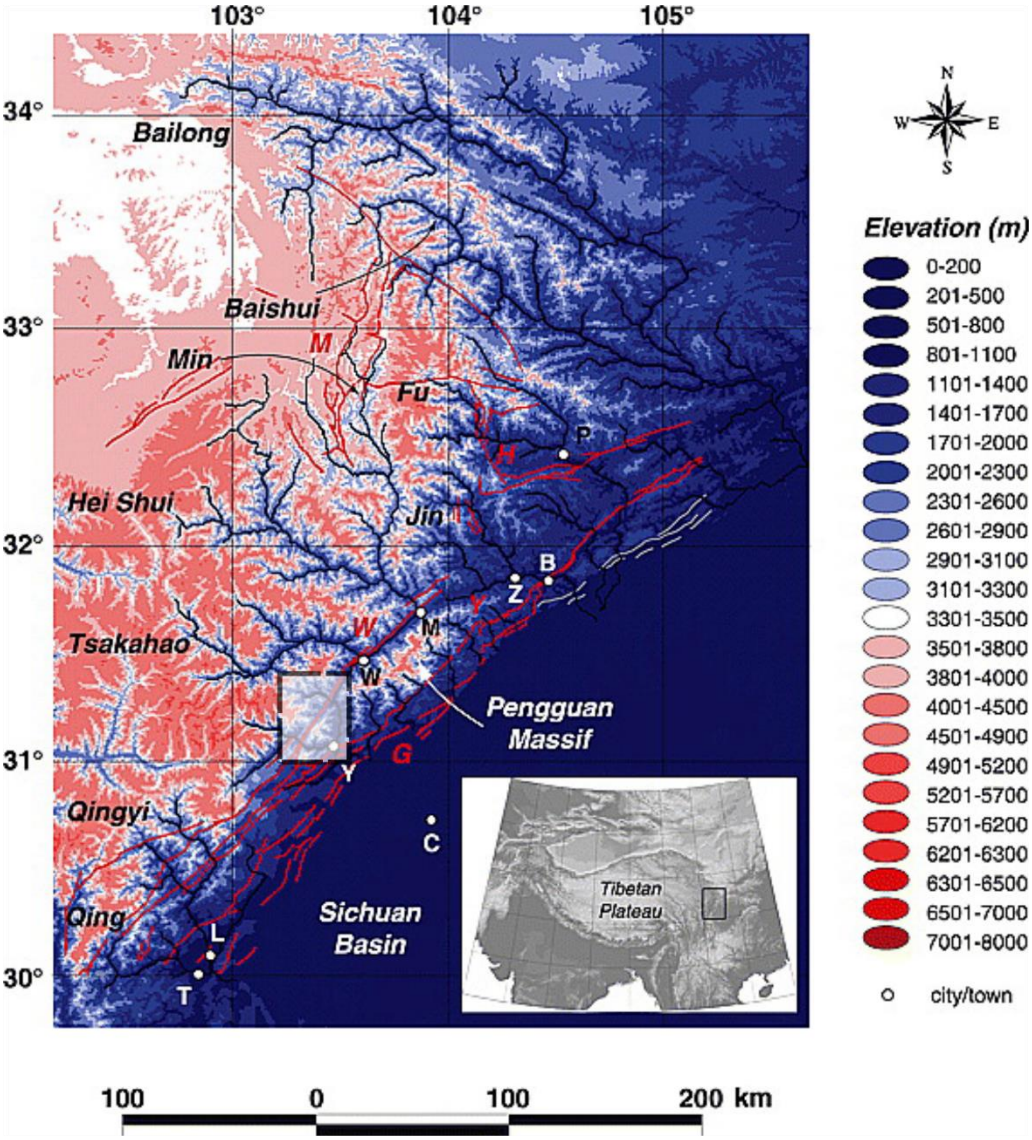

Figure 3.1

Topography of the Longmen Shan mountain range and the Tibetan Plateau taken from Kirby et al. (2003). Major faults are shown by red lines. The letters in white represent main cities (B, Beichuan; C, Chengdu; L, Lushan; M, Maowen; P, Pingwu; T, Tianquan; W, Wenchuan; Y, Yingxiuwan; Z, Zicheng). The shaded grey box shows the extent for Figure 3.2.

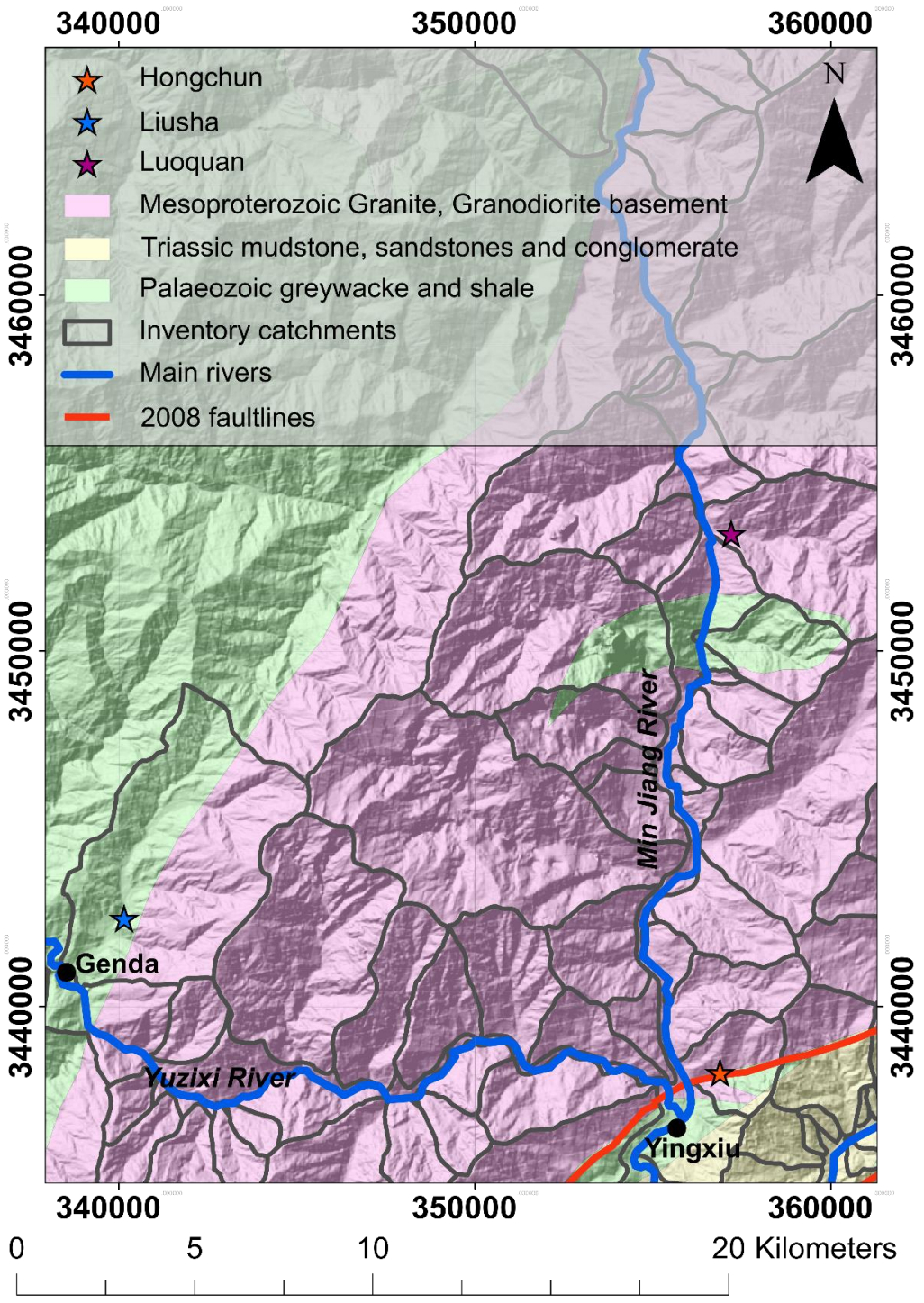

Figure 3.2

The geology of the Longmen Shan mountain range with stars representing locations referred to in this thesis. The Liusha and Luoquan debris flows were sampled to achieve the aims set out in Chapters 4 and 5. The 2010 Hongchun debris flow was used by Horton et al. (2019) to calibrate the model also used in Chapter 6. The faultlines that ruptured in the 2008 Wenchuan earthquake and are visible at this scale are shown in red. The faultlines are taken from Densmore et al. (2007). The geology base layer is based upon Ma (2002). The locations shown in Figure 3.2 is shown by the grey box in Figure 3.1.

3.2 The 2008 Wenchuan earthquake

On 12th May 2008, a Mw 7.9 earthquake occurred along the Longmen Shan thrust zone, rupturing both the Beichuan and Pengguan faults (Xu et al., 2009). The main component of rupture was through dextral thrust and oblique slip faults (Densmore et al., 2007). The earthquake occurred at a depth of 12 km and caused over 8 m of surface displacements in places (Densmore et al., 2010; Liu-Zeng et al., 2009). The earthquake resulted in almost 70 000 fatalities, with a further 375 000 people injured, 6.5 million homes damaged and 5 million people left homeless (Tang et al., 2010).

The earthquake triggered over 60 000 co-seismic landslides and was therefore considered one of the most erosive earthquakes in the last 100 years and displaced almost 3 km^3 of sediment (Fan et al., 2018b; Li et al., 2014; Marc et al., 2016b). The frequency of co-seismic landslides was higher in comparison to other events which occurred at a similar magnitude (e.g. 2015 Gorkha earthquake, ~4300 co-seismic landslides, M_W ~7.8) due to the type of fault rupture and its orientation (Fan et al., 2019a; Kargel et al., 2016). The co-seismic landslides triggered in Wenchuan had significant hazard implications, accounting for ~20 000 fatalities alone, almost one third of the total fatalities associated with the earthquake (Tang et al., 2010). Landslides also destroyed homes and blocked highways and bridges, isolating the city of Wenchuan and many other towns and villages (Tang et al., 2010). Thirty four large barrier lakes were also formed from landslide dams in the area, which led to secondary hazards such as flash flooding and debris flows (Tang et al., 2010).

In the years following the 2008 earthquake, the Wenchuan region has been inundated by post-earthquake hazards including landslides, debris flows and landslide dams (Figure 3.3; Tang et al. 2012; Fan et al. 2018; Yang et al. 2021). The high frequency of slope failures can be attributed to the large volumes of available sediment remaining on steep hillslopes and frequent monsoons in the region (Francis et al., 2020, 2022; Wang et al., 2015). An abundance of sediment also reached the fluvial channels in the region, with channels deposits several meters deep. These channels deposits have resulted in significant landslide dam and outburst flood risk (Fan et al., 2012). This post-seismic chain of geohazards has continued to shape the landscape in Wenchuan, with sediment gradually being delivered to channels through large

landslides, debris flows and fluvial erosion (Francis et al., 2022; Wang et al., 2015; Zhang et al., 2019, 2016).

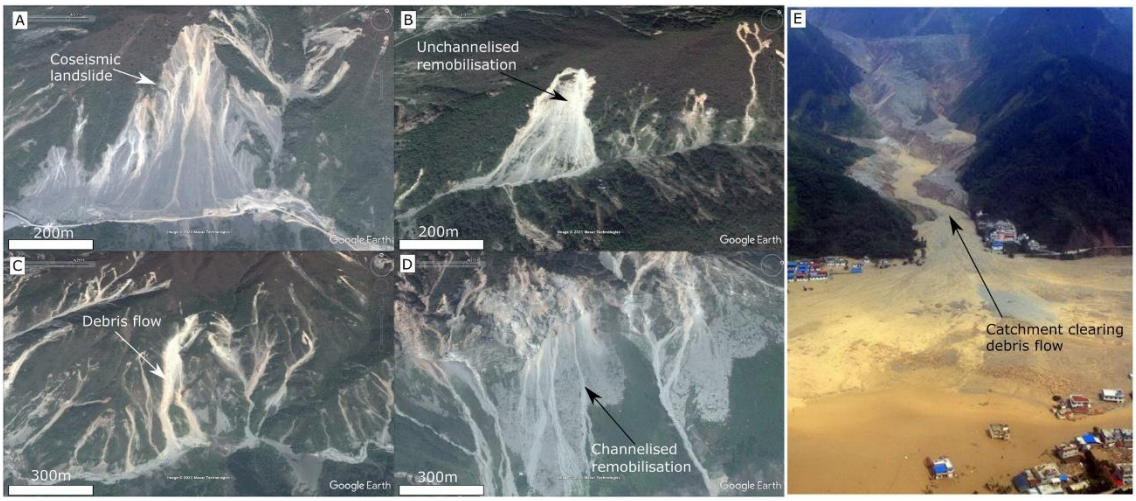

Figure 3.3

Photos of the post-earthquake hazards generated following the 2008 Wenchuan earthquake. E) is a catchment-clearing debris flow in the Wenjia catchment, which I refer to as a catastrophic debris flow in this thesis. Figure has been taken from Francis et al. (2022).

Through time debris flow frequency in Wenchuan has decreased as intensity-duration thresholds for debris flows return to normal (Figure 2.8). The change in debris flow frequency has been attributed to decreases in sediment supply (Zhang et al., 2013), increased vegetation cover (Yunus et al., 2020) and a change in the GSD of debris flow deposits (Chen et al., 2014; Domènech et al., 2019). Decreased debris flow frequency is unlikely to relate to the exhaustion of sediment on hillslopes as a large proportion of coarse sediment remains on hillslopes. Therefore, processes responsible for stabilising hillslope deposits are more likely (Fan et al., 2019a). In Wenchuan, debris flow deposit GSDs have been found to coarsen through time, with a particular decrease in the proportion of clay, silt and fine sand found in deposits (Figure 2.9; Chen et al. 2014; Yang et al. 2021). The coarsening of landslide deposits is thought to occur due to the winnowing of fine grains as they are easier to transport through overland flow and runoff. The removal of fine grains from deposits can increase the hydraulic conductivity of the deposits and reduce the probability of failure (Domènech et al., 2019; Sassa and Wang, 2005; Wang and Sassa, 2003). A high proportion of fine grains is essential to sustain the high pore pressures required for a debris flow to occur (Hu et al., 2017). However, observations of deposit coarsening have been based on a limited

number of samples from debris flow deposits over a restricted range of grain sizes. For example, most studies sample up to ~10 cm in diameter, when from field observations boulders >1 m can be found in most deposits in Wenchuan. In some cases only two samples were collected from 50 cm x 50 cm pits for debris flows up to 1 000 000 m^3 in volume (Chen et al., 2014). Furthermore, the material deposited in sections of a debris flow may not accurately represent source samples, with processes such as comminution also possible within the flows which can reduce the grain size during transit and bulking which can facilitate the entrainment of different sized grains (Davies and McSaveney, 2009; Makris et al., 2020). An alternative explanation for increased stability is the revegetation of hillslope and channel deposits (Domènech et al., 2019; Yunus et al., 2020). Vegetation cover can reduce the occurrence of debris flows by intercepting rainfall and decreasing the saturation state of deposits (McGuire et al., 2016; Wilkinson et al., 2002) as well as root reinforcement by new vegetation increasing the shear strength of the deposits (Hales, 2018; Wilkinson et al., 2002). The main colonising plants on deposits were grasses and shrubs, which are thought to have weak root structures, suggesting they are unlikely mechanisms for the decreased frequency of debris flows (Francis et al., 2022; Hales, 2018; Shen et al., 2020). In contrast, dense grasslands can decrease the potential for large volumes of runoff to form (Shen et al., 2020), which can be an important driver of debris flow initiation as seen in post-wildfire settings (Cannon et al., 2001a). Current estimates suggest post-earthquake debris flows will remain prominent for 10 to 20 years following an earthquake (Fan et al., 2019b, 2019a). However, these estimates are based on limited observations, which currently only extend a few decades (Fan et al., 2019a).

Post-earthquake debris flow magnitude is also thought to vary in response to the changing amounts of sediment available and debris flow properties (Chen et al., 2014). A study of two catchments between 2008 and 2011, found that the debris flow deposit grain size coarsened through time (Figure 2.9; Chen et al. 2014). From these values, they proposed estimates for each of the seven dimensionless values derived by Iverson (1997). The values generated suggested that as debris flows coarsen, inertial forces in the flow dominate over viscous forces. The study attributes the lower runout distances observed

for the coarser debris flows to the higher flow resistance experienced in less viscous flows. However, the relationships between fines (namely clay) content, the gravel content and runout are complex. For example large grain collisions dominated by inertial forces can enhance erosion rates (Hsu et al., 2008) and, depending on other gains in the GSD, can facilitate longer runouts (de Haas et al., 2015). The coarser deposits observed for extremely large debris flows in 2019 in Yang et al. (2021) also provide contrasting evidence. Regional scale studies of post-earthquake debris flow magnitude have found relationships between sediment supply (Guo et al., 2016b; Tang et al., 2012b) and topography (Dahlquist and West, 2019; Tang et al., 2012c). A regional study of >1000 post-earthquake debris flows from the Gorkha earthquake found that debris flow size related to catchment topography, such as the angle of the tributary junction (Dahlquist and West, 2019). Whilst this relationship highlights the importance of considering topography as a control on post-earthquake debris flow runout, which is particularly beneficial for large-scale regional hazard models, the study does not consider additional factors such as debris flow composition and rheology which have also been found to relate to debris flow deposition (Section 2.3.3). The rapidly evolving landscape, including the changing location of sediment within catchments and mass movement activity, make developing static, regional models to describe debris flow hazard and magnitude challenging and potentially inappropriate (Fan et al., 2021; Xie et al., 2022).

In 2019 a series of catastrophic debris flows inundated at least 13 catchments in the Wenchuan area, after a decrease in the frequency of debris flows over a period of years (Yang et al., 2021). These debris flows mobilised up to 1.9×10^{-2} ($\pm 3 \times 10^{-2}$) km^3 of sediment (Yang et al., 2021) and are thought to have delivered the same amount of sediment to the Min Jiang River as in the three years previously (Francis et al., 2022). The debris flows also had a high hillslope-channel connectivity (Figure 3.4; Dai et al. 2021) and fulfilled previous definitions of catchment-clearing debris flows (Francis et al., 2022). The debris flows differed from previous post-earthquake debris flows in Wenchuan by initiating within channel deposits as opposed to co-seismic and post-seismic landslide deposits on hillslopes (Yang et al., 2021). Despite the change in initiation location, the debris flows were triggered with intensity-

duration thresholds $^{1}/_{2}$ to $^{4}/_{5}$ lower than pre-earthquake levels (Yang et al., 2021). The 2019 debris flows provide evidence for the nonlinear response of landscapes to an earthquake (Fan et al., 2021). The 2019 events also highlight how debris flows remain an essential component in the post-earthquake sediment cascade. Therefore, understanding controls on debris flow magnitude and frequency is crucial to better predict future hazards.

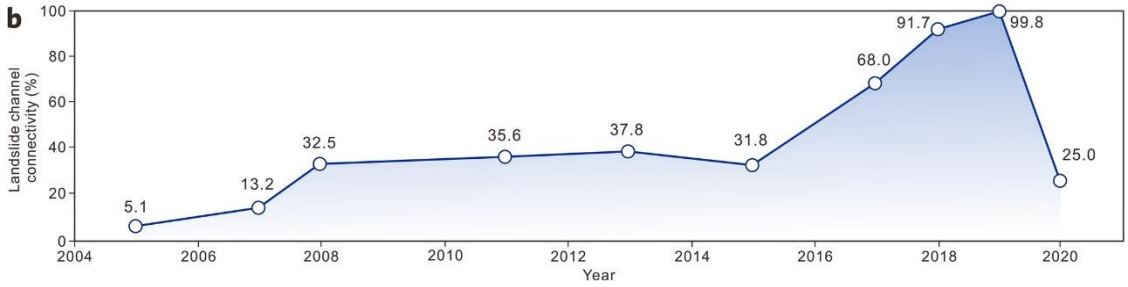

Figure 3.4

The percent hillslope-channel connectivity for landslide and debris flow events in the years following the Wenchuan earthquake taken from Dai et al., (2021). Note the 2019 debris flow events with a high connectivity (99.8%).

3.3 Inventory for Wenchuan earthquake

The 2008 Wenchuan earthquake is one of the most well-studied earthquakes, which is in part due to the advances in remote sensing and aerial imagery in recent decades (Fan et al., 2018b). There are at least six inventories documenting co-seismic landslides from the 2008 Wenchuan earthquake, with the number of landslides mapped ranging from 11 000 to almost 200 000 (Fan et al., 2019a). In the years following the 2008 Wenchuan earthquake, multi-temporal inventories were developed to capture changes in the location of sediment and the type of mass movement through time (Fan et al., 2018a).

In this thesis I use a multi-temporal inventory developed by Domènech et al. (2018) and Fan et al. (2019b) (Figure 3.5). The inventory mapped the number and area of mass movements which occurred immediately after the earthquake (2008) and at five later intervals (2011, 2013, 2015, 2017, and 2018). Mass movements were determined based on the absence of vegetation and given an activity level to determine whether the failure was still active (Domènech et al., 2018). The inventory maps the entire failure and therefore the total area includes the scar and deposit. Mapping was conducted by trained mappers as opposed to using automated algorithms, which can require

more data cleaning (Li et al., 2014). An uncertainty calculation, which considered the uncertainty introduced by using six mappers to map the area, as opposed to one, suggested there was a 19% uncertainty in mapped areas. The mass movements were separated by type; landslides, debris flows and channel deposits. Deposits were defined as debris flows if they were long and thin mass movements with clear flow patterns (Fan et al., 2019b).

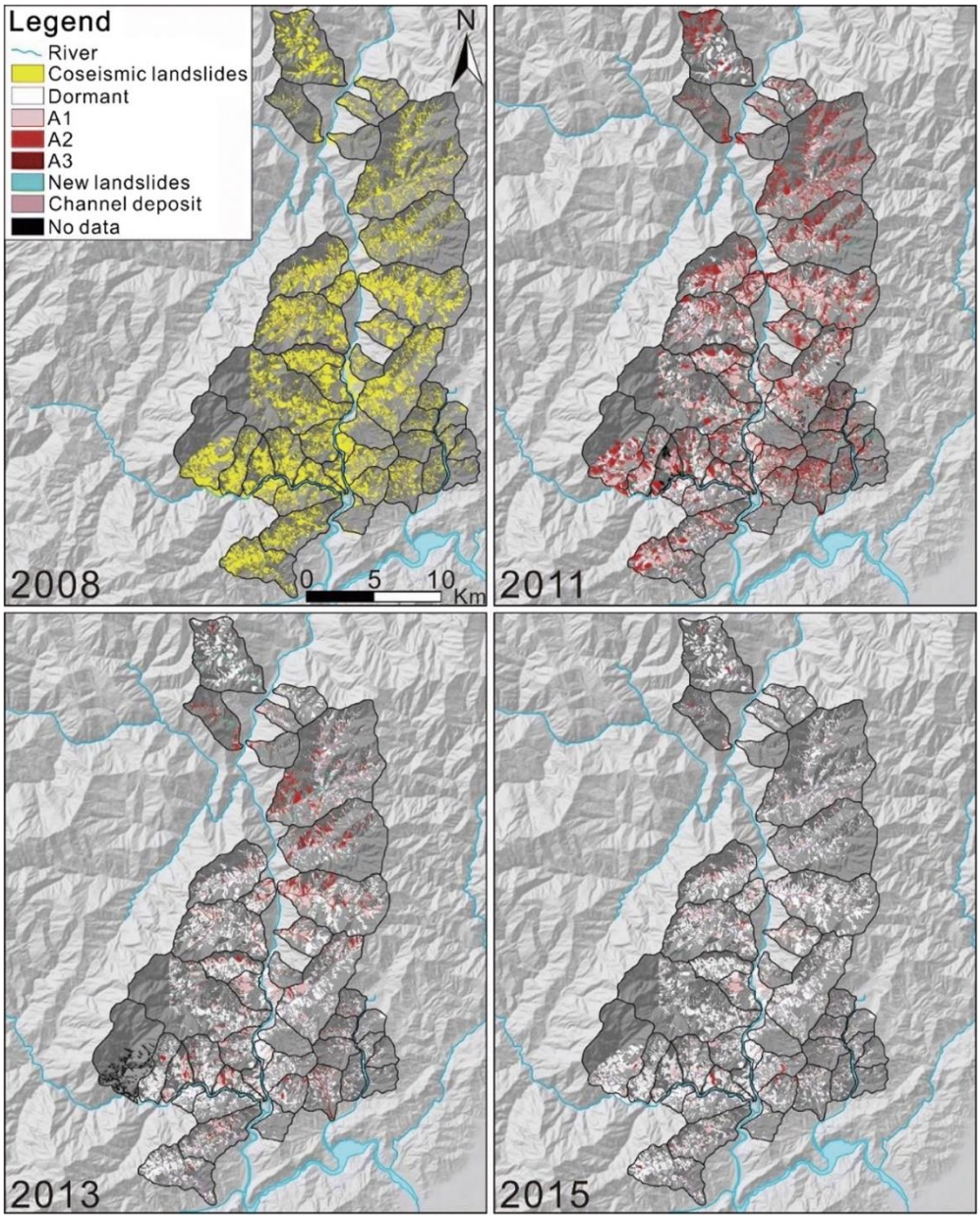

Figure 3.5

The co-seismic and post-seismic landslide inventory developed by Domènech et al. (2018) and Fan et al. (2019b). A1, A2 and A3 show the activity level for the mapped deposit which has previously been used to determine controls on deposit stability through time. Deposits which revegetated were classed as dormant and are shown in white. This figure has been taken from Fan et al. (2018a). These figures show the same catchments as shown in Figure 3.2.

In this thesis, I analyse the debris flow inventory for 31 of the mapped catchments between the years 2008 and 2018 (see Figure 3.6 and Chapter 6 Methods). Twenty of these catchments drain into the Min Jiang River (Figure 3.6). The Min Jiang is a major drainage system for the Longmen Shan mountain range. Therefore, transport along the Min Jiang River is a key process in the export of co-seismic sediment from the Longmen Shan mountains (Francis et al., 2022; Zhang et al., 2019). I supplement the debris flow inventory with a further 14 debris flows which occurred in 2019 and are mapped in Yang et al. (2021).

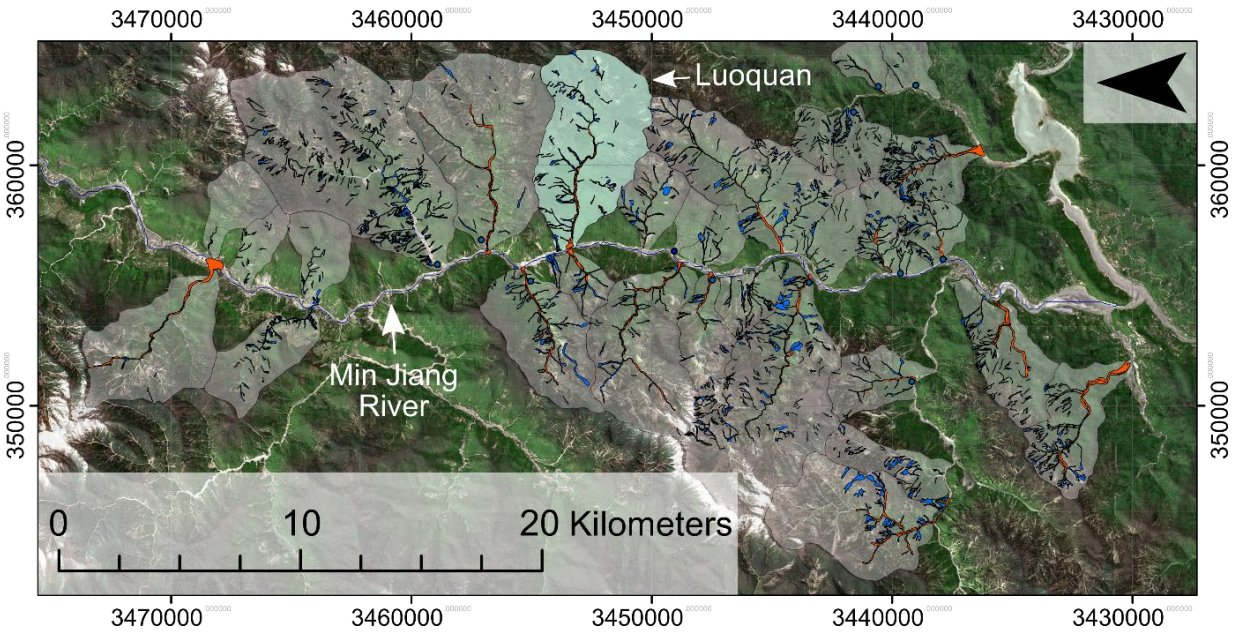

Figure 3.6

The debris flow inventory used in this thesis (2008 – 2019). Debris flows are mapped in blue, unless they fit the definition for catastrophic debris flows, in which case they are represented by red polygons.

3.4 Luoquan debris flow

The Luoquanwan catchment has an area of 28.6 km^2 and minimum and maximum elevations of 1040 m and 3525 m. Luoquanwan lies north of the town of Yingxiu and south of Wenchuan. The catchment drains Mesoproterozoic granitoids of the Pengguan massif into the Min Jiang River (Figures 3.6 and 3.7).

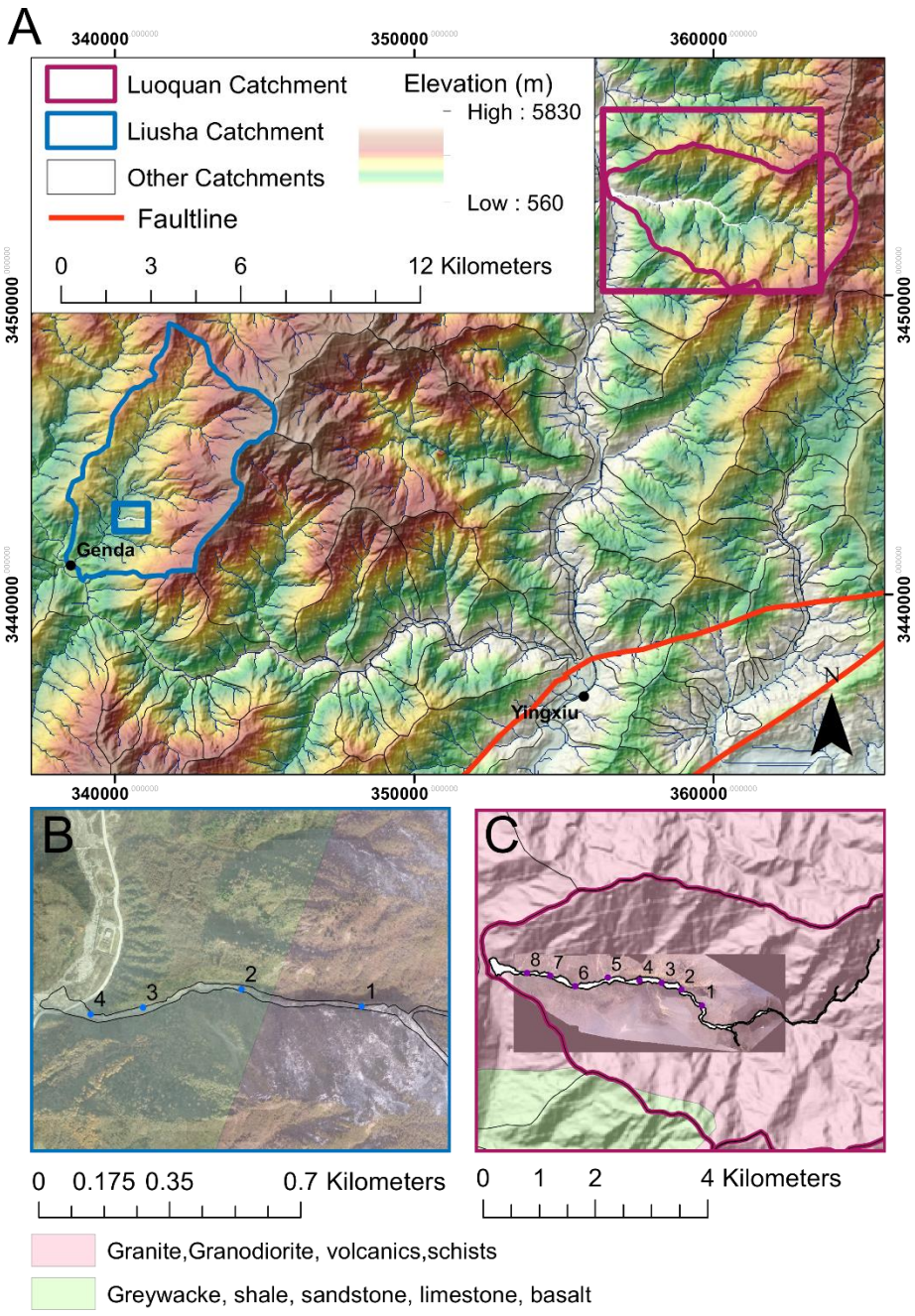

Figure 3.7

Maps showing the Longmen Shan mountain range. A) An elevation map for the Longmen Shan with the two debris flow catchments identified. The Liusha catchment is in blue and the Luoquan catchment is in purple. The active fault lines from the Wenchuan earthquake have also been included in red, mapped by Densmore et al. (2007). B) The Liusha catchment, with pit locations identified by blue markers and the extent of the debris flow shown. The main geology in the region is also shown. C) The Luoquan debris flow catchment, with the debris flow extent shown in white and the pit locations using markers and numbers. The main geology in the catchment is granitoids as shown by the pink basemap (Ma, 2002).

Throughout this thesis, I use the terms the Luoquan debris flow and Luoquan debris flow deposit to refer to the catastrophic debris flow which occurred in the Luoquanwan catchment following intense rainfall on the 20th August 2019

(Figures 3.8B and 3.8D). Using the Integrated Multi-satellitE Retrievals for GPM (IMERG) algorithm, it can be estimated that approximately 97 mm of rainfall fell on the Luoquan catchment on the 20th August, with an additional 87 mm in the 24 hours before (Huffman et al., 2014). I calculated the amount of daily rainfall by averaging the two 10 km x 10 km pixels which covered the Luoquanwan catchment. The 2019 debris flow had an area >420 000 m^2 and travelled up to 8 km in length over a change in elevation of 956 m. Based on the eight locations sampled in Chapter 5, the lower 4 km of the channel had an average channel width of 42 m and a slope of 9° (Figure 3.7). The 2019 debris flow mapped by Yang Fan (pers. Communication) travelled down a 4th order stream before depositing at the tributary junction to the Min Jiang River, defined topographically by a large increase in channel width (Figure 3.9). Three additional smaller debris flows also occurred within the catchment in 2019 with areas of 12 000 m^2, 19 000 m^2, 27 000 m^2 (Figure 3.9). These flows occurred in lower order channels and may have been part of the larger debris flow, but this section of the field was inaccessible so I could not investigate them.

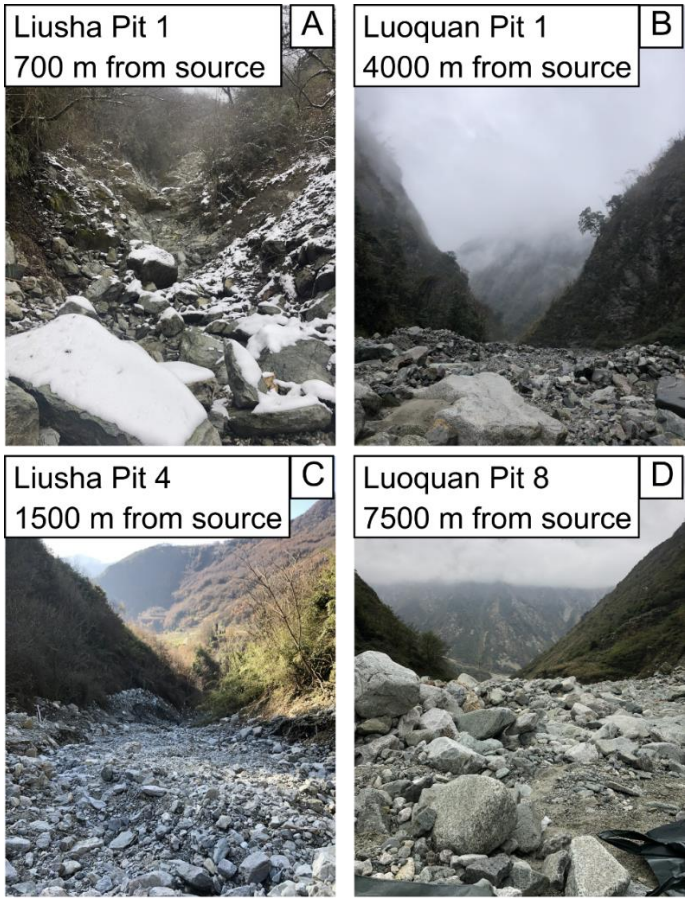

Figure 3.8

Field photographs of the Liusha and Luoquan deposits. The photos depict the change in flow composition between the most proximal and distal locations sampled. The contrast is particularly clear in Liusha where the channel above Pit 1 (700 m from source) was predominantly bedrock covered in snow.

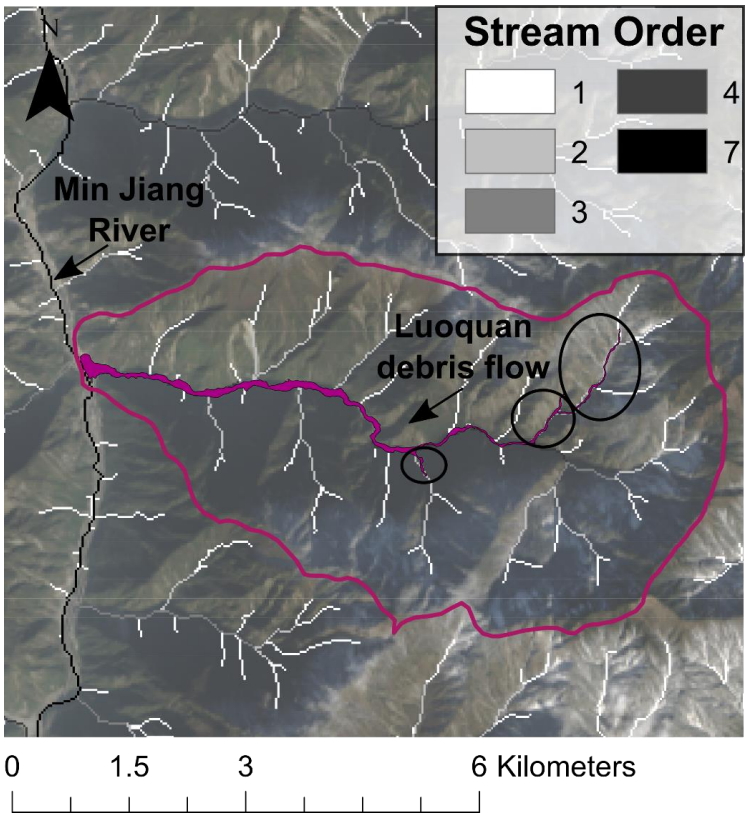

Figure 3.9

A map showing all 2019 debris flows in the Luoquan catchment. The three smaller debris flows which were mapped separately are circled. The central channel of the catchment is a fourth order channel. The location of the Luoquan debris flow with respect to nearby towns and other catchment analysed in this thesis can be found in Figures 3.6 and 3.7.

In 2008, 299 co-seismic landslides were triggered within the Luoquanwan catchment. The large volumes of available sediment within the catchment have subsequently led to a considerable number of post-earthquake landslides and debris flows. At least 100 debris flows have occurred within the Luoquanwan catchment in the 11 years following the earthquake (2008 to 2019) (Domènech et al., 2018; Fan et al., 2019b). Three of which have transported material from within the channel to the Min Jiang River. These catastrophic debris flows occurred in 2010, 2013 and 2019 and correspond with three of the five largest rainfall events in the previous 12 years. The 2010 and 2013 debris flows had smaller areas in comparison to the 2019

event, measuring 150 000 m^2 and 230 000 m^2. Unlike the 2010 and 2013 debris flows, the 2019 debris was triggered in the main channel of the catchment by runoff as opposed to reactivated landslide deposits (Fan et al., 2021; Yang et al., 2021). The deposits of the 2010 and 2013 debris flows could be identified in the field based on the surface vegetation. Evidence of debris flows within the catchment could also be found on the steep slopes surrounding the main channel, where an abundance of co-seismic landslide sediment is stored, or within steep tributary channels, which were also filled with seismically sourced sediment (Figure 3.10). These debris flows typically deposit upon reaching the main channel within the catchment, where channel width increases and slope sharply decreases.

Figure 3.10

Photos of smaller debris flows which occurred since 2008 in the Luoquan catchment. A) Shows an older debris flow deposit at the edge of the channel, ~4000 m downstream from the source of the 2019 event. B) Shows a steep hillslope debris flow. C) Shows the deposit of a debris flow which was triggered in a tributary channel in Luoquan.

3.5 Liusha debris flow

The Liusha debris flow also occurred following intense rainfall on the 20th August 2019. Based on the IMERG algorithm, approximately 99 mm of rainfall fell in close proximity (10 km x 10 km pixel) to the Liusha channel on the 19th August, followed by a further 76 mm on the 20th August. The debris flow occurred along a second order channel, which is a tributary for the Wachang catchment. The Wachang catchment is located north of the township Genda and has a catchment area of 33.9 km^2. The 2019 Liusha debris flow travelled 1.5 km downstream, blocking a local road, before stopping at the outlet of the Liusha gully into the Yuzi River (Figure 3.11). The debris flow had an area of 33 000 m^2 and was therefore more comparable to the smaller debris flows in Luoquan as opposed to the catastrophic debris flow observed in 2019 (Figure 3.7). The Liusha debris flow was steeper with an elevation change of 767 m in just 1.6 km. Based on the lower 800 m of the debris flow, which was sampled for Chapter 5, the average width of the flow was 8 m and the average slope was 23° (Figure 3.7B). I did not sample the upper 700 m of the flow as this appeared to be predominantly bedrock, suggesting the samples taken 700 m downstream were near the transition between an eroding debris flow and depositing debris flow (Figures 3.8A and 3.8C). In terms of geology, the source of the debris flow was defined by Mesoproterozoic granitoid material which persisted until ~900 m downstream, where the deposit was underlain by Palaeozoic greywacke and shale (Figures 3.7; Ma, 2002). The Liusha debris flow and Wachang catchment were not mapped as part of the inventory devised by Domènech et al. (2018). Therefore, I mapped the Liusha debris flow using a combination of aerial images taken during sampling in November and December 2019 and images available from Google Earth.

The lack of inventory data for the Liusha channel limits our understanding of how the catchment and channel were affected by the 2008 Wenchuan earthquake. From personal communication with Yang Fan, a PhD student at Chengdu University of Technology, I learnt that a debris flow also occurred in the gully in 2013. A well-preserved, vegetated deposit to the right of the 2019 deposit provided field evidence of this event. It is likely that this event corresponded with a large event in the Yuzi River, where the Liusha debris

flow stopped, which can be identified based on a significant increase in channel width between the 2010 and 2014 image available on Google Earth.

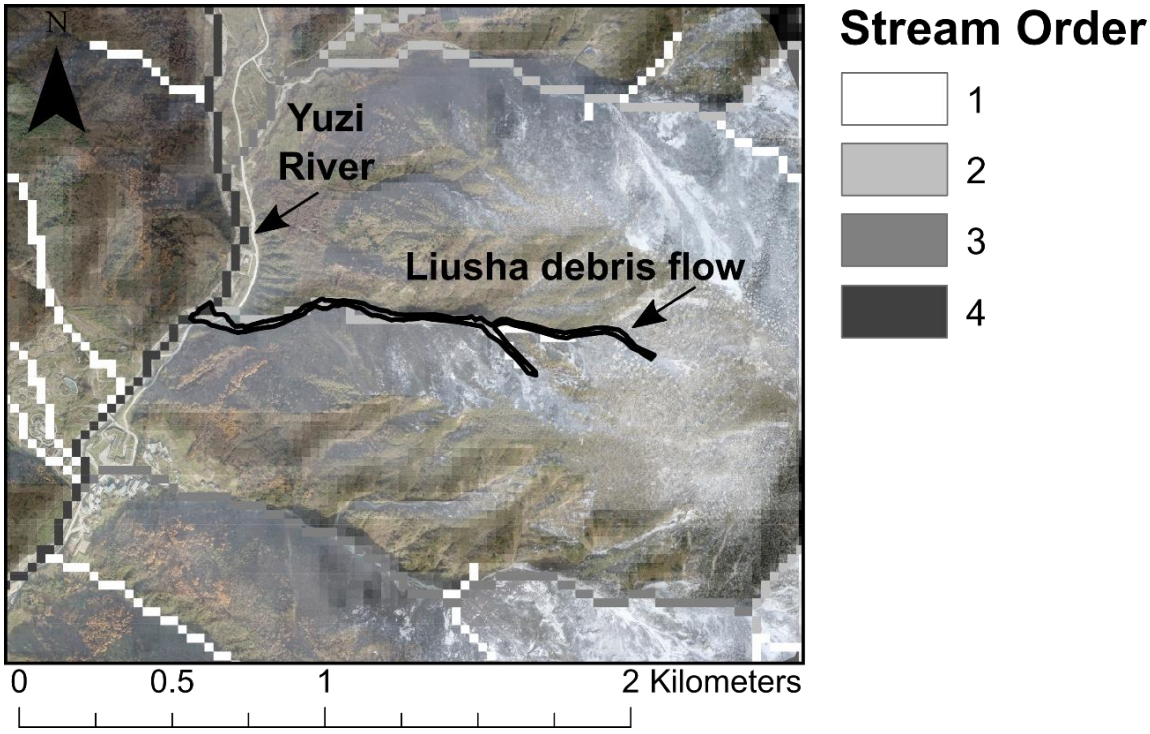

Figure 3.11

A map of the 2019 Liusha debris flow. The base map is the aerial image taken in November 2019. The Yuzi River, where the debris flow stopped is labelled. The location of the Liusha debris flow relative to the Luoquan debris flow is shown in Figure 3.7.

Chapter 4

Measuring the grain-size distributions of mass movement deposits

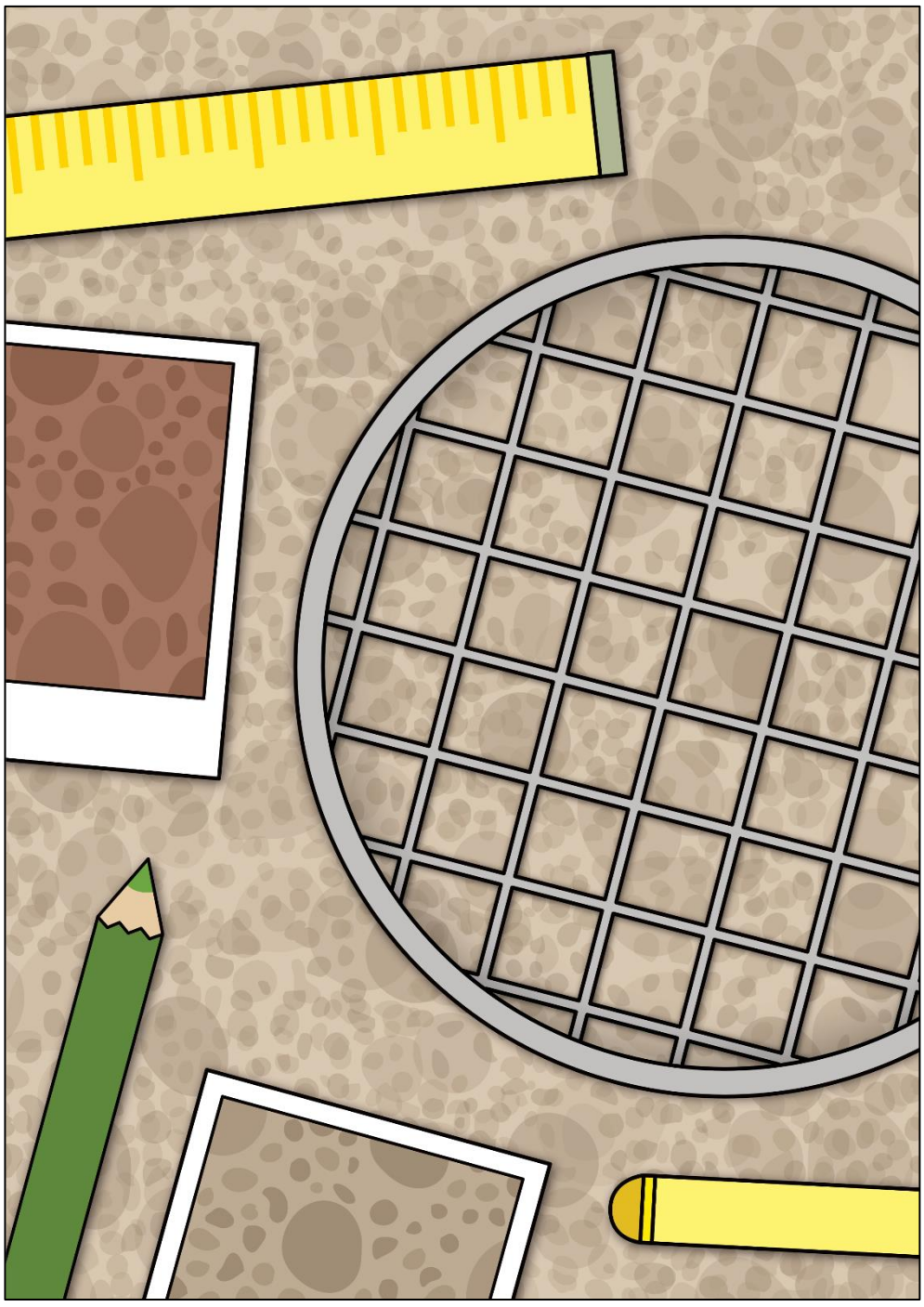

Image by Megan Harvey

Author contributions

The research presented in this chapter is based on a published manuscript by myself, TC Hales, DEJ Hobley, J Liu and X Fan:

Harvey E. L., Hales, T. C., Hobley, D. E. J., Liu, J., Fan, X. (2022). Measuring mass movement deposit grain-size distributions. Earth Surface Processes and Landforms. https://doi.org/10.1002/esp.5337.

While all the authors contributed to discussions and the writing of the manuscript, I am solely responsible for analysing all collected samples in the laboratory, analysing the GSDs and interpreting the results. The manuscript also benefited from three anonymous reviews. Whilst the wording of the manuscript has not been changed as it is the most concise and effective way to deliver the scientific points to the reader, sections of the paper have been rewritten to conform with the standard thesis narrative accepted by Cardiff University.

4.1 Abstract

Mass movement deposit grain-size distributions (GSDs) record initiation, transport, and deposition mechanisms, and contribute to the rate at which sediment is exported from hillslopes to channels. Defining the GSD of a mass movement deposit is a significant challenge because they are often difficult to access, are heterogeneous in planform and with depth, contain grain sizes from clay (<63 μm) to boulders (> 1 m), and require considerable time to calculate accurately. There are numerous methods used to measure mass movement GSDs, but no single method alone can measure the entire range of grain sizes. This chapter compares five common methods for determining mass movement deposit GSDs to assess how their accuracy may affect their applicability to different research areas. I applied an automated wavelet analysis (pyDGS), Wolman pebble counts, survey tape counts, manual photo counts and sieving to three different mass movement deposits (two debris flows, one rockslide) in Tredegar, Wales and the Longmen Shan, China. I found that pyDGS and survey tape counts produced comparable GSDs to sieving over a single order of magnitude. PyDGS required calibration to achieve accurate results, limiting its use for many applications. In Tredegar, Wolman pebble counts overestimated grain sizes in the lower 80% of the

distribution relative to the other four methods used. I demonstrate that method choice can introduce significant uncertainties, particularly at the edges of the distributions such that D_{16} values differ by up to a factor of five. These methodological uncertainties limit GSD comparisons across studies particularly where these are used to infer processes within deposits. To minimise these challenges, the methods chosen should both be carefully reported and consistent with the research question.

4.2 Introduction

Mass movement deposit GSDs can help constrain the source of the material eroded (Dunning, 2006; Marc et al., 2021), the transport and emplacement mechanisms of the deposit (de Haas et al., 2015; Makris et al., 2020) and moderate sediment transport rates in fluvial systems (Neely and DiBiase, 2020; Sklar et al., 2017, 2020). However, as outlined in Chapter 2, measuring the GSD of debris flow deposits is extremely challenging because grain sizes can range in up to eight orders of magnitude (from <1 μm to >10 m) and vary spatially and with depth due to processes such as segregation and winnowing (Crosta et al., 2007; Dufresne and Dunning, 2017; Johnson et al., 2012; Locat et al., 2006). There remains no single method that can record GSDs over the range and scale of most mass movement deposits (Table 4.1). Hence different approaches or combinations of approaches have been used to measure mass movement deposit GSDs across spatial and vertical changes and a range of grain sizes (e.g. Casagli et al., 2003; Attal and Lavé, 2006; Dunning, 2006; Crosta et al., 2007; Attal et al., 2015; Zhang et al., 2015). These approaches typically involve measuring the b-axis of grains using two methods, one which can capture the finest grains, such as sieving, and another for the coarsest grains, such as Wolman pebble counts or photo-based techniques, and combining these to produce a new distribution (Attal and Lavé, 2006; Casagli et al., 2003; Fripp and Diplas, 1993).

Table 4.1

A summary of the key advantages, limitations, and resolutions of the methods used to measure mass movement deposit GSDs in this chapter. I provide key references for the use of these methods.

Method	Advantages	Limitations	Sampling Range and Size	Key references
Volumetric Sieving Frequency-Volume	• Can collect subsurface GSDs by digging pits or using vertical exposures. • Can constrain the proportion of grains <1 mm.	• Limit to the maximum grain size obtained using sieving directly (typically 80 mm). • Time consuming, that limits its application to detailed, small sections of the deposit. • Difficult to apply to questions of spatial variability in deposits. • May require some larger grains to be measured by hand to obtain a full GSD for each pit.	<0.063 mm to 80 mm. I use a maximum limit of 80 mm and record grains >80 mm by hand in the field. I found a 1 m x 1 m x 0.5 m pit took ~ 6 – 8 hours to dig and sieve. As such, only a small proportion of the deposit can be sampled. Here, I sieved 1000 kg per pit. Church et al., (1987) recommend that the largest particles should represent no more than 5% of the total sample mass. However, this approach is often unachievable in mass movement deposits, where extremely large boulders are present. For example, if grains >50 kg are present, >950 kg of sediment must be sieved. As a result, mass movement GSDs are often generated from smaller than ideal sample sizes, without the rigorous reporting of sampling that is common in fluvial geomorphology.	e.g. Attal and Lavé, 2006; Bunte and Abt, 2001; Casagli et al., 2003; Chen et al., 2001; Dunning, 2006; Genevois et al., 2001; Hubert and Filipov, 1989; Ibbeken et al., 1998; Major and Voight, 1986; Sosio et al., 2007; Whipple and Dunne, 1992; Zhang et al., 2011, Zhang et al., 2015

Pebble Count and Survey Tape Frequency-Number	• Can record all three axes of a grain, which is useful when working with non-spherical grains. • Sampling typically involves >100 grains. This is quick relative to other methods (~ 1 hour)	• Only used to collect surface GSDs. • Field intensive. • Bias towards sampling only visible grains.	The smallest detectable grain size is typically gravel as this is easily visible. Studies typically give a minimum grain size of 4 to 5 mm (Casagli et al., 2003; Sklar et al., 2020). However, when survey tapes are used the minimum detectable grain size is thought to be lower (~2 mm) (Bunte and Abt, 2001a). The number of grains measured can be as low as 100, however this value increases with more heterogenous deposits. I used a sample size of 300 for a small, heterogeneous landslide deposit.	e.g. Attal and Lavé, 2006; Casagli et al., 2003; Hubert and Filipov, 1989; Kim and Lowe, 2004; Major and Voight, 1986; Vallance and Scott, 1997; Zhang et al., 2011
Manual Photo Analysis Frequency-Number	• Requires considerably less time in the field in comparison to other methods. • Does not disturb the surface of the deposit. This allows the method to be	• Only used to collect surface GSDs. • Bias towards sampling coarser grains. • Can only measure visible axes and some grains may overlap and therefore the b-axis	The minimum grain size depends on the resolution of the image and the maximum grain size depends on the extent of the photo. This technique can be used across large surface areas, for example by using UAVs. In this study photos were taken with a 50 cm x 50 cm frame for reference with a resolution >0.12 mm pi^{-1}.	e.g. Attal and Lavé, 2006; Casagli et al., 2003; Crosta et al., 2007; Genevois et al., 2001; Ibbeken et al., 1998; Kellerhals and

	compared directly to sieving for the same area. • UAV imagery can be used in less accessible locations. • The results can be reproduced.	will be measured incorrectly.		Bray, 1971; Zhang et al., 2015
pyDGS PyDGS is a texture-based approach which uses the spatial and spectral properties of an image to generate a GSD.	• Does not require calibration, though our results suggest some calibration is necessary when choosing the *shape parameter*. • Requires considerably less time in the field in comparison to other methods.	• Only used to collect surface GSDs. • Similar to manual photo counts, can only detect visible grains. • Coarsest grain size is determined by photo window size. • Errors may be generated if grains are wet, imbricated or are similar in colour.	Minimum grain size is determined by photo resolution and number of pixels required to clearly identify a grain. Based on version 4.0, pyDGS detects grains ~6 pixels in length. Maximum grain size is dependent on *maxscale* parameter. Whilst UAVs can be used to survey large surface areas, to measure grains 10 mm in size, photo resolution would need to be 1.66 mm pi^{-1}. Here, I use photos with at least 0.12 mm pi^{-1} resolution.	Buscombe (2013) Beach GSDs e.g. Prodger et al., 2017 Dryland Basin GSDs e.g. Michaelides et al., 2018

Frequency-Number	• UAV imagery can be used in less accessible locations. • Does not disturb the surface of the deposit.			

Table 4.2

The two main types of automated and semi-automated methods for measuring GSDs from photos. Key references refer to the use of these methods in mass movement deposits as well as other deposits.

Method	Advantages	Limitations	Sampling Range and Size	Key Examples and References
Image Segmentation *These techniques aim to isolate and measure the visible axes of the individual grains in an image.*	• Requires considerably less time in the field in comparison to other methods. • Does not disturb the surface of the deposit. • Methods may require extensive calibration and time to understand, however once running they can readily be applied to large areas. • UAV imagery can be used in less accessible locations.	• Only used to collect surface GSDs. • Most methods need calibrated detection algorithms to isolate individual grains or large calibration datasets. Therefore, not universally applicable. • Coarsest grain size is determined by photo window size, camera height and resolution. • Can only measure clearly visible grains.	The minimum grain size depends on the resolution of the image and the maximum grain size depends on the extent of the photo. The PebbleCounts algorithm can detect grains ≥20 pixels (Purinton and Bookhagen, 2019). Purinton and Bookhagen (2021) use automated PebbleCounts with minimum grain size of 2.5 cm. Automated image segmentation methods can	e.g. Graham et al., 2005, 2010; Storz-Peretz and Laronne, 2013 Two examples of semi- and automated image segmentation techniques. Both were developed using fluvial GSDs. ***Basegrain*** (Detert and Weitbrecht, 2012) ***PebbleCounts*** (Purinton and Bookhagen, 2019, 2021)

	• Do not require user intervention, which reduces operator bias. • Obtain measurements for each individual grain, from which interpolation is not required to obtain percentiles.	• Limited by image complexity, such as vegetation, variations in colour and texture (e.g. veins) and imbrication.	use cameras on tripods or UAVs to survey large areas. For example, Purinton and Bookhagen (2021) surveyed areas between 944 m^2 and 3470 m^2 for sand- and gravel-bed rivers in the South-Central Andes.	
Texture-based Approaches *These techniques generate grain-size distributions and grain-size percentiles using statistics based on the texture of a 2D or 3D image.*	• UAV imagery can be used in less accessible locations. • Does not necessarily require fieldwork, though often needs to be calibrated. • UAVs have been used successfully in homogenous fluvial environments to obtain GSDs.	• Only used to collect surface GSDs. • Requires very high resolution DEMs or images to measure the finest grains. • UAVs to generate 3D point clouds have not worked well in poorly sorted environments (Westoby et al., 2015)	The minimum grain size depends on the resolution of the image and the maximum grain size depends on the extent of the photo. Can be used to survey larger areas than sieving and Wolman pebble counts, based on the reduced field time required. Though	***Semi variance*** (e.g. Carbonneau et al. 2004; Carbonneau et al. 2005) ***Autocorrelation*** (e.g. Rubin 2004) ***Wavelet transforms*** (e.g. Buscombe 2013)

	• Does not disturb the surface of the deposit. • Once the photos are taken and the model is running, larger areas can be sampled quicker.	• Typically requires high computer processing power. • Bias towards coarse grains. • Coarsest grain size is determined by photo window size. • Requires site-specific calibration to establish relationships between texture and grain size in each location. • May require extensive measurements of GSDs in the field to compare to or train the algorithm.	high-resolution imagery is required to detect the finest grains.	***Convolutional neural networks*** (e.g. Buscombe 2020; Lang et al. 2021) ***3D based roughness*** (Brasington et al. 2012; Westoby et al. 2015; Neverman et al. 2019; Vázquez-Tarrío et al. 2017) **Structure from Motion and TLS to produce DEMs of mass movement deposits:** Bitelli et al. (2004); Cucchiaro et al. (2018); Dunning et al. (2009); Gupta and Shukla (2018); Saunders (2014)

Wide and multimodal GSDs also limit the applicability of single grain-size metrics like D_{50} to characterise a mass movement deposit (Casagli et al., 2003). A full GSD is useful for inferring processes that involve multiple different grain sizes, such as comminution and kinetic sieving (Dufresne and Dunning, 2017; Makris et al., 2020), and also provides insight into the textural properties of deposits (Casagli et al., 2003). It is therefore more useful to use several quartiles, such as D_5, D_{16}, D_{50}, D_{84} and D_{95}, as opposed to a single metric to characterise the entire GSD for mass movement deposits (Folk and Ward, 1957; Purinton and Bookhagen, 2021). The higher percentiles, such as D_{95} and D_{99}, are prone to larger uncertainty, which arises because of the difficulties associated with sampling the coarsest grains and the often heavy-tailed nature of the distributions. This uncertainty can be mitigated by increasing the sample size, to include as much of the coarser grains as possible (Eaton et al., 2019; Guerit et al., 2018; Purinton and Bookhagen, 2021). However, increasing sample size subsequently results in increased sampling time per site.

Automated and semi-automated techniques that obtain GSDs from static photos may mitigate the large sample sizes required for wide, multimodal GSDs (Table 4.2). Photo-based methods are also less invasive, typically require less field work, and can measure surface GSDs across larger areas over a shorter time period (Table 4.2; Purinton and Bookhagen, 2021). These methods include both image segmentation and texture-based approaches (Table 4.2). Image segmentation techniques isolate and measure the visible axes of individual grains (e.g Graham et al., 2005; Purinton and Bookhagen, 2019). Whereas, texture-based techniques are statistical approaches which produce GSDs using information about how intensity and colour vary within 2D and 3D images (Buscombe, 2013; Lang et al., 2021), for example a high resolution DEM.

Traditional methods used to measure GSDs are often limited by sampling size, inaccessibility, and time constraints, as described in Table 4.1. The disadvantages associated with using each method are likely to introduce uncertainty into the measured GSDs, for example by excluding fine grain sizes or using small sample sizes (Casagli et al., 2003). Uncertainty in measured GSDs may affect our ability to compare across different studies. Whilst the

uncertainty associated with comparing different methods has been widely discussed for fluvial GSDs (e.g. Bunte and Abt, 2001b, 2001a; Wohl et al., 1996), the effect of method choice on comparisons of mass movement deposit GSDs has been less well explored. The uncertainties associated with different methods may be more pronounced in mass movement deposits, which have wider GSDs, greater angularity, and grains in excess of 1 m. GSDs may differ in terms of methodological uncertainty, sample size and sample type, which can affect our ability to accurately develop process-based conclusions regarding transport and depositional mechanisms in mass movement deposits. Methodological uncertainties refer to how much the GSD varies depending on the method chosen, sample size refers to the number of grains measured, and sample type refers to the region of the deposit considered by each method, (e.g., surface or subsurface). In this chapter, I compare and combine GSDs generated for three different deposits using five different methods. I then compare the methods using D_{16}, D_{50} and D_{84} percentiles as well as statistically using chi square tests.

4.3 Research objectives

1. To generate GSDs for three mass movement deposits using five different techniques.
2. To compare the GSDs measured using different techniques.
3. To infer how using different methods to measure grain size can affect the geomorphic interpretation of GSDs.

4.4 Methods

A flow diagram depicting the methods used to measure deposit GSDs is shown in Figure 4.1.

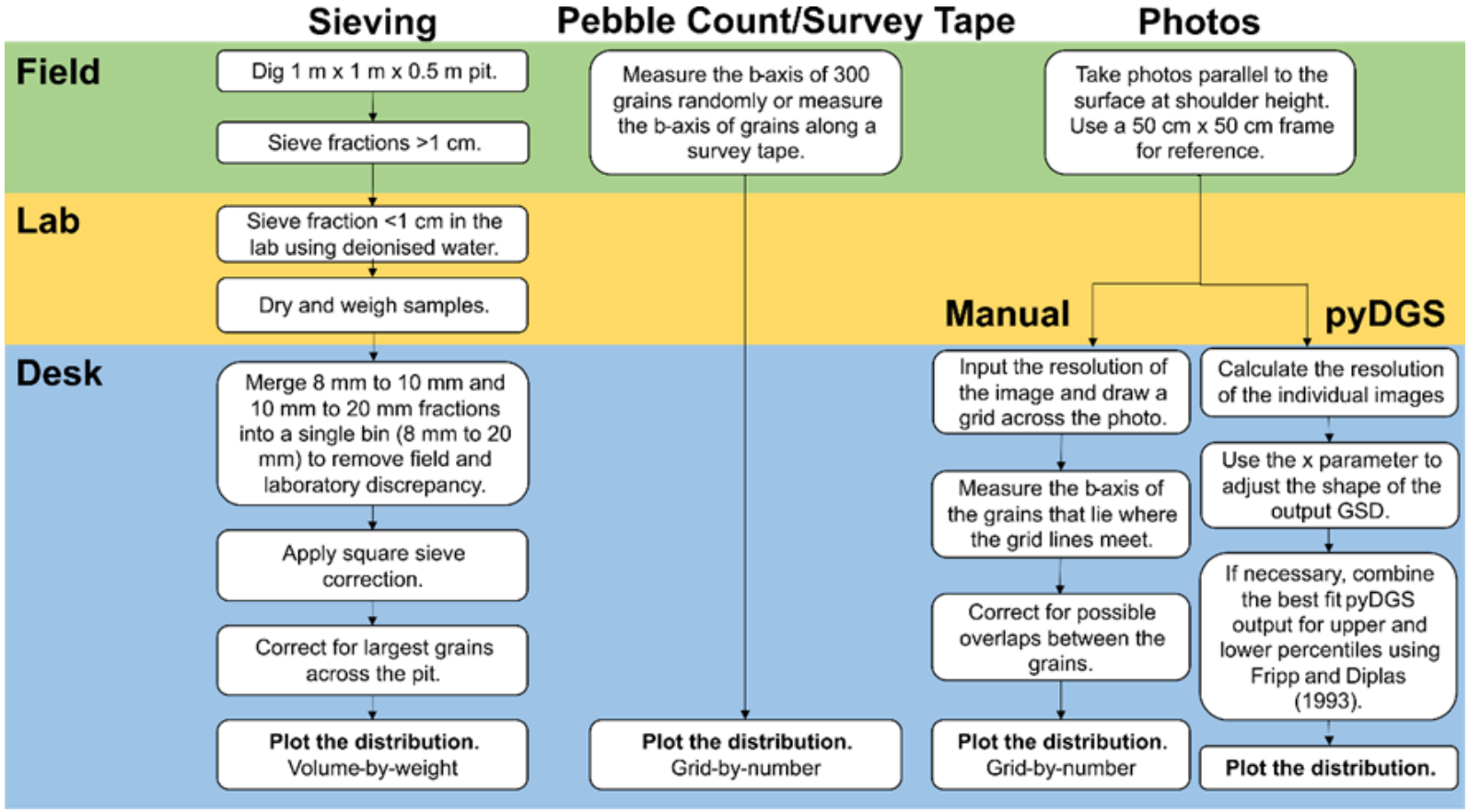

Figure 4.1

A flow diagram detailing the key steps taken for the methods used in this study. Sieving required field, laboratory and desk work. The second method, Wolman pebble counts, was split into two approaches, survey tape measurements and more randomised Wolman pebble counts. The final methods required photos taken in the field. These photos were then analysed using two different methods, automatic grain-size analysis using pyDGS and manual photo counts.

4.4.1 Study site

I compare GSDs collected from the Liusha and Luoquan debris flow deposits (Chapter 3) with a smaller rockslide deposit in Tredegar, South Wales to test the applicability of the five techniques to different mass movement deposits. The Tredegar rockslide was triggered within the Carboniferous Deri Formation, a sedimentary unit of interbedded sandstone, mudstone, and siltstone (Barclay et al., 1989; George, 2015). The rockslide was triggered in a former quarry face during a winter storm on a 26° slope and measured 26.5 m long and 15 m at the widest point. The deposits and their locations relative to one another are shown in Figure 4.2.

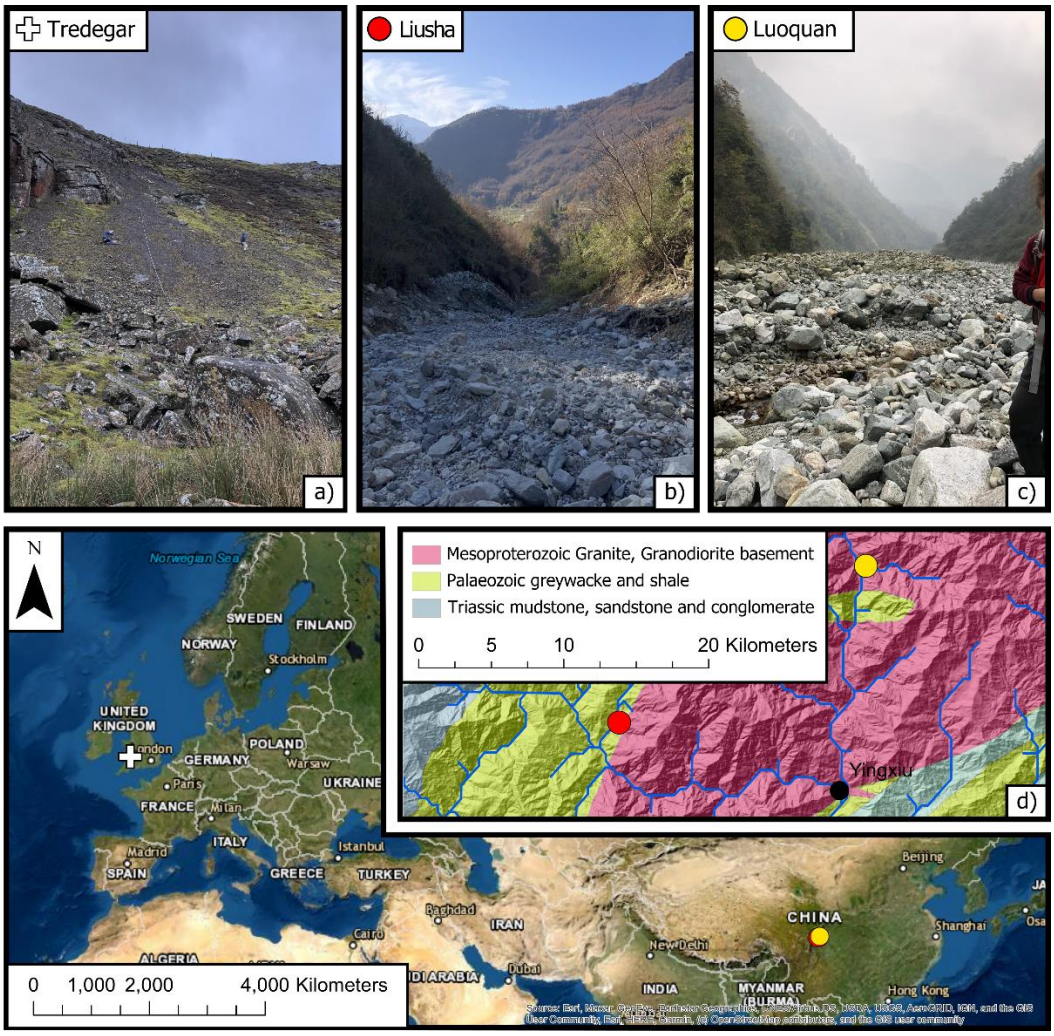

Figure 4.2

Map showing the three locations studied. Inset (a) shows the Tredegar landslide in South Wales. Insets (b) and (c) show the Liusha and Luoquan debris flows in the Longmen Shan, respectively. Inset (d) provides a closer location map for the debris flows in the Longmen Shan with the geology for the region also shown.

4.4.2 Volumetric sieving

I sieved each deposit using a protocol previously used for fluvial sediments, landslide deposits and debris flow deposits (Attal et al., 2015; Attal and Lavé, 2006; Bunte and Abt, 2001a; Zhang et al., 2014a). I measured a 1 m x 1 m pit in the centre of the deposit and excavated material at 10 cm increments to a depth of 30 cm in Tredegar and 50 cm in Longmen Shan (Figure 4.3). The shallower depth in Tredegar was due to the steeper slope and smaller apparent grain size and failure. The pits in Liusha and Luoquan analysed in this chapter were Pits 4 and 8 respectively (located 1500 m and 7500 m from the triggering locations) (Figure 3.7). I used square sieves to separate the remaining sediment into the following size fractions, >4 cm, 2 – 4 cm, 1 – 2 cm and <1 cm. I weighed all fractions in the field using fishing scales and separated 1 kg of sediment from the fraction of sediment <1 cm to analyse in the laboratory (Attal and Lavé, 2006; Hubert and Filipov, 1989). I sieved approximately 1000 kg of sediment per pit to fulfil the 5% of total weight limit for the largest grain set out in Church et al. (1987). The coarser sediment was not air dried in the field as the difference in weight for large gravels is negligible (Bunte and Abt, 2001b). I weighed and measured all three axes for grains >8 cm in diameter, which accounted for up to 35% of grains by weight. By measuring multiple axes for these grains, grain shape could also be quantified. Where large grains covered multiple layers (e.g., >10 cm on at least one axis), the grain was consistently sampled from the lowest layer to avoid disturbing layers unnecessarily. Sieving GSDs were adjusted to account for this by averaging the weight of grains with a b-axis >10 cm across the appropriate number of layers. More detail on this approach is given in Chapter 5, where I analyse the GSDs with depth.

In the lab, I wet sieved the 8 mm, 4 mm, 2 mm, 1 mm, 0.5 mm, 0.25 mm, 0.125 mm and 0.063 mm fractions. For samples containing a large proportion of gravels (>2 mm), a sieve shaker was used to separate the first four fractions. Manual end-point tests were carried out to ensure all grains had passed through each sieve (Dufresne and Dunning, 2017). The tests involved briefly shaking the sieve into a clean, dry sieve pan to see if any grains still passed through. I noticed that there were still grains passing through the five smallest sieves, the fraction <1 mm was also wet sieved.

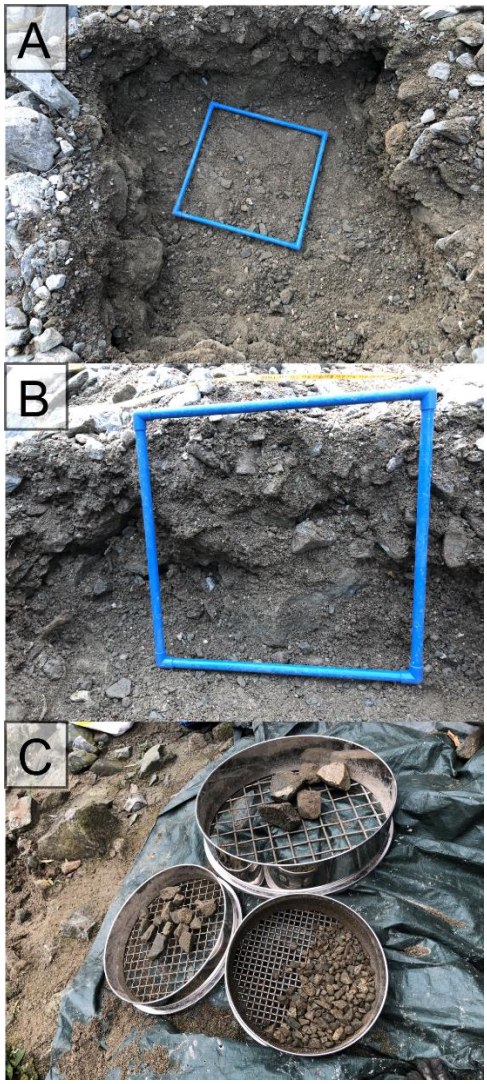

Figure 4.3

A) A 1 m x 1 m x 0.5 m pit in the Liusha debris flow deposit with a 0.5 m x 0.5 m frame for scale. B) The edge of an excavated sieving pit. C) The three sieves used in the field with 4 cm, 2 cm and 1 cm apertures.

A square sieve correction from Attal and Lavé (2006) of the form

$$b = \frac{2km}{\sqrt{1+k^2}} = \frac{k\sqrt{2}}{\sqrt{1+k^2}}S, \qquad \textit{Equation 4.1}$$

where *S* is the sieve mesh size, and k is the ellipse eccentricity (*k*) or the ratio between the b-axis and the c-axis of grains, was applied to our data. This equation calculates the maximum b-axis of an elliptical grain that would fit through each sieve based on the shape of grains in each pit. There were a large range of values obtained for *k* within both pits, with the sieves potentially overestimating the b-axis of each grain by a maximum of 41% in Liusha and 35% in Luoquan. The mean b-axis overestimate in Liusha and

Luoquan was 21% and 17% respectively. This equated to an approximately 0.7 cm difference between the adjusted size of a 4 cm sieve.

4.4.3 Wolman pebble counts and survey tape counts

I conducted a Wolman (1954) pebble count and survey tape pebble count across the surface of the deposit in Tredegar. Typically, at least 100 grains are required for a Wolman pebble count (Wolman, 1954). Due to the heterogeneity of landslide deposits, it was decided that rather than choose a particular number of samples, grains would be measured until the mean value converged (i.e., any additional grain measured did not change the mean beyond 0.1 mm). I found the mean, D_{50} and D_{84} converged when measuring 300 grains, while D_{90} did not.

The survey tape method involved placing three 50 m tapes horizontally across the deposit and one tape from the scar of the failure to the toe. I measured the b-axis of the grain directly below the tape at every 0.25 m interval. This spacing was decided based on the size of grains in the deposit, to ensure no grain covered two points on the tape (Kellerhals and Bray, 1971). If grains were too small to be measured, the nearest grain was chosen instead (Hubert and Filipov, 1989; de Scally and Owens, 2005). If grains were too large the same protocol would apply, however this was not encountered in Tredegar. For this method, I sampled 174 grains in total and obtained a mean of 17.1 mm, which was 0.7 mm larger than the mean obtained using random Wolman pebble counts. Grains as small as 1 mm (survey tape) and 3 mm (Wolman count) were included as they were visible in the field.

4.4.4 Manual photo counts

Manual photo counts involved measuring the apparent b-axis of grains using photos taken parallel to the surface (Attal and Lavé, 2006; Casagli et al., 2003; Crosta et al., 2007; Genevois et al., 2001; Ibbeken et al., 1998; Kellerhals and Bray, 1971; Zhang et al., 2011, 2015). I conducted manual photo counts in all three locations by taking photos using a smartphone camera (Figure 4.4, image resolutions ranged from 0.12 mm pi^{-1} in Tredegar to 0.39 mm pi^{-1} and 0.46 mm pi^{-1} in Liusha and Luoquan). I used a tape measure in Tredegar and a 50 cm x 50 cm frame in the Longmen Shan to determine the resolution of the image. The tape measure and frame also

helped to identify when photos were not taken parallel to the slope. These images were discarded alongside photos with inconsistent resolutions and photos of the same surface to ensure no grains were counted multiple times. I conducted manual photo counts on six images in Tredegar, measuring a total of 300 grains. In Longmen Shan, I took photos of the surface of the pit and used these photographs to conduct a grid-by-number analysis. The width and height of the grid was determined by the largest grain in the photo to ensure no grain was counted twice (Bunte and Abt, 2001b).

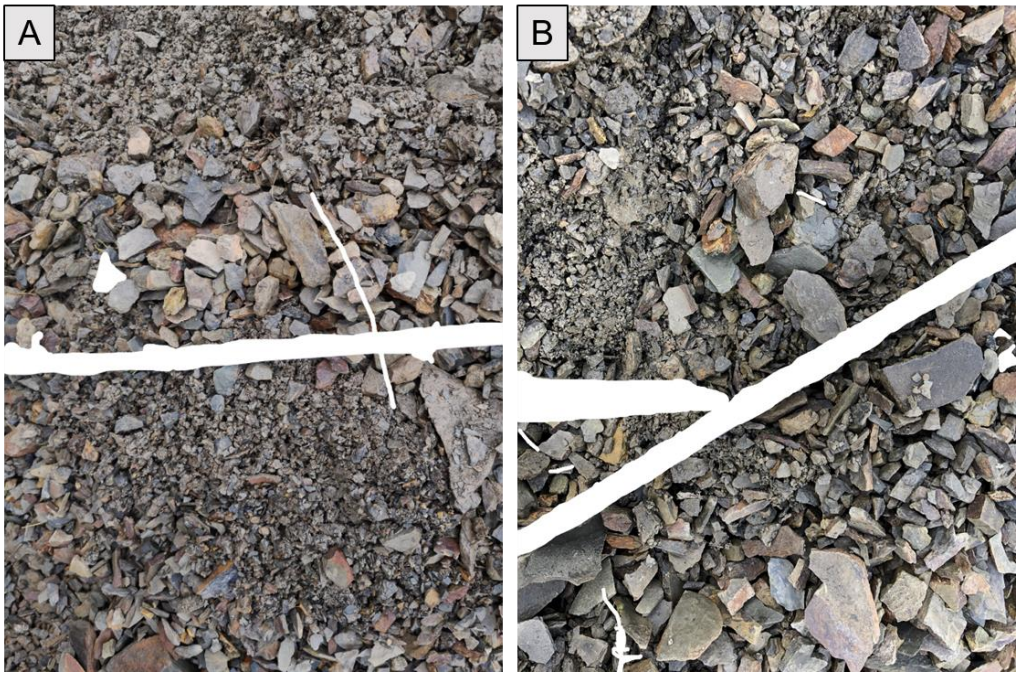

Figure 4.4

Two images taken of the Tredegar deposit. They have been masked to remove the survey tape and vegetation which was required for a previous version of pyDGS. They have a resolution of (A) 0.088 mm pi^{-1} and (B) 0.084 mm pi^{-1}.

4.4.5 Automated photo analysis (pyDGS)

I applied a texture-based approach, pyDGS (v4.0), as it allows for the rapid identification of GSDs from photos and is beneficial for obtaining a GSD for a large surface area. PyDGS has been successfully applied to dryland basins (Michaelides et al., 2018), beaches (Prodger et al., 2017) and bioclastic sediments (Cuttler et al., 2017) as well as a range of sorted and poorly sorted sediments (Buscombe, 2013). The algorithm requires minimal calibration and can detect grains ~6 pixels in length (~fine gravel) from photos taken using a smartphone camera. The algorithm works best for the coarse, well-sorted

grains where the brightness of the grains are not positively correlated with size and there are >100 grains in each image (Buscombe, 2013).

There are three key parameters in pyDGS (July 2020 version); *x*, *maxscale*, and resolution. *x* varies from 1 to -1 and is an exponent that converts the area-based pyDGS output to a volume-based GSD (Buscombe, 2013; Cuttler et al., 2017). The *x exponent* (hereafter referred to as the shape parameter) relates to the size of the grains, their porosity and sorting (Bunte and Abt, 2001b; Cuttler et al., 2017; Diplas and Fripp, 1992; Diplas and Sutherland, 1988). For example, a negative value of *x* (-1) can represent poorly sorted coarse gravels with low porosity and a high sand content, whereas a value of 0 is indicative of well-sorted gravel (Bunte and Abt, 2001b). I tune the *shape parameter* in this chapter based on the sieving data. In Tredegar, a single *shape parameter* consistently represented the GSD obtained using sieving (Figure 4.5). However, in the Longmen Shan, a single pyDGS *shape parameter* did not fit the GSD obtained using sieving or manual photo counts. Therefore, for Liusha and Luoquan I combined two pyDGS runs with different shape parameters (Section 4.4.6) to obtain a GSD that captured both the finest and coarsest grains measured using sieving. The *maxscale* parameter defines the maximum grain size that the algorithm searches for in the image as a fraction of the greatest dimension (Buscombe, 2013).

I ran a sensitivity analysis to test how the choices of these three parameters affect the output. In this chapter, in Tredegar I use the average GSD obtained by running 60 photos in pyDGS and using an average resolution of 0.12 mm pi^{-1}. I vary the *shape parameter* and *maxscale* throughout.

4.4.6 Combining GSDs

The distributions were combined to obtain the full GSD for each deposit, following the method of Fripp and Diplas (1993). Each GSD was split into 13 size fractions (0 – 0.063 mm, 0.063 – 0.125 mm, 0.125 – 0.25 mm, 0.25 – 0.5 mm, 0.5 – 1 mm, 1 – 2 mm, 2 – 4 mm, 4 – 8 mm, 8 – 20 mm, 20 – 40 mm, 40 – 80 mm, 80 – 100 mm, 100 – 200 mm). The two GSDs were compared and the grain-size fraction with the most similar proportion was chosen to be the match point. The remaining proportions are then rescaled based on the magnitude of the match point. In Tredegar, sieve and survey tape generated

GSDs were combined as these methods covered the largest range of GSD values. In Liusha and Luoquan, pyDGS GSDs with different shape parameters were required to create full GSDs compared to sieving. A *shape parameter* of -1 in Liusha best represent the coarsest percentiles and a *shape parameter* of 0 best fit the finest percentiles. In Luoquan I combine runs with a *shape parameter* of 1 and -1. I tested the sensitivity of the choice of match point, by comparing four possible combined GSDs from our Tredegar data and found that there was less than a 10% difference in D_{50} values across the combined GSDs.

4.4.7 Comparing the different methods

I compared the grain size for the 5th, 10th, 16th, 25th, 50th, 75th, 84th, 90th, and 95th percentiles (for all individual methods and combined GSDs) using the normalised root mean square error (NRMSE) (Buscombe, 2013). NRMSE provides a measure of how different two values are, that is more robust at higher percentiles than standard RMSE. Sieving captures the widest range of grain sizes so we consider it as the measured value. I calculated NRMSE as outlined in Buscombe (2013) (Equation 4.2)

$$NRMSE\ (\%) = \frac{\sqrt{\frac{\left(q^i_{meas} - q^i_{est}\right)^2}{n}}}{q^i_{meas}} \times 100, \qquad \textit{Equation 4.2}$$

where n is the number of observations, q^i_{meas} is the percentile grain size from sieving, and q^i_{est} is the percentile grain size for the method that is being compared.

For continuous datasets (manual photo counts, Wolman pebble counts and survey tape counts), I also calculated the percentile uncertainty using the QuantBD function (Eaton et al., 2019; Purinton and Bookhagen, 2021). The output from QuantBD is a minimum and maximum grain-size range for each percentile based on a 95% confidence interval, which I refer to as percentile uncertainty. Finally, two-sample goodness-of-fit chi squared (χ^2) tests allowed pairwise comparison of different distributions. The results of the NRMSE comparisons and the chi squared tests can be found in tables in the Appendix.

4.5 Results

For all deposits, grain size range varies with measurement method (Figures 4.5, 4.6 and 4.7). In Tredegar, sieving measured the widest grain size range (from <0.063 mm to 40 mm). Survey tape and pyDGS derived GSDs spanned two orders of magnitude, from 1 mm to 170 mm and 0.5 mm to 45 mm respectively. Wolman pebble count and manual photo count GSDs recorded an order of magnitude, 3 mm and 90 mm and 1 mm and 77 mm respectively.

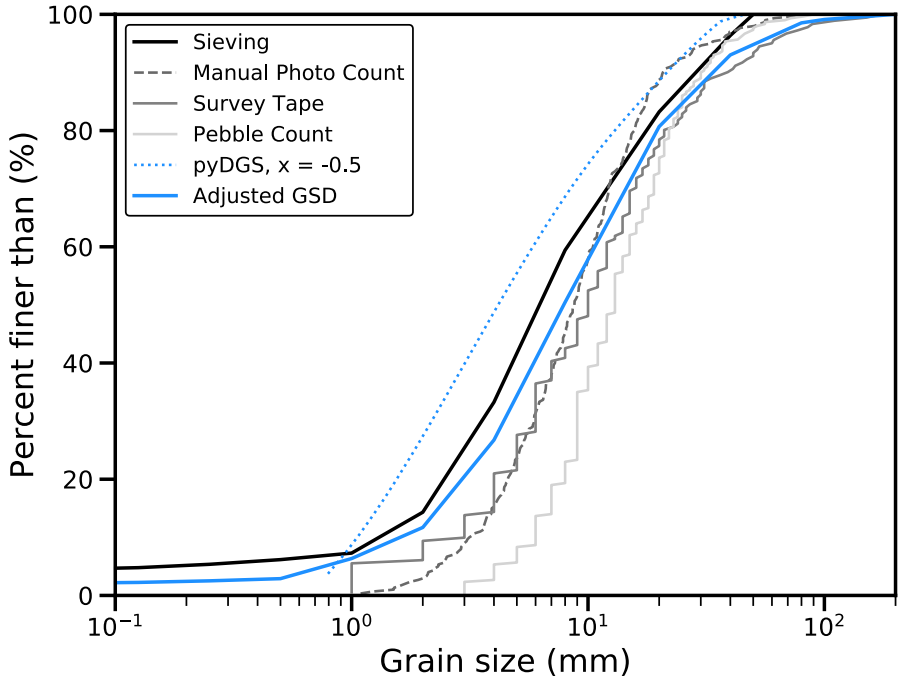

Figure 4.5

The surface GSDs of the Tredegar rockslide based on five sampling methods. The sieving GSD is based on a sample taken within the first 10 cm of the surface near the centre of the deposit. The survey tape count is based on a total of 181 grains across the entire deposit. Both the Wolman pebble count and manual photo count consisted of measuring 300 grains. The manual photo count was based on 6 photos taken in different parts of the deposit. The pyDGS curve is the average of the 60 GSDs generated using individual photos of the deposit. The adjusted GSD (blue) is calculated by combining the surface sieving GSD (black) and the survey tape GSD (grey) using the method outlined in Fripp and Diplas (1993) and briefly in Section 4.4.6. I used sieving and survey tape GSDs as these provided the minimum and maximum grain sizes respectively.

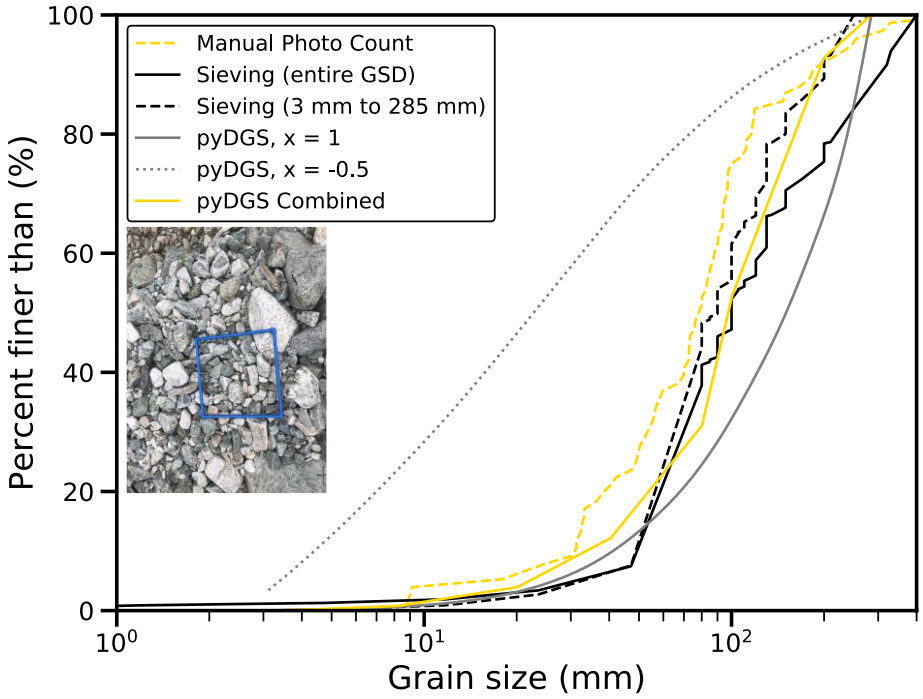

Figure 4.6

Sieving, manual and automated photo analysis-based surface GSDs for the Luoquan (Figure 4.2C) debris flow deposit. The solid gold line shows the GSD derived by combining two pyDGS runs. The inset photo shows the pit image used to estimate surface GSDs from manual photo counts and pyDGS. In total 76 grains were measured using a manual photo grid sampling technique.

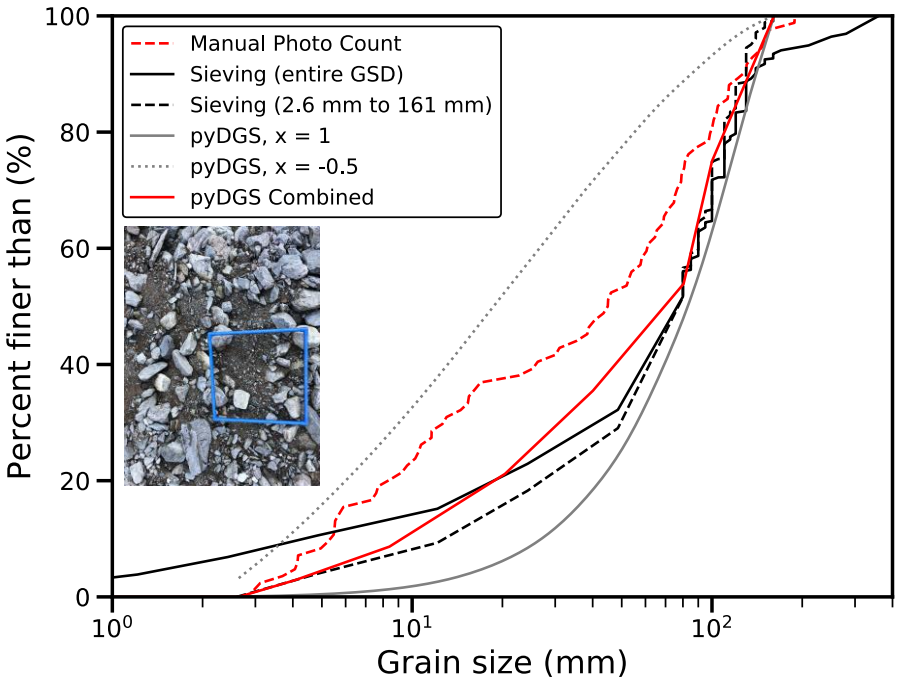

Figure 4.7

Sieving, manual and automated photo analysis-based surface GSDs for the Liusha (Figure 4.2B) debris flow deposit. The solid red line shows the GSD derived using two pyDGS runs. The inset photo shows the pit image used to estimate surface GSDs from

manual photo counts and pyDGS. In total, 84 grains were measured using a manual photo grid sampling technique.

Common percentiles used to describe GSDs, D_{16}, D_{50} and D_{84}, all varied by at least an order of magnitude across the different methods (Tables 4.3 and 4.4). In Tredegar, the D_{16} values obtained varied by the most compared to D_{50} and D_{84} as demonstrated by higher NRMSEs for lower percentiles (>50% error for percentiles smaller than D_{50}) (Table 4.3). The D_{16} value for Wolman pebble counts (7 mm) was five times larger than the D_{16} value obtained using pyDGS (1.4 mm) and sieving (2.2 mm) and exceeded all other D_{16} values and upper limits based on percentile uncertainty (Table 4.3). D_{16} values for the debris flow deposits also varied by over a factor of two across the different methods (5 mm – 13 mm in Liusha and 5.9 mm – 56 mm in Luoquan) (Table 4.4). D_{50} values differed by over a factor of two in Tredegar (4.5 mm – 13 mm) and over a factor of three in the Longmen Shan (Liusha: 19 mm – 83 mm, Luoquan: 23 mm – 150 mm) (Tables 4.3 and 4.4). In Tredegar, pyDGS and sieving also obtained the lowest D_{50} values and D_{16} values. Survey tape counts and manual photo counts produced similar measurements for both D_{16} (4 mm and 4.1 mm) and D_{50} (10 mm and 8.8 mm). Wolman pebble counts obtained the largest D_{50} value. In the Longmen Shan, when only considering the combined pyDGS GSDs, D_{50} values were largest for sieving GSDs (77 mm and 100 mm). The variation in D_{50} values coincides with the minimum resolutions for each of the respective methods. Larger percentiles, such as D_{84}, and the maximum grain size obtained also differed across methods (Figures 4.5, 4.6, 4.7; Tables 4.3 and Appendix). Photo-based grain-size techniques (both manual and pyDGS) D_{84} values were consistently smaller than the other methods in all locations. In Liusha and Luoquan, manual photo count and pyDGS GSDs underestimated the upper 20% of the distribution relative to sieving (Figures 4.6 and 4.7, Table 4.4). In some instances, visually calibrated pyDGS runs could be used to produce coarser distributions, however this was at the expense of lower percentile values (Figure 4.8, Appendix).

Table 4.3 (below)

The D_{16}, D_{50} and D_{84} grain sizes for the five different methods used in Tredegar. The first half of the table gives the percentiles for each method across their entire GSD. The second half of the table shows the percentiles for the single order grain size covered by all five methods. Values in brackets give the range of grain sizes for each percentile calculated using three different methods denoted by the symbol.

† Each sieving percentile was calculated using an assumed linear relationship between the minimum and maximum values of each grain-size bin. Therefore, we have also given the minimum and maximum grain-size bin for each percentile in brackets.

‡ These percentiles were generated using the QuantBD function developed by Eaton et al. (2019) and translated into Python by Purinton and Bookhagen (2021). The percentile uncertainty is quantified using binomial theory for each percentile based on the number of measurements. We provide the minimum and maximum grain-size range for each percentile generated using this technique in brackets for a 95% confidence interval.

§ These percentiles were generated using pyDGS. The range given in brackets is based on a conservative 25% error estimate based on the errors quantified in Buscombe (2013) for GSDs measured manually and pyDGS GSDs for individual images.

	Tredegar Entire GSD (mm)				
Percentile	**Sieving †**	**Wolman Pebble Count ‡**	**Survey Tape ‡**	**Manual Photo Counts ‡**	**pyDGS *x* = -0.5 §**
16	2.2 (2 – 4)	7 (6 – 8)	4 (3 – 5)	4.1 (3.6 – 4.6)	1.4 (1 – 1.8)
50	6.6 (4 – 8)	13 (12 – 14)	10 (8.4 – 12)	8.8 (7.8 – 9.5)	4.5 (3.4 – 5.6)
84	21 (20 – 40)	25 (22 – 28)	26 (20 – 33)	17 (15 – 20)	16 (12 – 20)
	Tredegar Truncated (3 mm to 34.3 mm) (mm)				

Percentile	Sieving †	Wolman Pebble Count ‡	Survey Tape ‡	Manual Photo Counts ‡	pyDGS x = -0.5 §	pyDGS x = 0 §
16	4.2 (4 – 8)	7 (6 – 7.3)	5 (4 – 5)	4.9 (4.5 – 5.4)	4.0 (3 – 5)	4.8 (3.6 – 6)
50	7.8 (4 – 8)	12 (11 – 13)	10 (8.3 – 11)	9.1 (8.2 – 9.9)	8.0 (6 – 10)	11 (8.3 – 14)
84	19 (10 – 20)	21 (20 – 23)	19 (16 – 23)	16 (15 – 18)	20 (15 – 25)	24 (18 – 30)

Table 4.4 (below)

Common statistical metrics used to describe GSDs. The Liusha pyDGS percentiles are based on a maxscale of 6. The Luoquan pyDGS percentiles are based on a maxscale of 4.

† Each sieving percentile was calculated using an assumed linear relationship between the minimum and maximum values of each grain-size bin. Therefore, we have also given the minimum and maximum grain-size bin for each percentile in brackets.

‡ These percentiles were generated using the QuantBD function developed by Eaton et al. (2019) and translated into Python by Purinton and Bookhagen (2021). The percentile uncertainty is quantified using binomial theory for each percentile based on the number of measurements. We provide the minimum and maximum grain-size range for each percentile generated using this technique in brackets for a 95% confidence interval.

§ These percentiles were generated using pyDGS. The range given in brackets is based on a conservative 25% error estimate based on the errors quantified in Buscombe (2013) for manually observed GSDs for individual images and pyDGS generated GSDs. The pyDGS combined percentiles in Liusha are based on a full GSD generated in pyDGS with a shape parameter of 0 and maxscale of 8 combined with the GSD for grains >80 mm with a shape parameter of -1 and maxscale of 6. In Luoquan the GSD are based on a full GSD with a shape parameter of 1 and maxscale of 8 combined with the GSD for grains >80 mm with a shape parameter of -1 and maxscale of 4.

¶ No range is given for this percentile as the surrounding grains also have the same b-axis.

	Liusha (mm)				
Percentile	**Sieving** †	**Manual Photo Counts** ‡	**pyDGS** ***x* = -0.5** §	**pyDGS** ***x* = 1** §	**pyDGS** ***Combined*** §
16	13 (12 – 24)	7.4 (5.1 – 10.4)	5.0 (3.8 – 6.3)	36 (27 – 45)	15 (11 – 19)
50	77 (49 – 80)	45 (25 – 61)	19 (14 – 24)	83 (62 – 104)	72 (54 – 90)
84	130 ¶	104	65	130	122

		(82 – 130)	(49 – 81)	(98 – 163)	(92 – 153)
	Luoquan (mm)				
Percentile	**Sieving** †	**Manual Photo Counts** ‡	**pyDGS *x* = -0.5** §	**pyDGS *x* = 1** §	**pyDGS *Combined*** §
16	56 (47 – 80)	33 (28 – 49)	5.9 (4.4 – 7.4)	57 (43 – 71)	49 (37 – 61)
50	100 ¶	79 (69 – 89)	23 (17 – 29)	150 (113 – 188)	98 (74 – 123)
84	248 (210 – 250)	119 (100 – 190)	89 (67 – 111)	248 (186 – 310)	178 (134 – 223)

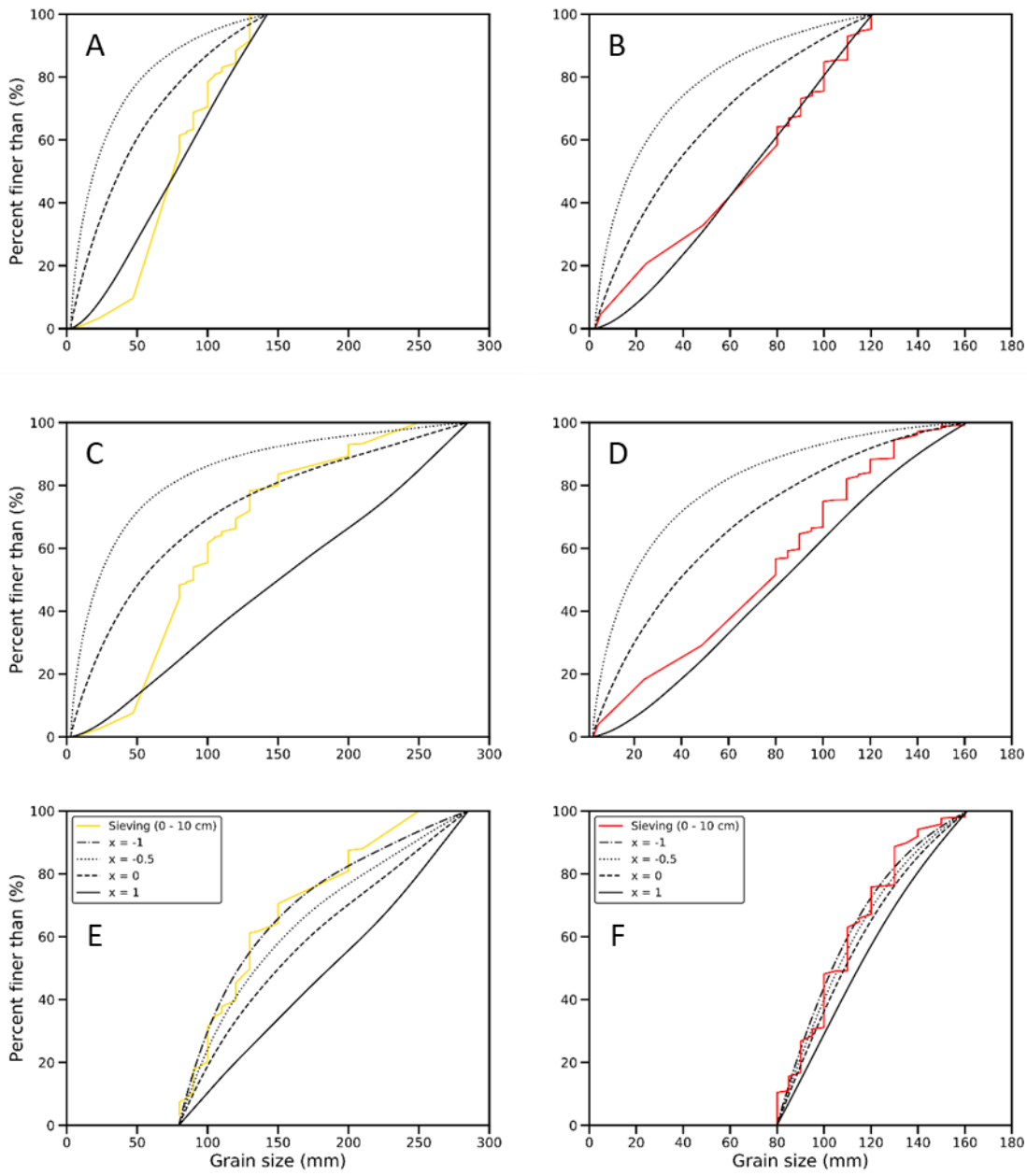

Figure 4.8

GSDs obtained using pyDGS with different maxscale values plotted alongside sieving GSDs for the same grain size range. A) Luoquan deposit with a maxscale of 8 and GSD limit of 3.1 mm to 142 mm. B) Liusha deposit with a maxscale of 8 and GSD limit of 2.6 mm to 121 mm C) Luoquan deposit with a maxscale of 4 and a GSD limit of 3.1 mm to 285 mm. D) Liusha deposit with a maxscale of 6 and GSD limit of 6.5 mm to 161 mm. E) Luoquan deposit, maxscale of 4 and GSD limit 80 mm to 285 mm. F) Liusha deposit, maxscale of 6 and GSD limit of 80 mm to 161 mm.

The GSDs measured were significantly different from the sieved distributions in Tredegar; Wolman pebble counts (χ^2= 64.14, d.f. = 3, p-value < 0.05), survey tape counts (χ^2= 13.03, d.f. = 5, p-value < 0.05), manual photo counts (χ^2= 28.95, d.f. = 3, p-value < 0.05) and pyDGS (χ^2= 25.95, d.f. = 5, p-value < 0.05) (Appendix Table 6). To infer the magnitude of methodological

uncertainty in these values I truncated the individual distributions in Tredegar to the grain size range covered by all methods (3 mm to 34.4 mm, Figure 4.9; Church et al., 1987). Within this range, survey tape counts, pyDGS and sieving GSDs were similar (sieving and survey tape: χ^2= 6.44, d.f. = 3, p-value > 0.05; sieving and pyDGS: χ^2= 1.01, d.f. = 3, p-value > 0.05; survey tape and pyDGS: χ^2= 5.45, d.f. = 3, p-value > 0.05) (Figure 4.9, Appendix Table 6). Manual photo counts and Wolman pebble counts were significantly different with 95% confidence to sieving GSDs (χ^2= 12.64, d.f. = 3, p-value < 0.05; χ^2= 29.91, d.f. = 3, p-value < 0.05) and survey tape GSDs (χ^2= 8.02, d.f. = 3, p-value < 0.05; x^2= 21.07, d.f. = 3, p-value < 0.05). Wolman pebble count GSDs overpredicted grain sizes in the lower 50% of the distribution when compared with all other methods.

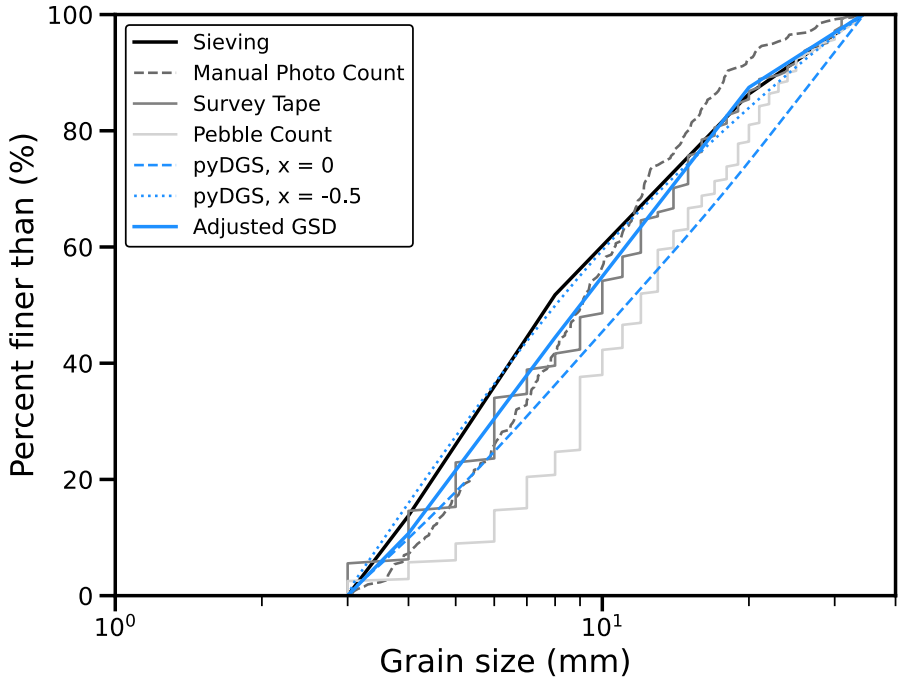

Figure 4.9

Comparison of truncated field-derived GSDs and pyDGS derived GSDs for the Tredegar rockslide. I found that the range 3 mm to 34.4 mm was covered by all five methods and therefore adjusted all curves to fit this range. The sieving GSD is based on a sample taken within the first 10 cm of the surface near the centre of the deposit. Approximately two thirds of the sample is within the truncated grain size range. The survey tape count is based on a total of 181 grains across the entire deposit. 144 of these grains were within the truncated range. Both the Wolman pebble count and manual photo count consisted of measuring 300 grains. In the Wolman pebble count 279 grains were within the truncated range. 259 grains from

the manual photo count were within the truncated range. The pyDGS curve is the average of the 60 GSDs generated using individual photos of the deposit. Approximately 60% of the full GSD for pyDGS shown in Figure 4.5 was within the truncated range. The adjusted GSD (blue) is calculated by combining the surface sieving GSD (black) and the survey tape GSD (grey) using the method outlined in Fripp and Diplas (1993) and briefly in Section 4.4.6. I used sieving and survey tape GSDs as these provided the minimum and maximum grain sizes for the location based on their generated GSDs.

4.6 Discussion

4.6.1 Sampling method uncertainty

There are several uncertainties inherent in each sampling method that can lead to systematic bias in the reported results (Table 4.1). Bias in the sieving GSDs may be introduced as each sample integrates the subsurface and surface grains into a single GSD (Bunte and Abt, 2001b; Dufresne and Dunning, 2017; Johnson et al., 2012). Where deposits are vertically stratified, this will lead to underestimation of coarse (or fine) surface fractions. These issues were mitigated by choosing sampling locations that showed no evidence of vertical stratification. No systematic change was observed in these three pits with depth, suggesting that differences in GSD are more likely to reflect primary variability in the deposits rather than vertical stratification (Figure 4.10). For example, while D_{16}, D_{50} and D_{84} values for the upmost three layers in Luoquan ranged from 30 – 56 mm, 100 – 137 mm and 248 – 306 mm respectively, there was no evidence of stratification with depth. Additionally, the D_{16} and D_{50} values obtained for sieving were consistently lower than the values obtained using Wolman pebble counts, survey tape counts and manual photo counts, demonstrating that the changes observed with depth should not result in simply a coarser or finer surface. The D_{84} values in Luoquan and Liusha were also larger than all other surface D_{84} values. Further bias could be introduced if the pit is not constructed correctly, which I avoided by consistently measuring the width and depth of the pit when digging. Whilst, sieving presents challenges in terms of the efficiency and accessibility, it is the only method able to successfully measure sand grains and finer. Where time or equipment is limited, an alternative method may be chosen, but no other method will be able to sample this fine fraction which represents up to 20% of the GSD by weight (Casagli et al., 2003). For the statistical comparisons in this chapter, I use sieving as the test statistic due to its larger sample sizes and

widest GSDs making it most likely to be representative of the true distribution across its sampling range.

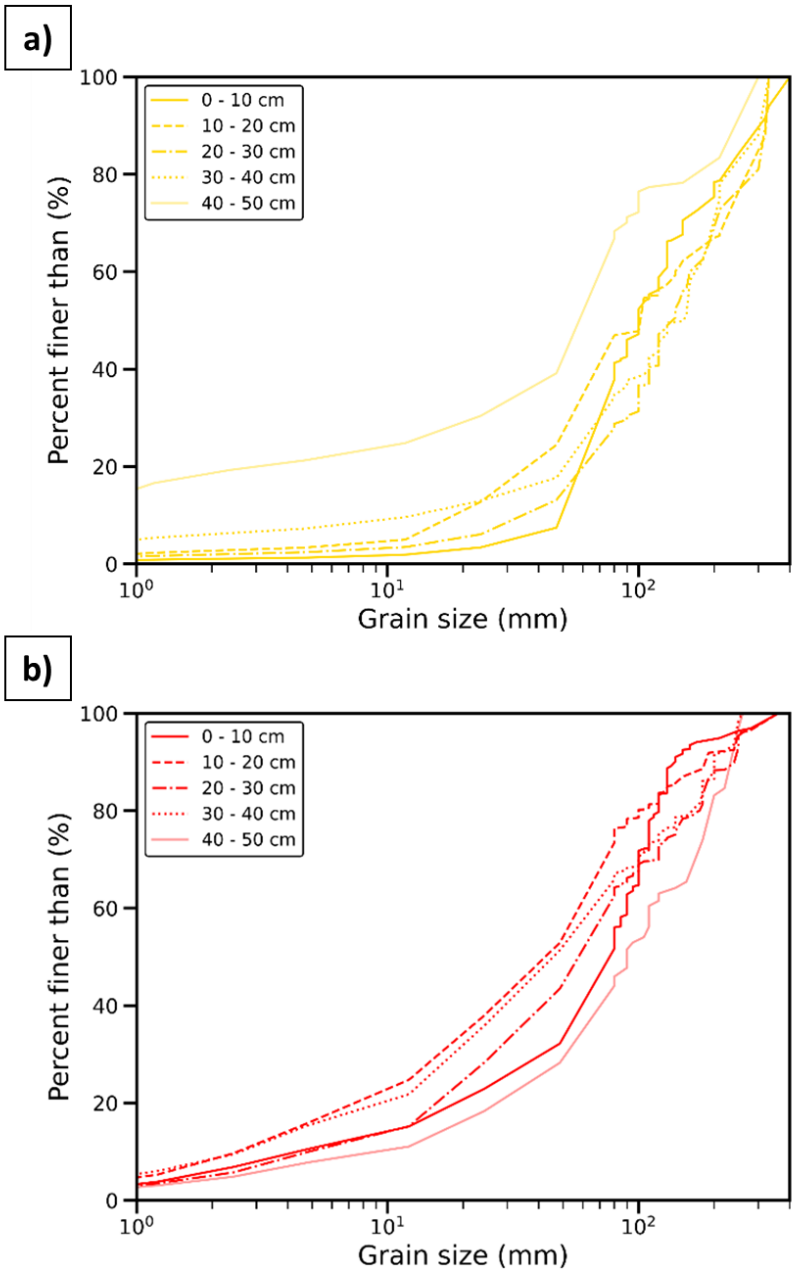

Figure 4.10

GSDs measured using sieving at 10 cm depth increments for the Luoquan (A) and Liusha (B) debris flows. Variations in depth are shown by the different line styles.

Photo-based techniques can be limited by photo extent, imbrication, overlap and mistakenly measuring the c-axis as opposed to the b-axis (Attal and Lavé, 2006; Casagli et al., 2003; Kellerhals and Bray, 1971). These limitations can result in GSDs that underestimate the coarse end of the distribution (Appendix). Furthermore, small sample sizes can also lead to underestimating

the D_{84} values. Despite using the same photos, we found significant differences when comparing manual photo count and pyDGS GSDs in Tredegar (Appendix; Full GSD: χ^2= 62.04, d.f. = 3, p-value < 0.05; Truncated GSD: χ^2= 22.21, d.f. = 3, p-value < 0.05). PyDGS with a *shape parameter* of 1 also underestimated the proportion of grains between 5 mm to 40 mm relative to manual photo counts in Liusha (Figure 4.7). The differences in the GSDs obtained using each method may be attributed to the lack of contrast between the fine grains in the image. The lack of contrast results in smaller changes in the texture of the image and therefore reduces the ability of the pyDGS algorithm to register these as grains. Images where the fine grains are all of similar colour are difficult to differentiate, resulting in the individual grains being considered as single larger grains (Buscombe, 2013, Figures 4.4, 4.7 and 4.11). This effect may be enhanced by wet grains in Figures 4.4A and 4.7 (Buscombe, 2013).

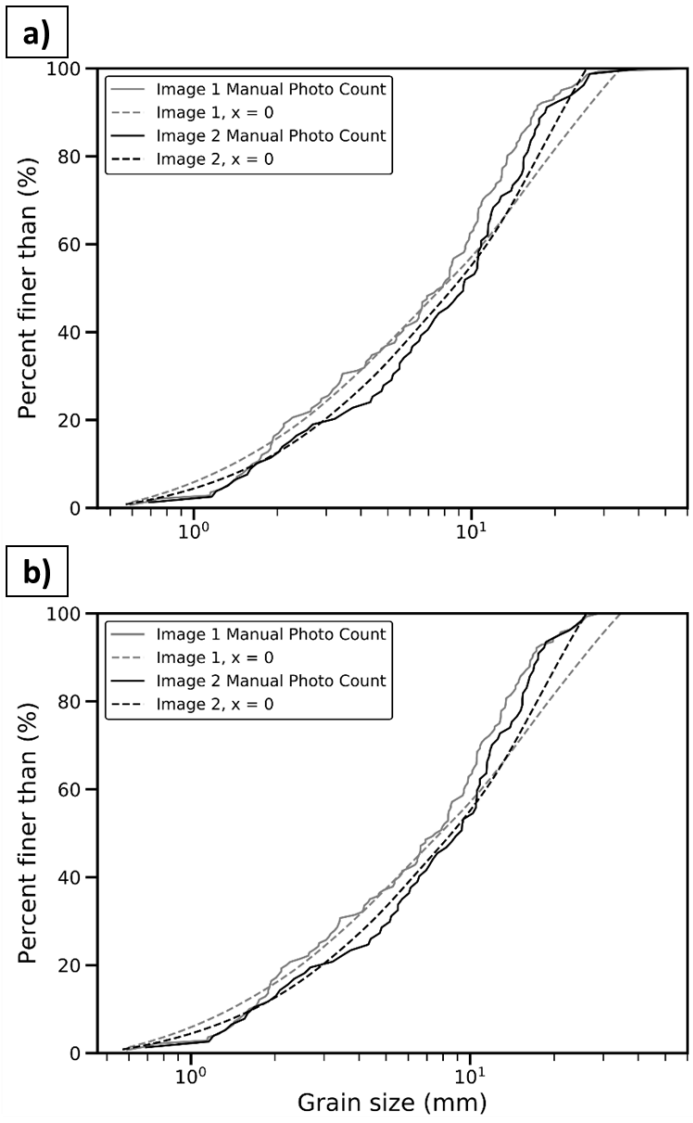

Figure 4.11

The GSDs obtained using pyDGS and manual photo counts for two individual photos taken in Tredegar (Figure 4.4A and 4.4B) A) Manual photo count of Images 1 (grey) and 2 (black) using a 1 000 mm^2 grid in ImageJ compared with pyDGS GSDs. pyDGS was run with the following parameters: maxscale: 8, x: 0, resolution: 0.088 mm pi^{-1} (Image 1) and 0.084 mm pi^{-1} (Image 2). B) Comparison of manual photo counts and pyDGS GSDs for the same grain size range. For Image 1 this is between 0.6 mm and 34.5 mm and Image 2 this is between 0.6 mm and 28.4 mm.

PyDGS was not well suited to the application of mass movement deposits as it requires calibration and multiple shape factors to capture complex GSDs (Figures 4.6 and 4.7, Appendix). Even when calibrated the GSD obtained using pyDGS was statistically different from the full GSDs obtained using sieving in all three locations (Tredegar: χ^2= 25.95, d.f. = 5, p-value < 0.05; Liusha: χ^2= 14.85, d.f. = 4, p-value < 0.05; Luoquan: χ^2= 22.01, d.f. = 5, p-value < 0.05). Whilst, pyDGS has the major benefit of automatically generating GSDs from photos, which can enhance our ability to record GSDs over high spatial and temporal resolutions, for complex, large mass movement deposits, pyDGS generated GSDs rely too heavily on the use of another method for calibration that it does not increase efficiency.

Wolman pebbles counts and survey tape counts cannot measure the finest grains and have minimum grain sizes of 3 mm and 1 mm for each method respectively (Figures 4.4 and 4.9; Table 4.3). The statistically different, coarser, GSD for random Wolman pebble counts when compared to survey tape counts (χ^2= 21.07, d.f. = 3, p-value < 0.05) is possibly to be due to fine pebbles being overlooked by the technique as a result of operator bias (Fripp and Diplas, 1993; Strom et al., 2010). Operator bias may be even more pronounced in heterogenous, multimodal mass movement deposits towards the extreme small or large grains (Daniels and McCusker, 2010; Strom et al., 2010). A limitation of the approach used here is the fact that I sampled grains <2 mm using the survey tape method and <4 mm using the Wolman count method (Bunte and Abt, 2001a). Whilst these are below the expected minimum grain sizes in Table 1, I wanted to provide the full GSD of grains visible in the field. The minimum GSDs often used, 4 mm – 8 mm, are dictated by work on fluvial GSDs, which are likely to be inundated by shallow water (e.g. Kellerhals and Bray 1971; Bunte and Abt 2001a). In a mass movement deposit, the smaller grains on the surface are more likely to be visible, which

may allow for the sampling of smaller grains. The exclusion of fine grains when conducting pebble counts, particularly randomly through a Wolman pebble count, will result in a mass movement GSDs, where fine grains are underestimated.

4.6.2 Methodological uncertainty, sample size and sample type

No single method accurately measured the full GSD in any of the mass movement deposits studied (Figures 4.5, 4.6 and 4.7). In Tredegar, I combined two GSDs collected using different methods to obtain a full GSD. When selecting which methods to combine it is important to consider the differences in the distribution produced based on methodological uncertainty, sample size, and sampling method. To identify differences in the GSDs associated with methodological uncertainties, I compared the GSDs measured using different methods across a restricted set of grain sizes, where issues of resolution are likely to be minimal. Wolman pebble counts and manual photo counts had significantly different distributions across this restricted grain size range suggesting that these methods are the least comparable to sieving and survey tape counts, and therefore least reliable. Survey tape counts and pyDGS GSDs were consistent with sieving GSDs over a restricted grain-size range (Appendix), implying that they are strong candidates for combining to create a full GSD. The statistically similar relationship between survey tape counts and sieving over a single order of magnitude, suggests that a more systematic approach to pebble counts can be used to represent the fraction of grains larger than fine gravel in a mass movement deposit better than a random pebble count (Kellerhals and Bray, 1971). Consequently, any statistical differences across the full GSD measured by these three methods are likely to be a result of the sample size and sample range of each method. The importance of method choice, and grain-size range, was further reflected in the percentile values for each method. For full GSDs, survey tape counts, manual photo counts and Wolman pebble counts all overestimated D_{16} relative to the sieving D_{16} value, due to their inability to sample grains smaller than gravel (Table 4.1; Wolman 1954; Casagli et al. 2003). Thus, the use of Wolman pebble counts or manual photo counts introduces methodological uncertainties to the sampling of mass movement deposits and results in statistically different, unreliable, GSDs.

Methodological differences in sample size may also affect the measured GSDs and explain the differences in manual photo count and Wolman pebble count GSDs (Church et al. 1987; Storz-Peretz and Laronne 2013; Purinton and Bookhagen 2021). Primarily, the issue of sample size relates to the ability to accurately capture the coarse end of the distribution (Church et al., 1987). Previous studies have suggested recommended sample sizes for different methods based on coarse fluvial deposits (e.g. Kellerhals and Bray 1971; Fripp and Diplas 1993; Graham et al. 2010; Eaton et al. 2019; Purinton and Bookhagen 2021). When we applied these methods to large, complex mass movement deposits, such as Liusha and Luoquan where the coarse grains were much larger than is typical in fluvial settings, it was challenging to strictly apply these sample sizes. Recommended sample sizes vary for survey tape and Wolman pebble count methods based on the range of grain sizes found in the deposit. Measuring enough grains for at least the 84^{th} percentile to converge provides a helpful criterion (Purinton and Bookhagen, 2021). For the finer mass movement deposit in Tredegar, the 84^{th} percentile converged after 300 measurements, which took approximately 1 – 2 hours of sample time. This timescale is not significantly different from that required to construct and sieve a pit in a fine deposit.

Photos counts have a recommended areal coverage of 100 to 200 times the D_{Max} to obtain <10% errors (Eaton et al., 2019; Graham et al., 2010; Purinton and Bookhagen, 2021; Storz-Peretz and Laronne, 2013). In the Longmen Shan, where the D_{Max} from the images used were 189 mm and 552 mm respectively, this would require a photo with a width of 11 m (an area of >100 m^2). Such photo could only be taken with UAV and would subsequently compromise the resolution of the finest grains (unless combined with a higher resolution photo) (Graham et al., 2010; Storz-Peretz and Laronne, 2013). This example highlights the primary challenges of sample size, as it is common to find grains > 500 mm in mass movement deposits that may be smaller than 100 m^2 or where larger areas are not spatially uniform, for example due to segregation.

In fluvial environments, there is a volumetric sieving target where a maximum of 5% of the total weight limit can be made up of the largest grain (Church et al. (1987). Occasionally, boulders >50 kg were still recorded in the debris flow

deposit pits that meant this criterion was not always achievable. Where deposits are small or only a fraction of the deposit needs to be sampled, sieving may be a more appropriate technique for obtaining a GSD. Though it is difficult to achieve the recommended sample sizes in mass movement deposits for any individual sampling method. As such, accurate GSDs, which meet the recommended sample sizes, are more likely to be achieved by combining multiple methods that are optimised to sample certain grain-size ranges (Attal and Lavé, 2006; Casagli et al., 2003; Fripp and Diplas, 1993).

Whilst spatially uniform sections of the deposit were chosen, it is important to note that each method has slightly different sampling frequencies and depths. I refer to uncertainty associated with differences in the location of sample as sample type. These field sites were chosen to minimise differences in sample type. Within the three pits sampled, there was no vertical stratification by grain size across the top 50 cm (which I sampled at 10 cm intervals) (Figure 4.10). Thus, there is no evidence that a surface sample would be significantly different to a sieved sample (Attal and Lavé, 2006). I combined the sieving and survey tape GSDs to produce a full distribution. In doing this, I assumed that sieving and survey tape GSDs could be merged due to the fact they do not produce statistically different distributions over a truncated range of grain sizes (Figure 4.5). Whilst the combined GSD will produce the widest GSD, I note that the uncertainties associated with combined methods are likely to be propagated in the adjusted distribution, for example the effect of sample size. In Luoquan and Liusha it was not necessary to combine multiple GSDs because sieving recorded the minimum and maximum grain size. Thus, combining complimentary methods that sample different grain size ranges, but without significant methodological uncertainty (e.g., sieving and survey tape), may provide the best opportunity to accurately report the full GSD of mass movement deposits.

4.6.3 Applying these methods to different types of mass movement

A solution to the challenges associated with developing accurate GSDs across the wide range of mass movement grain sizes is to vary the method based on the research question being asked. In many cases, only a portion of the entire GSD is required to identify the transport and depositional mechanisms occurring within a deposit and subsequently interpret the types of mass

movement (Blair, 1999; Cruden and Varnes, 1996; Kaitna et al., 2016; McKenna et al., 2012; Wang and Sassa, 2003). For example, flow-like failures are commonly associated with processes such as inverse grading and kinetic sieving, which result in a coarse surface layer, front and levees (Johnson et al., 2012). The GSD of levees may require characterisation of grain size across a wider spatial scale, using survey tape counts or manual point counts. In contrast sieving may be better suited when deposits have a high proportion of fine material, such as for viscous flows (Kaitna et al., 2016; Wang and Sassa, 2003).

Measurements of deposit GSDs have been used to infer the source of the material mobilised from the relationship between bedrock strength and the GSD of rock avalanche, rockfall and landslide deposits (Dunning, 2006; Marc et al., 2021). GSDs can also help to identify the source of the mobilised material. For example in California, finer, sandier debris flows were hillslope triggered, whereas the coarser debris flow mobilised material from within the channel (Kean et al., 2011). These findings may also be supported in the Longmen Shan, where rock type variability may explain the higher proportion of grains <10 mm in Liusha in comparison to Luoquan (Figures 4.6 and 4.7). As the fracture spacing of metasediments is smaller than the granitoids found in Luoquan (Figure 4.2D). This difference may have been overlooked by using a method that is biased towards coarser grain sizes.

Mass movement GSDs are more commonly obtained for rock avalanches, debris flows and landslides where grain size plays a role in controlling mobility through processes such as comminution, fragmentation and segregation (Crosta et al., 2007; Dufresne and Dunning, 2017; Dunning, 2006; Locat et al., 2006). These processes produce GSDs with potentially large spatial variability, a wide range of grain sizes and bimodal or multimodal distributions (Crosta et al., 2007; Dufresne and Dunning, 2017; Makris et al., 2020). An understanding of the entire GSD of rock avalanche deposits can also help to understand what controls the rate of different transport and depositional processes. All grain sizes were found to control segregation in an experimental setting for dry granular flows, which includes rock avalanches (Gray and Ancey, 2011). Here, a higher proportion of fine grains resulted in a longer distance being required for medium and large particles to segregate (Gray and Ancey, 2011). The

efficiency of fragmentation in deposits is also thought to relate to GSDs. For example, there is a decrease in the efficiency of fragmentation when the number of fines increases as the fines act to buffer interactions between larger grains (Locat et al., 2006). Whilst Locat et al., (2006) obtained this conclusion using photographs of grains, they did note that their proportions of fines were likely to be an underestimate. Hence, whilst broad patterns can be well captured using more accessible, common methods (Marc et al., 2021), it is important to capture full GSDs for deposits, using multiple methods, when identifying depositional and transport processes.

Examples of where a restricted sampling of the GSD of mass movement deposits might be useful is when considering their contribution to rockfall hazard and fluvial bedload transport. In rockfalls, deposited grain volume can predict runout hazards better than the initial volume which tends to overestimate the kinetic energy and runout (Ruiz-Carulla et al., 2015). Subsequently, only the coarse fraction (rocks >0.01 m^3) is required as this can provide an indication of the furthest point the runout will travel, which is most important for hazard models. Depending on the nature of the hazard, using a single method to rapidly constrain the GSD of coarser boulders may therefore outweigh the importance of spending considerable time extracting the entire GSD of the deposit using sieving. In terms of fluvial bedload, the GSD >1 mm of landslides has been successfully compared directly to the GSD of weathering products to understand the importance of landslides in hillslope and fluvial sediment budgets (Roda-Boluda et al., 2018). This was achievable because the study only focused on the surface material, where most fines have been washed away. However, the appropriate method will vary based on the mass movement deposit sampled and the GSD of the other processes acting within the catchment. The importance of the entire GSD has been shown for the Marsyandi River, where the pebble and suspended/bedload ratio were both affected by hillslope processes, including landslides (Attal and Lavé, 2006).

The methodological uncertainties associated with comparing GSDs and percentiles obtained using different methods can have consequences for accurate process interpretation. For example, the factor of two difference in grain-size percentile estimates from survey tape counts relative to sieving for

a fine deposit could shift the D_{50} value from suspended load to bedload, which would have implications for estimates of sediment export rates and onward transport (Croissant et al., 2021; Marc et al., 2021). Similarly, by excluding up to 20% by weight of the finest grains, all non-sieving methods are unable to find evidence for processes where the proportion of sand and silt is influential (de Haas et al., 2015; Kaitna et al., 2016; Makris et al., 2020). The rates and calibre of hillslope sediment supply to channels have also been increasingly used to drive landscape evolution and fluvial modelling (Attal et al., 2015; Croissant et al., 2021; Egholm et al., 2013; Roda-Boluda et al., 2018). Given mass movement derived sediment is an essential component in these problems (Sklar and Dietrich, 2006), improvements are needed in our ability to characterise this material to provide robust conclusions about the timescales and rates of bedrock incision and sediment transport.

4.7 Conclusion

Measurements of mass movement GSDs present concerns of accuracy, precision, and pragmatism. Each study is required to make choices about methodology, sampling locations and size that suit both the research question being asked and the practical challenges of field sites. Here I show that these choices about methodology can introduce up to a factor of five difference in simple metrics like D_{16} and D_{50}. This results in GSDs and grain-size percentiles that are not directly comparable to GSDs measured using different methods, especially when the same grain-size range is not considered. I demonstrate that for smaller, finer mass movement deposits, survey tape counts and pyDGS are a suitable alternative to sieving for measuring the GSD over a single order of magnitude. Whilst pyDGS could be used to obtain a representative GSD over a single order of magnitude for the smaller landslide deposit, once trained, I was unable to obtain a representative GSD using a single curve for the larger debris flow deposits. In the larger, coarser debris flow deposits in the Longmen Shan, manual photo counts were unable to obtain the maximum resolution measured using sieving. I was also unable to reach the desired sample size for manual photo counts for coarse deposits. In all cases clear, detailed descriptions of the protocol are essential so that uncertainties introduced by different methods can be quantified and the implications for process interpretation can be better understood.

This chapter highlights the challenges associated with measuring the GSD of debris flow deposits as well as how method choice can have significant implications on the measured GSDs and grain size percentiles. In the next chapter, I will apply three of the methods analysed in this chapter (sieving, manual photo counts and pyDGS) on a wider scale to obtain high resolution GSDs for two debris flow deposits in Wenchuan. The GSDs will be measured following the clear protocol set out in Chapter 4 (Section 4.4) in order to be as accurate, and comparable to future studies, as possible. The limitations identified when comparing pyDGS GSDs to sieving GSDs in Chapter 4 will be mitigated in Chapter 5 by using pyDGS only to provide a measure of coarseness for an image. The coarseness of the image will be described using the GSD integral, which is explained in Section 5.4.1. Chapter 4 has highlighted a need to continue developing automated approaches to measure surface grain size from images over a wide range of grain sizes.

Chapter 5

Comparing GSDs for two post-earthquake debris flows with different runout lengths

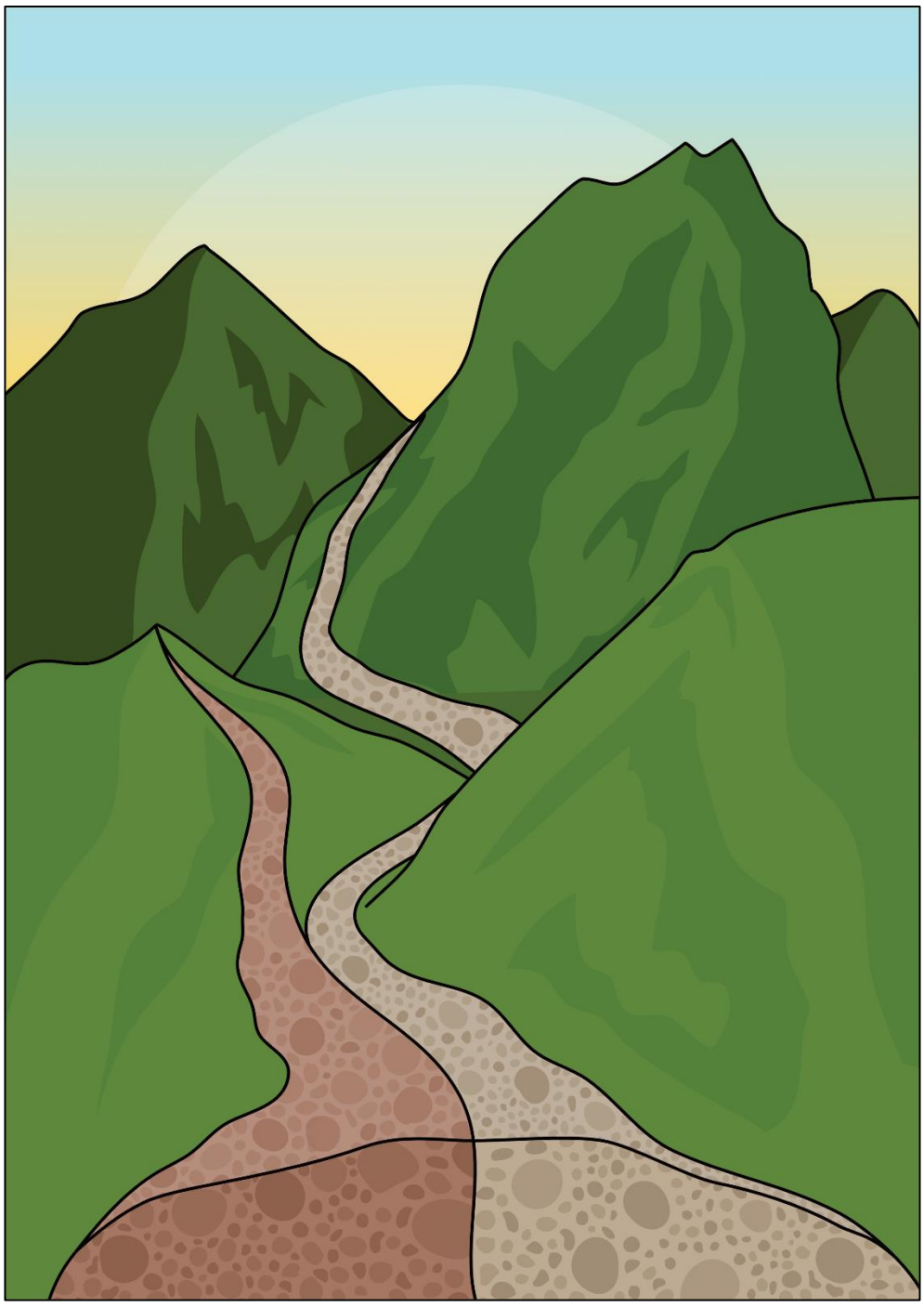

Image by Megan Harvey

5.1 Abstract

Debris flow grain-size distributions (GSDs) are challenging to obtain but are crucial in controlling how debris flows transport and deposit sediment. Studies which use debris flow GSDs to better understand flow processes, such as pore pressure dissipation, are typically performed under controlled physical or numerical conditions that do not correlate well to the field. In this chapter, I have collected high-resolution GSDs for modern-day debris flows by sampling two debris flows across three dimensions (vertically, laterally, and longitudinally). The two post-earthquake debris flows both occurred during the same intense rainfall event in 2019 in catchments located ~20 km apart and remobilised co-seismic sediment. Despite these similarities, the two flows have vastly different runout lengths and channel geometries, suggesting that controls on transport and deposition may contrast between the two flows. I analysed the deposit GSDs to infer what controlled transport and deposition in each flow. I found that both debris flow deposits had relatively consistent GSDs in terms of width and the maximum grain sizes transported. This indicates that grain size was not the main driver of the different runout lengths. However, the spatial pattern of deposited grains did differ in some locations of the flow. These differences suggest that the processes which control grain size segregation in debris flows, such as kinetic sieving, may behave differently in the two flows. The grain size of the smaller Liusha debris flow was vertically segregated in parts, whereas the larger Luoquan debris flow was uniform throughout. This lack of inverse grading may be driven by the higher water content in the larger, Luoquan debris flow, which buffers grain collisions within the flow and inhibits segregation. The GSDs deposited by the Luoquan debris flow appeared to correspond to changes in slope curvature and channel width, suggesting that topography may also affect processes of deposition in highly fluidised debris flows. From these findings, it appears that whilst debris flow GSDs are complex, they can provide insight into how debris flows characteristics and channel topography influence patterns of deposition within individual flows. This high resolution, local-scale approach will be beneficial when validating future debris flow hazard models.

5.2 Introduction

Debris flow GSDs can affect the runout length of debris flows by controlling the flow viscosity, the rate of excess pore pressure dissipation, and the frictional grain interactions (de Haas et al., 2015; Iverson et al., 2010; Pierson, 1981). The spatial pattern of debris flow GSDs can also provide insight into the mechanisms driving transport and deposition within the flow, such as size segregation and particle collisions (see Chapter 2; Pierson 1981; Whipple and Dunne 1992; Blair and McPherson 1998; Kim and Lowe 2004; de Haas et al. 2015). For example, debris flows have been found to form inversely graded deposits due to kinetic sieving (Sohn et al. 1999; Vallance and Savage 2000). These deposits can be identified in the field by a coarse surface layer and a finer base layer and are most commonly found in debris flows dominated by frictional forces and high solid contents (e.g. Sosio et al. 2007). Therefore, not only do debris flow GSDs control debris flow runout length but they can also be used to infer previous debris flow properties and characteristics which cannot be readily measured in the field, such as velocity and the flow water content. Few detailed field studies of debris flow grain size exist due to the challenges outlined in Chapter 4 (Chen et al., 2001; Genevois et al., 2000; Kim and Lowe, 2004; Sosio et al., 2007; Vallance and Scott, 1997; Yong et al., 2013). Most of our current understanding regarding debris flow GSDs and their relation to debris flow mobility stems from small-scale and large-scale flume experiments and numerical modelling (see Bagnold 1954; Major and Pierson 1992; Takahashi et al. 1992; Major and Iverson 1999; Iverson et al. 2011; de Haas et al. 2015; Sanvitale and Bowman 2017; Gray 2018; Pudasaini and Mergili 2019; Barker et al. 2021). An increase in the availability of debris flow GSDs from the field would be invaluable in validating these experiments and models.

In this chapter, I utilise the methods from Chapter 4 to measure the GSDs of two post-earthquake debris flows formed under similar initiation conditions (e.g., rainfall, abundance of post-earthquake sediment, geology) but with different catchment and channel geometries. The Liusha and Luoquan debris flows, which are discussed in more detail in Chapter 3, are post-earthquake debris flows that initiated in August 2019 (Figure 5.1). The Liusha debris flow travelled ~1.5 km before stopping, whilst the Luoquan debris flow travelled

up to ~8 km (Figure 3.7). I measure the GSDs for both debris flow deposits across three dimensions (vertically, laterally across cross sections of the deposit, and longitudinally with distance downstream) to collect the highest resolution spatial distribution of debris flow GSDs to date. I first compare the GSDs deposited by the two debris flows to assess whether grain size controlled the differences in runout length. I then investigate how GSDs can help to interpret transport and deposition mechanisms occurring within the two flows. I utilise three different methods to capture the wide range of grain sizes as well as both surface and subsurface distributions consistent with the conclusions of Chapter 4.

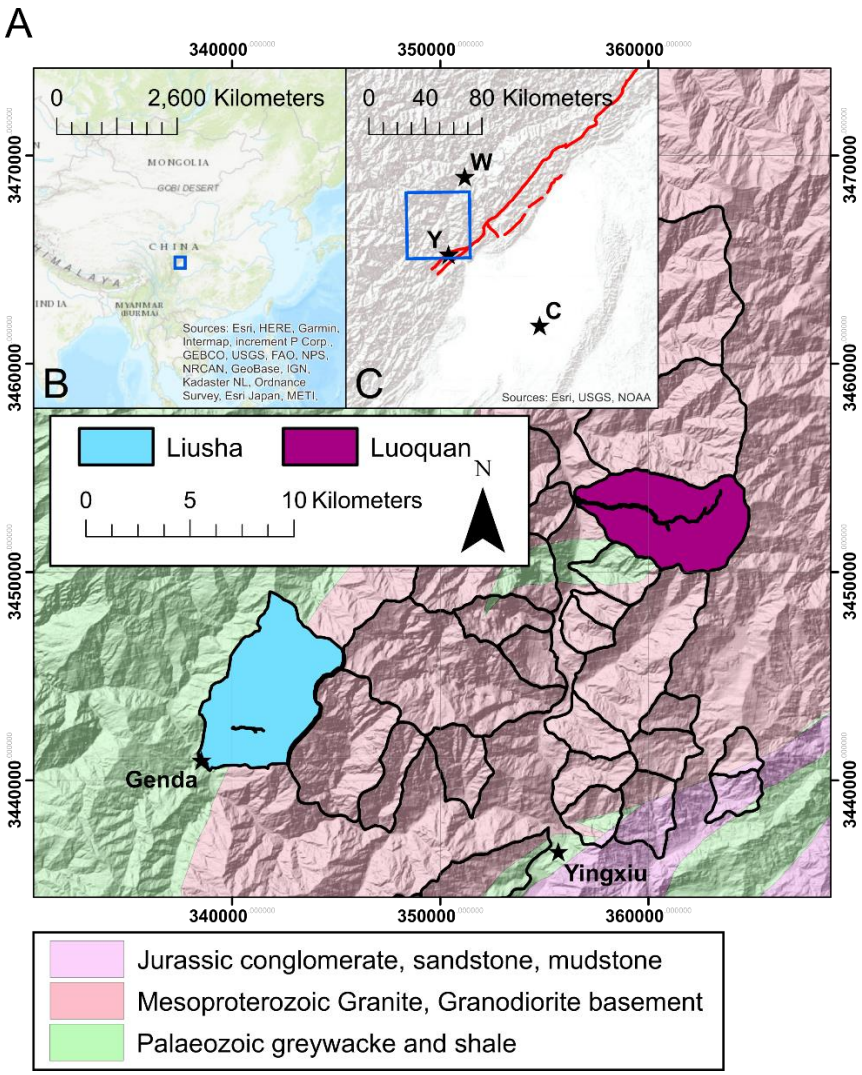

Figure 5.1

Map showing the Liusha and Luoquan debris flows in their respective catchments. The location of the catchments in China and relative to the 2008 fault lines (red) as well as local towns (W – Wenchuan and Y – Yingxiu) and cities (C – Chengdu) are shown in inset maps 5.1B and 5.1C. The underlying geology in the region is also mapped using data from Ma (2002).

5.3 Research objectives

1. To measure high-resolution GSDs for two post-earthquake debris flow deposits across three dimensions (vertical, lateral, and longitudinal).
2. To compare the GSDs deposited by the two debris flows in terms of composition and spatial patterns of deposition.
3. To use these GSD comparisons, to compare and infer mechanisms of transport and deposition for the two debris flows.

5.4 Methods

5.4.1 Grain-size distributions

The methods used to measure the GSDs for the two post-earthquake debris flow are based on our findings from Chapter 4. In this chapter, I extended the sampling area to cover the lower half of each debris flow (from source to toe) (Figure 5.2). This equated to 4 km in Luoquan and 0.8 km in Liusha. The debris flow deposits were sampled in November and December 2019, approximately three months after the debris flows occurred. Reworking of the deposits prior to this analysis is therefore unlikely.

Sieving

I sampled both debris flow deposits at equidistant intervals from the debris flow toe to the upmost accessible location. In Luoquan, I sampled eight pits from 4000 m to 7500 m downstream of the triggering location at 500 m intervals (Figure 5.3). In Liusha, I sampled four pits in total, at 200 - 300 m intervals. The pits in Liusha were located 700 m to 1500 m downstream of the triggering location (Figure 3.7). Pits are numbered based on their distance from the triggering location, for example Pit 1 in Luoquan was 4000 m from the triggering location and Pit 8 was 7500 m from the triggering location (Figure 5.2). I excavated pits measuring 1 m x 1 m x 0.5 m at 10 cm increments, and followed the process detailed in Section 4.4.2 to sieve sediment >1 cm in the field and <1 cm in the laboratory. For all sieving GSDs, I applied a volumetric correction to redistribute the effect of the largest grains which covered multiple layers. To correct for this, I assumed that grains with a b-axis >10 cm covered multiple layers and reallocated the weight of each grain based on the proportion of the grain assumed to be in the layer above. The correction was crucial because grains which covered

multiple layers were initially only sampled in the lowest layer, and hence biased vertical GSDs affecting interpretations of inverse grading. In total, each pit weighed ~1000 kg, which ensured that most pits met, or were close to, the minimum weight limit set out in Church et al. (1987).

All three axes of grains >8 cm were measured in the field to obtain an estimate of grain shape. Grain shape can provide an indication of processes occurring within the flow.

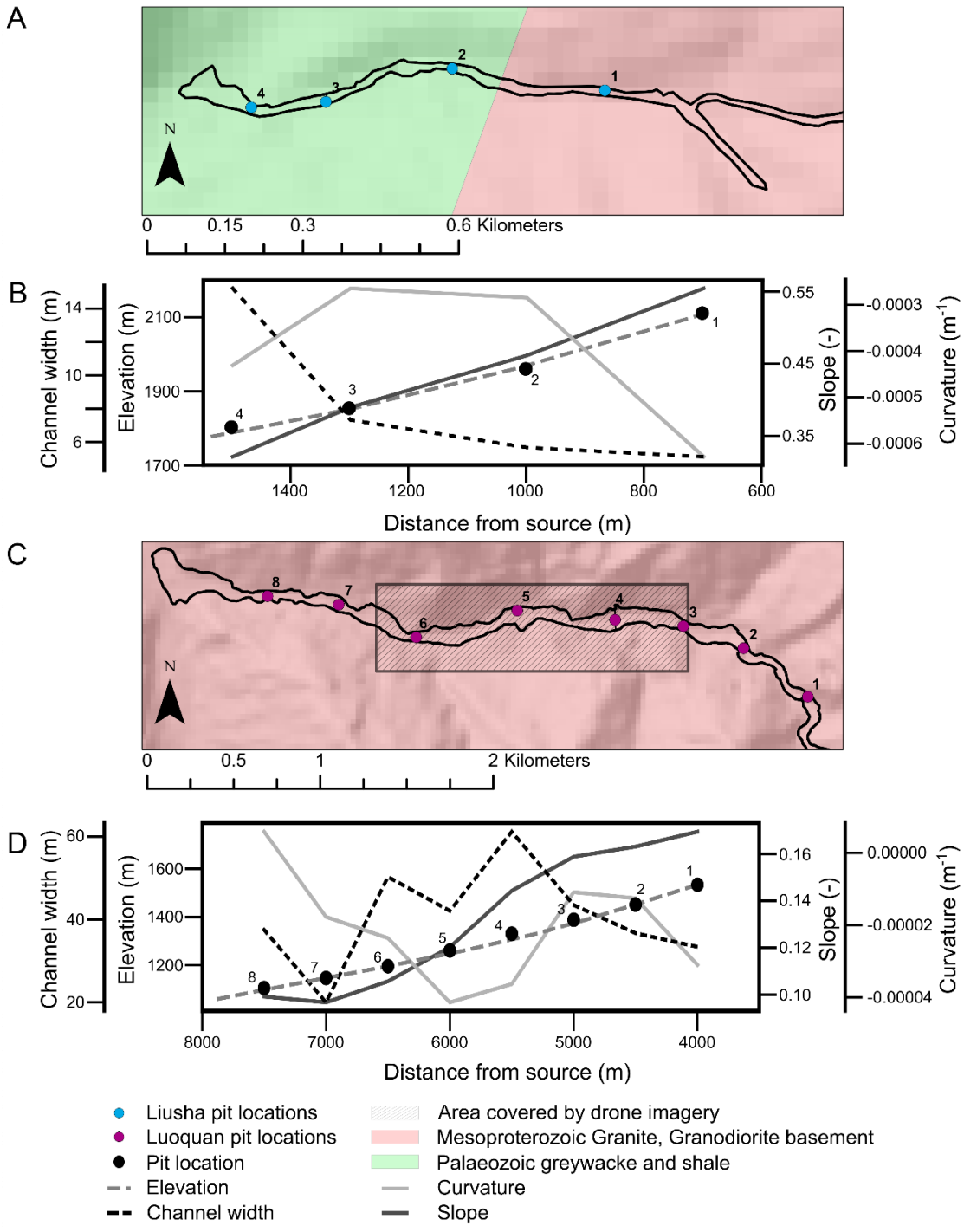

Figure 5.2

The location of the sieved pits, photo cross sections, and drone grain size measurements for the Liusha (5.2A) and Luoquan (5.2C) debris flow deposits. The geomorphological context for each deposit (elevation, slope, curvature and channel width) are shown in Figures 5.2B and 5.2D. The DEM used to produce the hillshade for both figures is 30 m resolution. Note that in Figures 2.B and 2.D the distance from source is increasing from right to left to be consistent with the maps shown in 2A and 2C.

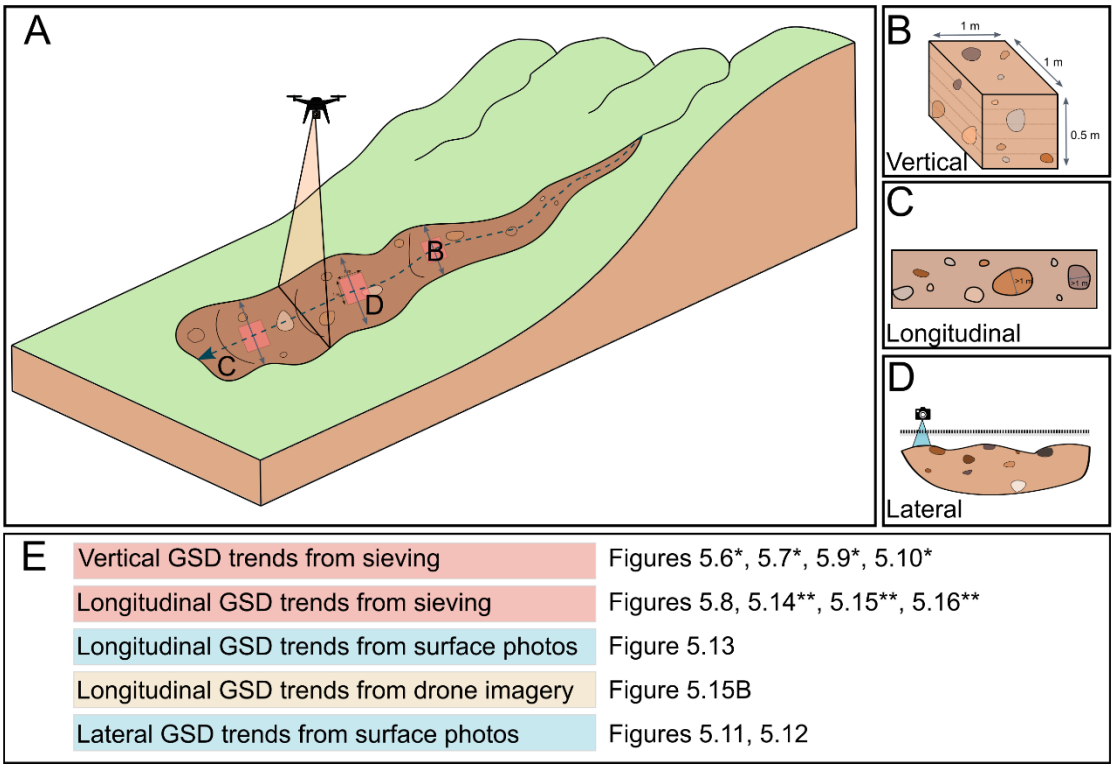

Figure 5.3

*Overview of the methods used to measure the grain size of debris flow deposits. The insets show the approaches taken for vertical GSDs from sieved pits (5.3B), longitudinal GSDs from surface photos and drone imagery (5.3C) and lateral GSDs from surface photos taken at channel cross sections (5.3D). Figure 5.3E shows which approaches were used to produce each figure in this chapter. * Indicates that the figure uses separate GSDs to represent each 10 cm layer in the pit. ** indicates that the sieved GSDs for each pit have been averaged to produce a single GSD for each pit location. This involved creating a new GSD for each pit based on the weight of grains in each size fraction. Average GSD integrals were calculated using the five GSD integrals for each pit.*

Photo analysis

I followed the protocol outlined in Sections 4.4.4 and 4.4.5 to obtain surface GSDs across both deposits using manual photo counts and pyDGS. Photos were taken at approximately equal distance apart along the sieving transects, which were perpendicular to the direction of flow (Figure 5.3). The transects

ran from the right and left edges of the deposit. Areas of the deposit that were older and vegetated were not photographed. I ensured the photos were parallel by using a 0.5 m x 0.5 m frame. This frame was also used to calculate the resolution of the photo in mm pi^{-1}.

Where the largest grains had a b-axis less than one third of the image width, I used the automated, texture-based grain size analysis tool pyDGS to measure the GSD of the photos (Buscombe, 2013). I ran pyDGS to obtain GSDs for >200 photos with a shape parameter of 0, inferred using sieving GSDs, and varied the maxscale (the maximum grain size the algorithm searches for) and resolution depending on each photo. The running time for pyDGS was approximately eight minutes per photo. In Chapter 4, I concluded that pyDGS needed to be tuned to measure the GSDs for complex mass movement deposits and that multiple shape parameter were required to achieve this. On balance, I decided to run pyDGS with a single shape parameter as this enabled the rapid identification of a general GSD for each image. I compared the 200 images with the pyDGS generated GSD and determined that pyDGS could sufficiently provide an indication of coarseness for each surface photo. I minimised the effect of using a single shape parameter by calculating the GSD integral for each distribution to provide a measure of coarseness as opposed to using the individual grain sizes determined, as detailed below. The individual grain sizes determined may be inaccurate whereas the relative coarseness between photos is accurate and will be sufficient to fulfil my research objectives. The GSD integral uses the area under the curve to represent the GSD at each location by a single value (Figure 5.4).

Manual photo counts were conducted on photos where a single grain occupied at least one third of the image width. I applied a grid to each image and measured the b-axis of grains where the gridlines intersected. I considered grains which intersected multiple gridlines as repeats and excluded these from counts. This is likely to result in underestimates of the GSDs collected, which may influence any single percentile values used to represent the distribution. I minimised the effect of this by considering the GSDs as GSD integrals as opposed to percentiles. I also manually measured the number and b-axis of grains >1 m in diameter between 5000 m and 6750 m downstream in Luoquan using drone images taken in November 2019 (Figures 5.2 and 5.3).

Photos were only at a high enough resolution and quality to conduct the analysis over this section of the channel. I normalised the number of boulders (>1 m) counted in each drone image by the length of channel in that image to ensure that the length of the channel in each image did not affect the results.

GSD integral

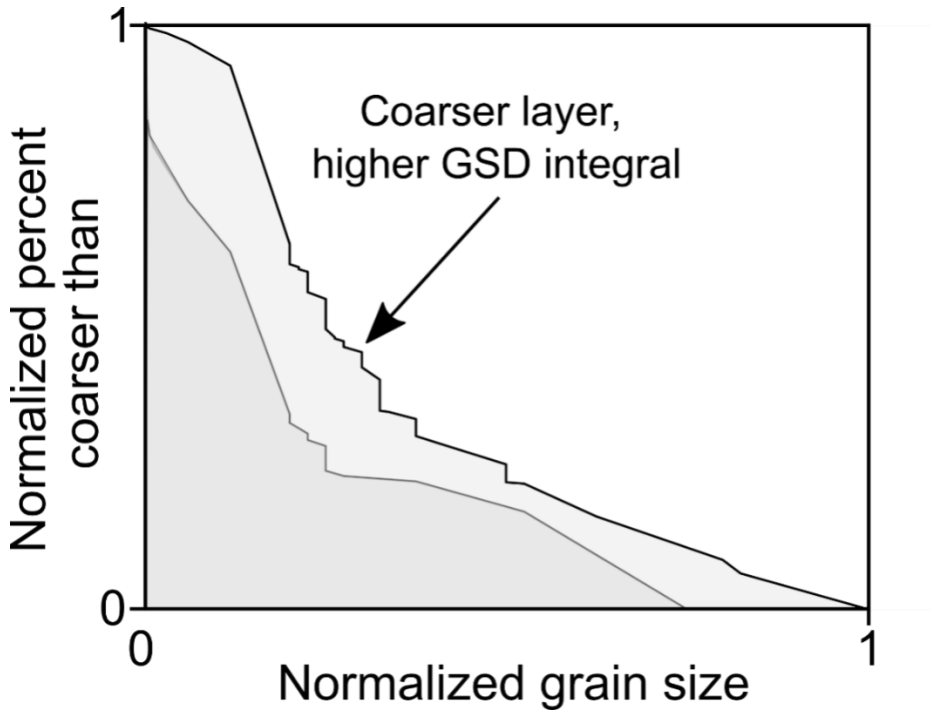

Figure 5.4

An example of the curves used to calculate the GSD integral. This figure uses the surface and deepest (40 – 50 cm) layers from 7500 m downstream of the Luoquan deposit as reference curves. All grain sizes were normalised by the maximum grain size measured for each method, therefore not all GSD curves extended to 1, as shown by the dark grey curve.

I quantified the shape of the GSDs by integrating underneath the normalised percent coarser than curve, similar to the hypsometric integral used to determine asymmetry in topography (Brocklehurst and Whipple, 2004; Strahler, 1952). I normalised grain size by the maximum grain size obtained using each method. As such, the integrals could not be compared across methods. A larger GSD integral is caused by a larger proportion by weight, and thus curve area, in the upper end of the distribution (Figure 5.4). The use of a GSD integral to determine the coarseness of the distributions was supported by the strong correlations between D_{50} and D_{84} with the GSD integral (Figure 5.5). The positive relationships, which were found for all percentiles above D_{50}, suggest that the GSD integral provides a single metric which can be

deemed appropriate to represent at least the coarsest 50% of the GSDs measured.

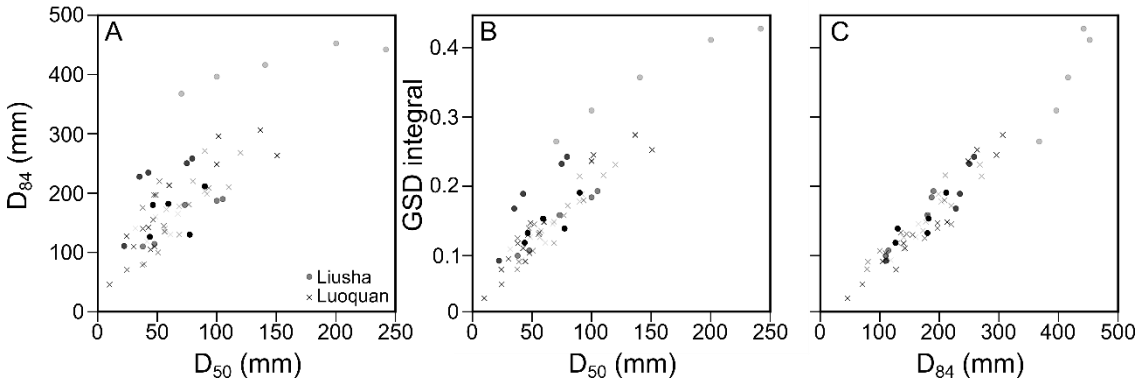

Figure 5.5

Relationship between D_{50}, D_{84} and the GSD integral for the GSDs generated from sieving individual pit layers in Liusha (circles) and Luoquan (crosses). This demonstrates how the GSD integral is effective in constraining the coarseness of each GSD.

5.4.2 Topography

I measured channel cross sections at each pit location using a laser range finder. Longitudinal channel bed topography was collected using the JAXA 30 m resolution digital elevation model (DEM). I calculated the slope and curvature between sampling locations for an elevation profile along the centreline of each debris flow deposit using the DEM. To account for the low resolution of the DEM, I smoothed the profile using locally weighted scatterplot smoothing (LOWESS) and a span of 0.3 (Cleveland, 1979).

5.5 Results

The GSDs in Liusha and Luoquan ranged over four orders of magnitude, from clay to boulders (Figures 5.6 and 5.7). The maximum sieved grain sizes were similar in both debris flows; 57 cm in Liusha and 42 cm in Luoquan. In Luoquan, I also measured grains with b-axes up to 400 cm using drone images. The proportions of sand and fine gravel (0.01 to 0.4 cm) by weight recorded in each pit were consistent across the two deposits (Figure 5.8). However, the Liusha deposit had a clay and silt content at least double the relative content by weight in Luoquan.

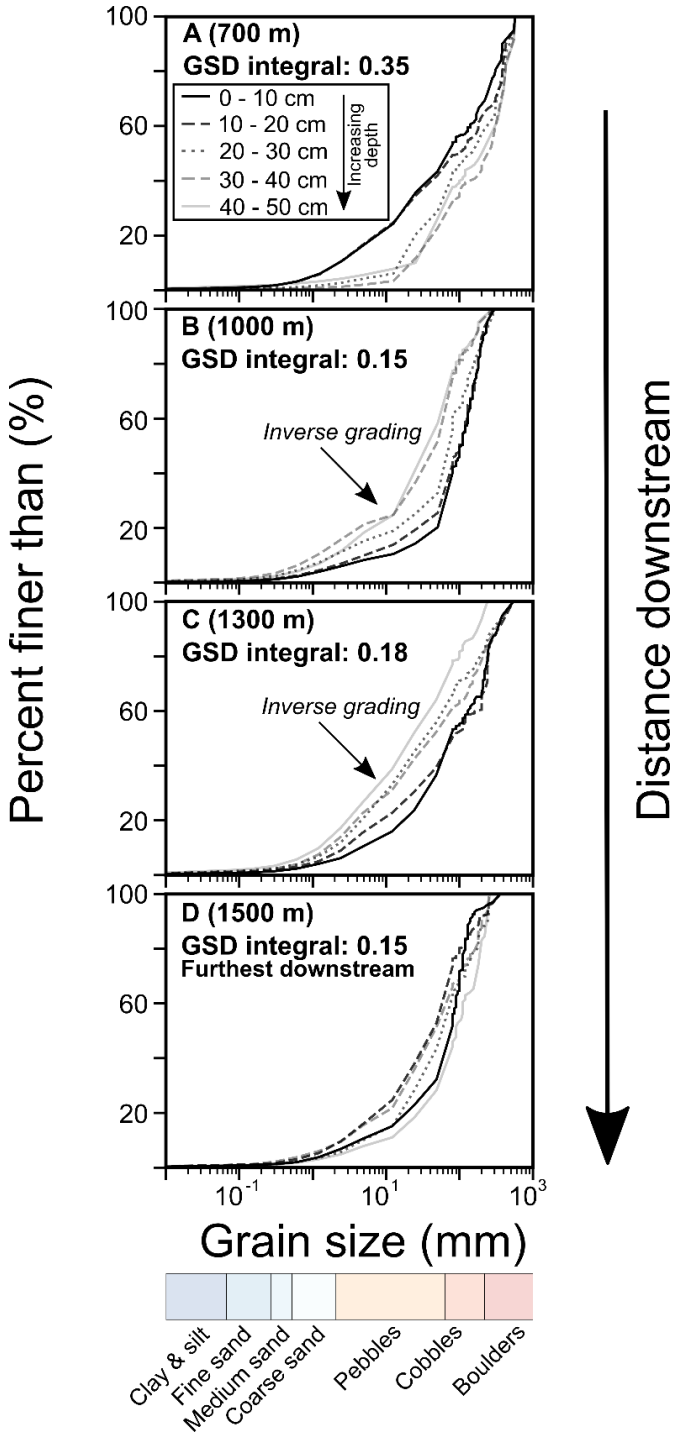

Figure 5.6

GSDs collected from pits dug along the centreline of the Liusha debris flow, with increasing distance downstream from top to bottom. The different pit layers (10 cm increments) are shown by the colour and style of the line. A bar can be found at the bottom of the figure showing the type of grain that corresponds to each size fraction. A) Pit 1, furthest upstream, located 700 m from the source. B) Pit 2 located 1000 m from the source, 300 m downstream of Pit 1. C) Pit 3 located 1300 m downstream of the source, 300 m from Pit 2. D) Pit 4 located the furthest downstream, approximately 30 m upstream from the road and 1500 m from the source. The GSD integral shown is the average of the individual GSD integrals calculated for each of the five layers.

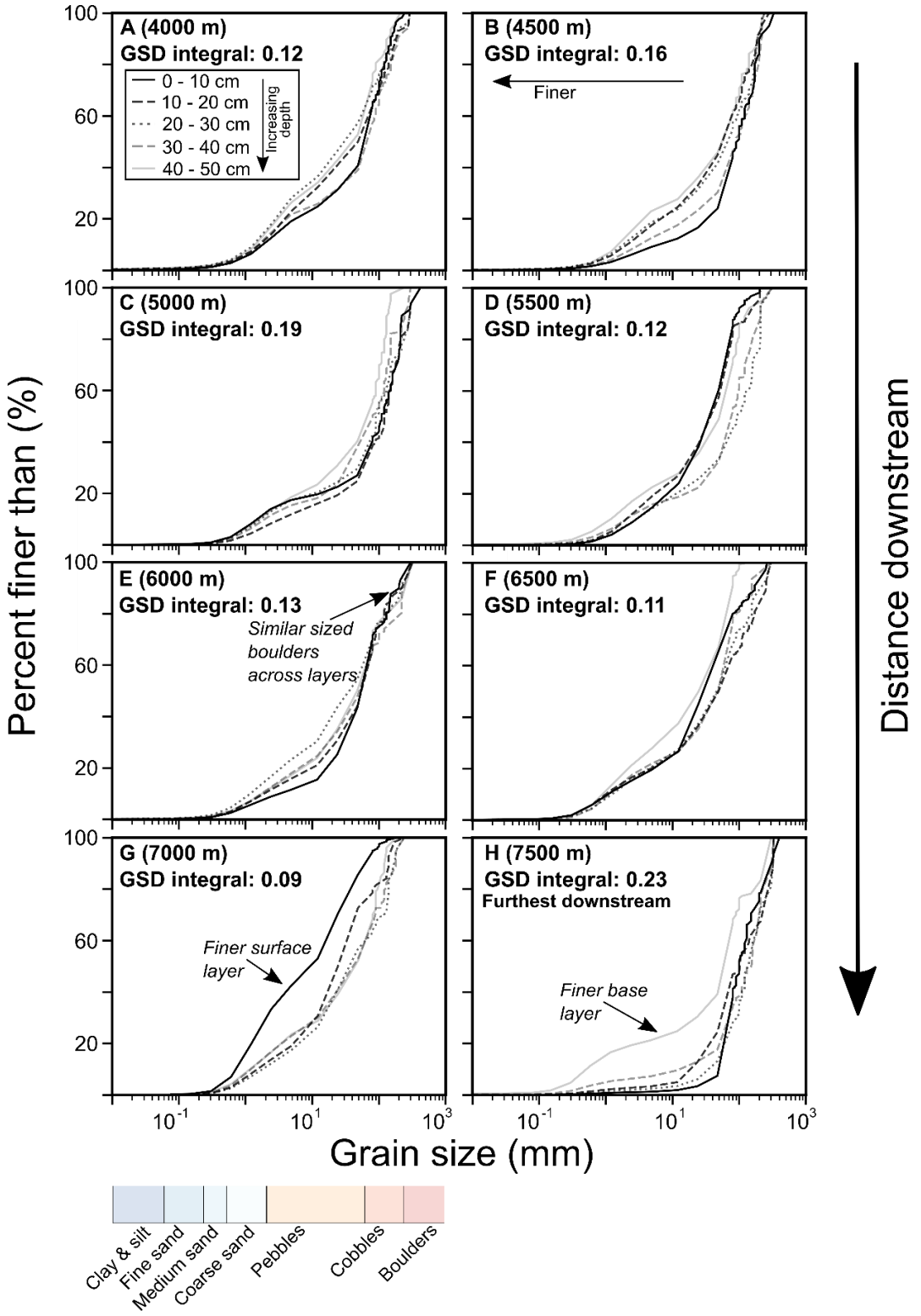

Figure 5.7

GSDs collected from pits dug along the centreline of the Luoquan debris flow, with increasing distance downstream from 7A to 7H. The distance from the estimated source location is given in brackets after each figure ID. The GSDs collected from the different pit layers are represented by the colour and style of the line. A bar can be found at the bottom of the figure showing the type of grain that corresponds to each size fraction. The GSD integral shown is the average of the individual GSD integrals calculated for each of the five layers.

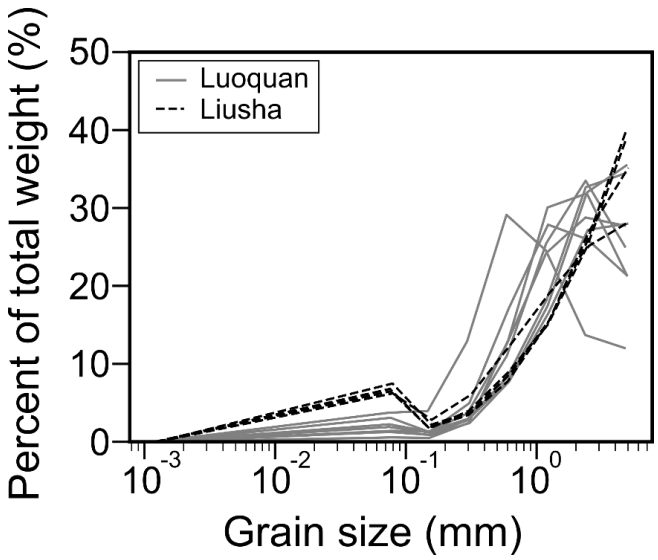

Figure 5.8

Proportion of grains by weight for each sieving size fraction relative to the total proportion of grains <4 mm by weight for the Luoquan (solid grey line) and Liusha (dotted black line) debris flows.

5.5.1 Geomorphic background

The Liusha debris flow occurred within a second-order channel (Figure 3.11). The Liusha catchment was characterised by a steep bedrock channel until ~700 m downstream of the triggering location, where the channel was covered by debris flow deposited sediment (Figure 3.8). The deposit was sampled on a range of slopes between 17° and 29° (Figure 5.2). Channel slope decreased with increasing distance from the source location. Channel width increased alongside this decrease in slope from 4 m (Pit 1) to 15.8 m (Pit 4). The channel had a negative curvature, however, increases in curvature were recorded at Pits 2 and 3, which were 1000 m and 1300 m from the triggering location respectively (Figure 5.2).

The Luoquan debris flow was triggered in a larger, shallower, fourth order catchment (Figures 3.8 and 3.9). At least, the lower 5500 m of the 8000 m debris flow channel was inundated with sediment (Figure 3.8). Generally, channel slope decreased with distance downstream from the triggering location from 9.6° (Pit 1) to 5.5° (Pit 7) (Figure 5.2). Channel width and curvature were more variable and did not appear to relate to the distance from the source location. The widest section of the channel sampled was found 5500 m downstream from the triggering locations (61.2 m, Pit 4) and the average channel width based on the eight sampling locations was 42 m

(Figure 5.2). All sampling locations apart from Pit 8 had a negative value for curvature.

5.5.2 Vertical GSDs

Vertical segregation by normal and inverse grading was evident in 75% of the pits sampled along the Liusha debris flow (Figures 5.6 and 5.9). The GSDs deposited were normally graded in the first sampling location, 700 m downstream from the triggering location (Figure 5.6A and 5.9A). The deposit was then inversely graded in the two middle pits, which were located 1000 m and 1300 m downstream from the triggering location (Pits 2 and 3) (Figures 5.6B, 5.6C, 5.9B and 5.9C). The pit located furthest downstream (Pit 4) displayed no evidence of normal or inverse grading (Figure 5.6D and 5.9D).

Normal and inverse grading can be observed using the GSDs for each layer as well as their GSD integrals (Figure 5.6 and 5.9). Pit 1 was normally graded due to the higher proportion of coarse pebbles, cobbles, and boulders in the lowest 30 cm of the pit. For example, grains >10 cm in size accounted for approximately 20% more by weight in the lowest 20 cm of the pit relative to the surface (Figure 5.6A). In contrast the upper 20 cm of the deposit was enriched in fine gravels and pebbles. In Pit 2, the inversely graded pit located 1000 m from the triggering location, grains >10 cm accounted for 40% less by weight in the lowest layer (50 cm deep) relative to the surface layer (Figure 5.6B). Pit 3, 300 m downstream from the Pit 2, was also inversely graded as shown by the decreasing GSD integral with depth (Figure 5.9C). The absence of grading in Pit 4, located the furthest downstream, is demonstrated by the fact that both the surface and deepest layer (40 cm – 50 cm) were the coarsest part of the deposit. The finest section of the deposit was found between 10 cm and 20 cm (Figure 5.6D). The lack of grading can be supported by the variation in the GSD integral with depth in Figure 5.9D

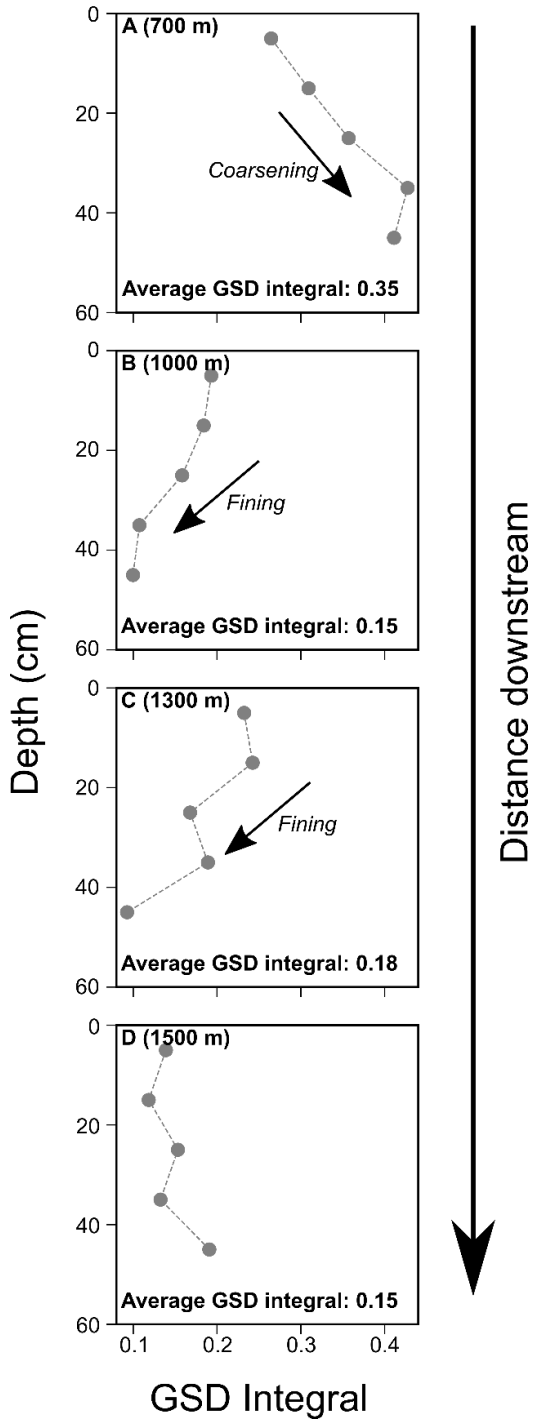

Figure 5.9

The change in GSD integral with depth for the Liusha debris flow. Average GSD integral is the average integral based on the GSD integrals calculated for each layer in the pit.

There was no evidence for size segregation in the Luoquan debris flow (Figure 5.7). The variation in GSD integrals with depth in Figure 5.8 supports the lack of systematic deposition by size within the deposit. The GSDs deposited by the debris flow remained consistent in the pits located furthest upstream (4000 m

to 6500 m downstream from the triggering location), with the proportion of sand, gravel and finer grains varying by up to 10% between layers (Figure 5.8 and 5.10). Across this 2500 m section of the deposit, the layer with the coarsest and finest GSD differed in each location. In sections of the deposit where a large grain covered all five layers, the GSD integrals varied the least (e.g., Figures 5.10A, 5.10B and 5.10E). The largest variation in the GSDs deposited vertically was found in the two pits located furthest downstream (7000 m and 7500 m from the triggering location). At 7000 m downstream (Pit 7), the surface layer was enriched in finer grains (coarse sand and fine pebbles) relative to the lower layers. This enrichment can be identified by the steep increase in percent coarseness between 0.6 mm and 10 mm (Figure 5.7G). A further 500 m downstream (Pit 8, 7500 m from the triggering location, 500 m from the toe of the deposit), the opposite was found, with the base layer much finer (enriched in sand) than the layers deposited above (Figure 5.7H).

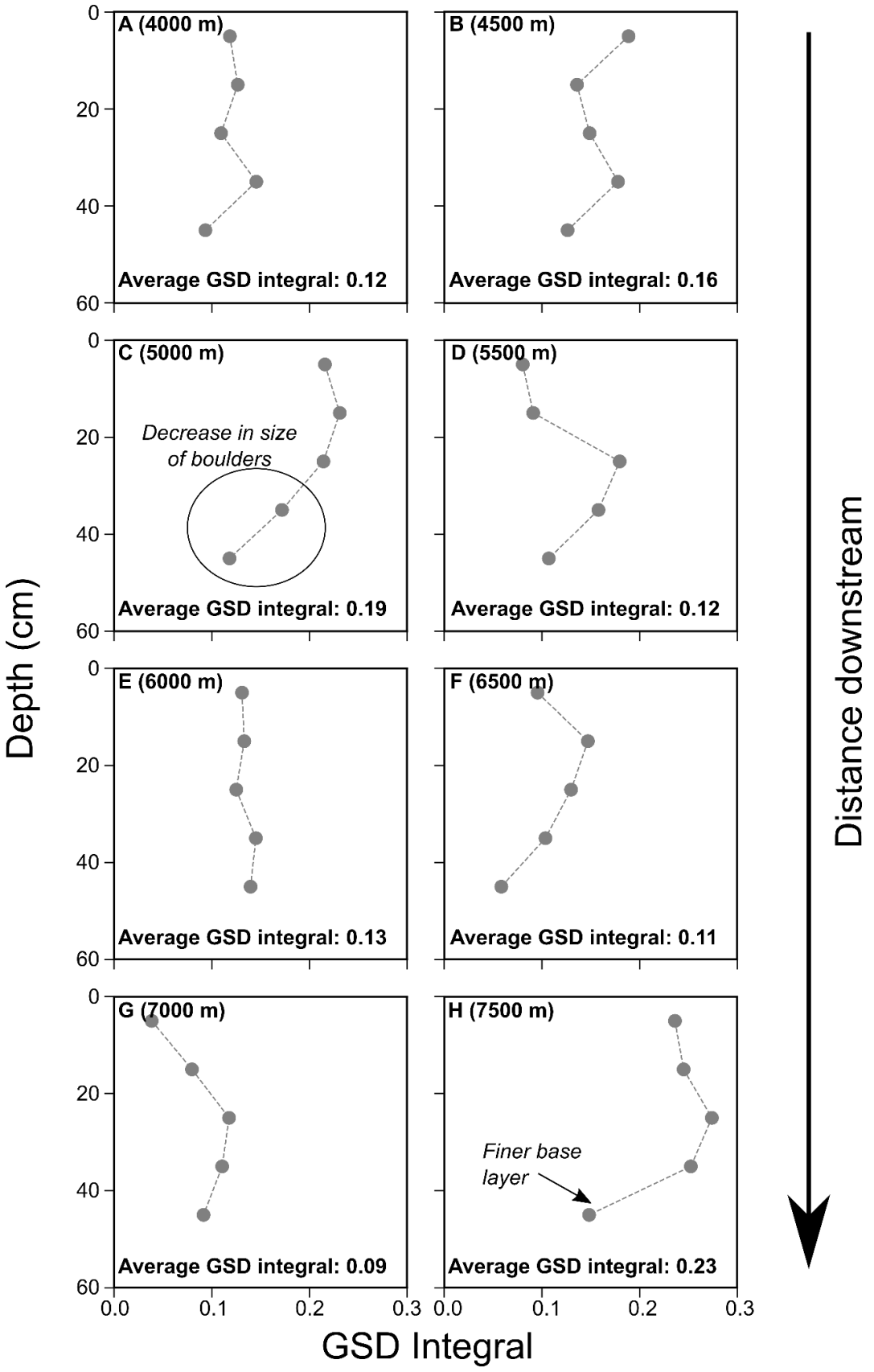

Figure 5.10

The change in GSD integral with depth for the Luoquan debris flow. Average GSD integral is the average integral based on the GSD integrals calculated for each layer in the pit.

5.5.3 Lateral (surface) GSDs

In both deposits peaks in surface coarseness occur both at the edges and in the centre of the deposit. From the 12 cross sections sampled, no section had coarser GSD integrals on both edges of the deposit, suggesting paired levees were not a feature of either debris flow (Figures 5.11 and 5.12). However, in the middle section of the Liusha debris flow deposit (1000 m to 1300 m downstream from the triggering location), the highest GSD integrals were found on one edge of the deposit. The side of the deposit with coarser grains also changed from the left side at 1000 m to the right side at 1200 m downstream (Figures 5.11C and 5.11E). These locations, particularly Pit 2, correspond with a slight bend in the debris flow channel (Figure 5.2). The coarser GSDs appear to have been deposited on the inside bend of the channel (Figure 5.11). The pits which correspond to these locations, in the middle of the Liusha debris flow deposit, were also inversely graded (Figure 5.6). The location of the higher GSD integral did not appear to relate to a change in the bed cross section profile, which only varied by 1 m at most in this section of the channel (Figures 5.11D and 5.11F). Further upstream (Pit 1), the surface GSD integral varied across the width of the channel, with finer surface GSDs dispersed in between a coarse deposit, with GSD integrals up to 0.19 (Figure 5.11A). These sharp transitions in grain size may be attributed to the fact this section of the deposit is located directly downstream of a predominantly bedrock channel. This section was also more deeply channelised than other sections of the deposit, however the channel was too narrow to accurately measure any change in deposit morphology (Figures 5.2 and 5.11B). At the furthest point downstream, where I found no evidence of vertical segregation, there is also no clear evidence of lateral segregation. Coarse surface GSDs can be found in both the centre and on the right side of the deposit (Figure 5.11G).

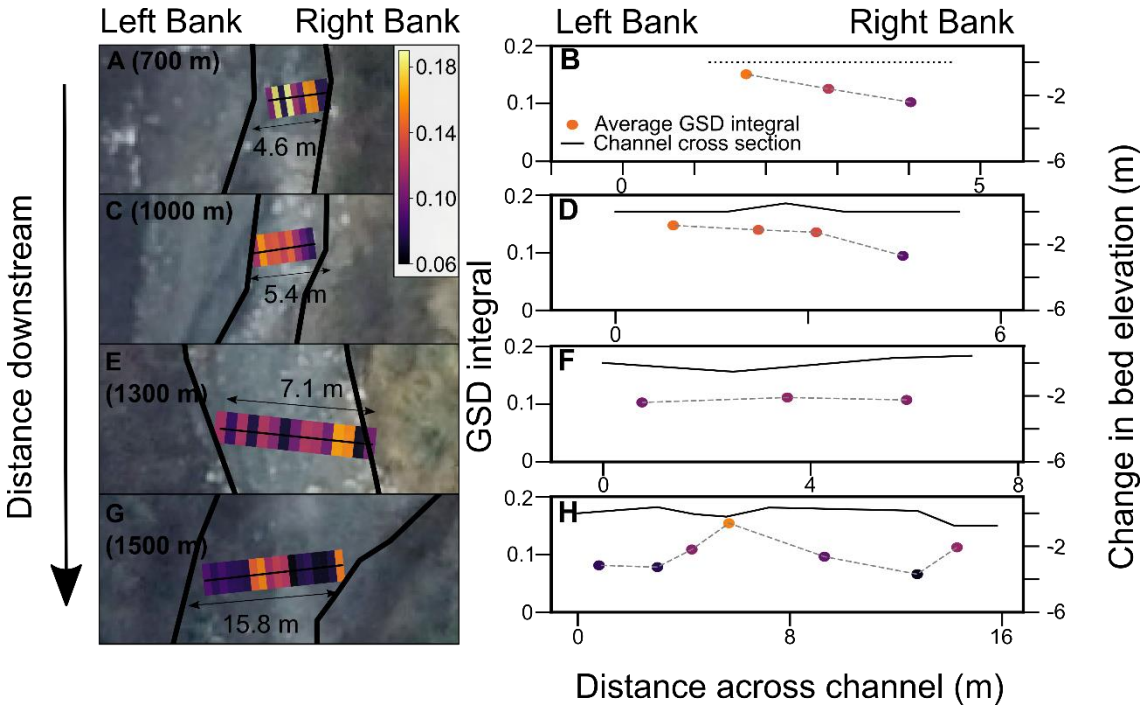

Figure 5.11

Lateral changes in the surface GSD deposited. The GSDs are based on surface photos and pyDGS or manual photo counts for the Liusha debris flow. The GSD is represented by a GSD integral calculated using a D_{max} of 399 mm. The GSD integral ranged from 0.06 to 0.19. A, C, E and G) show changes in GSD integral across the channel width. Each coloured segment (integral) represents a photo taken of the deposit surface. The left and right banks of the deposit when facing downstream are indicated. The black line shows the extent of the 2019 deposit. B, D, F and H) show the cross-sectional area, measured using a laser range finder, and the average GSD integral for each geomorphic section. Each plot corresponds to the same location along the channel as shown by the photo and bar on the left. The average GSD integral is calculated by averaging the GSD integrals for each section where there is a change in slope across the width of the channel. The distance of the pit downstream is shown in brackets next to the figure ID.

In Luoquan, the distribution of surface coarseness laterally across the deposit was also not clearly linked to downstream location, lateral position in the flow and channel cross section morphology (Figure 5.12). In fact, channel width appeared to be the main control on deposit coarseness (Figure 5.12). For example, as channel width increased between Pits 1 and 3 (4000 m to 5000 m downstream of the triggering location), there was also an increase in the relative coarseness of the deposit surface, with higher GSD integrals 5000 m downstream where channel width increased to 43.5 m (Figure 5.12E). A further 500 m downstream (Pit 4), the channel width increased by almost 20 m to reach its widest point (Figure 5.12G). At this location, 5500 m downstream from the triggering location, the GSD integrals for the surface of

the deposit decreased. Channel slope decreased more sharply at the location as well (Figure 5.2). The largest range of GSD integrals, and therefore variations in the surface grain size of the deposit, were found in Pits 3 (5000 m downstream) and 4 (5500 m downstream), alongside this large change in channel width (Figures 5.2 and 5.12). An increase in the GSD integrals with increasing channel width was also observed in the lower section of the flow, such as between Pit 6 and Pit 7 as well as Pit 7 and Pit 8. No relationships were observed between the morphology of the cross section and the associated average GSD integral. The changes in channel morphology and width were much larger in the Luoquan deposit, with changes in bed elevation of up to 6 m across the width of the channel in the upper sections of the deposit (Figures 5.12D and 5.12H).

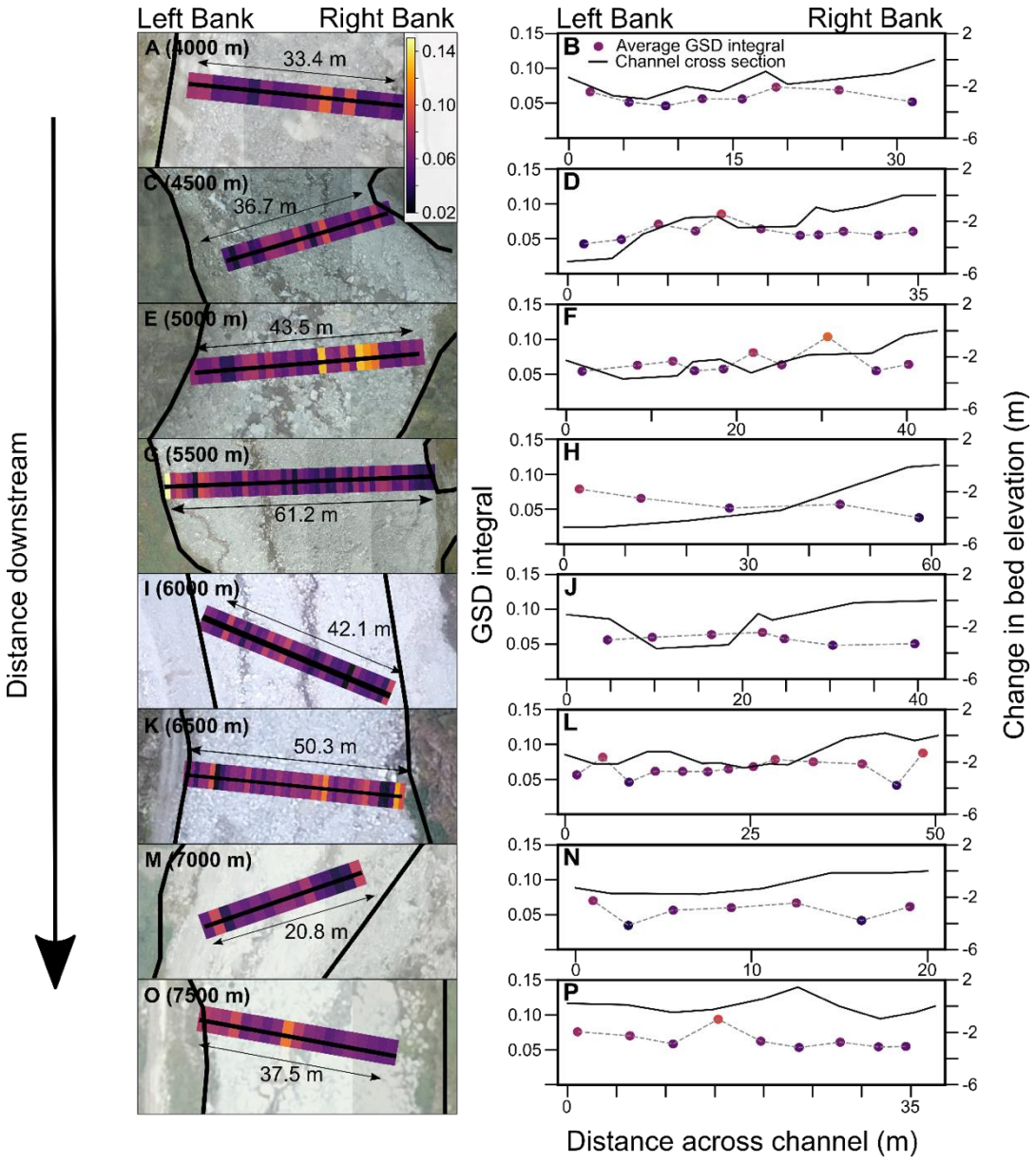

Figure 5.12

Lateral changes in the surface GSD deposited. The GSDs are based on surface photos and pyDGS or manual photo counts for the Luoquan debris flow. The GSD is represented by a GSD integral calculated using a D_{max} of 801 mm. The GSD integral ranged from 0.02 to 0.15. A, C, E, G, I, K, M and O) show changes in GSD integral across the channel width. Each coloured segment (integral) represents a photo taken of the deposit surface. The left and right banks of the deposit when facing downstream are indicated. The black line shows the extent of the 2019 deposit. B, D, F, H, J, L, N and P) show the cross-sectional area, measured using a laser range finder, and the average GSD integral for each geomorphic section. Each plot corresponds to the same location along the channel as shown by the photo and bar on the left. The average GSD integral is calculated by averaging the GSD integrals for each section where there is a change in slope across the width of the channel. The distance of the pit downstream is shown in brackets next to the figure ID.

5.5.4 Longitudinal (surface and subsurface) GSDs

In Liusha, there was a general increase in the D_{50}/D_{84} ratio and a decrease in the GSD integral with distance downstream for subsurface GSDs (average subsurface GSDs are calculated using the full pit GSD by weight, average pit GSD integrals are calculated by averaging the five layer GSD integrals) and surface GSDs (from individual photo GSDs) (Figures 5.3, 5.13 and 5.14A). These observations can be explained by a decrease in the D_{84} value with distance downstream. The decrease in D_{84} and the GSD integral is sharp between Pit 1 and 2 (700 m to 1000 m downstream of the triggering location). The average D_{84} value per pit decreased from 41 cm to 16 cm and the GSD integral decreased from 0.35 to 0.15 (Figure 5.6). The decrease observed in surface and subsurface GSDs between the furthest upstream pit and the remaining three pits may relate to the high proportion by weight of sand and pebbles in the lower three pits (Figure 5.14). The remaining sections of the deposit (Pit 2 to 4) had relatively consistent D_{84} values and GSD integrals (Figure 5.6). There was a small increase in the GSD integral between 1000 m and 1300 m downstream. This increase corresponded with a slight increase in the proportion of silt and clay deposited and a doubling of the proportion by weight of pebbles deposited (Figure 5.14B).

The Increase in sand and pebble content with distance downstream is consistent with the decrease in slope (from 29° to 17°) and elevation (Figure 5.14A). Channel width only increases gradually until 1300 m downstream of the triggering location, where there is a doubling in the channel width over a

200 m distance from 7.1 m to 15.8 m. In the section of the deposit following this sharp change in width, I observed an increase in the proportion of cobbles deposited by weight and a relative decrease in grains finer than cobbles (Figure 5.14B). This part of the deposit makes up the section immediately before the road, after which the debris flow continued for only a further 100 m and ceased upon meeting the Yuzi River, as shown in the satellite image in Figure 3.11.

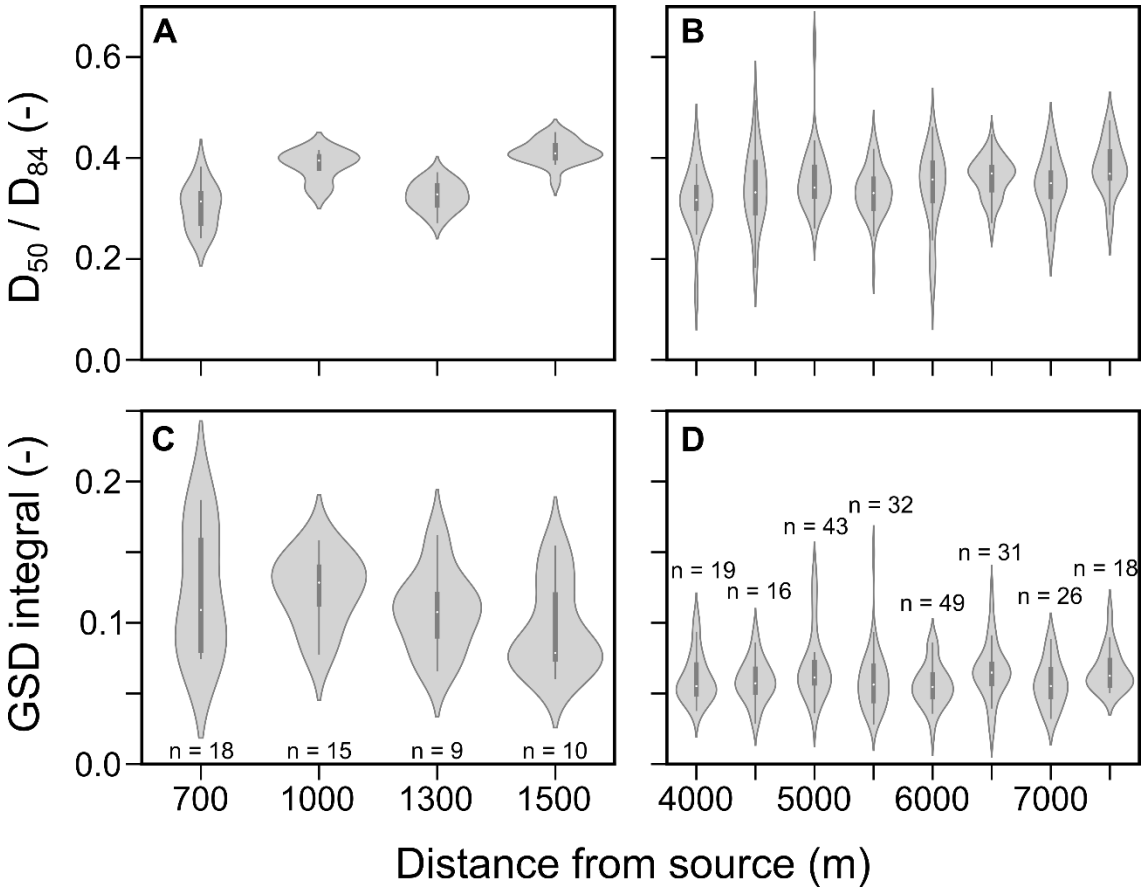

Figure 5.13

Violin plots showing the D_{50}/D_{84} ratio and GSD integral for different locations along the Liusha and Luoquan debris flow. The data shown is based on surface photo GSDs. The number of surface photos used to produce each violin plot is shown in Figures 5.13C and 5.13D. A and B) show the D_{50}/D_{84} ratio for GSDs generated from photos taken along a cross section of the Liusha and Luoquan debris flow respectively. C and D) compare the GSD integrals for the surface photos taken along the Liusha and Luoquan debris flow. It is important to note the D_{max} by which the GSD integral was calculated from is 399 mm in Liusha and 801 mm in Luoquan based on the maximum grain found in the photos.

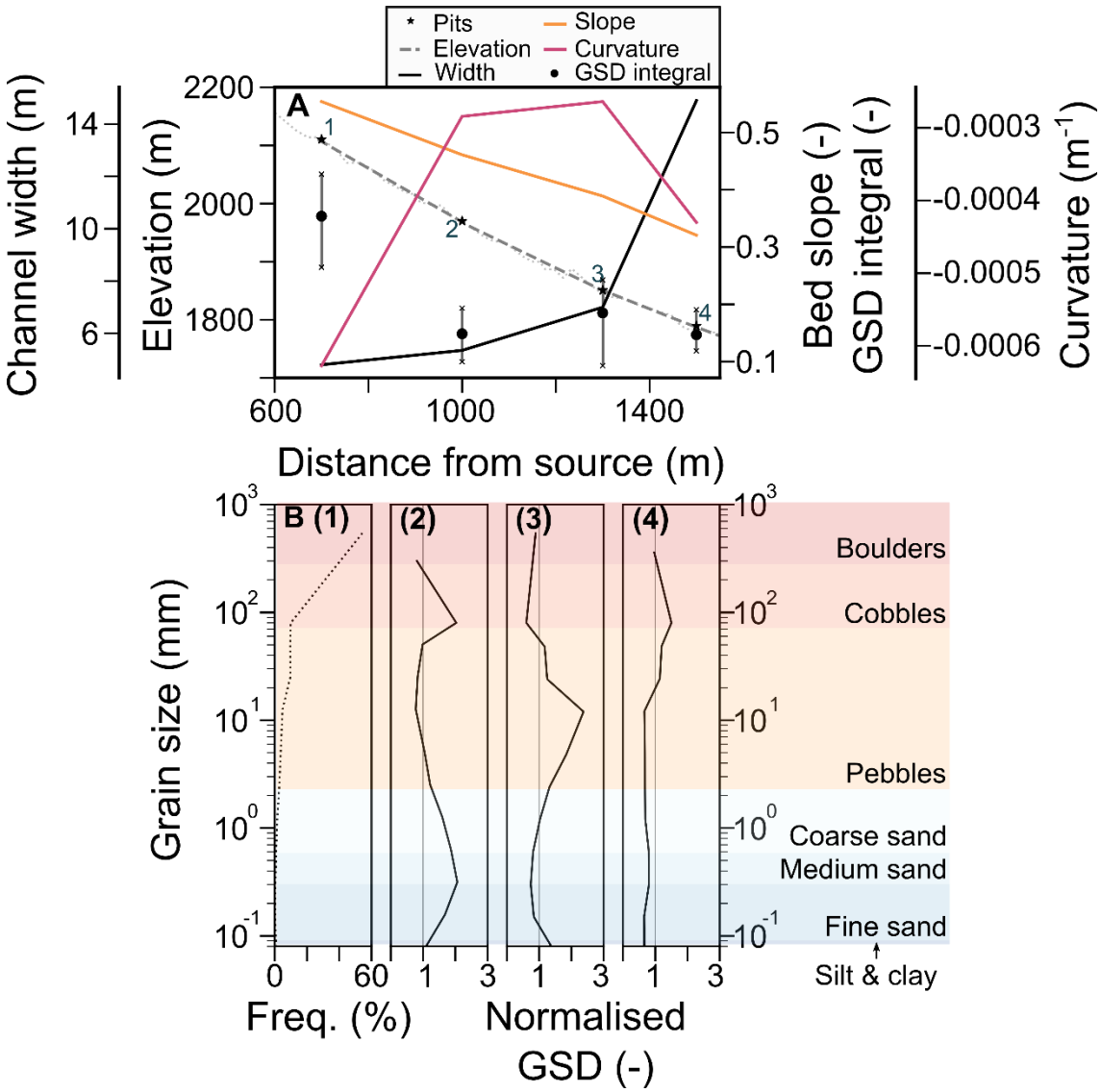

Figure 5.14

Change in surface and subsurface GSD with distance downstream for the Liusha debris flow based on sieved pits (Figure 5.3). A) shows the elevation, slope, curvature and channel width at each location as well as the GSD integral calculated by averaging across each sieved pit, as shown in Figure 5.6. The grey error bars show the maximum and minimum GSD integral for each pit. B) The GSD shown for Pit 1 is the original sieved GSD for the full 50 cm profile as a probability density function. The following three pits then show normalised GSDs based on the GSD immediately upstream. A value >1 suggests there has been an increase in that grain-size fraction being deposited and a value <1 suggests there has been a decrease in that size fraction.

Longitudinal GSDs for the Luoquan deposit suggest that channel topography can control the size of grains deposited in catastrophic debris flows in Wenchuan (Figure 5.15). For example, changes in curvature in the first five pits (Pits 1 to 5) corresponded to an increase or decrease in the proportion of fine sand, silt and clay deposited (Figure 5.15). An increase in slope curvature

between Pits 1 and 2 as well as Pits 2 and 3 (Pit 1: -3 x 10^{-5} m^{-1} to Pit 3: -1 x 10^{-5} m^{-1}) corresponded to a decrease in the proportions of fine sand, silt, and clay (Figures 5.15A and 5.15C). From Pit 3 to Pit 5 (between 5000 m and 6000 m downstream of triggering location), there is a decrease in slope curvature (from -1 x 10^{-5} m^{-1} to -4 x 10^{-5} m^{-1}) and an increase in the proportion of fine sand, silt and clay deposited (Figure 5.15C). These observations suggest that in the middle of the deposit, an increase in the proportion of fine sediment deposited by the debris flow may relate to a decrease in slope curvature. The three pits located furthest downstream (Pits 6 to 8, between 6500 m and 7500 m downstream) did not fit the relationship between slope curvature and the proportion of fine grains observed for the five pits immediately upstream (Figure 5.15C). Instead Pits 6 and 7 corresponded with the relationship observed from Pits 2 to 4 in Liusha, where a decrease in slope corresponded to an increase in the proportion of sand and pebbles (Figures 5.2, 5.14 and 5.15). Pit 8, located the furthest downstream (7500 m from the triggering location), differed from all upstream pits. This GSD was devoid of sand and pebbles but enriched in fine sand and had almost two times the proportion of cobbles and boulders by weight relative to the previous 500 m (Figure 5.15C). The increase in cobbles and boulders is reflected by the sharp increase in the GSD integral between Pit 7 and Pit 8 (Figure 5.15C).

Changes in the width of the debris flow deposit with distance downstream also appeared to control the size of grains deposited, particularly the size and frequency of boulders (Figure 5.15B). In Section 5.5.2, I observed an increase in deposit coarseness with increasing channel width for most sections of the deposit (Figure 5.12). Interestingly, the widest section of the deposit corresponded to a decrease in the coarseness of the surface GSD (Figure 5.12G). This observation fits with the change in boulder size and frequency with increasing channel width (Figure 5.15B). For example, as channel width increases from 43.5 m to 61.2 m, between 5000 m and 5500 m downstream from the triggering location, the number of boulders (per 10 m of channel length) decreased from 6.9 to 2.6, with a minimum number of boulders, 0.5, recorded 5350 m from the triggering location. The maximum boulder size observed using drone imagery (3.7 m) was also observed following a decrease in channel width between Pits 6 and 7, 6750 m from the triggering location

(Figure 5.15). The complex topographic characteristics of the Luoquan channel and sharp increases and decreases in channel width may explain the absence of a clear relationship between the D_{50}/D_{84} ratio (Figure 5.13). The spatial patterns observed in Luoquan suggest topography may in part control the grain sizes deposited by the Luoquan debris flow.

The shape of the grains >8 cm deposited by the two debris flows varied greatly, with no consistent pattern in both Liusha and Luoquan with distance downstream (Figure 5.16). All average grain shapes were disc-shaped, with a slight shift closer to spherically shaped grains between Pits 2 and Pit 3 in Liusha.

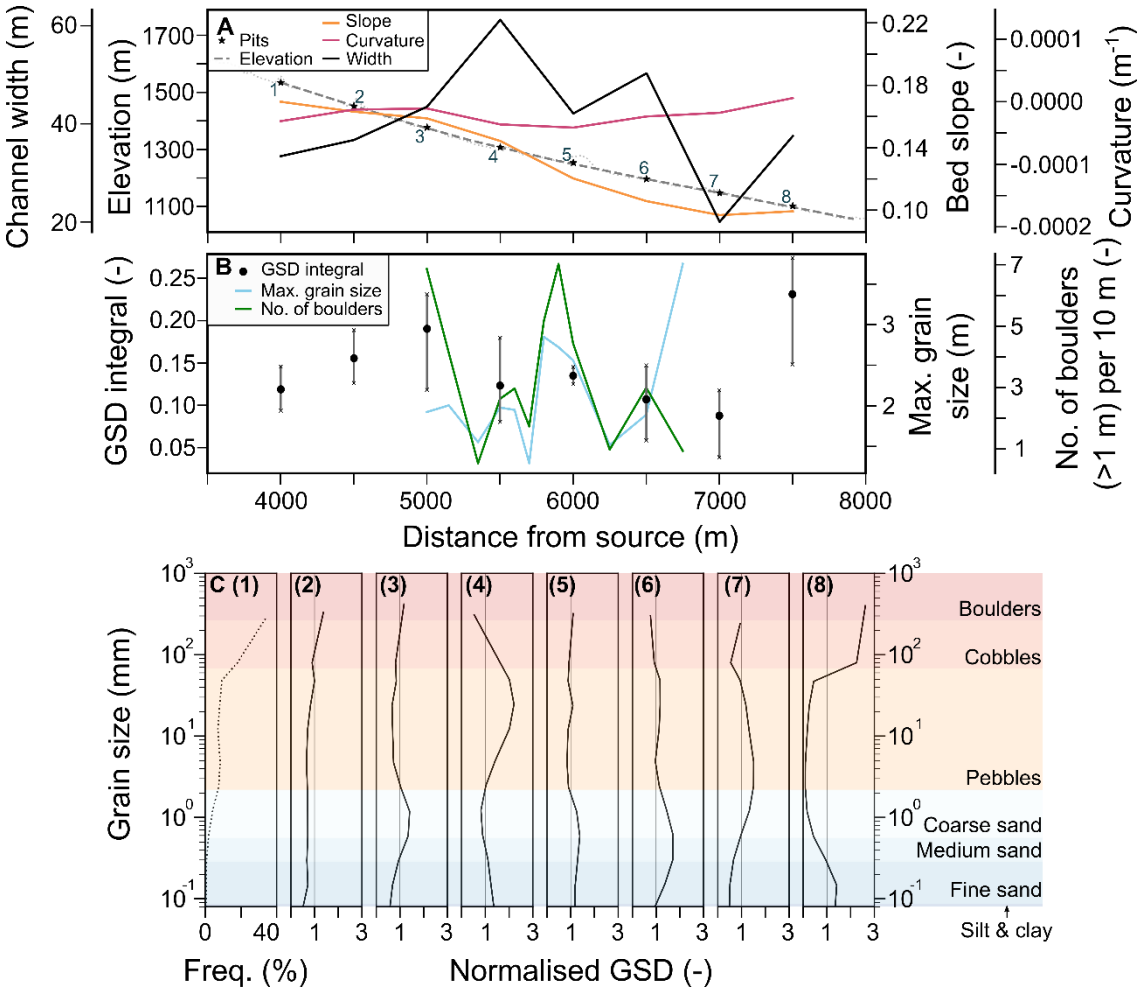

Figure 5.15

Topographic characteristics, drone grain size measurements and normalised GSDs for the Luoquan debris flow. The GSD integrals and GSDs are based on surface and subsurface sieving profiles (Figure 5.3). A) shows the elevation, slope, curvature and channel width at each pit. B) shows the average GSD integral calculated by averaging across each pit (see Figure 5.7) and the error bars with the maximum and minimum GSD integral for each pit as well as the maximum grain size and number of

boulders >1 m measured from drone imagery between 5000 and 6750 m downstream. C) shows the original sieved GSD for Pit 1 (pit furthest upstream) across the full 50 cm profile as a probability density function, followed by normalised GSDs for Pits 2, 3, 4, 5, 6, 7 and 8 respectively. The normalised GSD is calculated by dividing the GSD of each pit by the GSD of the previous pit.

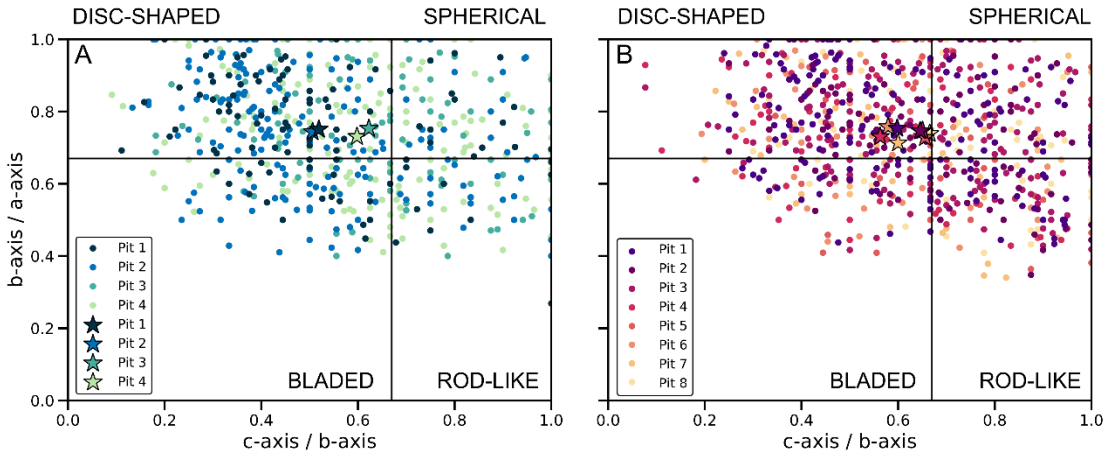

Figure 5.16

Shape of grains deposited in A) Liusha and B) Luoquan. Shapes are inferred using the b-axis/a-axis ratio and c-axis/b-axis ratio. The average of each ratio at each pit location is represent by a star, individual grains are shown by circles.

5.6 Discussion

The GSDs measured in Liusha and Luoquan had similar ranges and maximum grain sizes but differed through their spatial pattern of deposition across all three dimensions. Both debris flows consisted of grains from clay to boulders, with very similar relative proportions by weight of grains <4 mm (Figure 5.8), cobbles and boulders (Figures 5.6 and 5.7). The smaller Liusha deposit generated both normal and inverse grading (Figures 5.6 and 5.9), contrasting the lack of segregation by grain size with depth in the Luoquan debris flow deposit (Figures 5.7 and 5.10). Laterally, neither debris flow deposited coarser grains at both edges of the flow (Figures 5.11 and 5.12). Coarsening on one-side of the deposit was observed in the middle section of the flow in Liusha and in some locations in Luoquan. The longitudinal, downstream distribution of grains also differed across the two deposits, with the smaller Liusha deposit fining downstream in terms of D_{84} (Figures 5.6 and 5.13), whilst the most downstream 500 m of the larger Luoquan deposit was enriched in boulders relative to sand and pebbles (Figures 5.13 and 5.15). The relationship between deposited GSDs and distance downstream also related to

changes in channel topography, with wider channels and higher downstream curvature correlating with deposition of finer grain sizes in Luoquan.

The similarities observed in terms of composition suggest that the runout length of these debris flows is not primarily controlled by differences in grain size. The lack of significant difference between the two debris flow GSDs may be related to the similar geology in the triggering locations as well as the fact that they have both been mobilised from co-seismic sediment (Figure 3.7; Yang et al. 2021). Studies of debris flow composition have previously highlighted the importance of clay and gravel content in controlling debris flow runout. For example, increased clay and gravel contents can lead to dominant viscous and frictional forces respectively, which subsequently can control runout length (de Haas et al., 2015). The slightly higher proportion of clay and silt in the Liusha debris flow could suggest that the debris flow was more viscous and therefore had a shorter runout (Figure 5.8). However, both debris flow GSDs were dominated by coarser grains and therefore it is unlikely that a clay and silt content <10% of the fraction <4 mm can explain the differences in runout length. Further support can be found from the Rossiga debris flow in the Central Italian Alps, which had a clay content <15% of the fraction <20 mm and a high proportion of boulders (>50% by weight) (Sosio et al., 2007). Attempts to model the Rossiga debris flow highlighted that the rheological behaviour of a coarse debris flow could not be described simply from the composition of the fine grains in the interstitial fluid. The inverse grading observed in Liusha also highlights that viscous forces were not the only force controlling debris flow runout, as explained in further detail in Section 5.6.1. Overall, the similar GSDs measured for the two post-earthquake debris flows suggest that the mechanisms controlling the different runout lengths are not directly related to the material that is being transported.

The different spatial patterns of grain size found in the two debris flow deposits suggests that other properties which influence the distribution of grains within the flow may be crucial in controlling runout length. For example, changes in topography have been found to control erosion and deposition (Benda and Cundy, 1990; Fannin and Wise, 2001; Guthrie et al., 2010) as well as rate of kinetic sieving and segregation in debris flows (Vallance and Savage, 2000). I will consider how the spatial pattern of grain

size differs between the two debris flows, and how potential controls on these patterns can explain the differences in debris flow runout length.

5.6.1 Vertical GSD tends

No systematic grain size segregation with depth was observed in Luoquan or at the furthest downstream location in Liusha (Figures 5.6 and 5.7). Vertical grain size segregation was limited to the smaller and more constrained of the two debris flows. Where there was inverse grading, in the middle reaches of the Liusha deposit, it was limited to an ~300 m section of channel with slopes between 24.7° and 21°. In the remaining sections of the deposit, processes such as kinetic sieving and squeeze expulsion that govern the development of reverse grading were overprinted by other mechanisms (Figure 5.6). Kinetic sieving is the percolation of smaller grains through gaps separating larger grains and squeeze expulsion is the process by which all grains are levered upwards resulting in a net flux of smaller grains at the base (Gray et al., 2015; Vallance and Savage, 2000). Inverse grading is commonly found in debris flows controlled by dominant frictional forces and active particle collisions, which enable dilation and thus encourage segregation during the flow (de Haas et al., 2015; Kim et al., 1995; Pierson and Costa, 1987; Vallance and Savage, 2000). The importance of dilation in enabling segregation has also been demonstrated in numerical models (Golick and Daniels, 2009; Gray, 2018). Observations from the Rossiga debris flow in the Central Italian Alps suggest frictional and dispersive forces are more pronounced in debris flows with high solid volume fractions (Sosio et al., 2007). Inverse grading in Liusha therefore suggests the flow was dominated by more frictional and collisional forces, potentially due to a higher solid concentration, in comparison to the Luoquan debris flow. This is consistent with field observations that the larger Luoquan debris flow was more fluidised.

In Luoquan the lack of inverse and normal grading within the deposit could be indicative of high viscosity (Vallance and Savage, 2000), incremental deposition which does not preserve segregation (Sohn et al., 1999; Vallance and Scott, 1997), high pore fluid pressures that lubricate clast contacts and therefore reduce particle collisions in the flow (Sohn et al., 1999; Vallance and Savage, 2000) or high turbulence within the flow which prevents mixing and segregation (Shultz, 1984) (Figure 5.7). Previous observations found that

highly fluidised, turbulent debris flows inhibit segregation and particle collisions within a flow (Major, 1997; Major and Voight, 1986). These observations fit with field observations for the catastrophic debris flows witnessed in Luoquan and the surrounding catchments (Guo et al., 2016b; Yang et al., 2021). It should be noted that the deposit was sampled to a depth of 50 cm, which does not include the full deposit cross-section. A full profile is important as the deposit may switch from inverse grading at the base to normal grading at the surface (Major et al., 2007). However, the homogeneity of the top 50 cm is a strong indication that the flow did not segregate by grain size. Inverse grading can also be inhibited by more viscous flows with a high fine content in the interstitial fluid which buffers particle collisions (Thornton et al., 2006; Vallance and Savage, 2000). I found a higher clay content in the Liusha debris flow as opposed to the Luoquan debris flow, suggesting that the clay content is not critical in governing the mobility or dominant forces (i.e., frictional, collision or viscous) of the two debris flows studied here (Figure 5.8). This may be explained because a silt and clay content of ~7% by weight, as found in Liusha, is still lower than found in other natural debris flows (Sosio et al., 2007; Vallance and Scott, 1997; Whipple and Dunne, 1992). Segregation by grain size can also occur due to a decrease in slope as a result of a decrease in flow velocity (Vallance and Savage, 2000). The velocities of both the Liusha and Luoquan debris flows are not known and the geometrical differences between the flows, namely the larger channel length and width, imply that the Luoquan debris flow had a higher velocity irrespective of slope (Figure 5.2). As such, I do not anticipate that slope is the factor most likely to explain the lack of segregation, but the faster velocity anticipated in Luoquan may hold some importance. Modelling studies have also shown that many flow characteristics can influence the rate of segregation within a flow, such as grain size width, grain-size ratio (in bi-disperse mixtures) and runout length, which were not possible to compare here due to the similar GSDs and vastly different runout lengths (e.g. Scott and Bridgwater 1975; Gray and Ancey 2011; Gray 2018). Therefore, the absence of vertical segregation can be attributed to the fewer frictional and collisional forces within the Luoquan debris flow because of the high pore pressures. The presence of high pore

pressures also explain why the Luoquan debris flow entrained enough sediment to transit the fourth order catchment (Iverson et al., 2011).

The upper section of the deposit sampled in Liusha was normally graded with pebbles, cobbles and boulders accounting for at least 80% of the deposit by weight in the lowest three layers (Figure 5.6A). The normal grading may be due to differences in the settling velocity of particles, the immediate deposition of large boulders at the start of the flow (which is followed by a fine tail) or due to the landslide deposit on the channel bank encroaching on the pit (Figures 3.7, 3.8) (Kim et al., 1995; Pierson and Costa, 1987; Shultz, 1984; Vallance and Scott, 1997). The clear difference in the shape of the GSD for the top 20 cm in comparison to the lower 30 cm suggests the normal grading may relate to a change in process or deposition at the front of the debris flow, as opposed to settling. A normally graded deposit upstream of an inversely graded deposit, as found here, was observed by Naylor (1980), who suggested large grains were deposited first to preserve the competency of the flow. However, this relates particularly to clay-rich flows, and therefore is unlikely to apply to these deposits with clay and silt contents <10% and no field evidence of winnowing. I believe the normal grading in the upper section of the deposit is most likely due to a landslide deposit or the immediate deposition of larger grains followed by the deposition of the finer tail later.

5.6.2 Lateral GSD trends

The absence of a coarsening at both edges of the channel or any consistently raised paired ridges indicates that the shouldering of coarse grains by the debris flow front to form levees did not occur (Figures 5.11 and 5.12). Paired levees are most commonly found in unconfined debris flows, such as those on open hillslopes and when debris flows escape lateral confinement (Cannon et al., 2001a; Iverson, 2003; Iverson et al., 2010). Levees in unconfined flows channelise the flow and sustain momentum by stopping the debris flows spreading laterally (Gray et al., 2015; Johnson et al., 2012; Sosio et al., 2007; Turnbull et al., 2015). Liusha and Luoquan were confined by steep hillslopes on both sides, which may explain the absence of levees. Additionally, the absence of levees in Luoquan is consistent with the lack of vertical segregation by grain size (Figure 5.7). When large grains segregate to the surface of the flow due to kinetic sieving and squeeze expulsion, these larger

grains are propelled to the front by higher velocities at the free surface (Johnson et al., 2012; Woodhouse et al., 2012). Once the grains reach the debris flow snout they are overridden, recirculated and advected to the flow edges to form coarse levees (Johnson et al., 2012). I was unable to compare these findings with evidence of downstream segregation due to the fact the snout of both deposits had been disturbed in the three months prior to sampling. Major (1997) also found that levees were less likely to form in saturated flows, consistent with suggestions of high pore fluid pressures in Luoquan.

Despite no evidence for paired levees, unpaired levees (Benda, 1990; Cenderelli and Kite, 1998) were found in sections of both debris flows (Figures 5.11 and 5.12). Coarsening at one edge of the channel may be explained by variations in flow velocity laterally (Johnson and Rodine, 1984). In the middle reaches of the Liusha deposit, the coarsest edges were found on the inner bend of the channel (Figure 5.2). A levee deposit on the inner bend of the Luoquan deposit was observed in the field 6500 m from the triggering location (see Pit 6 in Figures 5.2 and 5.12). These levees on the inner bend of the channel may relate to the anticipated lower flow velocities on the inner bend as a result of centrifugal forces (Prochaska et al., 2008a; Scheidl et al., 2015). Prochaska et al. (2008a) found more deposition on the inside bend for some experimental debris flows. They attributed this to the upstream flow momentum interacting with the channel wall or by sediment reflecting off the outer bend onto the inner bend in non-uniform bends, which could be possible for these debris flows. The second possible explanation for coarser edges is unpaired levees, which poses interesting questions for how these levees form and why they can only be found in certain regions of the deposit (Benda, 1990; Cenderelli and Kite, 1998).

5.6.3 Longitudinal GSD trends

The GSD deposited in both Liusha and Luoquan varied with downstream topography, suggesting an element of topographic control on debris flow runout (Figures 5.14 and 5.15). In Luoquan, I found that the proportion of fines deposited may relate to changes in curvature with distance downstream (Figure 5.15). The importance of slope in controlling flow velocity and the deposition of debris flows is widely acknowledged (Cannon and Savage, 1988;

Guthrie et al., 2010; Lanzoni et al., 2017; Takahashi, 1981; Theule et al., 2015). As such, the increased deposition of fines in sections of the deposit with negative curvature or steeper decreases in slope may be related to a decrease in flow velocity and more rapid debris flow deposition once the debris flow stops, so more fine sediment is deposited. If more fine sediment is deposited from the flow, there would be a feedback effect, whereby the excess pore pressures in the flow may dissipate more readily encouraging further deposition in this part of the flow. Though, it is likely that the explanation for the enhanced fine content in deposits is more complex in this extremely large flow.

The importance of channel width with distance downstream is also prevalent in GSDs in Luoquan, especially with the decreased deposition of boulders with increased channel width (Figures 5.15A and 5.15B). The same can be observed with increasing boulder frequency and size where the channel has narrowed (Figures 5.2 and 5.15B). At the widest reach sampled, we also found an increase in pebble content and a decrease in boulders relative to the reach immediately upstream, where the flow narrowed (Figure 5.15). The increase in pebble content and decrease in boulders imply that the velocity and competency of the flow changed. The lateral spreading associated with an increase in channel width may have encouraged deposition by decreasing the downstream flow momentum, as reflected by the fact that unconfined debris flows typically deposit on higher slope angles (Benda and Cundy, 1990; Fannin and Wise, 2001; Guthrie et al., 2010; Hungr et al., 1984). Alternatively, as from field observations we know that the Luoquan debris flow was already travelling at speed, the increase in channel width may have increased the velocity and momentum of the debris flow. An increase in flow momentum may enable the transportation of coarser grains, as observed in 5th to 7th order streams following the catastrophic Montecito debris flow where despite channel widening, the flow entrained boulders (Morell et al., 2021). The GSDs sampled from the most downstream 1500 m in Luoquan displayed different trends to those observed upstream, with an increase in sand, pebbles, and cobbles relative to the pit directly upstream (Figure 5.15). There was also a high proportion of boulders in the most downstream pit (8) relative to all other upstream locations (Figures 5.13 and 5.15). The increased deposition of

boulders may relate to the shouldering of coarse grains associated with the front of debris flow deposits or be a result of the winnowing of fine sediment. Winnowing may be more likely to occur in the section of the deposit furthest downstream due to the pit being disturbed by construction related activities (Blair and McPherson, 1998). Explicit knowledge of where boulders are deposited within these catastrophic debris flows will provide further insight into segregation mechanisms in the flow and contribute to developing runout hazard models, because the impact of fast flowing boulders can be significant from a hazards and infrastructural perspective (Zhang et al., 2021b, 2021a). As such, future work should seek to acquire high-resolution images for immediately after the 2019 and other events.

In Liusha, the D_{84} and GSD integral decreased with distance downstream, which could relate to debulking (Makris et al., 2020), the recirculation of the coarsest grains (Johnson et al., 2012) or abrasion within the debris flow (Vallance and Scott, 1997) (Figures 5.13 and 5.14). Debulking is the deposition of coarse grains as the flow velocity decreases and the flow loses the ability to transport the coarsest grains (Makris et al., 2020). Decreases in slope and increases in width downstream may mean this effect dominates in the smaller Liusha debris flow. The potentially lower water content and shorter runout distance suggest that this effect is more likely in Liusha in comparison to the Luoquan debris flow. Alternatively, the recirculation and advection of coarse grains to levees once overtopped by the debris flow snout observed in flume experiments can also lead to the progressive loss of coarse grains in the distal sections of the flow (Johnson et al., 2012). However, the snout in Liusha was not clearly defined as the debris flow came to a halt in the Yuzi River. I also found no significant evidence of levee formation upstream that supports a segregation mechanism for the fining of material. The abrasion of medium to large sized grains because of grain-grain interactions and collisions can also reduce debris flow grain size with distance downstream (Stock and Dietrich, 2003; Vallance and Scott, 1997). Abrasion may also explain the shift from disc-shaped to slightly more spherical grains on average with distance downstream in Liusha (Vallance and Scott,1997; Figure 5.16). Coarser flows are more likely to abrade grains and increase sphericity (Caballero et al., 2012). Debris flow deposit GSDs have shown a tendency to become coarser or

finer depending on the geology of the reach (Berti et al., 1999; Tiranti et al., 2008; Vallance and Scott, 1997). As such, the shift from granitoids to greywacke shale and sandstones at approximately 900 m downstream may lead to a change in the GSDs deposited by the debris flow and the large shift in the GSD integral with distance downstream, though a change in source was not obvious from field observations (Figure 3.7). The comparable geology from the source location in both catchments may also explain why the GSDs deposited by the two flows are similar (Figure 3.7). However, for the three most downstream pits, I found that the deposited grain-size fraction from sand to small cobbles increased with distance downstream (Figures 5.14), suggesting that the change in GSDs with distance downstream is complex and most likely to be a result of all the factors discussed above.

No clear relationship was observed between the full GSDs deposited in Liusha and changes in topography. For example, only a slight increase in the proportion of silt, clay and fine sand deposited was observed with an increase in curvature, the opposite to our observation for the Luoquan debris flow (Figures 5.14 and 5.15). The lack of clear relationship suggests bed topography is less important in governing the deposition of different grain-size fractions in Liusha in comparison to Luoquan. The lack of relationship may relate to the fact that changes in channel width in Liusha are more systematic than in Luoquan and the channel is more constrained. The Liusha channel is also steeper (minimum slope of 17° at most downstream position sampled) than Luoquan.

The spatial pattern of GSDs in the Liusha and Luoquan deposits help explain the differences in runout lengths between the two debris flows. The Liusha debris flow deposit had evidence of inverse grading, which is prevalent in debris flows with active particle collisions and a high solid volume content. In contrast, the Luoquan deposit was massive and homogenous in structure with no lateral or vertical grading due to the higher water content, which acted as a buffer between grain contacts and reduced segregation within the flow. Bed topography also influenced the deposition of different grain sizes within the flows, despite the Luoquan debris flow being highly fluidised. This suggests that bed topography may still be important in controlling deposition in catastrophic debris flows. The suggested higher water content in the Luoquan

debris flow may in part explain the longer runout, and why the debris flow was able to travel at higher velocities and over shallower slopes.

5.7 Conclusions

In this chapter, I have presented some of the highest resolution GSDs collected for modern-day debris flow deposits. The two debris flows studied had very different runout lengths, despite occurring under similar initiation conditions and in close proximity. I found that both debris flows deposited GSDs of a similar range and maximum grain size. The similar GSDs, particularly with respect to the proportion of sand, cobbles, and boulders, suggest that the different runout lengths could not be explained by the deposit GSDs alone. However, the spatial pattern of deposited GSDs differed across the three dimensions analysed (lateral, vertical, and longitudinal) for both debris flows. The most notable difference was the presence of inverse grading in the middle sections of the smaller Liusha debris flow in comparison to the massive, homogenous vertical deposition of grains in Luoquan. The absence of inverse grading in the larger deposit is thought to be driven by higher pore fluid pressures, which can buffer grain contacts, and reduce the potential for segregation within the flow. The GSDs deposited were also somewhat influenced by the topography within the catchment, with channel width and curvature changing the proportion of the grain-size fractions deposited in different reaches of the flow. The role of topography was particularly prevalent in Luoquan, where both the fine content and boulder frequency reflected potential changes in flow velocity due to topography. The differences in the spatial pattern of GSDs deposited in Liusha and Luoquan highlight the importance of better understanding how transport and deposition mechanisms vary between different debris flows with different properties in a field context.

This chapter has shown that the vastly different runout lengths for two post-earthquake debris flows in Wenchuan may not be related to the composition of the debris flow deposits, with both deposits having consistent GSDs in terms of width and maximum grain size. By studying two debris flow deposits on a small scale at a high resolution, I have inferred that other controls beyond grain size may be responsible for the high frequency of catastrophic debris flows in Wenchuan. Based on the high frequency of debris flows

observed across the Wenchuan region, in the next chapter I will upscale my approach by analysing a regional debris flow inventory. This inventory includes >2 000 debris flows over a ten-year period. I will use the inventory and a 2D debris flow model, Massflow, to identify potential controls on the runout area of post-earthquake debris flows in Wenchuan. The controls which will be investigated include the debris flow source volume and the role of precipitation and how saturated the bed material is.

Chapter 6

Controls on the development of catastrophic debris flows

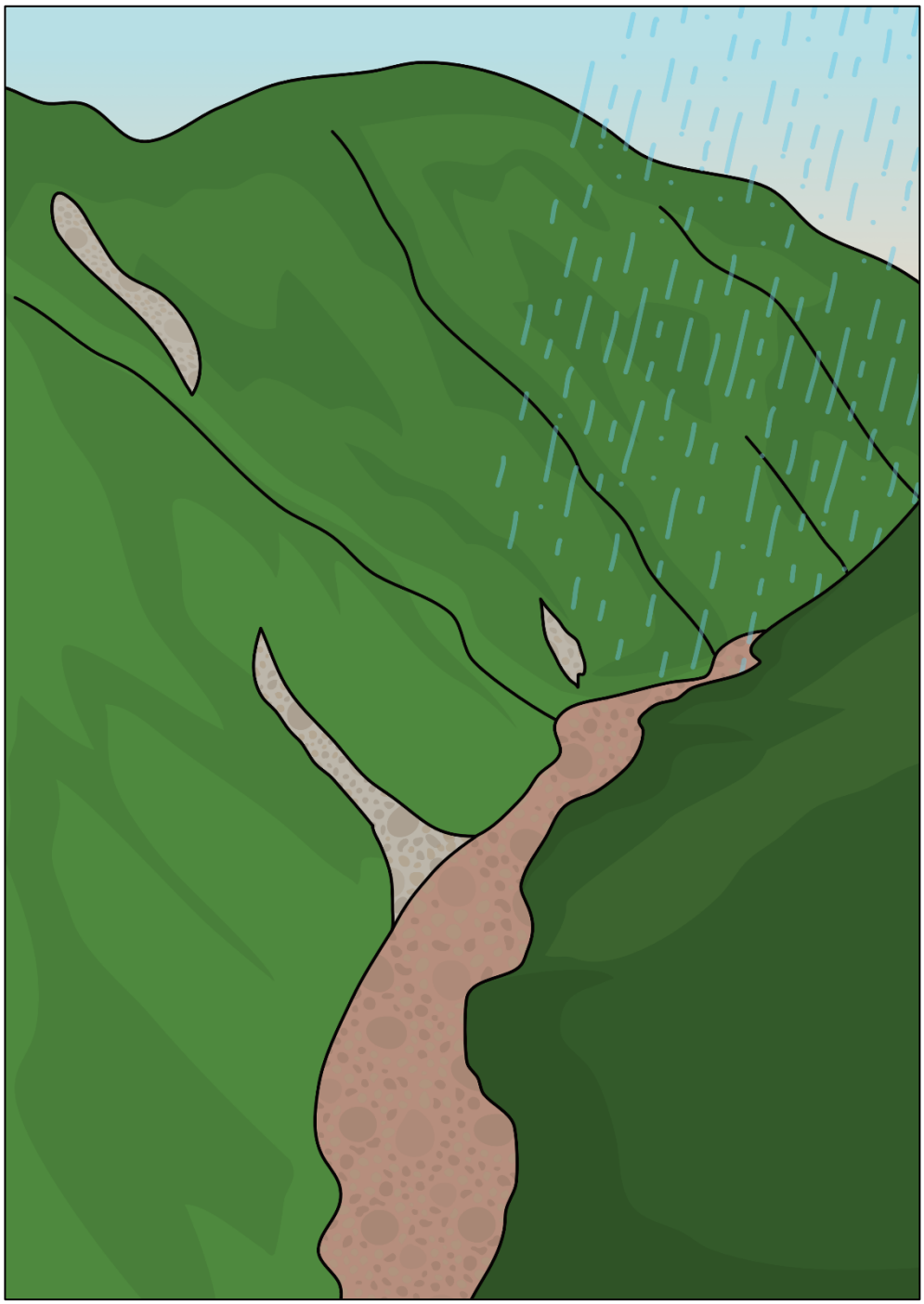

Image by Megan Harvey

6.1 Abstract

Catastrophic debris flows pose significant hazards to local communities, yet the mechanisms which control the runout and extent of these flows are poorly understood. The long distances travelled by catastrophic debris flows relative to their initiation volume suggest that these debris flows rapidly entrained sediment to bulk in size. Processes controlling entrainment in debris flows are poorly constrained due to the lack of field data, challenges associated with surveying the channel bed and the infrequent nature of catastrophic debris flows. The occurrence of multiple large debris flows in a single geological and climatic setting provides a unique opportunity to understand how entrainment controls debris flow hazards, in particular their magnitude. In this chapter, I first investigate whether catastrophic debris flows and non-catastrophic debris flows can be described using a single continuum of magnitude-frequencies. To achieve this, I analysed an unprecedented inventory of >2000 post-earthquake debris flows in Wenchuan. A break in slope in the magnitude-frequency distribution of inventory debris flows at ~10^5 m^2, where the frequency of catastrophic debris flows surpassed non-catastrophic debris flows, suggested that catastrophic debris flows were more frequent than predicted using a single continuum. To determine controls on the development of catastrophic debris flows in Wenchuan, I used the 2D dynamic debris flow model Massflow, which models debris flow runout and considers entrainment. From a sensitivity analysis of variable parameters, I found that low basal friction angles (~20°), large source volumes (>100 000 m^3) and high pore water ratios (degree of bed saturation, >0.8) were required to simulate catastrophic debris flows. I generated magnitude-frequency distributions from these simulations to assess the importance of each parameter (basal friction angle, pore water ratio and source volume). Simulated magnitude-frequency distributions underestimated the proportion of catastrophic debris flows when using both random uniform distributions and statistical distributions, inferred from field data, to represent the three parameters varied in Massflow. By considering debris flows as a single process in Wenchuan, the risk posed by large debris flows is significantly underestimated, potentially enhancing risk to infrastructure and people.

6.2 Introduction

Catastrophic debris flows entrain vast amounts of sediment and therefore bulk to volumes an order of magnitude larger than the initiation volumes, often over 10^6 m^3. These debris flows can be triggered by numerous factors, such as intense rainfall (e.g. Montecito, US, see Kean et al., 2019), large mass movements (e.g. Chamoli, India, see Shugar et al., 2021), landslide dam failures (e.g. Er Gou, China, see Guo et al., 2016b) and volcanic eruptions (e.g. Mount St Helens, US, see Major et al., 2007). Once initiated, these debris flows rapidly increase in volume by entraining sediment. Entrainment involves the exchange of sediment and water along the base of the flow (for example by drag) or from bank collapse due to undercutting (Hungr et al., 2005b; Sassa and Wang, 2005; Theule et al., 2012). Studies of dry experiment flows found that entrainment depended on slope angle, erodible bed thickness and the volume of material initiated (Edwards et al., 2021; Mangeney et al., 2010; Viroulet et al., 2019). Numerical models developed based on these experiments found that when there was sufficient sediment supply, and at suitable slopes angles, bed thicknesses and sources volumes, steady state flows were produced which consistently exchanged sediment with bed to propagate downslope (Edwards et al., 2021). Large-scale flume experiments demonstrated that flows across wet bed sediment grow rapidly via a positive momentum feedback effect (Iverson et al., 2011). Iverson et al. (2011) attributed this effect to the enhanced pore pressures when incorporating saturated material into the flow, which can reduce basal friction and encourage further erosion at the channel bed. Numerical modelling of debris flows across erodible beds highlighted the importance of the momentum threshold when using mass and momentum conservation equations to represent the erodible and flowing layers (Iverson and Ouyang, 2015). Under specific boundary conditions, simulations have been able to replicate the rapid entrainment and volume increase seen in experimental debris flows (Horton et al., 2019). Horton et al. (2019) found a threshold bed saturation, which once reached, led to a rapid increase in the debris flow volume produced. The presence of a positive momentum feedback and the subsequent rapid bulking in experimental and modelled flows suggests that

the size distribution of catastrophic debris flows may not fit into a single continuum for all debris flows and in fact be a separate population.

If catastrophic debris flows are governed by a different process, for example if their size is predominantly driven by the positive momentum feedback effect, their magnitude and frequency distributions may differ from debris flows that have not experienced significant bulking. Under- or overestimating the frequency and size of large debris flows limits our ability to both estimate rates of sediment supply to catchments (Anderson et al., 2015; Bennett et al., 2014; Fan et al., 2019a; Francis et al., 2022; Kirchner et al., 2001; McCoy, 2015) and to accurately model debris flow runout and extent (Frank et al., 2015; de Haas et al., 2022; Kean et al., 2019). Magnitude-frequency distributions of debris flows are an important component in developing hazard models and for describing stochastic processes (Bennett et al., 2014; Guzzetti et al., 2002; Hungr et al., 2008; Jakob et al., 2005; Riley et al., 2013). Therefore, the hazard posed by catastrophic debris flows could also be incorrectly assumed if large debris flows follow a different magnitude-frequency relationship than expected. The magnitude-frequency distribution of catastrophic debris flows can therefore be a source of epistemic uncertainty in these models due to a lack of available data. Field based studies of large debris flows and debris flow entrainment are limited due to the infrequent and unpredictable nature of flows as well as the complexities associated with surveying the channel bed (Iverson and Ouyang, 2015; Kean et al., 2015; McCoy et al., 2012; Stoffel, 2010). As such, most studies of large debris flows focus on single debris flow events (Berger et al., 2011b; Breien et al., 2008; Theule et al., 2012; Vallance and Scott, 1997), experiments (de Haas and Woerkom, 2016; Iverson et al., 2011) and numerical models (Frank et al., 2015; Horton et al., 2019; Iverson and Ouyang, 2015; Ouyang et al., 2015a).

In this chapter, I use an unprecedented dataset of post-earthquake debris flows in Wenchuan to determine whether catastrophic debris flows follow the same magnitude-frequency distribution as debris flows which have not experienced significant bulking. I then apply the 2D dynamic debris flow runout model, Massflow, to establish what controls the occurrence of these catastrophic debris flows and what conditions in Wenchuan led to the

unprecedented number of catastrophic debris flows. The large number of debris flows triggered in Wenchuan since the 2008 earthquake (>2000), including several catastrophic debris flows, provides a unique opportunity to develop and analyse magnitude-frequency distributions for debris flows which initiated under similar climatic and geologic conditions. The catastrophic debris flows in the inventory have caused considerable damage and accounted for over 60% (20.7; ±13.8 Mt) of earthquake-mobilised sediment deposited in the Min Jiang in the decade following the earthquake (Chapter 3; Francis et al., 2022; Guo et al., 2016b; Yang et al., 2021). Therefore, it is important to constrain controls on the magnitude and development of catastrophic debris flows.

6.3 Research objectives

1. To compare the magnitude-frequency distribution of catastrophic debris flows with debris flows that have not experienced significant bulking.
2. To determine how basal friction angle, source volume and pore water ratios control the development of catastrophic debris flows in the Luoquan catchment using Massflow.
3. To create a magnitude-frequency distribution using simulated debris flows to better constrain the conditions that led to the development of catastrophic debris flows in Wenchuan.

6.4 Methods

6.4.1 Debris flow inventory mapping

I analysed the inventory of >2000 active debris flows developed by Fan et al. (2019b) and Domènech et al. (2018) that was introduced in Chapter 3. The inventory consisted of debris flows that occurred between 2008 and 2018. A further 14 debris flows which occurred in 2019 were added to the inventory, 11 were located from Yang et al. (2021) and mapped using satellite imagery from Sentinel-2. Three additional debris flows which were triggered in the Luoquan catchment in 2019 were also added to the inventory. As the debris flow inventory for 2019 is incomplete, it is excluded from any temporal analyses. I also added an additional three catastrophic debris flows to the inventory as point files from the supporting datafile.

I conducted a simple topographic analysis on the dataset using a 30m JAXA DEM. This analysis involved measuring the elevation difference for each deposit, also referred to as the drop height (Marc et al., 2021) by subtracting the minimum elevation of each deposit from the maximum elevation. I also obtained the mean slope angle for each deposit using the Planar method in ArcMap 10.8.1. Debris flow area was calculated based on the polygon extent. The polygon extent included the entire area of the flow that was visible from aerial imagery, so generally included the source, transport and deposition sections of the flow. The catchments within our study area (Figures 3.2 and 3.6) were also downloaded from Domènech et al. (2018). I created stream orders for the study region using the Strahler method and a 200-pixel flow accumulation limit. I then removed any catchments that were too steep and therefore not clearly channelised, too small or had no debris flows, which left 31 catchments (Figure 3.6). I also combined some extremely small catchments following the stream order analysis.

I used field observations and quantitative metrics, such as stream order, to differentiate between debris flows which were likely to have entrained vast amounts of sediment along the flow path. Catastrophic debris flows were described as debris flows which transited multiple stream orders and deposited into a major catchment in Wenchuan. The criteria for catastrophic debris flow were as follows:

1. Transit at least a 3rd order channel
2. Deposit into at least a 4th order channel (most deposited into the Min Jiang River)

Following this step, I noticed that the Hongchun debris flow in 2010 would not be classified as a catastrophic debris flow. However, from field and modelling observations, the Hongchun debris flow appears to fit my criteria for a catastrophic debris flow (Horton et al., 2019; Tang et al., 2011a). I therefore added the Hongchun debris flow to the catastrophic debris flow category and checked any other 2nd order catchments to see whether debris flows deposited in the Min Jiang River. Where I was unsure if a flow was catastrophic, I did not include it. For the three additional flows, which occurred between 2008 and 2013, I only had total volume for the deposit. I

divided this by 3 m to obtain deposit area based on the relationships observed between area and volume for the debris flows included in both the mapped inventory and the table inventory (Domènech et al., 2018; Fan et al., 2018a). This depth estimate is likely to be on the lower end of the approximate distributions (Francis et al., 2022). In total, there were 37 catastrophic flows.

All remaining debris flows were classed as non-catastrophic debris flows (Figure 6.1). In some cases, multiple debris flows appeared to have been mapped as a single shape file. Where imagery was available, I split the merged debris flows. Where this was not possible, the merged debris flows were considered as a single debris flow. Most of the merged debris flows were non-catastrophic debris flows and therefore the areas of catastrophic debris flows are unlikely to be affected by the merged debris flows. In total, there were 2065 non-catastrophic flows.

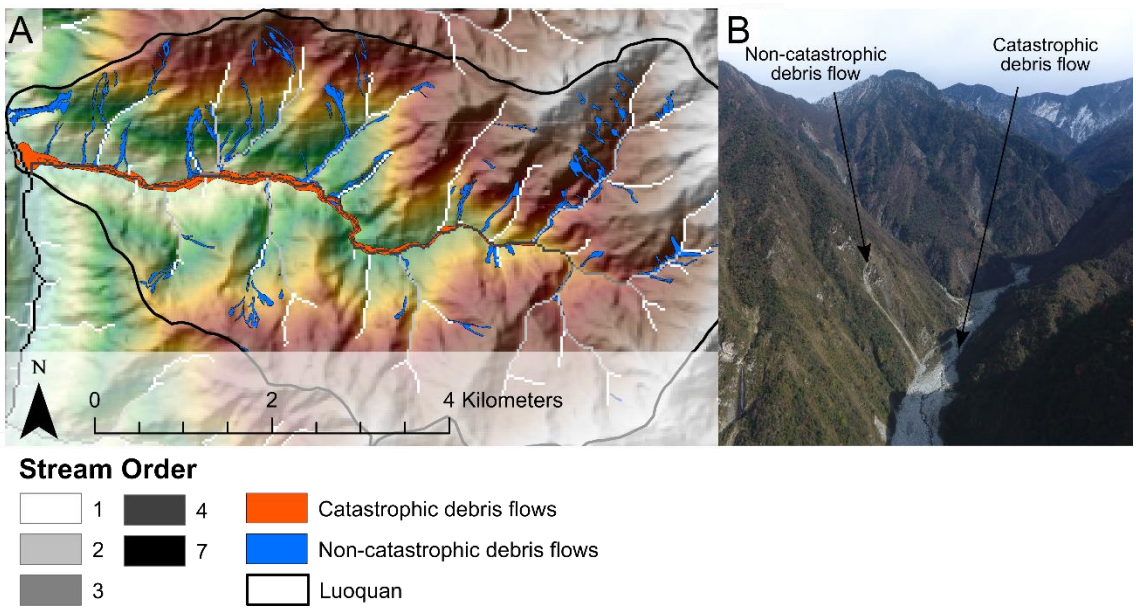

Figure 6.1

The distribution of catastrophic and non-catastrophic debris flows in Luoquan. A) Three catastrophic debris flows have occurred along the main channel in 2010, 2013 and 2019, shown in orange/red. All other debris flows which have occurred since 2008 are shown in blue B) A photo highlighting the difference between the two types of debris flows. Catastrophic debris flows in Luoquan in 2010 and 2013 are thought to have been triggered on the hillslopes, not in the channel. The 2019 triggering location is unclear.

I derived a magnitude frequency distribution for the two types of debris flow and fitted a powerlaw function using the Python powerlaw package (Alstott et al., 2014). The package uses the mathematical method developed in Clauset

et al. (2007) to determine whether a powerlaw can be fitted to a dataset. Where possible I selected the powerlaw with the lowest D value, which represents the minimal Kolmogorov-Smirnov distance between the data and the fitted line, and the lowest sigma value, which is the standard error and was <0.05 for the entire inventory (catastrophic and non-catastrophic debris flows) and the non-catastrophic subset of debris flows. The small number of catastrophic debris flows in comparison to the other inventories meant this threshold was not attainable. I then used the Python package Fitter to find distributions that best represented each set of debris flows.

6.4.2 Massflow background

Massflow is a 2D depth-integrated debris flow model developed by Ouyang et al. (2013, 2015b, 2015a). Massflow was developed to simulate large mountain hazards, such as debris flows and dam break floods, over natural terrain at a high resolution and relatively low computational intensity. An important component of Massflow which makes it well suited to the analyses conducted in this chapter, is the ability of the simulated flow to entrain sediment from a static bed, which also has a set of input characteristics. The acquisition of these equations has been published in full detail in Iverson and Ouyang (2015) and Ouyang et al. (2013; 2015b). The model is solved using a second order MacCormack-TVD finite difference method. Finite element methods solve partial and ordinary differential equations by converting the equations to a system of linear equations that can be solved more simply and quickly. The MacCormack and TVD methods are widely used to solve partial differential equations. The model is run in a rectangular global Cartesian frame which has been rotated so that it is parallel to the slope angle (Ouyang et al., 2015b).

Massflow uses the Reynolds-averaged Navier Stokes equation to describe a flowing mass. These equations are used to describe the time-averaged motion of a fluid. However, the complex nature of these equations makes them challenging to solve. As such, in Massflow they have been reduced to 2D mass and momentum conservation equations, also known as the shallow water equations, by integrating over depth. This step assumes that the horizontal length of the flow is significantly larger than the vertical length, which is appropriate when applied to debris flows. The coupled mass and momentum

equations used in Massflow to describe the flow layer over a static bed are shown below (Equations 6.1 to 6.3) (Ouyang et al., 2015b),

$$\frac{\partial \rho_1 h_1}{\partial t} + \frac{\partial (\rho_1 h_1 u_1)}{\partial x} + \frac{\partial \rho_1 h_1 v_1}{\partial y} = \rho_1 E_{1bot} \qquad \textit{Equation 6.1}$$

$$\frac{\partial h_1 \rho_1 u_1}{\partial t} + \frac{\partial h_1 \rho_1 u_1 u_1}{\delta x} + \frac{\partial h_1 \rho_1 u_1 v_1}{\partial y} = -\rho_1 g h_1 \frac{\partial (h_1 + z_{1bot})}{\partial x} - \tau_{1zxbot} + \rho_1 u_1 (z_{1bot}) E_{1bot} \qquad \textit{Equation 6.2}$$

$$\frac{\partial h_1 \rho_1 v_1}{\partial t} + \frac{\partial h_1 \rho_1 u_1 v_1}{\partial x} + \frac{\partial h_1 \rho_1 v_1 v_1}{\partial y} = -\rho_1 g h_1 \frac{\partial (h_1 + z_{1bot})}{\partial y} - \tau_{1zybot} + \rho_1 v_1 (z_{1bot}) E_{1bot} \qquad \textit{Equation 6.3}$$

where the subscript notation indicates the layer of the model, for example layer 1 is the flowing mass and layer 2 is the static sediment layer (Figure 6.2). u_1 and v_1 represent depth-averaged velocity in the x and y directions respectively, with $u_1(z_{1bot})$ and $v_1(z_{1bot})$ the velocities of materials at the boundary layer that are being entrained, $\rho_1$represents density of the flowing layer, z_{1top} the height of the free surface of the flow, z_{1bot} the height of the basal boundary between the two layers, h_1 flow depth (where $h_1 = z_{1top} - z_{1bot}$), τ_{1zxbot} and τ_{1zybot} are the basal shear traction between the flowing and static layers, E_{1bot} describes the entrainment rate of layer 1. Importantly Equations 6.1 to 6.3 consider the jump conditions associated with the entrainment of static material by a flowing mass, such as abrupt changes in density, velocity, or shear traction. The model assumes the flowing mass is a single phase. The method used to derive these equations is detailed in Iverson and Ouyang (2015).

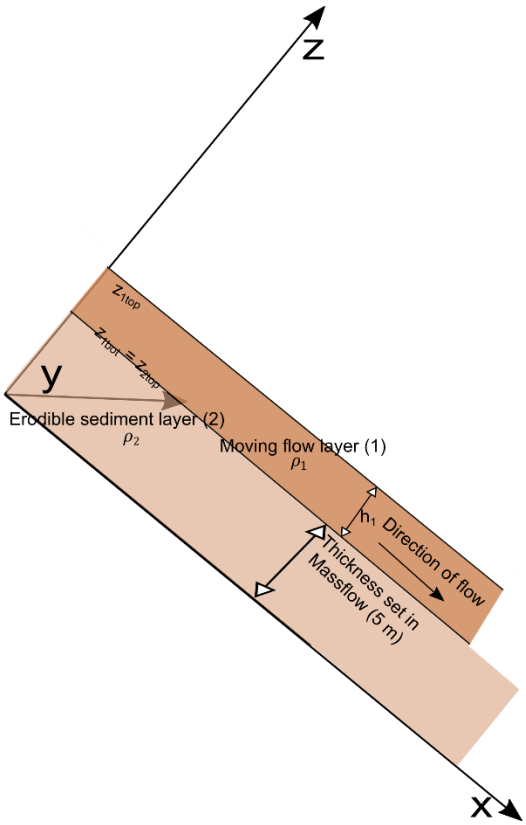

Figure 6.2

The relationship between the moving flow layer (1) and the erodible sediment layer (2) over a rotated plane. Figure is modified from Ouyang et al. (2015b).

In this chapter, I will use a modified version of Massflow (Horton et al., 2019; Ouyang et al., 2015b). In this version of the model, entrainment rate (E) must satisfy the following boundary condition, where ρ_1 is constant and topography is neglected,

$$E = -\frac{\partial z_{1bot}}{\partial t} = \frac{\tau_{1b} - \tau_{2s}}{\rho_1 \sqrt{u_1^2 + v_1^2}} \qquad \textit{Equation 6.4}$$

τ_{1b} is the basal traction of the flow and τ_{2s} is the resistive shear stress from the erodible layer. Importantly, the model uses both Coulomb and Voellmy friction laws when quantifying basal traction of the flow (Equation 6.5). By combining both friction laws, the model can simulate the flowing and stopping mechanisms associated with debris flows. For example, the Coulomb friction law does not consider flow velocity, which is thought to be an important control on entrainment (Hungr et al., 2005; McDougall and Hungr, 2005) and the Voellmy model has a smaller friction angle than the angle of repose. Previous studies have used an assigned critical velocity to encourage a debris flow modelled using a Voellmy simulation to stop (Medina et al., 2008; Ouyang

et al., 2015a). Therefore, the combined model can capture the increase in traction with velocity without decreasing the friction angle.

$$\tau_{1b} = max\left(\left(\rho_1 g_z h_1 tan(\varphi_{voellmy}\right) + \frac{\rho_1(u^2 + v^2)}{C_z^2}, \rho_1(1-s) g_z h tan(\delta)\right) \quad \textit{Equation 6.5}$$

Where, $s = \frac{\rho_w}{\rho}$, $\varphi_{voellmy}$ is the internal friction angle of the flowing mass, g_z is gravity acting normal to the inclined slope, C_z is the Chezy coefficient (which is a function of flow Reynolds number and the relative roughness of the channel), δ is the basal friction angle. $\varphi_{voellmy}$, C_z , δ and ρ are all parameters that can be input into Massflow by the user.

A Coulomb failure criterion is used to describe the total resistance stress from the bed, where;

$$\tau_{2s} = c + \rho_1 g_z h_1 (1 - \lambda)\tan(\phi_2) \quad \textit{Equation 6.6}$$

c is the cohesion of the bed material, ϕ_2 is the internal friction angle of the bed material, λ is the pore water ratio.

Equations 6.5 and 6.6 show the parameters which control bed entrainment by debris flows in Massflow. I use these equations as the basis for my sensitivity analysis, which is explained in more detail below, to identify controls on the development of catastrophic debris flows in Luoquan.

6.4.3 Massflow sensitivity analysis

I used Massflow to simulate debris flows in the Luoquan catchment. I chose this catchment because it includes the 2019 debris flow which I sampled the GSD for in Chapter 5 and also has been mapped since 2008 as part of the inventory (Domènech et al., 2018). I use the 2019 debris flow to validate my model runs. All input DEMs had a 30 m resolution (Horton et al., 2019). The parameters used in the analysis are shown in Table 6.1 and are based on Horton et al. (2019).

Table 6.1

A table displaying the input parameters for Massflow.

ρ_1	ρ_w	c	C_z	λ	$\varphi_{voellmy}$	δ	ϕ_2
2020 kg m^{-3}	1000 kg m^{-3}	2900 Pa	12	0 to 1.0	12 °	20 to 35 °	35 °

When running the model, I set the maximum entrainment depth as 5 m and 10 m to assess the importance of the limit in the model. I found that whilst 10 m is a reasonable limit, based on the large volumes of co-seismic material deposited in channels and previous debris flow depths, the simulated flow depths were exceptionally high (Francis et al., 2022; Horton et al., 2019). Therefore, I chose an entrainment limit of 5 m, which fit within previous studies of debris flow entrainment (Horton et al., 2019; Hungr et al., 2005a).

I then conducted a sensitivity analysis on all the variable parameters in Equations 6.5, which was used to describe entrainment by the flowing layer, and Equation 6.6, which described resistance from the static bed. The sensitivity analysis was used to determine which parameters would be varied systematically in Massflow. Only the basal friction angle and the pore water ratio value demonstrated clear relationships between the output volume and runout of the simulation. For example, debris flows were only able to reach the catchment outlet when using a basal friction angle of 20°. A basal friction angle of 45° produced no debris flow. The Chezy coefficient and internal friction angle, which also describe flow composition, had no systematic effect on debris flow runout for the source volumes and pore water ratios tested here. In Equation 6.6, variations in pore water ratio also influenced the runout length of the debris flow, with only pore water ratios >0.8 producing debris flows which exited the Luoquan catchment into the Min Jiang River. Cohesion had no systematic effect on debris flow runout in this analysis. Therefore, the values for the Chezy coefficient, the internal friction angle and cohesion remained constant throughout.

I ran Massflow varying three parameters (source volume, pore water ratio and basal friction angle) in a systematic approach. I used four input volumes: 24 300 m^3, 97 200 m^3, 172 800 m^3 and 270 000 m^3. These volumes were chosen based on the volumes used by Horton et al. (2019) in Hongchun and the co-seismic landslide areas in Luoquan. All input volumes were set to a depth of 3 m. Based on the sensitivity analysis above, I varied the pore water ratio, which gives an indication of how saturated the bed material is, at 0.1 increments from 0 to 1.0. The degree of bed saturation has been shown to relate to entrainment in experimental (Iverson et al., 2011; Reid et al., 2011) and field debris flows (McCoy et al., 2012). I varied the basal friction value

from 20°, 28° and 35° following the sensitivity analysis outlined above. Basal friction has been found to influence the runout of debris flows and avalanches in settings where the flows traverse different terrains, such as ice and river beds (Stinton et al., 2004). In total, I ran 132 runs of Massflow, varying each parameter in turn (Table 6.2).

Table 6.2

Example of the parameters varied in each run of the model Massflow. The 33 runs were conducted on four source volumes. In total, Massflow was ran 132 times.

		Basal Friction Angle		
		20	**28**	**35**
Pore Water Ratio	**0**	Run 1	Run 12	Run 23
	0.1	Run 2	Run 13	Run 24
	0.2	Run 3	Run 14	Run 25
	0.3	Run 4	Run 15	Run 26
	0.4	Run 5	Run 16	Run 27
	0.5	Run 6	Run 17	Run 28
	0.6	Run 7	Run 18	Run 29
	0.7	Run 8	Run 19	Run 30
	0.8	Run 9	Run 20	Run 31
	0.9	Run 10	Run 21	Run 32
	1	Run 11	Run 22	Run 33

6.4.4 Volume-Area conversion

In some of the simulations with low pore water ratios, shallow debris flows in Massflow spread across a wider area than would be expected in field conditions, in some instances flowing back upstream for several meters. To minimise the overestimated areas for smaller simulated debris flows, I developed a volume-area powerlaw distribution using the areas and volumes for simulated debris flows. This relationship will be used to derive more conservative area estimates using the volumes output in Massflow. These areas can then be compared with the field inventory, which considers debris flow magnitude using area. A powerlaw relationship has previously been used for debris flow volume-area conversions (Griswold and Iverson, 2008). Previous debris flow volume-area relationships did not fit the dataset well, which may in part relate to the fact all the debris flows modelled here had an area >37 800 m^2 and a volume >42 000 m^3, whereas in Griswold and Iverson (2008) a wider range of volumes (from 10 m^3 to 10^7 m^3) were considered. The powerlaw relationship used to describe the relationship between area and

volume was $A = 107V^{0.55}$. The relationship underpredicts the area covered by the largest volumes (Figure 6.3).

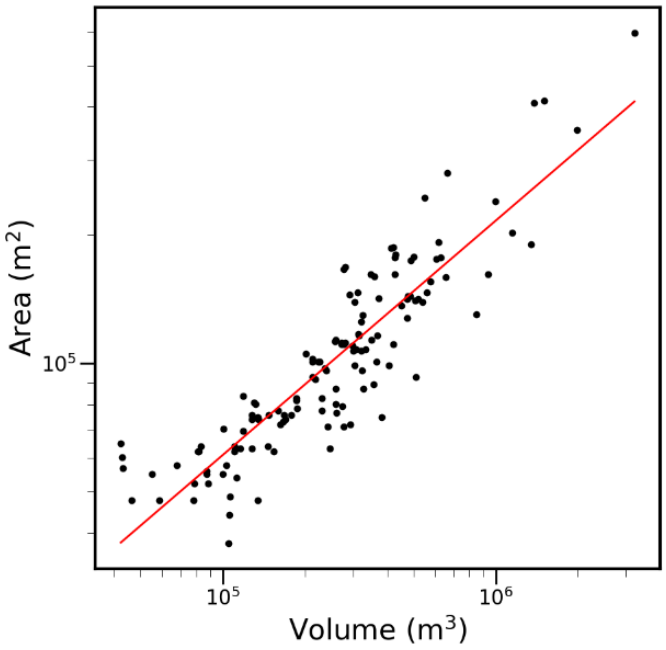

Figure 6.3

The area-volume relationship obtained between debris flows simulated in Massflow. The powerlaw used to describe the relationship is $A = 107V^{0.55}$.

6.4.5 Monte Carlo simulations: input distributions

To develop magnitude-frequency distributions using the simulated runouts, I needed to determine which statistical distributions represented the parameters varied in Massflow (source volume, basal friction angle and pore water ratio). To achieve this, I found field or remotely sensed datasets that could act as a proxy for each parameter. I then fitted a statistical distribution to each dataset and applied the distribution with the best fit to generate the parameter values for the Monte Carlo simulations (Section 6.4.6).

Precipitation was used to infer pore water ratios based on the assumption that intense precipitation values correspond to a higher degree of bed saturation. Precipitation is a well-established control on debris flow initiation, and intensity-duration thresholds are typically used to predict events in which a debris flow may occur (Caine, 1980). Precipitation values for the Luoquan catchment were downloaded from the IMERG (Integrated Multi-satellitE) Global Precipitation Model (Huffman et al., 2014). To obtain the daily rainfall in Luoquan, I averaged two 10 km x 10 km cells that overlapped the catchment. I grouped the daily rainfall into rainfall events. Here, a rainfall

event is defined as a period of consecutive days in which rainfall occurs. The beginning and end of each event is determined by a day with no rainfall. I use the maximum daily rainfall value to represent the effect of antecedent rainfall conditions. I removed all events with a maximum daily rainfall below the 24-hour intensity-duration threshold for debris flow initiation in Wenchuan (Guo et al., 2016a). This ensured only events above the rainfall thresholds, which therefore had the potential to trigger a debris flow, were considered. A lognormal distribution best represented the maximum daily rainfall events in Luoquan (Figure 6.4). I then normalised the rainfall values by the largest maximum daily rainfall value so that the largest precipitation event was represented by a value of 1 and the values closest to the triggering threshold had a value just above 0. These normalised values were assumed to directly correspond to the pore water ratio value input into Massflow, whereby the highest rainfall events corresponded to the highest pore water ratio values. There were eleven potential values for pore water ratio, ranging from 0 to 1 at intervals of 0.1

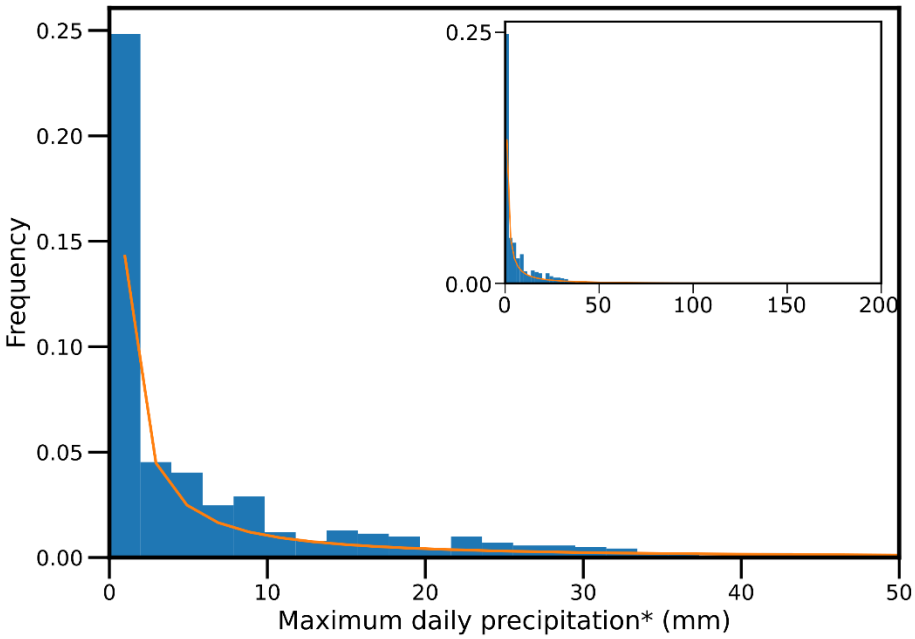

Figure 6.4

The distribution of daily maximum rainfall per rainfall event between 2008 and 2019 fitted using a lognormal distribution. A rainfall event is described as a set of days when precipitation occurred on all days. Events were separated by days when no rainfall occurred. The maximum daily precipitation per event reaches a maximum of 200 mm (inset graph), however most precipitation values fell within 0 mm and 50 mm.

For the source volumes I used a magnitude-frequency distribution for co-seismic landslides in the Luoquan catchment, as these are likely to be one of the main sources from which debris flows initiate in Wenchuan (Fan et al., 2019b; Francis et al., 2022; Huang and Li, 2014). Using the Python Fitter package, I found that an inverse gamma distribution best fit the distribution of co-seismic landslides (Malamud et al., 2004), in line with previous studies in Wenchuan (Fan et al., 2012). I sampled randomly from the inverse gamma distribution and chose the source volume closest to the random value (Figure 6.5). There were four possible source volumes to choose from.

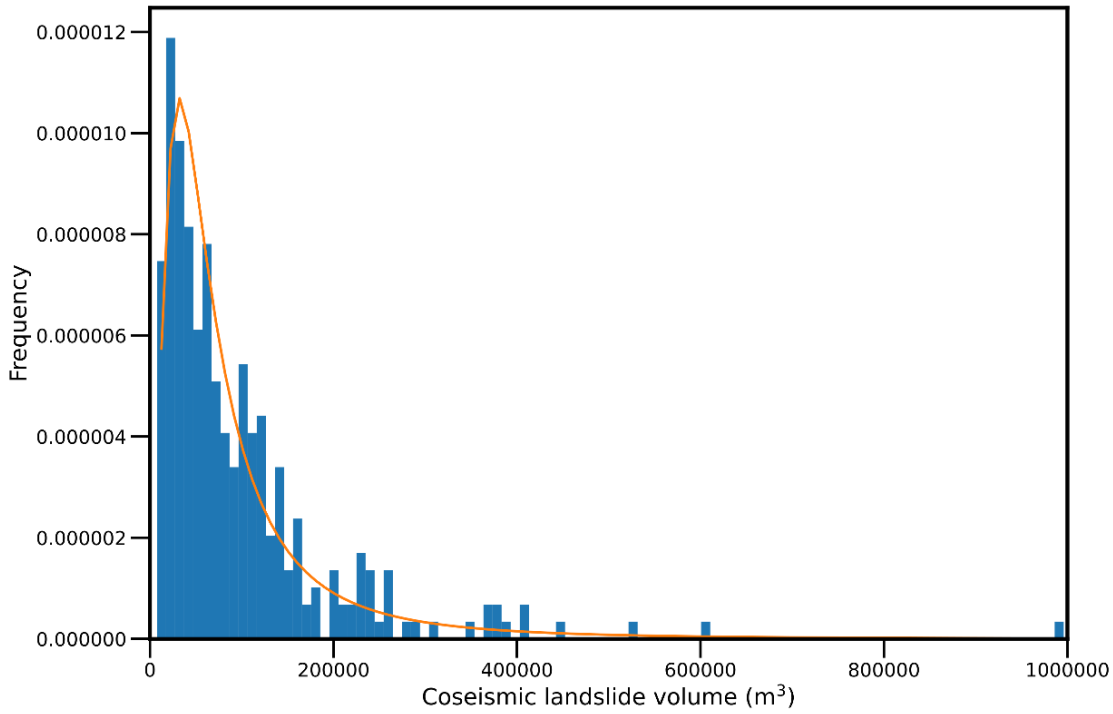

Figure 6.5

The distribution of co-seismic landslide volumes in the Luoquan catchment fitted with an inverse gamma distribution. The volumes were generated by multiplying landslide area by a depth of 3 m.

Finally, I constrained the basal friction angle using the D_{50} values for the 2019 debris flow event, collected in Chapter 5. The D_{50} values observed in Luoquan and Liusha were best described using an exponential normal distribution (Figure 6.6). Whilst the grain size and composition of a debris flow can influence its basal friction angle (Forterre and Pouliquen, 2008; Iverson et al., 2010), an explicit relationship between debris flow grain size and basal friction angle has not been established for field debris flows. Many studies have therefore inferred basal friction angles by using the angle of internal

friction for the flowing material (Iverson et al., 2010), based on the roughness of the underlying material (DiBiase et al., 2017; Stinton et al., 2004) or after an event using the runout length of a flow (Mangeney-Castelnau, 2003; Sheridan et al., 2005). Previous basal friction estimates for flows travelling over sediments have varied from 20° for an avalanche travelling over a moraine deposit (Stinton et al., 2004) to 40.7° for an experimental debris flow over a rough inclined bed (Iverson et al., 2010). The three basal friction angles used in Massflow (20°, 28° and 35°) fit within this range.

I used basal friction angles from previous debris flow events and their GSDs to infer potential basal friction angles in Luoquan. A basal friction angle of 20° was used to represent an avalanche travelling over a moraine deposit (Stinton et al., 2004). These moraines had median grain sizes between 0.1 cm and 6.4 cm (Mills, 1978). Moraine deposits measured in Owens Valley, California, U.S.A, were found to have D_{50} values also within this range, between 4 cm and 4.1 cm (D'Arcy et al., 2017). Therefore, I infer that a D_{50} value of <4 cm for the Luoquan debris flow deposit corresponds to a basal friction of ~20°. Coarse gravel was found to correspond to basal friction angles between 26.3° and 34° in experiments by Baselt et al. (2021). Therefore, I used D_{50} values between 4 cm and 20 cm to represent a basal friction angle of 28°. A basal friction angle of 28° was also used by Horton et al., (2019) to model the 2010 Hongchun debris flow. Therefore, the fact that most of the D_{50} values fell within this range is reasonable. All D_{50} values >20 cm were assumed to correspond to a basal friction angle of 35°. I used the exponential normal distribution shown in Figure 6.6 to obtain a D_{50} value. The D_{50} value then corresponded to a basal friction angle.

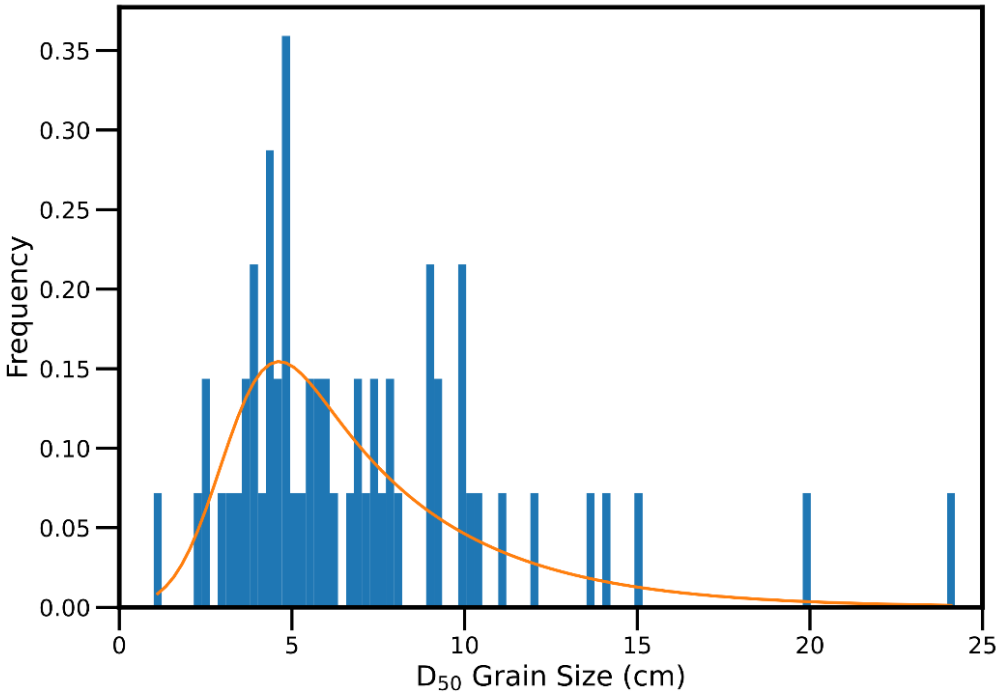

Figure 6.6

The distribution of D_{50} values measured using sieving of the Luoquan and Liusha debris flow deposits. The distribution is modelled using an exponential normal distribution.

6.4.6 Monte Carlo simulations

Finally, I ran eight Monte Carlo simulations to assess how the three parameters (source volume, basal friction angle and pore water ratio) when varied using Massflow affected the magnitude-frequency distribution of debris flows (Table 6.3). In each Monte Carlo simulation, I decided whether to use a random uniform distribution or an extreme value distribution to represent the three parameters. To account for all possible combinations, I ran the Monte Carlo analysis eight times (Table 6.3). When using a random uniform distribution, each discrete value used to represent the individual parameters in Massflow had an equal probability of being selected. All parameters were discrete, meaning that there were 11 pore water ratio values to choose from, 4 source volumes and 3 basal friction angles. Based on the combination of values selected to represent source volume, pore water ratio and basal friction angle, a runout volume (taken from the 132 Massflow runs) was output. This process occurred 10 000 times resulting in a magnitude-frequency distribution consisting of 10 000 volumes (made up of 132 values). Eight Monte Carlo simulations were executed to assess whether random uniform distributions or extreme value distributions produced a magnitude-frequency

distribution consistent with the Wenchuan post-earthquake debris flow inventory.

Table 6.3

List of distributions used to represent each parameter in each Monte Carlo simulation.

	Basal friction angle	**Pore water ratio**	**Source Volume**
Run 1	Random	Random	Random
Run 2	Random	Lognormal	Random
Run 3	Random	Random	Inverse gamma
Run 4	Exponential normal	Random	Random
Run 5	Random	Lognormal	Inverse gamma
Run 6	Exponential normal	Random	Inverse gamma
Run 7	Exponential normal	Lognormal	Random
Run 8	Exponential normal	Lognormal	Inverse gamma

6.5 Results and Discussion

6.5.1 Magnitude-frequency distributions: inventory data

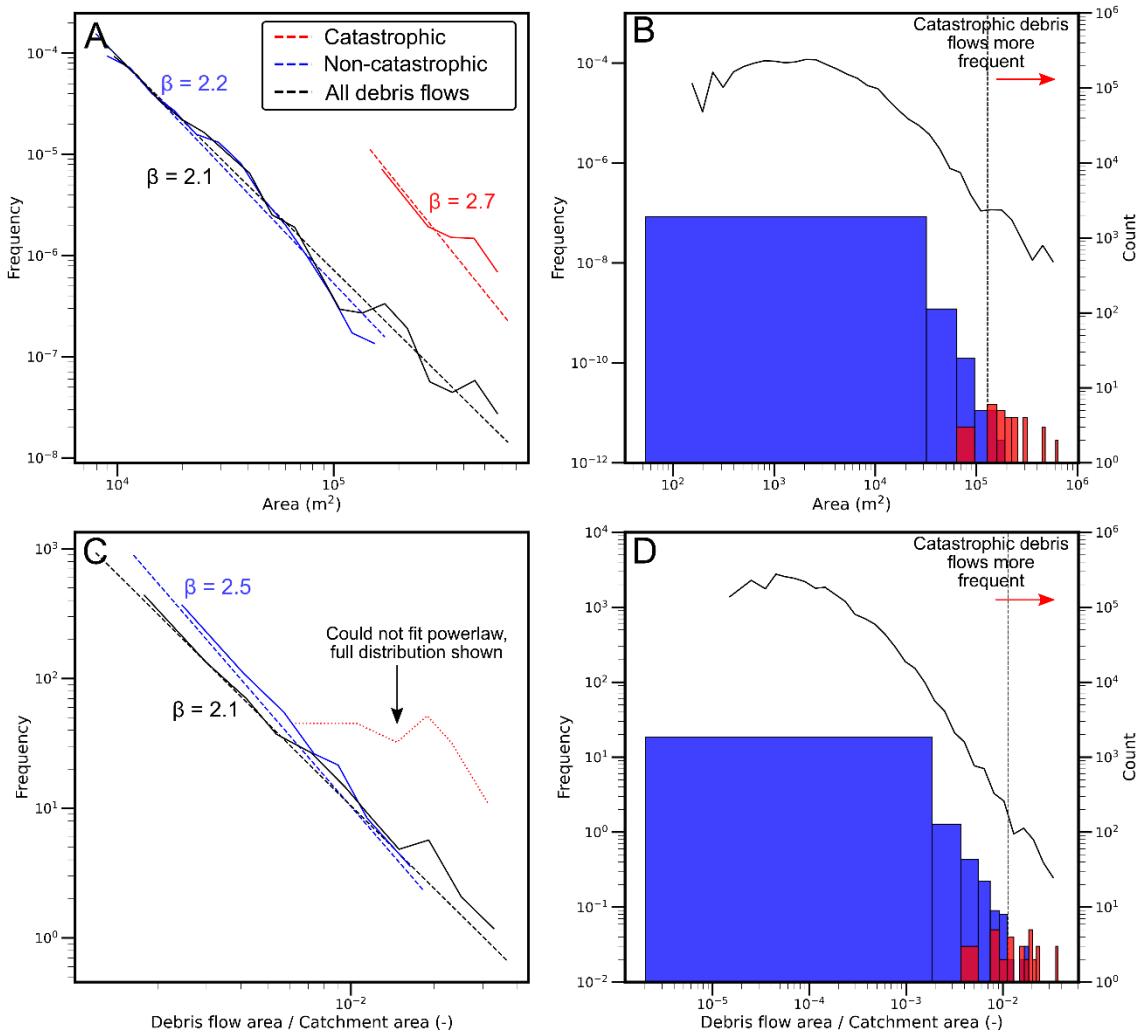

Figure 6.7

The magnitude-frequency distributions for the entire inventory dataset (n = 2102, black), for the subset of non-catastrophic debris flows (n = 2065, blue) and the subset of catastrophic debris flows (n = 37, red). A and B) Frequency against debris flow area. Powerlaws are fitted using Alstott et al. (2014). C and D) show the frequency for debris flow area normalised by catchment area.

The post-earthquake debris flow inventory analysed here consists of 2102 debris flows, which range in area from 53 m^2 to 640 000 m^2 (Figure 6.7B). I use area to define the magnitude of post-earthquake debris flows in the inventory. Area is chosen to avoid any assumptions relating to the depth of the flow when converting to volume (Griswold and Iverson, 2008).

The mean and median debris flow areas in the inventory remained relatively consistent between 2008 to 2018, despite a decrease in the mean and median

drop heights of ~100 m (Figure 6.8). The decrease in drop height relates to the movement of debris flow triggering locations downstream in the years following the earthquake. The average slope for each debris flow ranged from 6° to 77°, with 78% of average slopes between 25° and 45° (Figure 6.9). Catastrophic debris flows typically had slightly lower average slopes in comparison to those which did not bulk. The lower average slope is likely related to the debris flows travelling the entire length of the catchment and therefore across shallower slopes (Figure 6.9). Maximum slope was not necessarily higher for larger debris flows, with maximum slopes between 35° and 70° corresponding to areas spanning three orders of magnitude (10^3 to 10^6 m^2). These results suggest the maximum slope, likely near the initiation point, is not a crucial control on debris flow magnitude in Wenchuan (Figure 6.9B). No significant trend was observed between debris flow magnitude and catchment area (Figure 6.10). For the debris flows in Wenchuan, I found no relationship between the size of the debris flow and the maximum slope (Figure 6.9). Catastrophic debris flows did display a positive relationship with catchment area, suggesting these flows bulked until they were forced to stop when exiting into the Min Jiang River (Figure 6.10) (Gabet and Bookter, 2008). Topography therefore does not appear to be the main driver of debris flow magnitude in Wenchuan.

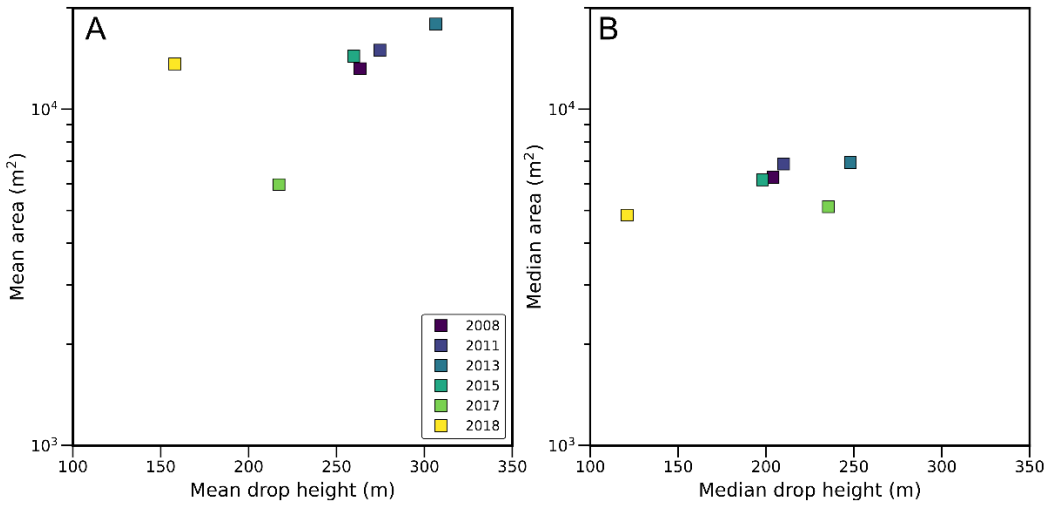

Figure 6.8

A) The mean drop height (maximum elevation – minimum elevation) and mean area for debris flows recorded between 2008 and 2018. N = 2008: 371 debris flows; 2011: 1007 debris flows; 2013: 389 debris flows; 2015: 81 debris flows; 2017: 4 debris flows; 2018: 7 debris flows. B) The median drop height and area for the debris flow inventory.

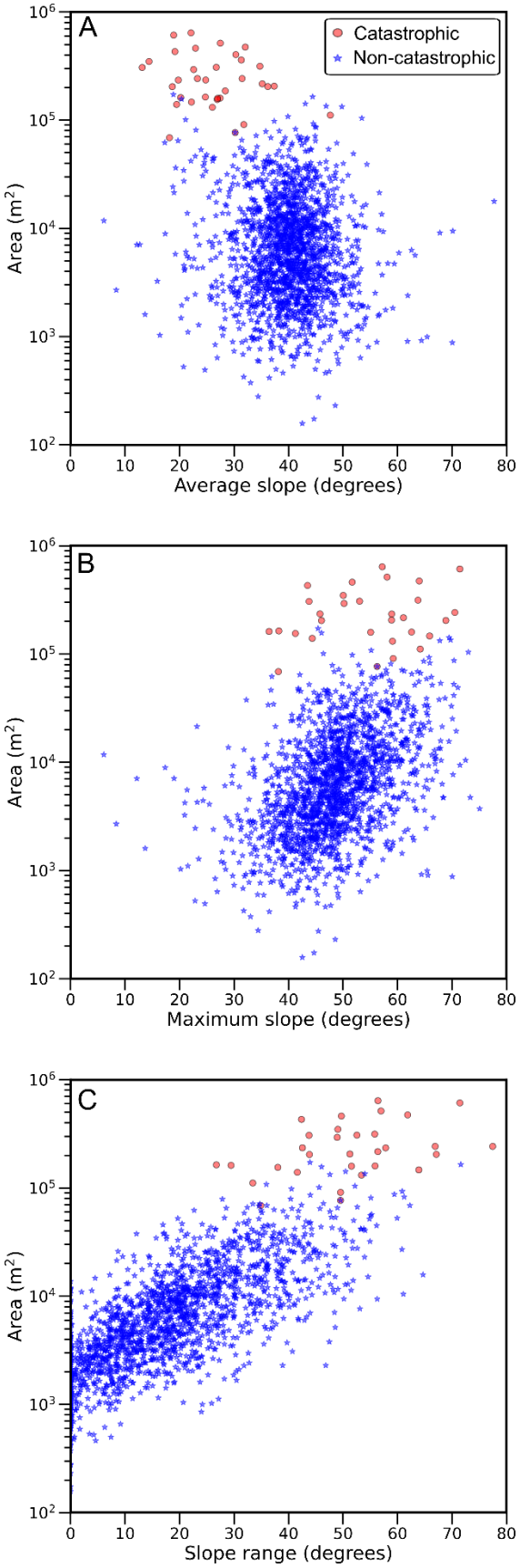

Figure 6.9

The average (A), maximum (B) and range (C) of slope angles for 1842 of the debris flow shapefiles. Catastrophic debris flows are shown in red and non catastrophic debris flows in blue.

The magnitude-frequency distribution for the debris flow inventory can be represented by a lognormal distribution and the tail can be described by a powerlaw (Figure 6.7). The powerlaw for the entire inventory has an exponent, which describes the slope of the power-law, of 2.1 and an x_{min}, which describes the minimum area to which the powerlaw can be fit, of 8500 m^2 (Figure 6.7A). The tail of the distributions contains 36% of debris flows ($x>x_{min}$). In the magnitude-frequency distribution for all debris flows, there is a change in slope of the relationship at 100 000 m^2 (Figure 6.7B). This change in slope implies that larger debris flows (>100 000 m^2) occur more frequently than expected when describing the distribution as a powerlaw. The change in the frequency of debris flows at 100 000 m^2 corresponds to the area at which catastrophic debris flows are more frequent than non-catastrophic debris flows (Figure 6.7B). When analysing the distributions of debris flows which did not bulk significantly and the distribution of catastrophic debris flows separately, I found that both distributions could be described using an inverse gamma distribution, which have been fit to landslide magnitude-frequency distributions previously by Malamud et al. (2004). The tail of both distributions could also be described by powerlaws. The powerlaw for non-catastrophic debris flows was consistent with the powerlaw observed for the full dataset, with an x_{min} of 7 900 m^2 and an exponent of 2.2 (Figure 6.7A). This powerlaw represents only the largest 39% of non-catastrophic debris flows. In contrast, the powerlaw for catastrophic debris flows included 84% of the distribution when having an x_{min} of 146 900 m^2 and an exponent of 2.7 (Figure 6.7A). Though the error on the powerlaw was much higher due to the low number of catastrophic debris flows from a statistical viewpoint. Both exponents ($\beta > 1$) suggest these parts of the distributions are heavy tailed. The slight differences in the exponent of the distributions when considering all debris flows, catastrophic debris flows and non-catastrophic debris flows may have considerable consequences. For example, Figure 6.7A suggests if a magnitude-frequency distribution is generated using the entire inventory, the frequency of large magnitude events may be underestimated.

The greater than expected frequency of high magnitude flows (100 000 m^2) in Wenchuan, in combination with the different powerlaw exponents fitted, suggests that catastrophic debris flows follow a different magnitude-

frequency relationship (Figure 6.7). If the magnitude and frequency of catastrophic debris flows is different, it implies that there are two populations of debris flows in Wenchuan, which are governed by different processes. The fact that the break in slope denoting more frequent, large debris flows, corresponds to catastrophic debris flows becoming more frequent than non-catastrophic debris flows supports the suggestion that catastrophic debris flows are a separate process. However, an alternative explanation for the higher frequency of high magnitude events could be limited sampling windows (Brardinoni and Church, 2004; Marchi and D'Agostino, 2004). For example, Brardinoni and Church (2004) found, in a study of 171 landslides, that large landslides (>4 000 m^3) had a lower frequency than predicted based on the powerlaw for the entire dataset. Whereas the dataset here includes all debris flows (>2000) that occurred between 2008 and 2018. In addition, Wenchuan is one of few places on Earth to witness this number of catastrophic debris flows in a 10-year period, therefore, it is unlikely that the break in slope is an artefact of too few large debris flows. Topography can also control the size of landslides and debris flows. Steeper, till-rich slopes in British Columbia were more unstable and therefore produced larger landslides than the surrounding catchments with a different lithology. Variations in lithology is thought to have contributed to the different magnitude frequency relationship for larger landslides (Brardinoni and Church, 2004). For the debris flows in Wenchuan, I found no relationship between the size of the debris flow and the maximum slope (Figure 6.9). Catchment area and debris flow area were also not strongly correlated, implying that the factors controlling most debris flows in Wenchuan was not catchment area (Figure 6.10). A shift in topographic characteristics is unlikely to explain the increased frequency of larger debris flows observed in Figure 6.7. Catastrophic debris flows did display a positive relationship with catchment area, suggesting the magnitude of these flows were confined by a physical limit, the Min Jiang River (Figure 6.10) (Gabet and Bookter, 2008). The constraint of catchment-area on the runout area of catastrophic debris flows supports the idea that the development of these debris flows are governed by a process which sustains enough momentum to traverse long distances when channelised, such as the positive momentum

feedback effect (Iverson et al., 2011). The longer channels in larger catchments may also provide sufficient sediment for the catastrophic debris flows to bulk in size.

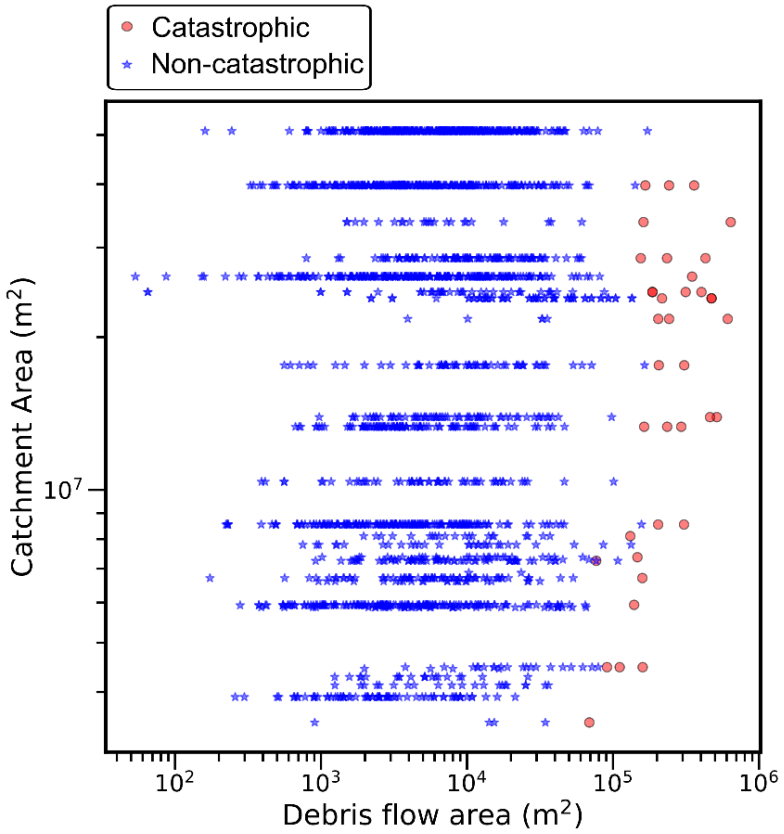

Figure 6.10

The relationship between catchment area and debris flow area for the different types of debris flows. There is no systematic relationship between catchment area and debris flow area for non-catastrophic debris flows (blue), yet there is an increase in the area of catastrophic debris flows (red) with catchment area.

The change in frequency of high magnitude events in Wenchuan may therefore be attributed to hydrological (e.g., initiating conditions and presence of positive pore pressures) and sediment supply (e.g. initiation and entrained volumes) controls. Both controls are closely tied to entrainment in debris flows in Wenchuan and have been found to influence the magnitude-frequency relationship of debris flows. The abundance of sediment supplied to channels from co-seismic and post-seismic landslides following the 2008 Wenchuan earthquake has sustained the higher frequency of debris flows (Huang and Fan, 2013; Zhang and Zhang, 2017a). The abundance of sediment in channels can facilitate entrainment and the development of larger debris flows (Mangeney et al., 2010). As debris flows and landslides move material

downslope and into channels, large channelised debris flows, which entrain material have been observed (Zhang and Zhang, 2017a). However, large debris flows also require high intensity rainfall events to initiate (Guo et al., 2016b). As such, hydrological controls may also play a part in the occurrence of large debris flows at a high frequency in Wenchuan. Annual monsoons have produced extremely large debris flows in 2008, 2010, 2013 and 2019 (Ge et al., 2015; Tang et al., 2011a; Yang et al., 2021). These large flows have travelled kilometres and, in many instances, rapidly entrained sediment to reach and block the Min Jiang River. The rapid entrainment and large, catastrophic debris flows during monsoons may relate to the monsoon storms saturating the channel bed (Iverson et al., 2011; McCoy et al., 2012; Reid et al., 2011).

6.5.2 Model scenarios

Each of the parameters varied in Massflow displayed a non-linear relationship with debris flow magnitude (both area and volume) (Figure 6.11). When referring to model scenarios, I use debris flow volume to avoid the potential overestimates for simulated debris flow areas briefly mentioned in Section 6.4.4 (Figure 6.11D). Debris flows reach the end of the Luoquan catchment in three scenarios out of a possible 132, with only one scenario depositing as a fan in the Min Jiang River (Figure 6.11A). The largest debris flow had a volume of over 3 200 000 m^3 and had the following combination of parameters: basal friction: 20°, pore water ratio: 0.9, source volume: 172 000 m^3 (Figure 6.11G). Three of the top four largest volumes fit within the classification of a catastrophic debris flow. The two flows which reached the Min Jiang but did not continue to produce a fan were approximately 1 400 000 m^3 (basal friction: 20°, pore water ratio (s): 0.8 and 0.9, source volume: 270 000 m^3). The second largest volume did not reach the mouth of the catchment (basal friction: 35°, pore water ratio: 0.9, source volume: 270 000 m^3). The smallest volume recorded was 42 000 m^3 (basal friction 28°, pore water ratio: 0.0, source volume: 24 300 m^3). The mean and median volumes were 351 000 m^3 and 273 000 m^3 respectively. The lack of extremely large debris flows produced using the different scenarios in Massflow is consistent with the low number of catastrophic debris flows in the field inventory (1.8%).

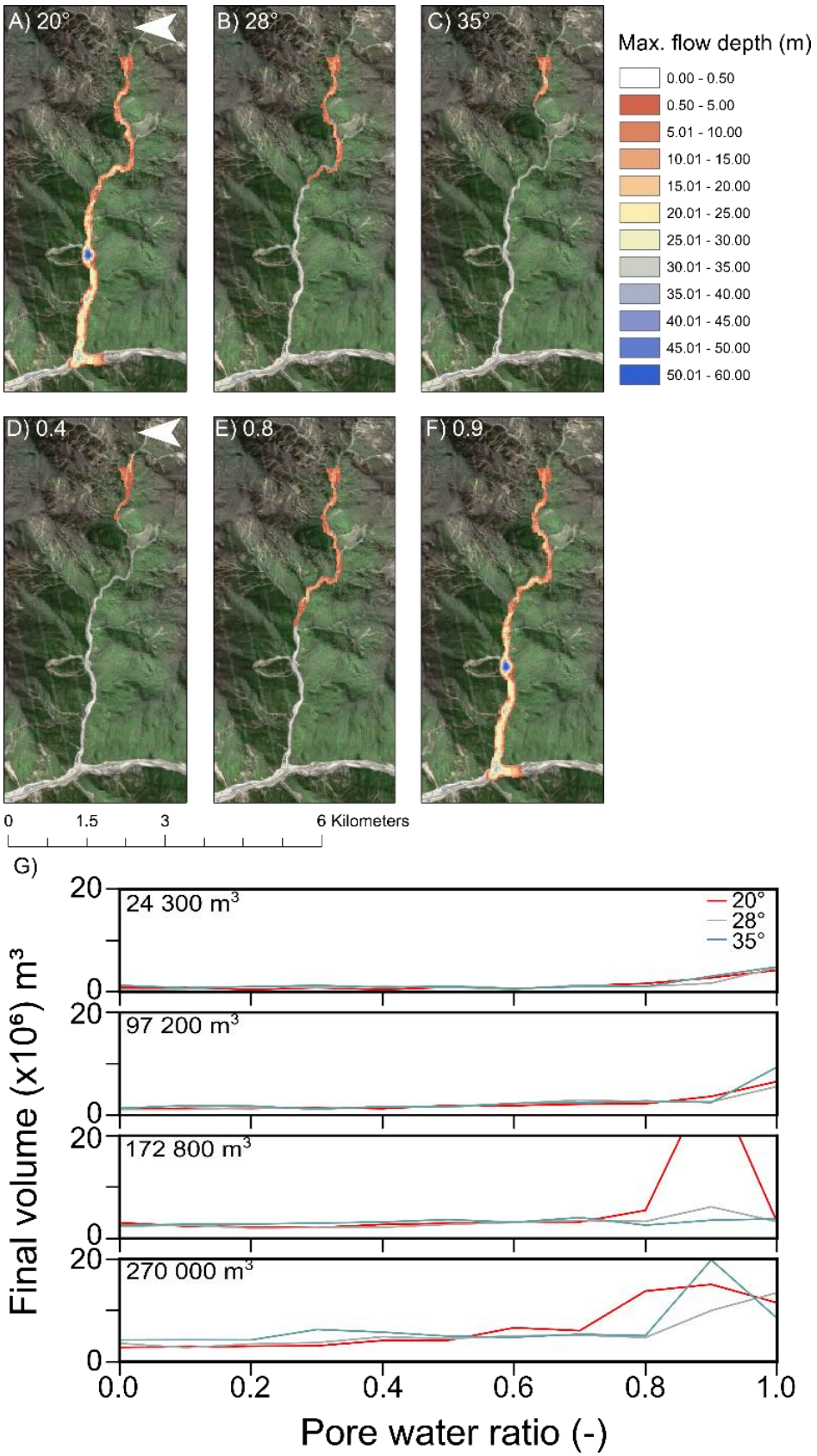

Figure 6.11

Examples of runouts created using Massflow. A to C) Show how changes in basal friction angle control runout in the simulated debris flows. These runs all had a source volume of 172 800 m³ and a pore water ratio of 0.8. D to F) Demonstrate how changes in pore water ratio can affect debris flow runout. These runs had a source

volume of 172 800 m^3 and a basal friction of 20°. G) Demonstrates how the final runout volume is affected by the three variable parameters.

A pore water ratio of at least 0.8 was required to simulate a catastrophic debris flow in the Luoquan catchment (Figure 6.11). A small change in pore water ratio led to a sharp change in the length and volume of the flow, highlighting rapid entrainment, with the debris flow in Figures 6.11E and 6.11F increasing in volume by almost a multiple of 6 with a 0.1 change in pore water ratio. In general, an increase in the volume and length of the debris flow occurred between a ratio 0.8 and 0.9 (Figure 6.11G). The importance of high pore fluid pressures when destabilising bed material and entraining sediment in debris flows is widely accepted (Breien et al., 2008; de Haas et al., 2022; Hungr et al., 2005a; Major and Iverson, 1999; McDougall and Hungr, 2005). The small change in the pore water ratio of the bed material required to induce rapid entrainment and a catastrophic debris flow fits with the positive momentum feedback effect observed in experimental flows (Iverson et al., 2011). A rapid change in debris flow volume was also observed for debris flows in Hongchun, Wenchuan, when pore water ratios exceed a threshold of 0.7 (Horton et al., 2019). The lower ratio to produce a catastrophic debris flow in Hongchun suggests topography may relate to the bed saturation required to induce a larger debris flow. For example, the catchment area in Luoquan is larger and the channel gradient in Hongchun is steeper.

Catastrophic debris flows were only triggered from source volumes of 172 800 m^3 and 270 000 m^3 (Figure 6.11G). Source volume and debris flow runout volume were also positively correlated, though the simulation which produced the largest flow used the second largest source volume. The positive relationship between source volume and debris flow runout fits with the concept that larger debris flows can entrain more sediment, and therefore increase in volume. Entrainment can be more rapid in larger flows due to larger flow depths increasing the normal stress on the bed and therefore increasing scour (de Haas et al., 2020, 2022). Horton et al. (2019) found initial failure volume was more important in controlling debris flow runout volume in comparison to triggering location, which fits with the inventory dataset where

median and mean area were consistent irrespective of the median change in elevation (Figure 6.8).

A low basal friction angle of 20° was required for simulated debris flows to reach the outlet of the Luoquan catchment (Figure 6.11A). These findings fit with field observations, where debris flows preferentially scoured smoother surfaces (Theule et al., 2015). Despite the fact that basal friction here corresponds to the Coulomb friction rheology in the flow model, the basal friction in Voellmy rheology equations has also been found to control runout length (Hürlimann et al., 2008). As detailed in Section 6.4.5, basal friction can relate to grain size. Based on this concept, the simulated debris flows with a basal friction angle of 35° may represent coarse-grained debris flows. Coarser grains in debris flows can lead to higher rates of scour, as seen at the debris flow front in some locations (Berger et al., 2011a; Ghasemi et al., 2019; de Haas and Woerkom, 2016; Schürch et al., 2011). Large debris flow volumes were simulated when using a basal friction angle of 35°, but these flows did not reach the catchment outlet (Figures 6.6 and 6.11G). This suggests that a low basal friction, and perhaps a finer debris flow, is required to reach the critical threshold for a positive momentum feedback effect in Luoquan. In contrast, debris flows with a basal friction of 28° reached the end of the Hongchun catchment (Horton et al., 2019). In Wenchuan, from field observations we would infer that the bed material is likely to be consistent across catchments (see Chapter 5). Therefore, any changes in basal friction may be related to lubrication from wet bed material which reduces the normal stress of the flow (Breard et al., 2020). The role of basal friction in controlling entrainment in catastrophic debris flows is likely to be more complex than modelled here. For example, field datasets have shown a close relationship between shear stress and basal friction, with higher values expected at the flow front, which will have consequences for bed erodibility (de Haas et al., 2022; McArdell et al., 2007; Schürch et al., 2011). Varying bed materials and friction properties have also been shown to effect debris flow mobility and runout, particularly when flows have travelled over snow and rocky terrain (McDougall et al., 2006; Sosio et al., 2012; Stinton et al., 2004).

6.5.3 Magnitude-frequency distributions: model scenarios

To account for the non-linearity in the parameters used in Massflow, I developed a Monte Carlo analysis and varied the inputs for each parameter using statistical distributions obtained using field and remotely sensed data (Sections 6.4.5 and 6.4.6). All Monte Carlo generated magnitude-frequency distributions underestimated the frequency of debris flows >100 000 m^3 (Figure 6.12). In fact, the magnitude-frequency distribution closest to the inventory dataset obtained using simulated debris flows modelled the three input parameters using random uniform distributions, over a range of 42 000 m^2 to 440 000 m^2 (5% of the field inventory). This may be attributed to the following three explanations, (1) that the statistical distributions obtained for pore water ratio, source volume and basal friction used here underestimated the frequency of the conditions required for a debris flow to entrain sediment; (2) that the current simulations are missing a mechanism which controls the development of catastrophic debris flows, and (3) the occurrence of catastrophic debris flows in Wenchuan is random in nature. The applicability of each explanation is discussed below.

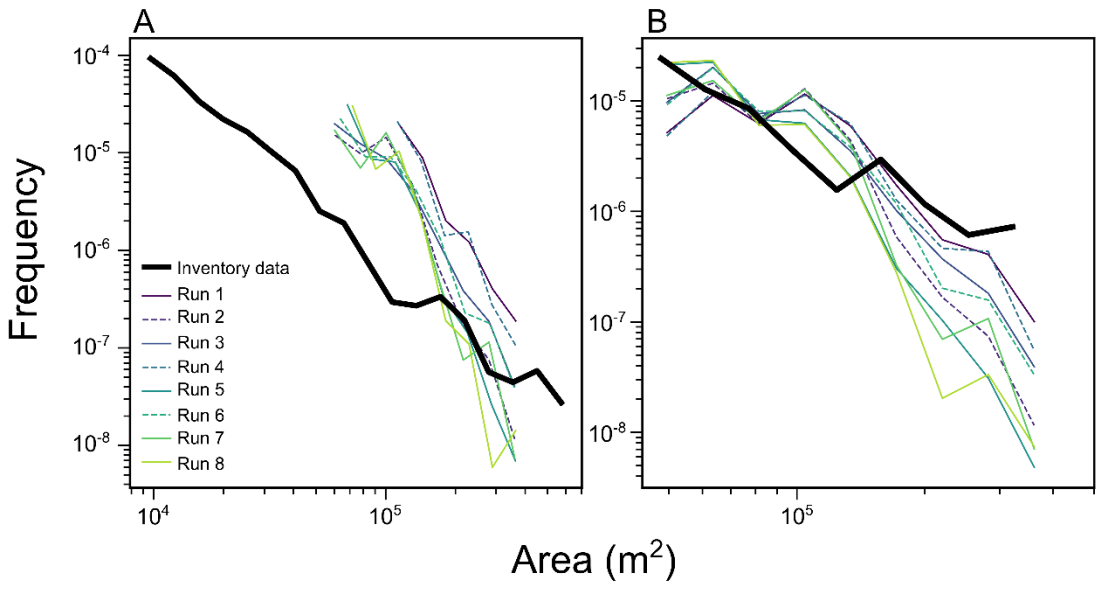

Figure 6.12

A) The magnitude-frequency distribution for the entire debris flow inventory (black line represents catastrophic and non-catastrophic debris flows) as well as the magnitude-frequency distributions for the eight Monte Carlo simulations. The run numbers correspond to those presented in Table 6.3. B) displays all the distributions used to generate a powerlaw across the same range of areas (42 000 m^2 to 410 000 m^2).

Monte Carlo simulations using representative distributions of pore water ratio, source volume and basal friction all underestimate the frequency of large debris flows. The greatest underestimation of large debris flows was seen when using maximum daily precipitation events to represent pore water ratios (Figure 6.12). The underestimation could suggest that maximum precipitation events do not correlate with antecedent conditions within the catchment and cannot explain the degree of bed saturation accurately. Antecedent conditions have been shown to control debris flow occurrence in Wenchuan and should be taken into account (Marino et al., 2022). However, a distribution of antecedent rainfall conditions is also likely to be heavy tailed and therefore would not increase the occurrence of large debris flows more than a random uniform distribution.

The inverse gamma distribution of source volumes (Run 3) and exponential normal distribution of basal friction angles (Run 4) appeared to reduce the frequency of catastrophic debris flows only slightly in comparison to a uniform random distribution. The use of median grain size to infer basal friction angle may be oversimplistic. For example, the full GSD of the bed material is likely to control basal friction and surface roughness, particularly considering the wide range of grain sizes recorded in debris flow deposits (see Chapter 5). Flume experiments which vary bed conditions based on grain size should be conducted in order to better constrain this relationship (Iverson et al., 2010; Roelofs et al., 2022). Whilst the extreme distribution of source volumes underestimated the largest flows, the kernel density plot only had a single mode value (Figure 6.13). The field inventory was also unimodal, albeit with a much lower mode due to the wider range of debris flow areas sampled, supporting the use of an inverse gamma distribution to represent volume. Obtaining accurate estimates of debris flow source volumes is challenging in locations where high resolution imagery is not available (Tang et al., 2019). Potential challenges with the use of co-seismic landslide volume could be that not all the sediment mobilised reached the channel, which is likely to be the case (Fan et al., 2012). As such, the amount of sediment that reaches the channel may be a better metric but is difficult to quantify (Francis et al., 2022). The bimodal distributions produced for the other variables analysed here may be a reflection on the limited number of simulations, particularly

using only three basal friction angles (= 44 simulations). To this end, whilst I may have underestimated the role of the three variables explored here using extreme value distributions, it is likely that alternative parameters used to model the antecedent rainfall conditions, the amount of sediment that reaches the channel and the role of pore water ratio on basal conditions would also be represented by heavy tailed distributions. Therefore, it is more likely that the more similar distribution found when using random uniform distributions to represent the three variables, demonstrates that a crucial mechanism in Wenchuan is missing for this scenario or catastrophic debris flows are simply random.

A parameter which has not been fully tested in this analysis is topography and the triggering location of the debris flows. It would be reasonable to assume that a debris flows which initiates higher up in the catchment on a steeper slope would be able to entrain more material (Abancó and Hürlimann, 2014; Benda and Cundy, 1990; Fannin and Wise, 2001; Guthrie et al., 2010). If triggering locations higher up in the catchment produced more frequent and larger debris flows using Massflow, the Monte Carlo simulations presented here may more closely fit the magnitude-frequency distribution observed in the field. Further analysis should investigate the role of topography using Massflow in the future. This work has previously been conducted in Massflow when modelling the 2010 catastrophic debris flow in Hongchun. They found that the volume of the debris flow was most likely controlled by pore water ratios and source volumes and less so by triggering location (Horton et al., 2019). The changing location of sediment stores, as hillslope deposits stabilise and sediment is deposited in main tributary channels, makes testing this hypothesis difficult in Wenchuan (Francis et al., 2022). Our observations, which demonstrated that debris flow magnitude was consistent despite a decrease in drop height through time, also suggest that topography is a secondary control on the development of catastrophic debris flows in Wenchuan (Figure 6.8). Topography may indirectly affect the development of catastrophic debris flows in Wenchuan by affecting the conditions controlling their occurrence. For example, non-catastrophic debris flows were simulated in the Luoquan catchment when using conditions which were able to simulate catastrophic debris flows in Hongchun (Horton et al., 2019). This implies that

higher pore water ratios and lower basal frictions are required to simulate catastrophic debris flows, and the positive momentum feedback effect, in larger catchments. The high pore water ratios may relate to the fact catastrophic debris flows in Wenchuan must runout over two times as far to reach the Min Jiang River. The main channel in the Luoquan catchment is also a fourth order stream on a shallower gradient, whereas the main channel in the Hongchun catchment is a steeper, second order stream. This comparison suggests individual topographic characteristics may also contribute to the development of catastrophic debris flows (Guo et al., 2016b).

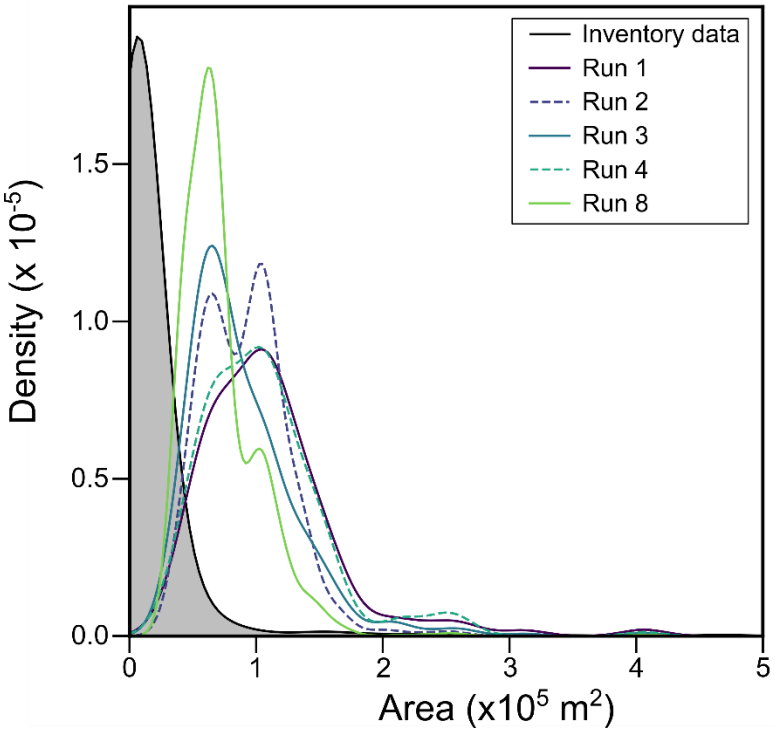

Figure 6.13

A kernel density estimate plot showing the probability density function of simulated debris flow areas for five Monte Carlo simulations (10 000 volumes) plotted against the values for the inventory dataset (2 000 volumes). Monte Carlo simulation Run 3 (Table 6.3), which used an inverse gamma distribution to represent volume and random uniform distributions for basal friction angle and pore water ratio, produced the only other unimodal distribution. Details of the distributions used to represent pore water ratio, source volume and basal friction angle in each run can be found in Table 6.3.

The close fit between the magnitude-frequency distributions as observed in the inventory and as generated when using random uniform distributions to describe the three variable parameters, implies that it is possible that controls on the occurrence of catastrophic debris flows in Wenchuan are

random. It is not unexpected that the random uniform distributions perform best because only 1.8% of simulated debris flows were catastrophic debris flows (Section 6.6), which is consistent with our field observations. The occurrence of catastrophic debris flows in Luoquan during only three of the five maximum rainfall events between 2008 and 2019 supports the random occurrence of large debris flows. The proportion of co-seismic and post-seismic sediment supplied to channels between 2018 and 2019 did not change greatly before the large 2019 events (Francis et al., 2022). Therefore, the conditions did not change significantly but a large debris flow occurred in 2019 and not in 2018, highlighting the stochastic nature of catastrophic debris flows. Thus, whilst non-catastrophic debris flows may be controlled by changing intensity-duration curves following the earthquake, the role of precipitation may not be as simple for catastrophic debris flows (Domènech et al., 2019; Guo et al., 2016a). Our current understanding of catastrophic debris flows is therefore insufficient to deterministically model the hazards posed. Whilst studies have demonstrated a decrease in the frequency of debris flows following the 2008 earthquake, it might be not be possible to model catastrophic debris flows in the same way (Francis et al., 2022; Zhang and Zhang, 2017b).

6.5.4 Wider implications

The magnitude-frequency distribution for post-earthquake debris flows in Wenchuan appears to be governed by two distributions. The two distributions can be identified by the higher frequency of large magnitude debris flows at ~100 000 m^2, above which catastrophic debris flows are more frequent than non-catastrophic debris flows. I have shown that the positive momentum feedback effect, where debris flows rapidly entrain sediment and bulk to much larger volumes (Iverson et al., 2011), may explain the development of catastrophic debris flow in Wenchuan. The rapid entrainment, which required high pore water ratios, low basal friction angles and large source volumes, necessary for simulations in Massflow to reach the end of the catchment provided evidence for this (Figure 6.11). Further support was found by the fact that only catastrophic debris flows displayed a relationship with catchment area (Figure 6.10). Catastrophic debris flows therefore only ceased once they reached a much higher order stream and a sharp tributary junction,

otherwise we can assume the flow would continue entraining sediment (Benda and Cundy, 1990; Chang et al., 2017; Tang et al., 2011a). Non-catastrophic debris flows were not limited by catchment area (Figure 6.10). The abundance of sediment from co-seismic and post-seismic sources as well as annual monsoons demonstrate that the conditions implemented in Massflow are applicable to Wenchuan. The much higher levels of co-seismic landsliding seen in Wenchuan relative to other earthquakes in recent times may also explain the high frequency of large, catastrophic debris flows seen in Wenchuan in comparison to other post-earthquake sediment cascades (Dahlquist and West, 2019; Fan et al., 2019a). Though, I note that there has been a considerable decrease in the frequency of post-earthquake debris flows more recently, as shown by the low numbers which occurred in 2017 and 2018 (Figure 6.8).

High pore water ratios, low basal friction angles and large source volumes are crucial for debris flows to develop into catastrophic debris flows in these simulations. However, when using field conditions to represent the variable parameters, the frequencies of high magnitude debris flows were underestimated. These findings suggest that the inverse gamma, log normal and exponential normal distributions used to describe field conditions do not directly explain the high frequency of large debris flows found in Wenchuan. As such, an alternative mechanism which has not been considered in this analysis may be crucial in controlling the occurrence of catastrophic debris flows in Wenchuan, such as the depth to which the debris flows entrain sediment. Debris flow composition may also be of importance, however the similarities in the range of grain sizes found for two different post-earthquake debris flows in Chapter 5 suggest this is unlikely to be the case. Therefore, although I have demonstrated how the three variable parameters affect the development of catastrophic debris flows, the conditions required to produce catastrophic debris flows in Wenchuan remain not fully understood.

If catastrophic debris flows are described by a separate magnitude-frequency distribution, as shown here, current debris flow hazard models may have underpredicted the frequency of large debris flows in Wenchuan (Figure 6.7). Previous models which sought to predict debris flow volume, will have considered all debris flows as a continuum, considering large debris flows as

the same process. For example, Huang et al. (2020) used machine learning to predict debris flows volumes based on the relationship between a set of debris flow volumes and topography. A proportion of the flows included in this analysis had volumes > 2 x 10^6 m^3, which are consistent with the catastrophic debris flows modelled in Massflow (Figure 6.11). By analysing catastrophic debris flows separately, the magnitude of which is driven by a different process, it is likely that more accurate predictions can be made in the future. The underestimated frequency of large debris flows from precipitation thresholds in this work demonstrates that current methods using rainfall intensity-duration curves as a predictor of large debris flows may not provide adequate warning. However, Guo et al. (2016b) has suggested that larger thresholds are required for debris flows in larger catchments. The amount of sediment in the channels also appears to be a crucial control on the development of large debris flows in Wenchuan (Edwards et al., 2021; Francis et al., 2022; Jakob et al., 2005; Tang et al., 2011a). Through time as hillslope deposits stabilise, alternative metrics such as the depth of sediment in the tributary channels may be required to better predict the frequency of catastrophic debris flows (Domènech et al., 2019; Shen et al., 2020). Quantifying this is particularly challenging in sediment-rich channels in comparison to bedrock channel which are excavated in a single flow (Benda and Dunne, 1997b; Berger et al., 2011b).

6.6 Conclusions

To conclude, the size of catastrophic debris flows in Wenchuan appear to be governed by the positive momentum feedback effect, which encourages entrainment and allows debris flows to bulk in volume. The feedback effect results in a higher frequency of large debris flows than expected based on a single magnitude-frequency continuum for all debris flows. From this, I infer that catastrophic debris flows are more frequent than expected for flows of that magnitude and therefore should be described as a separate population. To understand what governs the occurrence of large flows in Wenchuan, I then simulated debris flows for the Luoquan catchment in Massflow, which can model the positive momentum feedback effect. From simulations, I show that the degree of bed saturation (pore water ratio), basal friction angle and source volume are all crucial in developing catastrophic debris flows. I then

placed these findings in the wider context of Wenchuan by using statistical distributions from field and remotely sensed data to model the pore water ratios, basal friction angles and source volumes. After 10 000 simulations, the field conditions used in this model underpredicted the frequency of catastrophic debris flows. These findings suggest that other conditions are also controlling the occurrence of catastrophic debris flows. Future hazard models should therefore consider controls on the magnitude-frequency of catastrophic debris flows separately to avoid underestimating the risk posed by these extremely large, fluidised flows.

In this chapter, I have demonstrated that following the 2008 Wenchuan earthquake, the frequency of large, catastrophic debris flows has been greater than expected based on the magnitude-frequency distribution of all post-earthquake debris flows in the region. As a result of this, I infer that current models which predict the risk posed by post-earthquake debris flows in Wenchuan may underestimate the frequency of the largest and most catastrophic events. To ensure the risk of catastrophic debris flows in Wenchuan is not underrepresented, future research should aim to both better understand why catastrophic debris flows are more frequent and how the risk posed by catastrophic debris flows can be considered separately in runout prediction models. Accurate estimates of the magnitude and frequency of catastrophic debris flows is crucial to limit damage to property and life in debris flow prone regions. In the next chapter of this thesis, I will discuss how the research conducted in this thesis has contributed to our understanding of post-earthquake sediment hazards and provide suggestions for future work.

Chapter 7

Discussion and Conclusion

7.1 Chapter summaries

In this thesis, I have used field GSDs, remote sensing, and numerical modelling to demonstrate that catastrophic debris flows are governed by a different process in comparison to debris flows which have not experienced significant bulking. An overview of my findings and potential directions for future research can be seen in Figure 7.1.

In chapter 4, I compared GSDs measured using five different methods for three mass movement deposits. I found that depending on the choice of method, D_{50} values could vary by up to a factor of three (Tables 4.3 and 4.4). These differences in percentile value can have significant consequences on our ability to interpret the GSDs measured. For example, a D_{50} value from sieving (6.6 mm) for the Tredegar rockslide was half the size of the D_{50} value from Wolman pebble counts (13 mm). Both methods are widely used, yet the GSDs produced were not comparable. The discrepancies introduced by method choice could impact future studies, for example when using the percentile values to model sediment export. Therefore, it is essential that GSD studies state the assumptions made and the proportion of grains overlooked by method choice. Accounting for method choice will reduce the likelihood of inaccurate geomorphic conclusions.

In chapter 5, I analysed the grain-size distribution of two post-earthquake debris flow deposits with different runout lengths. Both deposits had relatively consistent GSDs in terms of width (clay to boulders) and the maximum grain size measured using sieving. The similarities in the GSDs deposited suggests that the differences in runout length may not relate directly to the grain size of debris flows in Wenchuan. The spatial distribution of deposited grain sizes differed between the two flows. For example, evidence of inverse grading was found in the Liusha debris flow, which travelled 1.5 km (Figure 5.4), whereas the catastrophic Luoquan debris flow, which travelled 8 km, did not show evidence of inverse or lateral grading. I suggest that the absence of grading can be attributed to the high pore pressures required for the Luoquan debris flow to travel such long distances. The spatial pattern of boulders in the catastrophic debris flow also related to topography, suggesting changes in channel width, slope and curvature may

also encourage deposition and erosion in even these extremely large flows (Figure 5.8).

In chapter 6, I investigated controls on the magnitude of catastrophic debris flows in Wenchuan using a multi-temporal inventory and the model Massflow. I identified catastrophic debris flows based on their stream order and whether they reached the Min Jiang River (or a similar order river). I observed a disconnect in the magnitude-frequency distribution for the Wenchuan debris flow inventory (Figure 6.7). This disconnect corresponded with the magnitude at which catastrophic debris flow became the most frequent type of debris flow. The change in magnitude-frequency at this point, suggested that the process controlling debris flow magnitude was different for catastrophic debris flows. In fact, using a single continuum to represent debris flow magnitude-frequency would underestimate the frequency of catastrophic flows. Catastrophic debris flows in Wenchuan have been observed to bulk several orders in volume. In Massflow, bulking through the positive momentum feedback effect (high degree of bed saturation) was able to reproduce catastrophic debris flows in the Luoquan catchment. Source volume and basal friction angle were also important in the development of these catastrophic debris flows (Figure 6.11). When accounting for the non-linearity of these input parameters (source volume, basal friction angle and pore water ratio), my model simulations underpredicted the frequency of catastrophic debris flows. This suggests that alternative parameters must also be considered, such as source location or sediment depth, or that catastrophic debris flows are a stochastic process (Figure 6.12).

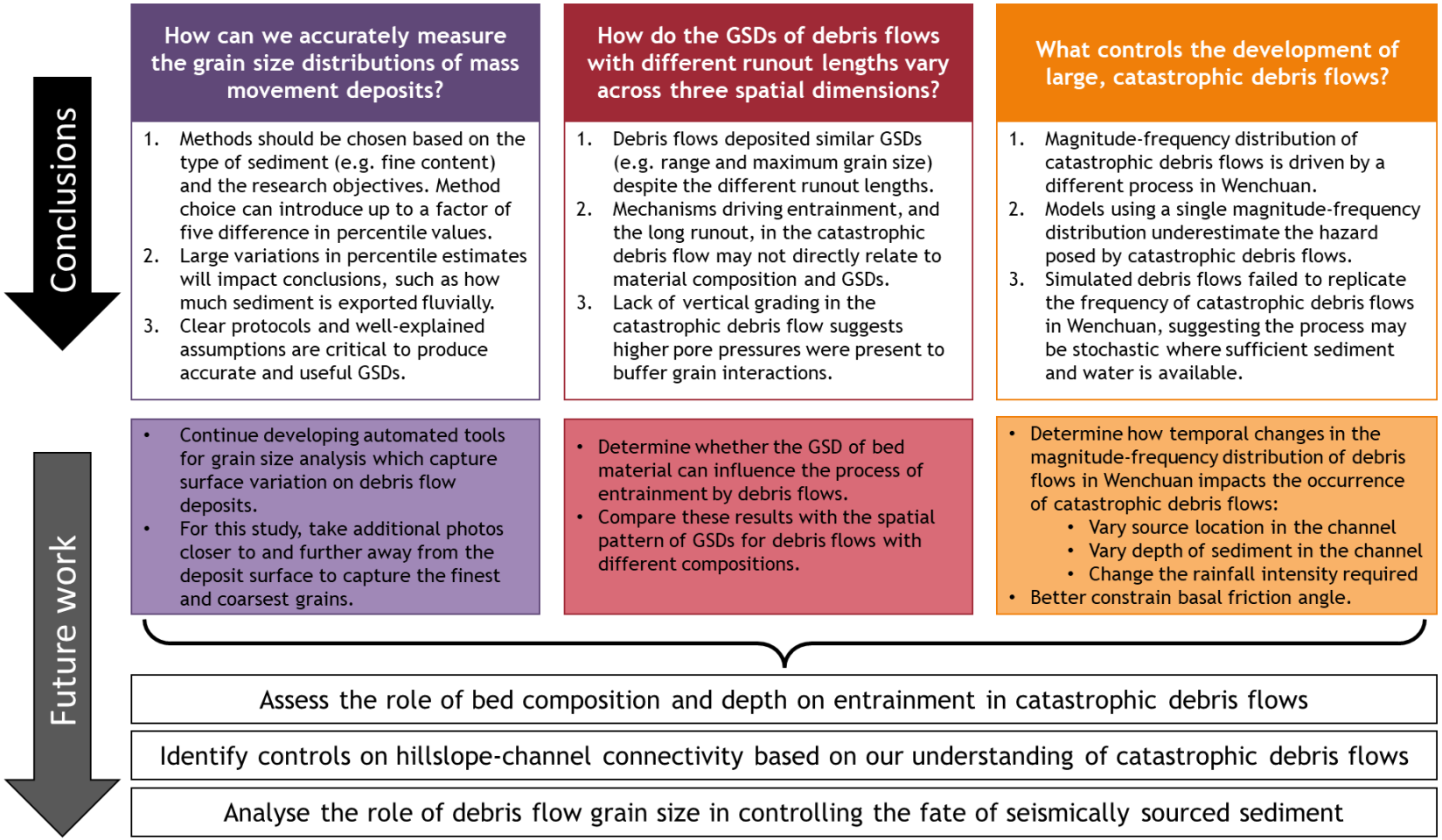

Figure 7.1

A summary of the conclusions for each research question assessed in this thesis as well as potential directions for future work specific to that question and more broad research questions.

7.2 Wider importance and significance

This thesis has combined local-scale observations of debris flow deposition mechanisms (Chapter 5) and a landscape-scale inventory analysis (Chapter 6) to provide evidence that catastrophic debris flows should be considered as a separate process. From this analysis, it can be inferred that catastrophic debris flows, which pose a major hazard to communities in mountain landscapes, are driven by the positive momentum feedback effect (Iverson et al., 2011). The rapid bulking required for catastrophic debris flows to reach volumes large enough to transit entire catchments means that the magnitude-frequency distribution of these flows should be considered separately. Prior to this analysis, the positive momentum feedback effect has previously only been observed experimentally (Iverson et al., 2011) and in single catchments where it was not explicitly defined (de Haas et al., 2022; McCoy et al., 2012). Therefore, these results provide the first field observations and model analysis, in support of this physical explanation of entrainment in extremely large debris flows. In addition to bed saturation (Horton et al., 2019; Luna et al., 2012), basal friction angle and source volume were also sensitive parameters for the development of catastrophic debris flows (Figure 6.11). Volume was previously found to be a sensitive parameter for debris flow runout for three of the catastrophic debris flows in Montecito in 2018 (Barnhart et al., 2021). These catastrophic debris flows were also observed to entrain large volumes of sediment during transit (Morell et al., 2021). By pairing field observations to physical explanations of entrainment using numerical models, I have identified controls on the development of catastrophic debris flows, which as briefly outlined above may also hold true for other locations where debris flows frequently occur. These findings reiterate the need to prioritise models which consider entrainment when simulating catastrophic debris flows (Barnhart et al., 2021; Frank et al., 2015; Horton et al., 2019; Iverson and Ouyang, 2015; Luna et al., 2012). An understanding of what controls the development of catastrophic debris flows will also aid studies where the largest debris flows cannot be constrained. For example, the magnitude of catastrophic debris flows was underestimated in Wenchuan when considering debris flows as a single continuum. Therefore, I have demonstrated that it may not be possible to simply extrapolate the same

powerlaw relationship to represent catastrophic debris flows. These simple assumptions could have consequences on hazard runout models which use magnitude-frequency relationships (Huang et al., 2020) and analyse the role of debris flows in landscape evolution models (McGuire et al., 2022). These findings are particularly unique due to the fact that there is no other location, to my best knowledge, which has a comparable high-resolution record of high frequency debris flows which were triggered in close proximity. Since magnitude-frequency distributions that include several catastrophic debris flows can therefore not be produced in other locations, these findings, such as how catastrophic debris flows may be a separate process, should be considered when studying and modelling large debris flows elsewhere.

I explored how topography related to the GSDs deposited by post-earthquake debris flows as well as the runout of catastrophic debris flows. I found that whilst topography could not solely explain the transition to catastrophic debris flows in Wenchuan, it could be used to predict potential regions of deposition in catastrophic debris flows. On an individual debris flow scale, the catastrophic Luoquan debris flow showed a decrease in the deposition of boulder size and frequency with increases in channel width. In the catastrophic debris flows in Montecito, wider channels (>5^{th} order) corresponded to increases in scour (Morell et al., 2021), whereas in lower order sections of the channel (closer to the source) an increase in widths corresponded to an increase in deposition due to the decrease in momentum. These observations, combined with my results showing a relationship between channel width and boulder deposition, imply that the sediment deposited by debris flows differs as debris flows bulk in volume. The comparable findings for two catastrophic debris flows, indicate that channel topography may control the amount and size of sediment deposited along channels. An understanding of where and how much sediment is stored in different channel reaches is invaluable for quantifying sediment budgets as well as estimating the likelihood of hazards, such as debris flows (Benda, 1990; Francis et al., 2022). Predictions of where debris flows will deposit and erode may provide insight into where future debris flows will erode and deposit. de Haas et al. (2020) observed a memory effect in Illgraben, where channel sections previously eroded by debris flows, aggraded during the next flow. The high-

resolution GSDs measured in this thesis also provide an indication of the composition of bed material for future debris flows. Whilst, controls on debris flow entrainment have been explored in flume studies, the bed composition in these experiments typically remains the same (Roelofs et al., 2022). For future events along the Luoquan channel it will be interesting to compare how the deposited GSDs change during subsequent flows and influence bulking within the flow.

This thesis also presents some of the first high-resolution GSDs for the main sediment stores in the 2008 Wenchuan earthquake sediment cascade and the first, to our knowledge, from a recent earthquake. Accurate estimates of the coarse grains mobilised by post-earthquake processes are crucial as coarse grains are expected to account for up to 93% of all sediment mobilised by the landslides (Li et al., 2016; Xie et al., 2022), as supported by the GSD measurements in Chapter 5. These constraints on debris flow GSDs in Wenchuan can therefore be supplemented into models of post-earthquake sediment cascades to better constrain potential residence times for all seismically sourced material (Xie et al., 2022). The similar GSDs produced by both debris flows suggest that the GSD mobilised may be consistent across the region, or at least within the Pengguan Massif. In addition to the grain size mobilised, hillslope-channel connectivity also governs sediment export rates in the post-earthquake cascade (Dai et al., 2021; Li et al., 2016). Catastrophic debris flows are the main process connecting hillslopes and channels in the years following the Wenchuan earthquake (Francis et al., 2022). By determining controls on the runout length of catastrophic debris flows in Wenchuan, I have identified important parameters to consider when modelling hillslope-channel connectivity in the post-earthquake sediment cascade (Xie et al., 2022). I note that the occurrence of catastrophic debris flows in Wenchuan is more frequent than predicted using the parameters in this thesis. The occurrence of catastrophic debris flows in Wenchuan is therefore potentially stochastic or related to other conditions within the catchment. This research provides strong foundations to better understand the high frequency of debris flows following the 2008 Wenchuan earthquake. By comparing the post-earthquake debris flows in Wenchuan with other recent earthquakes, such as the 2015 Gorkha earthquake, we will also begin to

better constrain which future earthquakes are likely to induce a high frequency of cascading hazards in the years that follow.

Large, catastrophic debris flows have considerable societal and environmental consequences, such as fatalities, damage to infrastructure and large volumes of sediment deposited into streams (Dowling and Santi, 2014; Francis et al., 2022; Kean et al., 2019; Yang et al., 2021). Catastrophic debris flows occur across the globe, as seen by the 2018 Montecito, US, debris flows (Kean et al., 2019) and the 2019 debris flows in Wenchuan, China, analysed in this thesis (Yang et al., 2021). Current understanding of catastrophic debris flows is limited due to their unpredictable nature, inaccessible locations and extremely large volumes. Therefore, the research presented in this thesis, which has provided unique insight into the composition of catastrophic debris flow deposits (see GSDs in Chapter 5) as well as controls on the magnitude and frequency of catastrophic debris flows (see Chapter 6), is beneficial to debris flow research globally. The different magnitude and frequency relationship for catastrophic debris flows observed using the high-resolution dataset from Wenchuan will have practical implications for our ability to more accurately predict large debris flows and how far they will runout. For example, by highlighting the need to account for catastrophic debris flows individually in muti-hazard models. Further work which seeks to build on this in Wenchuan may involve identifying locations and buildings most at risk of catastrophic debris flows. The variables found to control catastrophic debris flow development in Wenchuan should also be explored for other debris flows globally as both sediment stores and source volume, which were important in Wenchuan, also appear important in recent literature (Barnhart et al., 2021; Morell et al., 2021). The high-resolution GSD dataset in Chapter 5, alongside the clear methodological protocols set out in Chapter 4, aim to improve the comparability of current grain size measurements. Additional datasets in combination with the dataset developed in this thesis, will be useful when validating numerical models which include debris flow grain size as well as developing tools for debris flow prediction which consider the amount and type of sediment available in channels (Benda, 1990; de Haas et al., 2020; Morell et al., 2021).

7.3 Further work

7.3.1 Bed composition and entrainment

My results have demonstrated that channel bed properties are crucial in controlling the development of catastrophic debris flows. This finding fits with previous studies which have shown that a high degree of saturation can increase the rate of erosion along the channel bed (Iverson et al., 2011; McCoy et al., 2012). Despite this, quantitative estimates of the sediment deposited in debris flow channels and entrained by future events remain scarce (Morell et al., 2021). Based on the results presented in this thesis, I believe that future work should focus on how the grain size of bed material controls entrainment by debris flows. This could be achieved by using small scale flume experiments, which have previously been used to demonstrate the role of flow grain size in controlling runout length but not bed composition (de Haas et al., 2015; Roelofs et al., 2022). Better constraints on the GSDs deposited by debris flows, as devised in this thesis, will add further insight into how channel sediment affects bulking in catastrophic debris flows.

In many mountain environments, debris flows scour until they reach bedrock (Benda, 1990; Morell et al., 2021), whereas the Wenchuan earthquake region is a transport-limited system and so the channels remain filled with sediment (Francis et al., 2022). The Wenchuan earthquake region therefore presents a potential location to record how much sediment is required for debris flows to bulk and become catastrophic debris flows. The entrainment rate in Massflow can be varied to account for different sediment depths. Field records of channel sediment depth are much more limited, and would require the use of high resolution DEMs of difference as used in other debris flow channels globally (de Haas et al., 2020; Morell et al., 2021).

7.3.2 Hillslope-channel connectivity and catastrophic debris flows

Hillslope-channel connectivity controls the rate of sediment exported from a catchment in the years following an earthquake (Croissant et al., 2019; Li et al., 2016). Recent studies have highlighted how landslide and debris flow size and location can influence hillslope-channel connectivity through time (Dai et al., 2021; Xie et al., 2022). As catastrophic debris flows are the main driver of hillslope-channel connectivity in Wenchuan in recent years (Francis et al., 2022), future research should focus on determining how much sediment from

these flows is directly exported to fluvial channels and how much remains in channels. This can be achieved using models and setting a cut off for the channel outlet (Horton et al., 2019). Studies of how debris flow entrainment related to runout length would also provide an interesting research topic. However, more automated approaches are required to analyse debris flow channel lengths on the scale observed in Wenchuan (n>2000). Recent research on rivers, which extracts centrelines along channels to later determine width, suggests that this may be possible for debris flows in the near future (Clubb et al., 2022).

7.3.3 Fluvial export of debris flow sediment

Episodic pulses from landslide and debris flows can increase the grain size of fluvial sediment and alter fluvial dynamics by increasing the bedload and influencing rates of fluvial incision and channel morphology (Attal and Lavé, 2006; Dingle et al., 2017; Sklar and Dietrich, 2004; Whittaker et al., 2010). Yet the export of seismically sourced sediment fluvially is poorly constrained, and predominantly focused on suspended sediment concentrations. To obtain a full picture of how an earthquake impacts fluvial systems, full GSDs are needed (Cook et al., 2018; Finnegan et al., 2018). Current estimates, which consider a full GSD are typically numerical models with a single median grain size for landslide deposits (Croissant et al., 2019). In this thesis, I have provided quantitative GSD estimates for post-earthquake debris flow deposits. These results provide an ideal basis from which sediment cascade models can be developed to account for the range of grain sizes found in post-earthquake deposits. This could involve upscaling an established model which considers how different sized sediment moves within fluvial networks (e.g. Czuba 2018). In addition, future work could seek to measure the GSDs of river bar sediment to better constrain the grain size signal associated with catastrophic debris flow pulses. Since gravel bars in Wenchuan are likely to be sources of coarse sediment, the methodological approach established in Chapter 4 could be used.

Appendix

The appendix contains tables showing the NRMSE and two-sample goodness-of-fit chi squared (χ^2) tests applied in Chapter 4 to compare GSDs measured using different techniques. These tables are included as Supplementary Material in the following published manuscript: Harvey E. L., Hales, T. C., Hobley, D. E. J., Liu, J., Fan, X. (2022). Measuring mass movement deposit grain-size distributions. Earth Surface Processes and Landforms. https://doi.org/10.1002/esp.5337.

Appendix Table 1

The NRMSE values when comparing entire GSDs and GSDs within the same range for methods in Tredegar. The same range refers to 3 mm to 34.3 mm for all techniques. All values given are in %. Dark red represents an NRMSE of 200% +, medium red 100 – 200% NRMSE, light red 50 – 100% NRMSE, orange 30 – 50% NRMSE, green <30% NRMSE

		Entire GSDs								GSDs with the same range							
Technique		Sieving	Survey Tape	Manual Photo Count	Pebble Count	pyDGS				Sieving	Survey Tape	Manual Photo Count	Pebble Count	pyDGS			
						1	0	-0.5	-1					1	0	-0.5	-1
Sieving	0.05		478	1244	2213			394			10.8	10.6	18.9			3.4	
	0.10		117	127	333			19.5			7.3	16.2	61			4.1	
	0.16		83.7	87.6	221			34.1			18	16	65.2			5.5	
	0.25		59.9	64.3	188			36.1			15.8	14.2	69.8			8	
	0.50		52.5	33.5	98.2			31.6			28	16.5	53.6			2.6	
	0.75		13.5	11.5	26.1			32.4			6.6	15.5	18.3			4.8	
	0.84		22.7	18.3	18			26.1			1	16.1	9.5			4.4	
	0.9		17.1	31.6	1			31.9			1	24.1	0.7			1.5	
	0.95		58.2	12.2	0.2			28.7			1.3	23	3.7			1.4	
Survey Tape	0.05					305	25							59.8	15.4	8.3	
	0.10					106	38.9							61.9	0.4	10.7	
	0.16					115	35.6							68.1	5	19.9	
	0.25					143	23.2							88.3	0.6	20.5	
	0.50					110	9.9							92.5	11.9	19.9	
	0.75					66.1	4.2							78.6	34.3	1.9	
	0.84					28.2	7.9							55.4	28.8	5.4	
	0.90					0.5	19.7							32.8	17.8	2.5	
	0.95					37.2	44.4							14.6	7.7	0.1	

Appendix Table 2

The NRMSE values when comparing entire GSDs and GSDs within the same range for methods in Liusha. The same range refers to a different range depending on the technique. All values given are in %. Dark red represents an NRMSE of 200% +, medium red 100 – 200% NRMSE, light red 50 – 100% NRMSE, orange 30 – 50% NRMSE, green <30% NRMSE.

Technique		Entire GSD							GSDs with the same range					
		Manual Photo Count	pyDGS						pyDGS					
			1 (MS 8)	1 (MS 6)	0 (MS 8)	0 (MS 6)	-0.5 (MS 8)	-0.5 (MS 6)	1 (MS 8)	1 (MS 6)	0 (MS 8)	0 (MS 6)	-0.5 (MS 8)	-0.5 (MS 6)
Sieving	0.05	143	809	950			72.8	74.5	182	183	20.6	27.8	46.4	52.9
	0.10	23	417	504			16.6	15.1	102	107	42.2	45.9	67.5	71
	0.16	44.9	131	171			63.5	62.6	66.3	71.8	47.8	50.4	73.7	76.3
	0.25	64	40.1	66.6			75.9	75.1	26.9	25.6	54.4	58.5	78.2	81.2
	0.50	41.8	12	7.4			77.3	75.8	2.3	6.7	50.3	49.8	74.7	76
	0.75	25.5	14.2	5.7			62.5	58.6	0.7	5.7	31.1	30.1	56.5	58.6
	0.84	20	20.3	0.1			55.7	50.3	3.6	8.9	18.2	18.2	42.4	45.8
	0.90	8.2	21.3	0.7			47.3	38.8	0.2	8	14.1	12.1	33.2	34.4
	0.95	29.8	45.8	29.2			56.2	48.1	2.6	11.8	10	1.3	21.5	18.1
Manual Photo Count	0.05		274	331			29	28.3	286	332	8.6	10.1		
	0.10		333	406			30.1	28.9	356	410	30.8	33.5		
	0.16		375	458			24.8	22.9	446	500	71.5	73.2		
	0.25		296	371			31.9	29.5	342	377	58.9	57.8		
	0.50		51.5	84.8			60.9	58.4	92.7	91	1.9	10.2		

	0.75		16.1	43			49.2	44	34.3	45.5	6.9	3.8		
	0.84		0.6	24.7			44.7	37.9	28.1	28.3	1.1	3.6		
	0.90		13.4	10.7			42	32.8	11.8	23.2	3.7	0.3		
	0.95		22.4	1.2			37.4	25.9	10.8	10.7	2.5	2.3		

Appendix Table 3

The NRMSE values when comparing entire GSDs and GSDs within the same range for methods in Luoquan. All values given are in %. Dark red represents an NRMSE of 200% +, medium red 100 – 200% NRMSE, light red 50 – 100% NRMSE, orange 30 – 50% NRMSE, green <30% NRMSE.

Technique		Entire GSD							GSDs with the same range					
			pyDGS						pyDGS					
		Manual Photo Count	1 (MS 8)	1 (MS 4)	0 (MS 8)	0 (MS 4)	-0.5 (MS 8)	-0.5 (MS 4)	1 (MS 8)	1 (MS 4)	0 (MS 8)	0 (MS 4)	-0.5 (MS 8)	-0.5 (MS 4)
Sieving	0.05	50.7	48.3	19.4			89.9	89.6	42.3	23.5	83.7	84.3	88.7	90.2
	0.10	37.8	48.7	17.5			91.5	91.2	46	16.5	84.5	82.2	91.1	91.1
	0.16	41.4	39.1	1.5			90.2	89.6	33.5	4.6	79.1	75.6	89.3	89.3
	0.25	24.4	30.5	23			88	86.9	20.7	29.5	71.4	66.1	86.3	86.2
	0.50	21	22.3	50.5			80.5	77.3	2.7	67.2	50	40.9	74.2	74.8
	0.75	48	44.6	14.9			77.2	70.5	8.6	73.3	26.7	6.8	55.2	55.5
	0.84	52.1	51.5	0.1			74.5	64.2	2.9	60.9	21.1	8.6	46	42.3
	0.90	40.2	57.8	14			73	58.4	2.8	31	13.9	4.9	34.2	36.7
	0.95	27.8	60.4	20.1			69.3	45.6	4.2	24.1	5.1	12.2	19.2	15.5
Manual Photo Count	0.05		4.9	63.4			79.5	79	73.9	88.4	6.4	26.1		
	0.10		17.2	33.2			86.4	85.8	0.3	38.8	52.1	52.1		
	0.16		3.2	72			83.4	82.4	10	77.1	49	41		
	0.25		5.9	66.4			83.7	82.2	16.5	72	44.5	42.1		
	0.50		0.5	92.7			75	71	8	99.1	39.9	19.4		
	0.75		8.8	126			55.1	42	20.4	132	13.2	34.3		
	0.84		1.4	109			46.8	25.1	24.6	112	2.1	50.4		
	0.90		29.3	44.1			54.7	30.4	22.7	76.4	5.5	45.7		
	0.95		45	11.1			57.3	24.3	17.1	44.4	8.3	32.2		

Appendix Table 4

The NRMSE when comparing pyDGS GSDs obtained using varying x exponents with the sieving GSDs over the size range for grains >80 mm. All values shown are in % and all values are below 30%.

	Liusha			Luoquan		
Sieving vs pyDGS (>80 mm)	**pyDGS *maxscale* 6 (80 mm to 161 mm)**			**pyDGS *maxscale* 4 (80 mm to 285 mm)**		
Percentiles	**x = -0.5 (%)**	**x = 0 (%)**	**x = -1 (%)**	**x = -0.5 (%)**	**x = 0 (%)**	**x = -1 (%)**
0.05	2.7	3.1	2.3	4.1	5.7	3
0.10	5.5	6.4	4.8	1.8	1.2	3.8
0.16	0.7	1.9	0.4	2.6	7.3	0.7
0.25	2	3.8	0.4	0.9	7.9	4
0.50	3.5	1.1	5.8	3.7	15.8	6
0.75	4.7	7.3	2	13.1	24.7	1.2
0.84	4.2	6.4	1.8	12.6	19.8	3.2
0.90	5.9	7.7	4	13.7	18.1	7.5
0.95	4.4	5.4	3.2	13.4	15.7	10.3

Appendix Table 5

The NRMSE when comparing sieving GSDs, both across the same range and the entire distribution, with the GSD derived by combining two pyDGS GSDs. For Liusha, this involved combining the GSD derived for 2.6 mm to 121 mm with a maxscale of 8 and an x exponent of 0 with the GSD derived for 80 mm to 161 mm with a maxscale of 6 and x exponent of -1. For Luoquan we combined the GSD derived for the range 3 mm to 142 mm with a maxscale of 8 and x exponent of 1 with the GSD derived for 80 mm to 285 mm with a maxscale of 4 and an x exponent of -1. All values given are in %. Dark red represents an NRMSE of 200% +, medium red 100 – 200% NRMSE, light red 50 – 100% NRMSE, orange 30 – 50% NRMSE, green <30% NRMSE.

	Liusha		Luoquan	
Percentiles	**Sieve Truncated & pyDGS Merged (%)**	**Sieve Full GSD & pyDGS Merged (%)**	**Sieve Truncated & pyDGS Merged (%)**	**Sieve Full GSD & pyDGS Merged (%)**
0.05	8.9	237	34.3	30.8
0.10	25.8	117	28.8	29.6
0.16	27.1	14.9	11.3	13.9
0.25	34.9	13.7	7.4	2
0.50	7.6	7	8.7	2.2
0.75	9.1	9.1	19.7	20.6
0.84	2.2	6.2	15.6	28.3
0.90	5.1	2	3.5	36.6
0.95	10.7	29.9	2.5	34

Appendix Table 6

The χ^2 values obtained from two-sample chi square goodness-of-fit tests. The tests were carried out on full GSDs for methods used in Tredegar, Luoquan and Liusha as well as truncated GSDs in Tredegar. Pebble count refer to a Wolman pebble count in the table.

Tredegar						
Entire GSDs						
Method 1	**Method 2**	**Degrees of Freedom**	**χ^2**	**$\chi^2_{0.05}$**	**$\chi^2_{0.01}$**	**Null hypothesis where $p < 0.05$**
Sieving	Survey Tape Counts	5	13.03	11.07	15.09	Reject
Sieving	Pebble Count	3	64.14	7.82	11.35	Reject
Sieving	pyDGS	5	25.95	11.07	15.09	Reject
Sieving	Manual Photo Count	3	28.95	7.82	11.35	Reject
Survey Tape Counts	Pebble Count	4	27.38	9.49	13.28	Reject
Survey Tape Counts	Manual Photo Count	3	11.54	7.82	11.35	Reject
Survey Tape Counts	pyDGS	5	83.55	11.07	15.09	Reject
Manual Pebble Count	pyDGS	3	62.04	7.82	11.35	Reject
Truncated GSDs						
Sieving	Survey Tape Counts	3	6.44	7.82	11.35	Not Reject
Sieving	Pebble Count	3	29.91	7.82	11.35	Reject
Sieving	pyDGS	3	1.01	7.82	11.35	Not Reject
Sieving	Manual Photo Count	3	12.64	7.82	11.35	Reject
Survey Tape Counts	Pebble Count	3	21.07	7.82	11.35	Reject
Survey Tape Counts	Manual Photo Counts	3	8.02	7.82	11.35	Reject
Survey Tape Counts	pyDGS	3	5.45	7.82	11.35	Not Reject
Manual Photo Count	pyDGS	3	22.21	7.82	11.35	Reject
Luoquan						
Sieving	Manual Photo Count	5	69.53	11.07	15.09	Reject
Sieving	pyDGS (x = -0.5)	5	762.42	11.07	15.09	Reject
Sieving	pyDGS (x = 1)	5	22.01	11.07	15.09	Reject
Liusha						
Sieving	Manual Photo Count	5	248.04	11.07	15.09	Reject

Sieving	pyDGS (x = -0.5)	5	159.13	11.07	15.09	Reject
Sieving	pyDGS (x = 1)	4	14.85	9.49	13.28	Reject

References

Abancó C, Hürlimann M. 2014. Estimate of the debris-flow entrainment using field and topographical data. Natural Hazards **71** : 363–383. DOI: 10.1007/s11069-013-0930-5

Allstadt KE, Farin M, Iverson RM, Obryk MK, Kean JW, Tsai VC, Rapstine TD, Logan M. 2020. Measuring Basal Force Fluctuations of Debris Flows Using Seismic Recordings and Empirical Green's Functions. Journal of Geophysical Research: Earth Surface **125** DOI: 10.1029/2020JF005590

Alstott J, Bullmore E, Plenz D. 2014. Powerlaw: A python package for analysis of heavy-tailed distributions. PLoS ONE **9** DOI: 10.1371/journal.pone.0085777

Anderson SW, Anderson SP, Anderson RS. 2015. Exhumation by debris flows in the 2013 Colorado front range storm. Geology **43** : 391–394. DOI: 10.1130/G36507.1

Attal M, Lavé J. 2006. Changes of bedload characteristics along the Marsyandi River (central Nepal): Implications for understanding hillslope sediment supply, sediment load evolution along fluvial networks, and denudation in active orogenic belts. Tectonics, Climate, and Landscape Evolution **398** : 143–171. DOI: 10.1130/2006.2398(09)

Attal M, Mudd SM, Hurst MD, Weinman B, Yoo K, Naylor M. 2015. Impact of change in erosion rate and landscape steepness on hillslope and fluvial sediments grain size in the Feather River basin (Sierra Nevada, California). Earth Surface Dynamics **3** : 201–222. DOI: 10.5194/esurf-3-201-2015

Bagnold RA. 1954. Experiments on a gravity-free dispersion of large solid spheres in a Newtonian fluid under shear. Proceedings of the Royal Society of London. Series A. Mathematical and Physical Sciences **225** : 49–63. DOI: 10.1098/rspa.1954.0186

Barclay WJ, Jackson DI, Mitchell M, Owens B, Riley NJ, White DE, Strong GE, Monkhouse RA. 1989. Geology of the South Wales Coalfield : Memoir for 1:50,000 geological sheet 232 (England and Wales) . HMSO: London

Bardou E, Jaboyedoff M. 2008. Debris flows as a factor of hillslope evolution controlled by a continuous or a pulse process? Geological Society Special

Publication **296** : 63–78. DOI: 10.1144/SP296.5

Barker T, Rauter M, Maguire ESF, Johnson CG, Gray JMNT. 2021. Coupling rheology and segregation in granular flows. Journal of Fluid Mechanics **909** DOI: 10.1017/jfm.2020.973

Barnhart KR, Jones RP, George DL, McArdell BW, Rengers FK, Staley DM, Kean JW. 2021. Multi-Model Comparison of Computed Debris Flow Runout for the 9 January 2018 Montecito, California Post-Wildfire Event. Journal of Geophysical Research: Earth Surface **126** DOI: 10.1029/2021JF006245

Baselt I, Queiroz de Oliveira G, Fischer JT, Pudasaini SP. 2021. Evolution of stony debris flows in laboratory experiments. Geomorphology **372** DOI: 10.1016/j.geomorph.2020.107431

Benda L. 1990. The influence of debris flows on channels and valley floors in the Oregon Coast Range, U.S.A. Earth Surface Processes and Landforms **15** : 457–466.

Benda L, Cundy TW. 1990. Predicting deposition of debris flows in mountain channels. Canadian Geotechnical Journal **27** : 409–417.

Benda L, Dunne T. 1997a. Stochastic forcing of sediment routing and storage in Channel Networks. Water Resources Research **33** : 2865–2880.

Benda L, Dunne T. 1997b. Stochastic forcing of sediment supply to channel networks from landsliding and debris flow. Water Resources Research **33** : 2849–2863.

Bennett GL, Molnar P, McArdell BW, Burlando P. 2014. A probabilistic sediment cascade model of sediment transfer in the Illgraben. Water Resources Research **50** : 1225–1244. DOI: 10.1002/2013WR014979.Reply

Berger C, McArdell BW, Schlunegger F. 2011a. Direct measurement of channel erosion by debris flows, Illgraben, Switzerland. Journal of Geophysical Research: Earth Surface **116** : 1–18. DOI: 10.1029/2010JF001722

Berger C, McArdell BW, Schlunegger F. 2011b. Sediment transfer patterns at the Illgraben catchment, Switzerland: Implications for the time scales of debris flow activities. Geomorphology **125** : 421–432. DOI: 10.1016/j.geomorph.2010.10.019

Berti M, Genevois R, Simoni A, Tecca PR. 1999. Field observations of a debris flow event in the Dolomites. Geomorphology **29** : 265–274. DOI: 10.1016/S0169-555X(99)00018-5

Bitelli G, Dubbini M, Zanutta A. 2004. Terrestrial laser scanning and digital photogrammetry techniques to monitor landslide bodies. International Archives of Photogrammetry, Remote Sensing and Spatial Information Sciences **35** : 246–251.

Blair TC. 1999. Cause of dominance by sheetflood vs. debris-flow processes on two adjoining alluvial fans, Death Valley, California. Sedimentology **46** : 1015–1028.

Blair TC, McPherson JG. 1998. Recent debris-flow processes and resultant form and facies of the dolomite alluvial fan, Owens Valley, California. Journal of Sedimentary Research **68** : 800–818. DOI: 10.2110/jsr.68.800

Von Boetticher A, Turowski JM, McArdell BW, Rickenmann D, Kirchner JW. 2016. DebrisInterMixing-2.3: A finite volume solver for three-dimensional debris-flow simulations with two calibration parameters - Part 1: Model description. Geoscientific Model Development **9** : 2909–2923. DOI: 10.5194/gmd-9-2909-2016

Boniello MA, Calligaris C, Lapasin R, Zini L. 2010. Rheological investigation and simulation of a debris-flow event in the Fella watershed. Natural Hazards and Earth System Science **10** : 989–997. DOI: 10.5194/nhess-10-989-2010

Brardinoni F, Church M. 2004. Representing the landslide magnitude-frequency relation: Capilano River basin, British Columbia. Earth Surface Processes and Landforms **29** : 115–124. DOI: 10.1002/esp.1029

Brasington J, Vericat D, Rychkov I. 2012. Modeling river bed morphology, roughness, and surface sedimentology using high resolution terrestrial laser scanning. Water Resources Research **48** : 1–18. DOI: 10.1029/2012WR012223

Brayshaw D, Hassan MA. 2009. Debris flow initiation and sediment recharge in gullies. Geomorphology **109** : 122–131. DOI: 10.1016/j.geomorph.2009.02.021

Breard ECP, Dufek J, Fullard L, Carrara A. 2020. The Basal Friction Coefficient of Granular Flows With and Without Excess Pore Pressure: Implications for Pyroclastic Density Currents, Water-Rich Debris Flows, and Rock and

Submarine Avalanches. Journal of Geophysical Research: Solid Earth **125** : 1–22. DOI: 10.1029/2020JB020203

Breien H, De Blasio F V., Elverhøi A, Høeg K. 2008. Erosion and morphology of a debris flow caused by a glacial lake outburst flood, Western Norway. Landslides **5** : 271–280. DOI: 10.1007/s10346-008-0118-3

Brocklehurst SH, Whipple KX. 2004. Hypsometry of glaciated landscapes. Earth Surface Processes and Landforms **29** : 907–926. DOI: 10.1002/esp.1083

Bunte K, Abt SR. 2001a. Sampling frame for improving pebble count accuracy in coarse gravel-bed streams. Journal of the American Water Resources Association **37** : 1001–1014. DOI: 10.1111/j.1752-1688.2001.tb05528.x

Bunte K, Abt SR. 2001b. Sampling surface and sub-surface particle size distributions in wadeable gravel- and cobble-bed streams for analysis in sediment transport, hydraulics, and streambed monitoring

Buscombe D. 2013. Transferable wavelet method for grain-size distribution from images of sediment surfaces and thin sections, and other natural granular patterns. Sedimentology **60** : 1709–1732. DOI: 10.1111/sed.12049

Buscombe D. 2020. SediNet: A configurable deep learning model for mixed qualitative and quantitative optical granulometry. Earth Surface Processes and Landforms **45** : 638–651. DOI: https://doi.org/10.1002/esp.4760

Caballero L, Sarocchi D, Borselli L, Cárdenas AI. 2012. Particle interaction inside debris flows: Evidence through experimental data and quantitative clast shape analysis. Journal of Volcanology and Geothermal Research **231–232** : 12–23. DOI: 10.1016/j.jvolgeores.2012.04.007

Caine N. 1980. The Rainfall Intensity: Duration Control of Shallow Landslides and Debris Flows. Geografiska Annaler. Series A, Physical Geography **62** : 23–27.

Cannon SH, Bigio ER, Mine E. 2001a. A process for fire-related debris flow initiation, Cerro Grande fire, New Mexico. Hydrological Processes **15** : 3011–3023. DOI: 10.1002/hyp.388

Cannon SH, Ellen SD. 1985. Rainfall conditions for abundant debris avalanches in the San Francisco Bay region, California. California Geology **38** : 267–272.

Cannon SH, Kirkham RM, Parise M. 2001b. Wildfire-related debris-flow initiation processes, Storm King Mountain, Colorado. Geomorphology **39** : 171–188. DOI: 10.1016/S0169-555X(00)00108-2

Cannon SH, Savage WZ. 1988. A mass-change model for the estimation of debris flow runout. Journal of Geology **96** : 221–227. DOI: 10.5962/bhl.part.18644

Carbonneau PE, Bergeron N, Lane SN. 2005. Automated grain size measurements from airborne remote sensing for long profile measurements of fluvial grain sizes. Water Resources Research **41** : 1–9. DOI: 10.1029/2005WR003994

Carbonneau PE, Lane SN, Bergeron NE. 2004. Catchment-scale mapping of surface grain size in gravel bed rivers using airborne digital imagery. Water Resources Research **40** : 1–11. DOI: 10.1029/2003WR002759

Casagli N, Ermini L, Rosati G. 2003. Determining grain size distribution of the material composing landslide dams in the Northern Apennines: Sampling and processing methods. Engineering Geology **69** : 83–97. DOI: 10.1016/S0013-7952(02)00249-1

Cenderelli DA, Kite JS. 1998. Geomorphic effects of large debris flows on channel morphology at North Fork Mountain, Eastern West Virginia, USA. Earth Surface Processes and Landforms **23** : 1–19.

Chang M, Tang C, Van Asch TWJ, Cai F. 2017. Hazard assessment of debris flows in the Wenchuan earthquake-stricken area, South West China. Landslides **14** : 1783–1792. DOI: 10.1007/s10346-017-0824-9

Chen C. 1988. Generalized viscoplastic modeling of debris flow. Journal of Hydraulic Engineering Engineering **114** : 237–258.

Chen H, Dadson S, Chi YG. 2006. Recent rainfall-induced landslides and debris flow in northern Taiwan. Geomorphology **77** : 112–125. DOI: 10.1016/j.geomorph.2006.01.002

Chen H, Petley DN. 2005. The impact of landslides and debris flows triggered by Typhoon Mindulle in Taiwan. Quarterly Journal of Engineering Geology and Hydrogeology **38** : 301–304. DOI: 10.1144/1470-9236/04-077

Chen H, Su D, Chen K. 2001. Some Case Studies on the Engineering Geological

Characteristics of Debris Flows in Taiwan. Western Pacific Earth Sciences **1** : 265–296.

Chen HX, Zhang LM, Zhang S. 2014. Evolution of debris flow properties and physical interactions in debris-flow mixtures in the Wenchuan earthquake zone. Engineering Geology **182** : 136–147. DOI: 10.1016/j.enggeo.2014.08.004

Chen SF, Wilson CJL. 1996. Emplacement of the Longmen Shan Thrust-Nappe Belt along the eastern margin of the Tibetan Plateau. Journal of Structural Geology **18** : 413–430. DOI: 10.1016/0191-8141(95)00096-V

Church MA, McLean DG, Wolcott JF. 1987. River bed gravels: sampling and analysis. In Gravel Bed Rivers , Thorne CR, Bathurst JC, and Hey RD (eds). John Wiley: Chichester; 43–87.

Clauset A, Shalizi CR, Newman MEJ. 2007. Power-law distributions in empirical data. DOI: 10.1137/070710111

Cleveland WS. 1979. Robust locally weighted regression and smoothing scatterplots. Journal of the American statistical association **74** : 829–836.

Clubb FJ, Weir EF, Mudd SM. 2022. Continuous measurements of valley floor width in mountainous landscapes. Earth Surface Dynamics **10** : 437–456. DOI: 10.5194/esurf-10-437-2022

Cook KL, Andermann C, Gimbert F, Adhikari BR, Hovius N. 2018. Supplementary Materials for Glacial lake outburst floods as drivers of fluvial erosion in the Himalaya. Science **362** : 53. DOI: 10.1126/science.aat4981

Cook KL, Royden LH, Burchfiel BC, Lee YH, Tan X. 2013. Constraints on cenozoic tectonics in the southwestern longmen shan from low-temperature thermochronology. Lithosphere **5** : 393–406. DOI: 10.1130/L263.1

Coussot P, Laigle D, Arattano M, Deganutti A, Marchi L. 1998. Direct Determination of Rheological Characteristics of Debris Flow. Journal of Hydraulic Engineering **124** : 865–868. DOI: 10.1061/(asce)0733-9429(2000)126:2(158)

Cowie PA, Whittaker AC, Attal M, Roberts G, Tucker GE, Ganas A. 2008. New constraints on sediment-flux-dependent river incision: Implications for extracting tectonic signals from river profiles. Geology **36** : 535–538. DOI: 10.1130/G24681A.1

Croissant T, Hilton RG, Li GK, Howarth J, Wang J, Harvey EL, Steer P, Densmore AL. 2021. Pulsed carbon export from mountains by earthquake-triggered landslides explored in a reduced-complexity model. Earth Surface Dynamics Discussions **9** : 823–844. DOI: 10.5194/esurf-2020-95

Croissant T, Steer P, Lague D, Davy P, Jeandet L, Hilton RG. 2019. Seismic cycles, earthquakes, landslides and sediment fluxes: Linking tectonics to surface processes using a reduced-complexity model. Geomorphology **339** : 87–103. DOI: 10.1016/j.geomorph.2019.04.017

Crosta GB, Frattini P, Fusi N. 2007. Fragmentation in the Val Pola rock avalanche, Italian Alps. Journal of Geophysical Research: Earth Surface **112** : 1–23. DOI: 10.1029/2005JF000455

Cruden DM, Varnes DJ. 1996. Landslide types and processes. In Landslides Investigation and Mitigation. Special Report 247, Transportation Research Board, National Research Council , Turner AK and Schuster RL (eds). National Academy Press: Washington DC; 36–75.

Cucchiaro S, Cavalli M, Vericat D, Crema S, Llena M, Beinat A, Marchi L, Cazorzi F. 2018. Monitoring topographic changes through 4D-structure-from-motion photogrammetry: application to a debris-flow channel. Environmental Earth Sciences **77** : 1–21. DOI: 10.1007/s12665-018-7817-4

Cui P, Zhu Y yan, Han Y shun, Chen X qing, Zhuang J qi. 2009. The 12 May Wenchuan earthquake-induced landslide lakes: Distribution and preliminary risk evaluation. Landslides **6** : 209–223. DOI: 10.1007/s10346-009-0160-9

Cuttler MVW, Lowe RJ, Falter JL, Buscombe D. 2017. Estimating the settling velocity of bioclastic sediment using common grain-size analysis techniques. Sedimentology **64** : 987–1004. DOI: 10.1111/sed.12338

Czuba JA. 2018. A Lagrangian framework for exploring complexities of mixed-size sediment transport in gravel-bedded river networks. Geomorphology **321** : 146–152. DOI: 10.1016/j.geomorph.2018.08.031

D'Agostino V, Cesca M, Marchi L. 2010. Field and laboratory investigations of runout distances of debris flows in the Dolomites (Eastern Italian Alps). Geomorphology **115** : 294–304. DOI: 10.1016/j.geomorph.2009.06.032

D'Arcy M, Roda-Boluda DC, Whittaker AC. 2017. Glacial-interglacial climate

changes recorded by debris flow fan deposits, Owens Valley, California. Quaternary Science Reviews **169** : 288–311. DOI: 10.1016/j.quascirev.2017.06.002

Dadson SJ et al. 2004. Earthquake-triggered increase in sediment delivery from an active mountain belt. Geology **32** : 733–736. DOI: 10.1130/G20639.1

Dahlquist MP, West AJ. 2019. Initiation and Runout of Post-Seismic Debris Flows: Insights From the 2015 Gorkha Earthquake. Geophysical Research Letters **46** : 9658–9668. DOI: 10.1029/2019GL083548

Dai F, Lee CF, Wang S. 1999. Analysis of rainstorm-induced slide–debris flows on natural terrain of Lantau Island, Hong Kong. Engineering Geology **51** : 279–290.

Dai L, Scaringi G, Fan X, Yunus AP, Liu-Zeng J, Xu Q, Huang R. 2021. Coseismic Debris Remains in the Orogen Despite a Decade of Enhanced Landsliding. Geophysical Research Letters **48** : 1–11. DOI: 10.1029/2021GL095850

Daniels MD, McCusker MH. 2010. Operator bias characterizing stream substrates using Wolman pebble counts with a standard measurement template. Geomorphology **115** : 194–198. DOI: 10.1016/j.geomorph.2009.09.038

Davies T, McSaveney M, Kelfoun K. 2010. Runout of the Socompa volcanic debris avalanche, Chile: A mechanical explanation for low basal shear resistance. Bulletin of Volcanology **72** : 933–944. DOI: 10.1007/s00445-010-0372-9

Davies TR, McSaveney MJ. 2009. The role of rock fragmentation in the motion of large landslides. Engineering Geology **109** : 67–79. DOI: 10.1016/j.enggeo.2008.11.004

Densmore AL, Ellis MA, Li Y, Zhou R, Hancock GS, Richardson N. 2007. Active tectonics of the Beichuan and Pengguan faults at the eastern margin of the Tibetan Plateau. Tectonics **26** : 1–17. DOI: 10.1029/2006TC001987

Densmore AL, Hovius N. 2000. Topographic fingerprints of bedrock landslides. Geology **28** : 371–374.

Densmore AL, Li Y, Richardson NJ, Zhou R, Ellis M, Zhang Y. 2010. The role of late quaternary upper-crustal faults in the 12 may 2008 Wenchuan

earthquake. Bulletin of the Seismological Society of America **100** : 2700–2712. DOI: 10.1785/0120090294

Detert M, Weitbrecht V. 2012. Automatic object detection to analyze the geometry of gravel grains - A free stand-alone tool. River Flow 2012 - Proceedings of the International Conference on Fluvial Hydraulics **1** : 595–600.

Di B, Zeng H, Zhang M, Ustin SL, Tang Y, Wang Z, Chen N, Zhang B. 2010. Quantifying the spatial distribution of soil mass wasting processes after the 2008 earthquake in Wenchuan, China. A case study of the Longmenshan area. Remote Sensing of Environment **114** : 761–771. DOI: 10.1016/j.rse.2009.11.011

DiBiase RA, Lamb MP, Ganti V, Booth AM. 2017. Slope, grain size, and roughness controls on dry sediment transport and storage on steep hillslopes. Journal of Geophysical Research: Earth Surface **122** : 941–960. DOI: 10.1002/2016JF003970

Dingle EH, Attal M, Sinclair HD. 2017. Abrasion-set limits on Himalayan gravel flux. Nature **544** : 471–474. DOI: 10.1038/nature22039 [online] Available from: http://dx.doi.org/10.1038/nature22039

Diplas P, Fripp JB. 1992. Properties of Various Sediment Sampling Procedures. Journal of Hydraulic Engineering **118** : 955–970. DOI: 10.1061/(asce)0733-9429(1992)118:7(955)

Diplas P, Sutherland AJ. 1988. Sampling Techniques for Gravel Sized Sediments. Journal of Hydraulic Engineering **114** : 484–501. DOI: 10.1061/(asce)0733-9429(1988)114:5(484)

Domènech G, Fan X, Scaringi G, van Asch TWJ, Xu Q, Huang R, Hales TC. 2019. Modelling the role of material depletion, grain coarsening and revegetation in debris flow occurrences after the 2008 Wenchuan earthquake. Engineering Geology **250** : 34–44. DOI: 10.1016/j.enggeo.2019.01.010

Domènech G, Yang F, Guo X, Fan X, Scaringi G, Dai L, He C, Xu Q, Huang R. 2018. Two multi-temporal datasets to track the enhanced landsliding after the 2008 Wenchuan earthquake (Version V2) [Data set]. Zenodo [online] Available from: https://doi.org/10.5281/zenodo.1484667

Dowling CA, Santi PM. 2014. Debris flows and their toll on human life: A global

analysis of debris-flow fatalities from 1950 to 2011. Natural Hazards **71** : 203–227. DOI: 10.1007/s11069-013-0907-4

Dufresne A, Dunning SA. 2017. Process dependence of grain size distributions in rock avalanche deposits. Landslides **14** : 1555–1563. DOI: 10.1007/s10346-017-0806-y

Dunning SA. 2006. The grain-size distribution of rock avalanche deposits in valley-confined settings. Italian Journal of Engineering Geology and Environment **1** : 117–121. DOI: 10.4408/IJEGE.2006-01.S-15

Dunning SA, Massey CI, Rosser NJ. 2009. Structural and geomorphological features of landslides in the Bhutan Himalaya derived from Terrestrial Laser Scanning. Geomorphology **103** : 17–29. DOI: 10.1016/j.geomorph.2008.04.013

Eaton BC, Dan Moore R, Mackenzie LG. 2019. Percentile-based grain size distribution analysis tools (GSDtools)-Estimating confidence limits and hypothesis tests for comparing two samples. Earth Surface Dynamics **7** : 789–806. DOI: 10.5194/esurf-7-789-2019

Eaton LS, Morgan BA, Kochel RC, Howard AD. 2003. Role of debris flows in long-term landscape denudation in the central Appalachians of Virginia. Geology **31** : 339–342. DOI: 10.1130/0091-7613(2003)031<0339:RODFIL>2.0.CO;2

Edwards AN, Viroulet S, Johnson CG, Gray JMNT. 2021. Erosion-deposition dynamics and long distance propagation of granular avalanches. Journal of Fluid Mechanics **915** : 1–40. DOI: 10.1017/jfm.2021.34

Egholm DL, Knudsen MF, Sandiford M. 2013. Lifespan of mountain ranges scaled by feedbacks between landsliding and erosion by rivers. Nature **498** : 475–478. DOI: 10.1038/nature12218

Evans SG, Bishop NF, Fidel Smoll L, Valderrama Murillo P, Delaney KB, Oliver-Smith A. 2009. A re-examination of the mechanism and human impact of catastrophic mass flows originating on Nevado Huascarán, Cordillera Blanca, Peru in 1962 and 1970. Engineering Geology **108** : 96–118. DOI: 10.1016/j.enggeo.2009.06.020

Evans SG, Delaney KB, Rana NM. 2021. The occurrence and mechanism of catastrophic mass flows in the mountain cryosphere . 2nd ed. Elsevier Inc.

[online] Available from: http://dx.doi.org/10.1016/B978-0-12-817129-5.00004-4

Fan X et al. 2019a. Earthquake-Induced Chains of Geologic Hazards: Patterns, Mechanisms, and Impacts. Reviews of Geophysics **57** : 421–503. DOI: 10.1029/2018RG000626

Fan X et al. 2019b. Two multi-temporal datasets that track the enhanced landsliding after the 2008 Wenchuan earthquake. Earth System Science Data **11** : 35–55. DOI: 10.5194/essd-11-35-2019

Fan X, Domènech G, Scaringi G, Huang R, Xu Q, Hales TC, Dai L, Yang Q, Francis OR. 2018a. Spatio-temporal evolution of mass wasting after the 2008 M w 7.9 Wenchuan earthquake revealed by a detailed multi-temporal inventory. Landslides **15** : 2325–2341. DOI: 10.1007/s10346-018-1054-5

Fan X, Juang CH, Wasowski J, Huang R, Xu Q, Scaringi G, Westen CJ Van, Havenith H. 2018b. What we have learned from the 2008 Wenchuan Earthquake and its aftermath : A decade of research and challenges. Engineering Geology **241** : 25–32. DOI: 10.1016/j.enggeo.2018.05.004

Fan X, van Westen CJ, Korup O, Gorum T, Xu Q, Dai F, Huang R, Wang G. 2012. Transient water and sediment storage of the decaying landslide dams induced by the 2008 Wenchuan earthquake, China. Geomorphology **171**–**172** : 58–68. DOI: 10.1016/j.geomorph.2012.05.003

Fan X, Yunus AP, Scaringi G, Catani F, Siva Subramanian S, Xu Q, Huang R. 2021. Rapidly Evolving Controls of Landslides After a Strong Earthquake and Implications for Hazard Assessments. Geophysical Research Letters **48** : 1–12. DOI: 10.1029/2020GL090509

Fannin RJ, Wise MP. 2001. An empirical-statistical model for debris flow travel distance. Canadian Geotechnical Journal **38** : 982–994. DOI: 10.1139/cgj-38-5-982

Finnegan NJ, Broudy KN, Nereson AL, Roering JJ, Handwerger AL, Bennett G. 2018. Fluvial boulder transport controls valley blocking by earthflows in the California Coast Range, USA. Earth Surface Dynamics Discussions : 1–35.

Folk RL, Ward WC. 1957. Brazos River bar: a study in the significance of grain size parameters. Journal of Sedimentary Petrology **27** : 3–26.

Forterre Y, Pouliquen O. 2008. Flows of dense granular media. Annual Review of Fluid Mechanics **40** : 1–24. DOI: 10.1146/annurev.fluid.40.111406.102142

Foster AD, Claeson SM, Bisson PA, Heimburg J. 2020. Aquatic and riparian ecosystem recovery from debris flows in two western Washington streams, USA. Ecology and Evolution **10** : 2749–2777. DOI: 10.1002/ece3.5919

Francis OR, Fan X, Hales T, Hobley D, Xu Q, Huang R. 2022. The Fate of Sediment After a Large Earthquake. Journal of Geophysical Research: Earth Surface **127** : 1–19. DOI: 10.1029/2021jf006352

Francis OR, Hales TC, Hobley DEJ, Fan X, Horton AJ, Scaringi G, Huang R. 2020. The impact of earthquakes on orogen-scale exhumation. Earth Surface Dynamics **8** : 579–593. DOI: 10.5194/esurf-8-579-2020

Frank F, McArdell BW, Huggel C, Vieli A. 2015. The importance of entrainment and bulking on debris flow runout modeling: Examples from the Swiss Alps. Natural Hazards and Earth System Sciences **15** : 2569–2583. DOI: 10.5194/nhess-15-2569-2015

Fripp JB, Diplas P. 1993. Surface Sampling in Gravel Streams. Journal of Hydraulic Engineering **119** : 473–490. DOI: 10.1061/(asce)0733-9429(1993)119:4(473)

Gabet EJ, Bookter A. 2008. A morphometric analysis of gullies scoured by post-fire progressively bulked debris flows in southwest Montana, USA. Geomorphology **96** : 298–309. DOI: 10.1016/j.geomorph.2007.03.016

Gabet EJ, Mudd SM. 2006. The mobilization of debris flows from shallow landslides. Geomorphology **74** : 207–218. DOI: 10.1016/j.geomorph.2005.08.013

Ge Y, Cui P, Zhang J, Zeng C, Su F. 2015. Catastrophic Debris Flows on July 10th 2013 along the Min River in Areas Seriously-hit by the Wenchuan Earthquake. Journal of Mountain Science **12** : 186–206.

Genevois R, Galgaro A, Tecca PR. 2001. Image analysis for debris flow properties estimation. Physics and Chemistry of the Earth, Part C: Solar, Terrestrial and Planetary Science **26** : 623–631. DOI: 10.1016/S1464-1917(01)00059-9

Genevois R, Tecca PR, Berti M, Simoni A. 2000. Debris flows in Dolomites :

experimental data from a monitoring system. 2nd International Conference on Debris-Flow Hazard Mitigation

George GT. 2015. The Geology of South Wales . Second Edi. George GT (ed). Geoserv Publishing

Ghasemi A, Kaitna R, Fritton P, Blankenship BT, Feng Q, Densmore A, de Haas T, Hill KM. 2019. Erosion by experimental debris flows: Particle size effects. Debris-Flow Hazards Mitigation: Mechanics, Monitoring, Modeling, and Assessment - Proceedings of the 7th International Conference on Debris-Flow Hazards Mitigation : 10–17.

Godard V, Lavé J, Carcaillet J, Cattin R, Bourlès D, Zhu J. 2010. Spatial distribution of denudation in Eastern Tibet and regressive erosion of plateau margins. Tectonophysics **491** : 253–274. DOI: 10.1016/j.tecto.2009.10.026

Godard V, Pik R, Lav J, Cattin R, Tibari B, De Sigoyer J, Pubellier M, Zhu J. 2009. Late Cenozoic evolution of the central Longmen Shan, eastern Tibet: Insight from (U-Th)/He thermochronometry. Tectonics **28** : 1–17. DOI: 10.1029/2008TC002407

Golick LA, Daniels KE. 2009. Mixing and segregation rates in sheared granular materials. Physical Review E - Statistical, Nonlinear, and Soft Matter Physics **80** : 1–4. DOI: 10.1103/PhysRevE.80.042301

Graham DJ, Reid I, Rice SP. 2005. Automated sizing of coarse-grained sediments: Image-processing procedures. Mathematical Geology **37** : 1–28. DOI: 10.1007/s11004-005-8745-x

Graham DJ, Rollet AJ, Piégay H, Rice SP. 2010. Maximizing the accuracy of image-based surface sediment sampling techniques. Water Resources Research **46** : 1–15. DOI: 10.1029/2008WR006940

Gray JMNT. 2018. Particle Segregation in Dense Granular Flows. Annual Review of Fluid Mechanics **50** : 407–433. DOI: 10.1146/annurev-fluid-122316-045201

Gray JMNT, Ancey C. 2011. Multi-component particle-size segregation in shallow granular avalanches. Journal of Fluid Mechanics **678** : 535–588. DOI: 10.1017/jfm.2011.138

Gray JMNT, Ancey C. 2015. Particle-size and -density segregation in granular

free-surface flows. Journal of Fluid Mechanics **779** : 622–668. DOI: 10.1017/jfm.2015.438

Gray JMNT, Gajjar P, Kokelaar P. 2015. Particle-size segregation in dense granular avalanches. Comptes Rendus Physique **16** : 73–85. DOI: 10.1016/j.crhy.2015.01.004

Griswold JP, Iverson RM. 2008. Mobility Statistics and Automated Hazard Mapping for Debris Flows and Rock Avalanches Scientific Investigations Report 2007 – 5276. USGS Scientific Investigations Report : 62.

Guerit L, Barrier L, Liu Y, Narteau C, Lajeunesse E, Gayer E, Métivier F. 2018. Uniform grain-size distribution in the active layer of a shallow, gravel-bedded, braided river (the Urumqi River, China) and implications for paleo-hydrology. Earth Surface Dynamics **6** : 1011–1021. DOI: 10.5194/esurf-6-1011-2018

Guo X, Cui P, Li Y, Ma L, Ge Y, Mahoney WB. 2016a. Intensity-duration threshold of rainfall-triggered debris flows in the Wenchuan Earthquake affected area, China. Geomorphology **253** : 208–216. DOI: 10.1016/j.geomorph.2015.10.009

Guo X, Cui P, Li Y, Zou Q, Kong Y. 2016b. The formation and development of debris flows in large watersheds after the 2008 Wenchuan Earthquake. Landslides **13** : 25–37. DOI: 10.1007/s10346-014-0541-6

Gupta SK, Shukla DP. 2018. Application of drone for landslide mapping, dimension estimation and its 3D reconstruction. Journal of the Indian Society of Remote Sensing **46** : 903–914. DOI: 10.1007/s12524-017-0727-1

Guthrie RH, Hockin A, Colquhoun L, Nagy T, Evans SG, Ayles C. 2010. An examination of controls on debris flow mobility: Evidence from coastal British Columbia. Geomorphology **114** : 601–613. DOI: 10.1016/j.geomorph.2009.09.021

Guzzetti F, Malamud BD, Turcotte, Donald L, Reichenbach P. 2002. Power-law correlations of landslide areas in central Italy. Earth and Planetary Science Letters **195** : 169–183.

de Haas T, Braat L, Leuven JRFW, Lokhorst IR, Kleinhans MG. 2015. Effects of debris flow composition on runout, depositional mechanisms, and deposit morphology in laboratory experiments. Journal of Geophysical Research: Earth

Surface **120** : 1949–1972. DOI: 10.1002/2015JF003525

de Haas T, Kruijt A, Densmore AL. 2018. Effects of debris-flow magnitude-frequency distribution on avulsions and fan development. Earth surface processes and landforms. **43** : 2779–2793. [online] Available from: http://dx.doi.org/10.1037/xge0000076

de Haas T, McArdell BW, Nijland W, Åberg AS, Hirschberg J, Huguenin P. 2022. Flow and Bed Conditions Jointly Control Debris-Flow Erosion and Bulking. Geophysical Research Letters **49** : 1–10. DOI: 10.1029/2021gl097611

de Haas T, Nijland W, de Jong SM, McArdell BW. 2020. How memory effects, check dams, and channel geometry control erosion and deposition by debris flows. Scientific Reports **10** DOI: 10.1038/s41598-020-71016-8

de Haas T, Woerkom T van. 2016. Bed scour by debris flows: experimental investigation of effects of debris-flow composition. Earth Surface Processes and Landforms **41** : 1951–1966. DOI: 10.1002/esp.3963

Hales TC. 2018. Modelling biome-scale root reinforcement and slope stability. Earth Surface Processes and Landforms **43** : 2157–2166. DOI: 10.1002/esp.4381

Havenith H-B, Torgoev A, Schlögel R, Micu M, Braun A. 2016. A new classification of earthquake-induced landslide event sizes based on seismotectonic, topographic, climatic and geologic factors. Geoenvironmental Disasters **3** : 1–24. DOI: 10.1186/s40677-016-0041-1

Hill KM, Tan DS. 2014. Segregation in dense sheared flows: Gravity, temperature gradients, and stress partitioning. Journal of Fluid Mechanics **756** : 54–88. DOI: 10.1017/jfm.2014.271

Horton AJ, Hales TC, Ouyang C, Fan X. 2019. Identifying post-earthquake debris flow hazard using Massflow. Engineering Geology **258** DOI: 10.1016/j.enggeo.2019.05.011

Hovius N, Meunier P. 2012. Earthquake ground motion and patterns of seisrnically induced landsliding. In Landslides: Types, Mechanisms and Modeling , Clague JJ and Stead D (eds). Cambridge University Press: Cambridge; pp.24-36.

Hovius N, Meunier P, Lin CW, Chen H, Chen YG, Dadson S, Horng MJ, Lines M.

2011. Prolonged seismically induced erosion and the mass balance of a large earthquake. Earth and Planetary Science Letters **304** : 347–355. DOI: 10.1016/j.epsl.2011.02.005

Hovius N, Stark CP, Allen PA. 1997. Sediment flux from a mountain belt derived by landslide mapping. Geology **25** : 231–234. DOI: 10.1130/0091-7613(1997)025<0231:SFFAMB>2.3.CO;2

Hovius N, Stark CP, Hao-Tsu C, Jiun-Chuan L. 2000. Supply and Removal of Sediment in a Landslide-Dominated Mountain Belt: Central Range, Taiwan. The Journal of Geology **108** : 73–89. DOI: 10.1086/314387

Howarth JD, Fitzsimons SJ, Norris RJ, Jacobsen GE. 2012. Lake sediments record cycles of sediment flux driven by large earthquakes on the Alpine fault, New Zealand. Geology **40** : 1091–1094. DOI: 10.1130/G33486.1

Hsu L, Dietrich WE, Sklar LS. 2008. Experimental study of bedrock erosion by granular flows. Journal of Geophysical Research: Earth Surface **113** DOI: 10.1029/2007JF000778

Hsu L, Dietrich WE, Sklar LS. 2014. Mean and fluctuating basal forces generated by granular flows: Laboratory observations in a large vertically rotating drum. Journal of Geophysical Research: Earth Surface **119** : 1283–1309. DOI: 10.1002/2013JF003078

Hu W, Scaringi G, Xu Q, Pei Z, Van Asch TWJ, Hicher PY. 2017. Sensitivity of the initiation and runout of flowslides in loose granular deposits to the content of small particles: An insight from flume tests. Engineering Geology **231** : 34–44. DOI: 10.1016/j.enggeo.2017.10.001

Huang J, Hales TC, Huang R, Ju N, Li Q, Huang Y. 2020. A hybrid machine-learning model to estimate potential debris-flow volumes. Geomorphology **367** DOI: 10.1016/j.geomorph.2020.107333

Huang MYF, Montgomery DR. 2012. Fluvial response to rapid episodic erosion by earthquake and typhoons, Tachia River, central Taiwan. Geomorphology **175**–**176** : 126–138. DOI: 10.1016/j.geomorph.2012.07.004

Huang R, Fan X. 2013. The landslide story. Nature Geoscience **6** : 325–326. DOI: 10.1038/ngeo1806

Huang R, Li W. 2014. Post-earthquake landsliding and long-term impacts in

the Wenchuan earthquake area, China. Engineering Geology **182** : 111–120. DOI: 10.1016/j.enggeo.2014.07.008

Hubert JF, Filipov AJ. 1989. Debris-flow deposits in alluvial fans on the west flank of the White Mountains, Owens Valley, California, U.S.A. Sedimentary Geology **61** : 177–205. DOI: 10.1016/0037-0738(89)90057-2

Huffman G, Bolvin D, Braithwaite D, Hsu K, Joyce R, Xie P. 2014. Integrated Multi-satellitE Retrievals for GPM (IMERG), version 4.4. NASA's Precipitation Processing Center : ftp://arthurhou.pps.eosdis.nasa.gov/gpmdata/. [online] Available from: ftp://arthurhou.pps.eosdis.nasa.gov/gpmdata/ (Accessed 26 June 2022)

Hungr O, McDougall S, Bovis M. 2005a. Entrainment of material by debris flows. In Debris-flow hazards and related phenomena , Jakob M and Hungr O (eds). Springer: Berlin, Heidelberg; 135–158.

Hungr O, McDougall S, Bovis M. 2005b. Entrainment of material by debris flows. In Debris-flow hazards and related phenomena , . Springer: Berlin, Heidelberg; 135–158.

Hungr O, McDougall S, Wise M, Cullen M. 2008. Magnitude-frequency relationships of debris flows and debris avalanches in relation to slope relief. Geomorphology **96** : 355–365. DOI: 10.1016/j.geomorph.2007.03.020

Hungr O, Morgan GC, Kellerhals R. 1984. Quantitative analysis of debris torrent hazards for design of remedial measures. Canadian Geotechnical Journal **21** : 663–677. DOI: 10.1139/t84-073

Hürlimann M, McArdell BW, Rickli C. 2015. Field and laboratory analysis of the runout characteristics of hillslope debris flows in Switzerland. Geomorphology **232** : 20–32. DOI: 10.1016/j.geomorph.2014.11.030

Hürlimann M, Rickenmann D, Medina V, Bateman A. 2008. Evaluation of approaches to calculate debris-flow parameters for hazard assessment. Engineering Geology **102** : 152–163. DOI: 10.1016/j.enggeo.2008.03.012

Ibbeken H, Warnke DA, Diepenbroek M. 1998. Granulometric study of the Hanaupah Fan, Death Valley, California. Earth Surface Processes and Landforms **23** : 481–492.

Innes JL. 1985. Magnitude-Frequency Relations of Debris Flows in Northwest

Europe. Geografiska Annaler, Series A: Physical Geography **67** : 23–32.

Iverson RM. 1997. The Physics of Debris Flows. Review of Geophysics **35** : 245–296.

Iverson RM. 2003. The debris-flow rheology myth. International Conference on Debris-Flow Hazards Mitigation: Mechanics, Prediction, and Assessment, Proceedings **1** : 303–314.

Iverson RM. 2005. Regulation of landslide motion by dilatancy and pore pressure feedback. Journal of Geophysical Research: Earth Surface **110** : 1–16. DOI: 10.1029/2004JF000268

Iverson RM, Denlinger RP. 2001. Flow of variably fluidized granular masses across three-dimesnional terrain 1.Coulomb mixture theory. Journal of Geophysical Research **106** : 537–552.

Iverson RM, Logan M, LaHusen RG, Berti M. 2010. The perfect debris flow? Aggregated results from 28 large-scale experiments. Journal of Geophysical Research **115** DOI: 10.1029/2009jf001514

Iverson RM, Ouyang C. 2015. Entrainment of bed material by Earth-surface mass flows: Review and reformulation of depth-integrated theory. Reviews of Geophysics **53** : 27–58. DOI: 10.1029/88EO01108

Iverson RM, Reid ME, Lahusen RG. 1997. Debris-flow mobilization from landslides. Annu. Rev. Earth Planet Sci. **25** : 85–138.

Iverson RM, Reid ME, Logan M, LaHusen RG, Godt JW, Griswold JP. 2011. Positive feedback and momentum growth during debris-flow entrainment of wet bed sediment. Nature Geoscience **4** : 116–121. DOI: 10.1038/ngeo1040

Iverson RM, Vallance JW. 2001. New views of granular mass flows. Geology **29** : 115–118. DOI: 10.1130/0091-7613(2001)029<0115:NVOGMF>2.0.CO;2

Jakob M. 2005. A size classification for debris flows. Engineering Geology **79** : 151–161. DOI: 10.1016/j.enggeo.2005.01.006

Jakob M, Bovis M, Oden M. 2005. The significance of channel recharge rates for estimating debris-flow magnitude and frequency. Earth Surface Processes and Landforms **30** : 755–766. DOI: 10.1002/esp.1188

Jakob M, Hungr O. 2005. Debris flow hazards and related phenomena

Jakob M, Stein D, Ulmi M. 2012. Vulnerability of buildings to debris flow impact. Natural Hazards **60** : 241–261. DOI: 10.1007/s11069-011-0007-2

Johnson AM. 1970. Physical Processes in Geology . Freeman Cooper: San Francisco

Johnson AM, Rodine JR. 1984. Debris Flow. In Slope Instability , . 257–361.

Johnson CG, Kokelaar BP, Iverson RM, Logan M, Lahusen RG, Gray JMNT. 2012. Grain-size segregation and levee formation in geophysical mass flows. Journal of Geophysical Research: Earth Surface **117** : 1–23. DOI: 10.1029/2011JF002185

Jones JN, Boulton SJ, Stokes M, Bennett GL, Whitworth MRZ. 2021. 30-year record of Himalaya mass-wasting reveals landscape perturbations by extreme events. Nature Communications **12** : 1–15. DOI: 10.1038/s41467-021-26964-8

Kaitna R, Dietrich WE, Hsu L. 2014. Surface slopes, velocity profiles and fluid pressure in coarse-grained debris flows saturated with water and mud. Journal of Fluid Mechanics **741** : 377–403. DOI: 10.1017/jfm.2013.675

Kaitna R, Palucis MC, Yohannes B, Hill KM, Dietrich WE. 2016. Effects of coarse grain size distribution and fine particle content on pore fluid pressure and shear behavior in experimental debris flows. Journal of Geophysical Research: Earth Surface **121** : 415–441. DOI: 10.1002/2015JF003725

Kargel JS et al. 2016. Geomorphic and geologic controls of geohazards induced by Nepal's 2015 Gorkha earthquake. Science **351** DOI: 10.1126/science.aac8353

Kean JW, Coe JA, Coviello V, Smith JB, McCoy SW, Arattano M. 2015. Estimating rates of debris flow entrainment from ground vibrations. Geophysical Research Letters **42** : 6365–6372. DOI: 10.1002/2015GL064811

Kean JW, Staley DM, Cannon SH. 2011. In situ measurements of post-fire debris flows in southern California: Comparisons of the timing and magnitude of 24 debris-flow events with rainfall and soil moisture conditions. Journal of Geophysical Research: Earth Surface **116** : 1–21. DOI: 10.1029/2011JF002005

Kean JW, Staley DM, Lancaster JT, Rengers FK, Swanson BJ, Coe JA, Hernandez JL, Sigman AJ, Allstadt KE, Lindsay DN. 2019. Inundation, flow dynamics, and damage in the 9 January 2018 Montecito debris-flow event,

California, USA: Opportunities and challenges for post-wildfire risk assessment. Geosphere **15** : 1140–1163. DOI: 10.1130/GES02048.1

Keefer DK. 1984. Landslides caused by earthquakes. Geological Society of America Bulletin **95** : 406–421.

Kellerhals R, Bray D. 1971. Sampling Procedures for Coarse Fluvial Sediments. Journal of the Hydraulics Division **97** : 1165–1180.

Kim BC, Lowe DR. 2004. Depositional processes of the gravelly debris flow deposits, South Dolomite alluvial fan, Owens Valley, California. Geosciences Journal **8** : 153–170.

Kim SB, Chough SK, Chun SS. 1995. Bouldery deposits in the lowermost part of the Cretaceous Kyokpori Formation, SW Korea: cohesionless debris flows and debris falls on a steep-gradient delta slope. Sedimentary Geology **98** : 97–119. DOI: 10.1016/0037-0738(95)00029-8

Kirby E, Whipple KX, Tang W, Chen Z. 2003. Distribution of active rock uplift along the eastern margin of the Tibetan Plateau: Inferences from bedrock channel longitudinal profiles. Journal of Geophysical Research: Solid Earth **108** DOI: 10.1029/2001jb000861

Kirchner JW, Finkel RC, Riebe CS, Granger DE, Clayton JL, King JG, Megahan WF. 2001. Mountain erosion over 10 yr, 10 k.y., and 10 m.y. time scales. Geology **29** : 591–594. DOI: 10.1130/0091-7613(2001)029<0591:MEOYKY>2.0.CO;2

Kober F, Hippe K, Salcher B, Ivy-Ochs S, Kubik PW, Wacker L, Hählen N. 2012. Debris-flow-dependent variation of cosmogenically derived catchment-wide denudation rates. Geology **40** : 935–938. DOI: 10.1130/G33406.1

Kokelaar BP, Graham RL, Gray JMNT, Vallance JW. 2014. Fine-grained linings of leveed channels facilitate runout of granular flows. Earth and Planetary Science Letters **385** : 172–180. DOI: 10.1016/j.epsl.2013.10.043

Lai VH, Tsai VC, Lamb MP, Ulizio TP, Beer AR. 2018. The Seismic Signature of Debris Flows: Flow Mechanics and Early Warning at Montecito, California. Geophysical Research Letters **45** : 5528–5535. DOI: 10.1029/2018GL077683

Lang N, Irniger A, Rozniak A, Hunziker R, Wegner JD, Schindler K. 2021. GRAINet: Mapping grain size distributions in river beds from UAV images with

convolutional neural networks. Hydrology and Earth System Sciences **25** : 2567–2597. DOI: 10.5194/hess-2020-196

Lanzoni S, Gregoretti C, Stancanelli LM. 2017. Coarse-grained debris flow dynamics on erodible beds. Journal of Geophysical Research: Earth Surface **122** : 592–614. DOI: 10.1002/2016JF004046

Li GK, West AJ, Densmore AL, Hammond DE, Jin Z, Zhang F, Wang J, Hilton RG. 2016. Connectivity of earthquake-triggered landslides with the fluvial network: Implications for landslide sediment transport after the 2008 Wenchuan earthquake. Journal of Geophysical Research: Earth Surface **121** : 703–724. DOI: 10.1002/2015JF003718

Li GK, West AJ, Densmore AL, Jin Z, Parker RN, Hilton RG. 2014. Seismic mountain building: Landslides associated with the 2008 Wenchuan earthquake in the context of a generalized model for earthquake volume balance. Geochemistry, Geophysics, Geosystems **15** : 833–844. DOI: 10.1002/2013GC005067

Lin CW, Shieh CL, Yuan BD, Shieh YC, Liu SH, Lee SY. 2004. Impact of Chi-Chi earthquake on the occurrence of landslides and debris flows: Example from the Chenyulan River watershed, Nantou, Taiwan. Engineering Geology **71** : 49–61. DOI: 10.1016/S0013-7952(03)00125-X

Lin GW, Chen H, Chen YH, Horng MJ. 2008. Influence of typhoons and earthquakes on rainfall-induced landslides and suspended sediments discharge. Engineering Geology **97** : 32–41.

Liu-Zeng J et al. 2009. Co-seismic ruptures of the 12 May 2008, Ms 8.0 Wenchuan earthquake, Sichuan: East-west crustal shortening on oblique, parallel thrusts along the eastern edge of Tibet. Earth and Planetary Science Letters **286** : 355–370. DOI: 10.1016/j.epsl.2009.07.017

Liu-Zeng J, Wen L, Oskin M, Zeng L. 2011. Focused modern denudation of the Longmen Shan margin, eastern Tibetan Plateau. Geochemistry, Geophysics, Geosystems **12** : 1–21. DOI: 10.1029/2011GC003652

Locat P, Couture R, Leroueil S, Locat J, Jaboyedoff M. 2006. Fragmentation energy in rock avalanches. Canadian Geotechnical Journal **43** : 830–851. DOI: 10.1139/T06-045

Logan M, Iverson RM, Obryk MK. 2018. Video documentation of experiments at the USGS debris-flow flume 1992–2017 (ver 1.4, January 2018). U.S. Geological Survey Open-File Report 2007–1315 : https://doi.org/10.3133/ofr20071315.

Luna BQ, Remaître A, van Asch TWJ, Malet JP, van Westen CJ. 2012. Analysis of debris flow behavior with a one dimensional run-out model incorporating entrainment. Engineering Geology **128** : 63–75. DOI: 10.1016/j.enggeo.2011.04.007

Ma L. 2002. Geological Atlas of China . Geological Publishing House: Beijing

Major JJ. 1997. Depositional processes in large-scale debris-flow experiments. Journal of Geology **105** : 345–366. DOI: 10.1086/515930

Major JJ, Iverson RM. 1999. Debris-flow deposition: Effects of pore-fluid pressure and friction concentrated at flow margins. GSA Bulletin **111** : 1424–1434.

Major JJ, Pierson TC. 1992. Debris Flow Rheology' Experimental Analysis of Fine-Grained Slurries

Major JJ, Pierson TC, Scott KM. 2007. Debris flows at Mount St. Helens, Washington, USA. Debris-flow Hazards and Related Phenomena : 685–731. DOI: 10.1007/3-540-27129-5_27

Major JJ, Voight B. 1986. Sedimentology and clast orientations of the 18 May 1980 southwest-flank lahars, Mount St. Helens, Washington. Journal of Sedimentary Petrology **56** : 691–705. DOI: 10.1306/212F8A1C-2B24-11D7-8648000102C1865D

Makris S, Manzella I, Cole P, Roverato M. 2020. Grain size distribution and sedimentology in volcanic mass-wasting flows: implications for propagation and mobility. International Journal of Earth Sciences DOI: 10.1007/s00531-020-01907-8

Malamud BD, Turcotte DL, Guzzetti F, Reichenbach P. 2004. Landslide inventories and their statistical properties. Earth Surface Processes and Landforms **29** : 687–711.

Mangeney-Castelnau A. 2003. Numerical modeling of avalanches based on Saint Venant equations using a kinetic scheme. Journal of Geophysical

Research **108** : 1–18. DOI: 10.1029/2002jb002024

Mangeney A, Roche O, Hungr O, Mangold N, Faccanoni G, Lucas A. 2010. Erosion and mobility in granular collapse over sloping beds. Journal of Geophysical Research: Earth Surface **115** : 1–21. DOI: 10.1029/2009JF001462

Marc O, Hovius N, Meunier P. 2016a. The mass balance of earthquakes and earthquake sequences. Geophysical Research Letters **43** : 3708–3716. DOI: 10.1002/2016GL068333

Marc O, Hovius N, Meunier P, Gorum T, Uchida T. 2016b. A seismologically consistent expression for the total area and volume of earthquake-triggered landsliding. Journal of Geophysical Research: Earth Surface **121** : 640–663. DOI: 10.1002/2015JF003732

Marc O, Turowski JM, Meunier P. 2021. Controls on the grain size distribution of landslides in Taiwan : the influence of drop height , scar depth and bedrock strength. Earth Surf. Dynam **9** : 995–1011. DOI: https://doi.org/10.5194/esurf-9-995-2021

Marchi L, Arattano M, Deganutti AM. 2002. Ten years of debris-flow monitoring in the Moscardo Torrent (Italian Alps). Geomorphology **46** : 1–17.

Marchi L, D'Agostino V. 2004. Estimation of debris-flow magnitude in the Eastern Italian Alps. Earth Surface Processes and Landforms **29** : 207–220. DOI: 10.1002/esp.1027

Marino P, Siva Subramanian S, Fan X, Greco R. 2022. Changes in debris-flow susceptibility after the Wenchuan earthquake revealed by meteorological and hydro-meteorological thresholds. Catena **210** DOI: 10.1016/j.catena.2021.105929

May CL, Gresswell RE. 2004. Spatial and temporal patterns of debris-flow deposition in the Oregon Coast Range, USA. Geomorphology **57** : 135–149. DOI: 10.1016/S0169-555X(03)00086-2

McArdell BW, Bartelt P, Kowalski J. 2007. Field observations of basal forces and fluid pore pressure in a debris flow. Geophysical Research Letters **34** : 2–5. DOI: 10.1029/2006GL029183

McCoy SW. 2012. Controls on Erosion and Transport of Mass by Debris Flows, University of Colorado [online] Available from:

https://vpn.utm.my/docview/1095127242?accountid=41678

McCoy SW. 2015. Infrequent, large-magnitude debris flows are important agents of landscape change. Geology **43** : 463–463. DOI: 10.1130/focus052015.1

McCoy SW, Kean JW, Coe JA, Tucker GE, Staley DM, Wasklewicz TA. 2012. Sediment entrainment by debris flows: In situ measurements from the headwaters of a steep catchment. Journal of Geophysical Research: Earth Surface **117** : 1–25. DOI: 10.1029/2011JF002278

McCoy SW, Tucker GE, Kean JW, Coe JA. 2013. Field measurement of basal forces generated by erosive debris flows. Journal of Geophysical Research: Earth Surface **118** : 589–602. DOI: 10.1002/jgrf.20041

McDougall S, Boultbee N, Hungr O, Stead D, Schwab JW. 2006. The Zymoetz River landslide, British Columbia, Canada: Description and dynamic analysis of a rock slide-debris flow. Landslides **3** : 195–204. DOI: 10.1007/s10346-006-0042-3

McDougall S, Hungr O. 2005. Dynamic modelling of entrainment in rapid landslides. Canadian Geotechnical Journal **42** : 1437–1448. DOI: 10.1139/t05-064

McGuire LA, Kean JW, Staley DM, Rengers FK, Wasklewicz TA. 2016. Constraining the relative importance of raindrop- and flow-driven sediment transport mechanisms in postwildfire environments and implications for recovery time scales. Journal of Geophysical Research: Earth Surface **121** : 2211–2237. DOI: 10.1002/2016JF003867

McGuire LA, McCoy SW, Marc O, Struble W, Barnhart KR, Mcguire L. 2022. Steady-state forms of channel profiles shaped by debris-flow and fluvial processes. Earth Surface Dynamics Discussions : 1–33.

McKenna JP, Santi PM, Amblard X, Negri J. 2012. Effects of soil-engineering properties on the failure mode of shallow landslides. Landslides **9** : 215–228. DOI: 10.1007/s10346-011-0295-3

Meunier P, Hovius N, Haines AJ. 2007. Regional patterns of earthquake-triggered landslides and their relation to ground motion. Geophysical Research Letters **34** : 1–5. DOI: 10.1029/2007GL031337

Meunier P, Hovius N, Haines JA. 2008. Topographic site effects and the location of earthquake induced landslides. Earth and Planetary Science Letters **275** : 221–232. DOI: 10.1016/j.epsl.2008.07.020

Michaelides K, Hollings R, Singer MB, Nichols MH, Nearing MA. 2018. Spatial and temporal analysis of hillslope–channel coupling and implications for the longitudinal profile in a dryland basin. Earth Surface Processes and Landforms **43** : 1608–1621. DOI: 10.1002/esp.4340

Mills HH. 1978. Some characteristics of glacial sediments of Mount Rainier, Washington. Journal of Sedimentary Research **48** : 1345–1356. DOI: 10.1306/212f7685-2b24-11d7-8648000102c1865d

Morell KD, Alessio P, Dunne T, Keller E. 2021. Sediment Recruitment and Redistribution in Mountain Channel Networks by Post-Wildfire Debris Flows. Geophysical Research Letters **48** : 1–10. DOI: 10.1029/2021GL095549

Naylor MA. 1980. The origin of inverse grading in muddy debris flow deposits - a review. Journal of Sedimentary Petrology **50** : 1111–1116. DOI: 10.1306/212f7b8f-2b24-11d7-8648000102c1865d

Neely AB, DiBiase RA. 2020. Drainage Area, Bedrock Fracture Spacing, and Weathering Controls on Landscape-Scale Patterns in Surface Sediment Grain Size. Journal of Geophysical Research: Earth Surface **125** : 1–22. DOI: 10.1029/2020JF005560

Neverman AJ, Fuller IC, Procter JN, Death RG. 2019. Terrestrial laser scanning and structure-from-motion photogrammetry concordance analysis for describing the surface layer of gravel beds. Progress in Physical Geography **43** : 1–22. DOI: 10.1177/0309133318822966

Nishiguchi Y, Uchida T, Takezawa N, Ishizuka T, Mizuyama T. 2012. Runout Characteristics and Grain Size Distribution of Large-scale Debris Flows Triggered by Deep Catastrophic Landslides. International Journal of Erosion Control Engineering **5** : 16–26. DOI: 10.13101/ijece.5.16

O'Brien JS, Julien PY. 1985. Physical properties and mechanics of hyperconcentrated sediment flows. Proceedings of the specialty conference on delineation of landslide, flash flood and debris flow hazard in Utah, Utah State University, Utah. : 260–279.

O'Brien JS, Julien PY. 1988. Laboratory Analysis of Mudflow Properties. Journal of Hydraulic Engineering **114** : 877–887.

Oakley NS, Cannon F, Munroe R, Lancaster JT, Gomberg D, Martin Ralph F. 2018. Brief communication: Meteorological and climatological conditions associated with the 9 January 2018 post-fire debris flows in Montecito and Carpinteria, California, USA. Natural Hazards and Earth System Sciences **18** : 3037–3043. DOI: 10.5194/nhess-18-3037-2018

Ouyang C, He S, Tang C. 2015a. Numerical analysis of dynamics of debris flow over erodible beds in Wenchuan earthquake-induced area. Engineering Geology **194** : 62–72. DOI: 10.1016/j.enggeo.2014.07.012

Ouyang C, He S, Xu Q. 2015b. MacCormack-TVD Finite Difference Solution for Dam Break Hydraulics over Erodible Sediment Beds. Journal of Hydraulic Engineering **141** : 06014026. DOI: 10.1061/(asce)hy.1943-7900.0000986

Ouyang C, He S, Xu Q, Luo Y, Zhang W. 2013. A MacCormack-TVD finite difference method to simulate the mass flow in mountainous terrain with variable computational domain. Computers and Geosciences **52** : 1–10. DOI: 10.1016/j.cageo.2012.08.024

Parker RN, Densmore AL, Rosser NJ, de Michele M, Li Y, Huang R, Whadcoat S, Petley DN. 2011. Mass wasting triggered by the 2008 Wenchuan earthquake is greater than orogenic growth. Nature Geoscience **4** : 449–452.

Parsons JD, Whipple KX, Simoni A. 2001. Experimental study of the grain flow, fluid-mud transition in Debris flows. Journal of Geology **109** : 427–447. DOI: 10.1086/320798

Pearce AJ, Watson AJ. 1986. Effects of earthquake-induced landslides on sediment budget and transport over a 50-year period. Geology **14** : 52–55.

Perron JT. 2017. Climate and the Pace of Erosional Landscape Evolution. Annual Review of Earth and Planetary Sciences **45** : 561–591. DOI: 10.1146/annurev-earth-060614-105405

Phillips CJ, Davies TRH. 1991. Determining rheological parameters of debris flow material. Geomorphology **4** : 101–110. DOI: 10.1016/0169-555X(91)90022-3

Pierson TC. 1981. Dominant particle support mechanisms in debris flows at Mt

Thomas, New Zealand, and implications for flow mobility. Sedimentology **28** : 49–60. DOI: 10.1111/j.1365-3091.1981.tb01662.x

Pierson TC. 1995. Flow characteristics of large eruption-triggered debris flows at snow-clad volcanoes: constraints for debris-flow models. Journal of Volcanology and Geothermal Research **66** : 283–294. DOI: 10.1016/0377-0273(94)00070-W

Pierson TC, Costa JE. 1987. A rheologic classification of subaerial sediment-water flows. GSA Reviews in Engineering Geology **7** : 1–12. DOI: 10.1130/REG7-p1

Pierson TC, Janda RJ, Thouret JC, Borrero CA. 1990. Perturbation and melting of snow and ice by the 13 November 1985 eruption of Nevado del Ruiz, Colombia, and consequent mobilization, flow and deposition of lahars. Journal of Volcanology and Geothermal Research **41** : 17–66. DOI: 10.1016/0377-0273(90)90082-Q

Prochaska AB, Santi PM, Higgins JD, Cannon SH. 2008a. A study of methods to estimate debris flow velocity. Landslides **5** : 431–444. DOI: 10.1007/s10346-008-0137-0

Prochaska AB, Santi PM, Higgins JD, Cannon SH. 2008b. Debris-flow runout predictions based on the average channel slope (ACS). Engineering Geology **98** : 29–40. DOI: 10.1016/j.enggeo.2008.01.011

Prodger S, Russell P, Davidson M. 2017. Grain-size distributions on high-energy sandy beaches and their relation to wave dissipation. Sedimentology **64** : 1289–1302. DOI: 10.1111/sed.12353

Pudasaini SP, Hutter K. 2003. Rapid shear flows of dry granular masses down curved and twisted channels. Journal of Fluid Mechanics **495** : 193–208. DOI: 10.1017/S0022112003006141

Pudasaini SP, Mergili M. 2019. A Multi-Phase Mass Flow Model. Journal of Geophysical Research: Earth Surface **124** : 2920–2942. DOI: 10.1029/2019JF005204

Pudasaini SP, Wang Y, Hutter K. 2005. Modelling debris flows down general channels. Natural Hazards and Earth System Science **5** : 799–819. DOI: 10.5194/nhess-5-799-2005

Purinton B, Bookhagen B. 2019. Introducing PebbleCounts: A grain-sizing tool for photo surveys of dynamic gravel-bed rivers. Earth Surface Dynamics **7** : 859–877. DOI: 10.5194/esurf-2019-20

Purinton B, Bookhagen B. 2021. Tracking Downstream Variability in Large Grain-Size Distributions in the South-Central Andes. Journal of Geophysical Research: Earth Surface **126** : 1–29. DOI: 10.1029/2021jf006260

Rana NM, Ghahramani N, Evans SG, McDougall S, Small A, Take WA. 2021. Catastrophic mass flows resulting from tailings impoundment failures. Engineering Geology **292** : 106262. DOI: 10.1016/j.enggeo.2021.106262

Reid ME, Iverson RM, Logan M, Lahusen RG, Godt JW, Griswold JP. 2011. Entrainment of bed sediment by debris flows: Results from large-scale experiments. International Conference on Debris-Flow Hazards Mitigation: Mechanics, Prediction, and Assessment, Proceedings : 367–374. DOI: 10.4408/IJEGE.2011-03.B-042

Reid ME, LaHusen RG, Iverson RM. 1997. DEBRIS-FLOW INITIATION EXPERIMENTS USING DIVERSE HYDROLOGIC TRIGGERS. Debris-Flow Hazards Mitigation: Mechanics, Prediction and Assessment : 1–11.

Reinaldo G-M, López JL. 2005. Debris flows of December 1999 in Venezuela. In Debris-flow hazards and related phenomena , Jakob M and Hungr O (eds). Springer: Berlin, Heidelberg; 519–538.

Rickenmann D. 1999. Empirical relationships for Debris Flow. Natural hazards **19** : 47–77.

Riley KL, Bendick R, Hyde KD, Gabet EJ. 2013. Frequency-magnitude distribution of debris flows compiled from global data, and comparison with post-fire debris flows in the western U.S. Geomorphology **191** : 118–128. DOI: 10.1016/j.geomorph.2013.03.008

Roback K, Clark MK, West AJ, Zekkos D, Li GK, Gallen SF, Chamlagain D, Godt JW. 2018. The size, distribution, and mobility of landslides caused by the 2015 Mw7.8 Gorkha earthquake, Nepal. Geomorphology **301** : 121–138. DOI: 10.1016/j.geomorph.2017.01.030

Roda-Boluda DC, D'Arcy M, McDonald J, Whittaker AC. 2018. Lithological controls on hillslope sediment supply: insights from landslide activity and

grain size distributions. Earth Surface Processes and Landforms **43** : 956–977. DOI: 10.1002/esp.4281

Roelofs L, Colucci P, de Haas T. 2022. How debris-flow composition affects bed erosion quantity and mechanisms: An experimental assessment. Earth Surface Processes and Landforms : 2151–2169. DOI: 10.1002/esp.5369

Rubin DM. 2004. A simple autocorrelation algorithm for determining grain size from digital images of sediment. Journal of Sedimentary Research **74** : 160–165. DOI: 10.1306/052203740160

Ruiz-Carulla R, Corominas J, Mavrouli O. 2015. A methodology to obtain the block size distribution of fragmental rockfall deposits. Landslides **12** : 815–825. DOI: 10.1007/s10346-015-0600-7

Santi PM, deWolfe VG, Higgins JD, Cannon SH, Gartner JE. 2008. Sources of debris flow material in burned areas. Geomorphology **96** : 310–321. DOI: 10.1016/j.geomorph.2007.02.022

Sanvitale N, Bowman ET. 2017. Visualization of dominant stress-transfer mechanisms in experimental debris flows of different particle-size distribution. Canadian Geotechnical Journal **54** : 258–269. DOI: 10.1139/cgj-2015-0532

Sassa K, Wang G. 2005. Mechanism of landslide-triggered debris flow: Liquefaction phenomena due to the undrained loading of torrent deposits. In Debris flow hazards and related phenomena , Jakob M and Hungr O (eds). 81–101.

Sattar A, Haritashya UK, Kargel JS, Karki A. 2022. Transition of a small Himalayan glacier lake outburst flood to a giant transborder flood and debris flow. Scientific Reports : 1–15. DOI: 10.1038/s41598-022-16337-6

Saunders G. 2014. Development of photogrammetric methods for landslide analysis, University of Oslo [online] Available from: http://urn.nb.no/URN:NBN:no-46693

Savage SB. 1984. The Mechanics of Rapid Granular Flows

Savage SB, Hutter K. 1989. The motion of a finite mass of granular material down a rough incline. Journal of Fluid Mechanics **199** : 177–215. DOI: 10.1017/S0022112089000340

Savage SB, Lun CKK. 1988. Particle size segregation in inclined chute flow of dry cohesionless granular solids. Journal of Fluid Mechanics **189** : 311–335. DOI: 10.1017/S002211208800103X

de Scally FA, Owens IF. 2005. Depositional processes and particle characteristics on fans in the Southern Alps, New Zealand. Geomorphology **69** : 46–56. DOI: 10.1016/j.geomorph.2004.11.021

Scheidl C, McArdell BW, Rickenmann D. 2015. Debris-flow velocities and superelevation in a curved laboratory channel. Canadian Geotechnical Journal **52** : 305–317. DOI: 10.1139/cgj-2014-0081

Schippa L. 2020. Modeling the effect of sediment concentration on the flow-like behavior of natural debris flow. International Journal of Sediment Research **35** : 315–327. DOI: 10.1016/j.ijsrc.2020.03.001

Schürch P, Densmore AL, Rosser NJ, McArdell BW. 2011. Dynamic controls on erosion and deposition on debris-flow fans. Geology **39** : 827–830. DOI: 10.1130/G32103.1

Scott AM, Bridgwater J. 1975. Interparticle Percolation: a Fundamental Solids Mixing Mechanism. Ind. Eng. Chem., Fundam. **14** : 22–27.

Scott KM, Vallance JW, Kerle N, Macías JL, Strauch W, Devoli G. 2005. Catastrophic precipitation-triggered lahar at Casita volcano, Nicaragua: Occurrence, bulking and transformation. Earth Surface Processes and Landforms **30** : 59–79. DOI: 10.1002/esp.1127

Shen P, Zhang LM, Fan RL, Zhu H, Zhang S. 2020. Declining geohazard activity with vegetation recovery during first ten years after the 2008 Wenchuan earthquake. Geomorphology **352** : 106989. DOI: 10.1016/j.geomorph.2019.106989

Sheridan MF, Stinton AJ, Patra A, Pitman EB, Bauer A, Nichita CC. 2005. Evaluating Titan2D mass-flow model using the 1963 Little Tahoma Peak avalanches, Mount Rainier, Washington. Journal of Volcanology and Geothermal Research **139** : 89–102. DOI: 10.1016/j.jvolgeores.2004.06.011

Shugar DH et al. 2021. A massive rock and ice avalanche caused the 2021 disaster at Chamoli, Indian Himalaya. Science **373** : 300–306. [online] Available from: https://doi.org/10.1126/science.abh4455

Shultz AW. 1984. Subaerial debris-flow deposition in the upper paleozoic cutler formation, western Colorado. Journal of sedimentary petrology **54** : 759–772.

Sklar LS, Dietrich WE. 2004. A mechanistic model for river incision into bedrock by saltating bed load. Water Resources Research **40** : 1–22. DOI: 10.1029/2003WR002496

Sklar LS, Dietrich WE. 2006. The role of sediment in controlling steady-state bedrock channel slope: Implications of the saltation-abrasion incision model. Geomorphology **82** : 58–83. DOI: 10.1016/j.geomorph.2005.08.019

Sklar LS, Dietrich WE, Foufoula-Georgiou E, Lashermes B, Bellugi D. 2006. Do gravel bed river size distributions record channel network structure? Water Resources Research **42** : 1–22. DOI: 10.1029/2006WR005035

Sklar LS, Riebe CS, Genetti J, Leclere S, Lukens CE. 2020. Downvalley fining of hillslope sediment in an alpine catchment: implications for downstream fining of sediment flux in mountain rivers. Earth Surface Processes and Landforms **45** : 1828–1845. DOI: 10.1002/esp.4849

Sklar LS, Riebe CS, Marshall JA, Genetti J, Leclere S, Lukens CL, Merces V. 2017. The problem of predicting the size distribution of sediment supplied by hillslopes to rivers. Geomorphology **277** : 31–49. DOI: 10.1016/j.geomorph.2016.05.005

Sohn YK, Rhee CW, Kim BC. 1999. Debris flow and hyperconcentrated flood-flow deposits in an alluvial fan, northwestern part of the Cretaceous Yongdong Basin, Central Korea. Journal of Geology **107** : 111–132. DOI: 10.1086/314334

Sosio R, Crosta GB, Chen JH, Hungr O. 2012. Modelling rock avalanche propagation onto glaciers. Quaternary Science Reviews **47** : 23–40. DOI: 10.1016/j.quascirev.2012.05.010

Sosio R, Crosta GB, Frattini P. 2007. Field observations, rheological testing and numerical modelling of a debris-flow event. Earth Surf. Process. Landforms **32** : 290–306. DOI: 10.1002/esp

Stinton A, Sheridan M, Patra A, Dalbey K, Namikawa N. 2004. Incorporation of variable bed friction into Titan2D mass-flow model: Application to Little

Tahoma Peak avalanches (Washington). Acta Vulcanologica **16** : 1–11.

Stock J, Dietrich WE. 2003. Valley incision by debris flows: Evidence of a topographic signature. Water Resources Research **39** DOI: 10.1029/2001WR001057

Stock JD, Dietrich WE. 2006. Erosion of steepland valleys by debris flows. Bulletin of the Geological Society of America **118** : 1125–1148. DOI: 10.1130/B25902.1

Stoffel M. 2010. Magnitude-frequency relationships of debris flows - A case study based on field surveys and tree-ring records. Geomorphology **116** : 67–76. DOI: 10.1016/j.geomorph.2009.10.009

Storz-Peretz Y, Laronne JB. 2013. Automatic grain sizing of vertical exposures of gravelly deposits. Sedimentary Geology **294** : 13–26. DOI: 10.1016/j.sedgeo.2013.05.004

Strahler AN. 1952. Hypsometric (area-altitude) analysis of erosional topography. Bulletin of the Geological Society of America **63** : 1117–1142.

Strom KB, Kuhns RD, Lucas HJ. 2010. Comparison of Automated Image-Based Grain Sizing to Standard Pebble-Count Methods. Journal of Hydraulic Engineering **136** : 461–473. DOI: 10.1061/(asce)hy.1943-7900.0000198

Takahashi BT, Nakagawa H, Harada T, Yamashiki Y. 1992. Routing debris flows with particle segregation. Journal of Hydraulic Engineering **118** : 1490–1507.

Takahashi T. 1981. Debris Flow. Annu. Rev. Fluid Mech **13** : 57–77.

Takahashi T. 2007. Debris flow: mechanics, prediction and countermeasures. . 2nd ed. Taylor & Francis

Tang C, Van Asch TWJ, Chang M, Chen GQ, Zhao XH, Huang XC. 2012a. Catastrophic debris flows on 13 August 2010 in the Qingping area, southwestern China: The combined effects of a strong earthquake and subsequent rainstorms. Geomorphology **139–140** : 559–576. DOI: 10.1016/j.geomorph.2011.12.021

Tang C, Zhu J, Chang M, Ding J, Qi X. 2012b. An empirical-statistical model for predicting debris-flow runout zones in the Wenchuan earthquake area. Quaternary International **250** : 63–73. DOI: 10.1016/j.quaint.2010.11.020

Tang C, Zhu J, Chang M, Ding J, Qi X. 2012c. An empirical-statistical model for predicting debris-flow runout zones in the Wenchuan earthquake area. Quaternary International **250** : 63–73. DOI: 10.1016/j.quaint.2010.11.020 [online] Available from: http://dx.doi.org/10.1016/j.quaint.2010.11.020

Tang C, Zhu J, Ding J, Cui X, Chen L, Zhang J. 2011a. Catastrophic debris flows triggered by a 14 August 2010 rainfall at the epicenter of the Wenchuan earthquake. Landslides **8** : 485–497. DOI: 10.1007/s10346-011-0269-5

Tang C, Zhu J, Li WL, Liang JT. 2009. Rainfall-triggered debris flows following the Wenchuan earthquake. Bulletin of Engineering Geology and the Environment **68** : 187–194. DOI: 10.1007/s10064-009-0201-6

Tang C, Zhu J, Qi X. 2010. Landslide hazard assessment of the 2008 Wenchuan earthquake: a case study in Beichuan area. Canadian Geotechnical Journal **48** : 128–145. DOI: 10.1139/t10-059

Tang C, Zhu J, Qi X, Ding J. 2011b. Landslides induced by the Wenchuan earthquake and the subsequent strong rainfall event: A case study in the Beichuan area of China. Engineering Geology **122** : 22–33. DOI: 10.1016/j.enggeo.2011.03.013

Tang H, McGuire LA, Rengers FK, Kean JW, Staley DM, Smith JB. 2019. Evolution of Debris-Flow Initiation Mechanisms and Sediment Sources During a Sequence of Postwildfire Rainstorms. Journal of Geophysical Research: Earth Surface **124** : 1572–1595. DOI: 10.1029/2018JF004837

Tecca PR, Deganutti AM, Genevois R, Galgaro A. 2003. Velocity distributions in a coarse debris flow. International Conference on Debris-Flow Hazards Mitigation: Mechanics, Prediction, and Assessment, Proceedings **2** : 905–916.

Theule JI, Liébault F, Laigle D, Loye A, Jaboyedoff M. 2015. Channel scour and fill by debris flows and bedload transport. Geomorphology **243** : 92–105. DOI: 10.1016/j.geomorph.2015.05.003

Theule JI, Liébault F, Loye A, Laigle D, Jaboyedoff M. 2012. Sediment budget monitoring of debris-flow and bedload transport in the Manival Torrent, SE France. Natural Hazards and Earth System Science **12** : 731–749. DOI: 10.5194/nhess-12-731-2012

Thornton AR, Gray JMNT, Hogg AJ. 2006. A three-phase mixture theory for

particle size segregation in shallow granular free-surface flows. Journal of Fluid Mechanics **550** : 1–25. DOI: 10.1017/S0022112005007676

Tiranti D, Bonetto S, Mandrone G. 2008. Quantitative basin characterisation to refine debris-flow triggering criteria and processes: An example from the Italian Western Alps. Landslides **5** : 45–57. DOI: 10.1007/s10346-007-0101-4

Tucker GE, Hancock GR. 2010. Modelling Landscape Evolution. Earth Surface Processes and Landforms **35** : 28–50. DOI: 10.1002/esp

Turnbull B, Bowman ET, McElwaine JN. 2015. Debris flows: Experiments and modelling. Comptes Rendus Physique **16** : 86–96. DOI: 10.1016/j.crhy.2014.11.006

Valagussa A, Marc O, Frattini P, Crosta GB. 2019. Seismic and geological controls on earthquake-induced landslide size. Earth and Planetary Science Letters **506** : 268–281. DOI: 10.1016/j.epsl.2018.11.005

Vallance JW, Savage SB. 2000. Particle segregation in granular flows down chutes. In International Union of Theoretical and Applied Mechanics Symposium on Segregation in Granular Flows , Rosato A and Blackmore D (eds). Dordrecht, The Netherlands; 31–51.

Vallance JW, Scott KM. 1997. The Osceola Mudflow from Mount Rainier: Sedimentology and hazard implications of a huge clay-rich debris flow. Bulletin of the Geological Society of America **109** : 143–163.

Vázquez-Tarrío D, Borgniet L, Liébault F, Recking A. 2017. Using UAS optical imagery and SfM photogrammetry to characterize the surface grain size of gravel bars in a braided river (Vénéon River, French Alps). Geomorphology **285** : 94–105. DOI: 10.1016/j.geomorph.2017.01.039

Vilímek V, Klimeš J, Vlcko J, Carreño R. 2006. Catastrophic debris flows near Machu Picchu village (Aguas Calientes), Peru. Environmental Geology **50** : 1041–1052. DOI: 10.1007/s00254-006-0276-3

Viroulet S, Edwards AN, Johnson CG, Kokelaar BP, Gray JMNT. 2019. Shedding dynamics and mass exchange by dry granular waves flowing over erodible beds. Earth and Planetary Science Letters **523** : 115700. DOI: 10.1016/j.epsl.2019.07.003

Wang G, Sassa K. 2003. Pore-pressure generation and movement of rainfall-

induced landslides: Effects of grain size and fine-particle content. Engineering Geology **69** : 109–125. DOI: 10.1016/S0013-7952(02)00268-5

Wang J, Jin Z, Hilton RG, Zhang F, Densmore AL, Li GK, West AJ. 2015. Controls on fluvial evacuation of sediment from earthquake-triggered landslides. Geology **43** : 115–118. DOI: 10.1130/G36157.1

Westoby MJ, Dunning SA, Woodward J, Hein A, Marrero SM, Winter K, Sugden DE. 2015. Sedimentological characterization of Antarctic moraines using UAVs and Structure-from-Motion photogrammetry. Journal of Glaciology **61** : 1088–1102. DOI: 10.3189/2015jog15j086

Whipple KX. 1992. Predicting debris-flow runout and deposition on fans: the importance of the flow hydrograph. Erosion, debris flows and environment in mountain regions. Proc. international symposium, Chendgu, 1992 : 337–345.

Whipple KX, Dunne T. 1992. The influence of debris-flow rheology on fan morphology, Owens Valley, California. Geological Society Of America Bulletin **104** : 887–900.

Whittaker AC, Attal M, Allen PA. 2010. Characterising the origin, nature and fate of sediment exported from catchments perturbed by active tectonics. Basin Research **22** : 809–828. DOI: 10.1111/j.1365-2117.2009.00447.x

Wilkinson PL, Anderson MG, Lloyd DM. 2002. An integrated hydrological model for rain-induced landslide prediction. Earth Surface Processes and Landforms **27** : 1285–1297. DOI: 10.1002/esp.409

Wohl EE, Anthony DJ, Madsen SW, Thompson DM. 1996. A comparison of surface sampling methods for coarse fluvial sediments. Water Resources Research **32** : 3219–3226. DOI: 10.1029/96WR01527

Wolman MG. 1954. A method of sampling coarse river-bed material. Eos, Transactions American Geophysical Union **35** : 951–956. DOI: 10.1029/TR035i006p00951

Woodhouse MJ, Thornton AR, Johnson CG, Kokelaar BP, Gray JMNT. 2012. Segregation-induced fingering instabilities in granular free-surface flows. Journal of Fluid Mechanics **709** : 543–580. DOI: 10.1017/jfm.2012.348

Xie J, Coulthard TJ, McLelland SJ. 2022. Modelling the impact of seismic triggered landslide location on basin sediment yield, dynamics and

connectivity. Geomorphology **398** : 108029. DOI: 10.1016/j.geomorph.2021.108029

Xu X, Wen X, Yu G, Chen G, Klinger Y, Hubbard J, Shaw J. 2009. Coseismic reverse- and oblique-slip surface faulting generated by the 2008 Mw 7.9 Wenchuan earthquake, China. Geology **37** : 515–518. DOI: 10.1130/G25462A.1

Yang F, Fan X, Siva Subramanian S, Dou X, Xiong J, Xia B, Yu Z, Xu Q. 2021. Catastrophic debris flows triggered by the 20 August 2019 rainfall, a decade since the Wenchuan earthquake, China. Landslides **18** : 3197–3212. DOI: 10.1007/s10346-021-01713-6

Yanites BJ, Tucker GE, Mueller KJ, Chen YG. 2010. How rivers react to large earthquakes: Evidence from central Taiwan. Geology **38** : 639–642. DOI: 10.1130/G30883.1

Yong L, Xiaojun Z, Pengcheng S, Yingde K, Jingjing L. 2013. A scaling distribution for grain composition of debris flow. Geomorphology **192** : 30–42. DOI: 10.1016/j.geomorph.2013.03.015

Yunus AP, Fan X, Tang X, Jie D, Xu Q, Huang R. 2020. Decadal vegetation succession from MODIS reveals the spatio-temporal evolution of post-seismic landsliding after the 2008 Wenchuan earthquake. Remote Sensing of Environment **236** : 111476. DOI: 10.1016/j.rse.2019.111476

Zhang F et al. 2019. Monsoonal control on a delayed response of sedimentation to the 2008 Wenchuan earthquake. Science Advances **5** : eaav7110. DOI: 10.1126/sciadv.aav7110

Zhang LM, Xu Y, Huang RQ, Chang DS. 2011. Particle flow and segregation in a giant landslide event triggered by the 2008 Wenchuan earthquake, Sichuan, China. Natural Hazards and Earth System Science **11** : 1153–1162. DOI: 10.5194/nhess-11-1153-2011

Zhang S, Wang F, Li R. 2022. First insight into the catastrophic Atami debris flow induced by a rain gush on 3 July 2021 in Shizuoka, Japan. Landslides **19** : 527–532. DOI: 10.1007/s10346-021-01788-1 [online] Available from: https://doi.org/10.1007/s10346-021-01788-1

Zhang S, Zhang L, Lacasse S, Nadim F. 2016. Evolution of Mass Movements near Epicentre of Wenchuan Earthquake, the First Eight Years. Scientific

Reports **6** DOI: 10.1038/srep36154

Zhang S, Zhang LM. 2017a. Impact of the 2008 Wenchuan earthquake in China on subsequent long-term debris flow activities in the epicentral area. Geomorphology **276** : 86–103. DOI: 10.1016/j.geomorph.2016.10.009 [online] Available from: http://dx.doi.org/10.1016/j.geomorph.2016.10.009

Zhang S, Zhang LM. 2017b. Impact of the 2008 Wenchuan earthquake in China on subsequent long-term debris flow activities in the epicentral area. Geomorphology **276** : 86–103. DOI: 10.1016/j.geomorph.2016.10.009

Zhang S, Zhang LM, Chen HX. 2014a. Relationships among three repeated large-scale debris flows at Pubugou Ravine in the Wenchuan earthquake zone. Canadian Geotechnical Journal **51** : 951–965. DOI: 10.1139/cgj-2013-0368

Zhang S, Zhang LM, Chen HX, Yuan Q, Pan H. 2013. Changes in runout distances of debris flows over time in the Wenchuan earthquake zone. Journal of Mountain Science **10** : 281–292. DOI: 10.1007/s11629-012-2506-y

Zhang W, Wang Q, Chen J, Li H, Que J, Kong Y. 2015. Grain-size analysis of debris flow alluvial fans in Panxi Area along Jinsha River, China. Sustainability (Switzerland) **7** : 15219–15242. DOI: 10.3390/su71115219

Zhang Y, Cheng Y, Yin Y, Lan H, Wang J, Fu X. 2014b. High-position debris flow: A long-term active geohazard after the Wenchuan earthquake. Engineering Geology **180** : 45–54. DOI: 10.1016/j.enggeo.2014.05.014

Zhang Z, Walter F, McArdell BW, de Haas T, Wenner M, Chmiel M, He S. 2021a. Analyzing Bulk Flow Characteristics of Debris Flows Using Their High Frequency Seismic Signature. Journal of Geophysical Research: Solid Earth **126** : 1–19. DOI: 10.1029/2021JB022755

Zhang Z, Walter F, McArdell BW, Wenner M, Chmiel M, de Haas T, He S. 2021b. Insights From the Particle Impact Model Into the High-Frequency Seismic Signature of Debris Flows. Geophysical Research Letters **48** : 1–11. DOI: 10.1029/2020GL088994